UNIVERSIDAD AUTÓNOMA DE MADRID

DEPARTAMENTO DE FÍSICA DE LA MATERIA CONDENSADA

MAGNETIC RESONANCE IMAGING OF APPETITE-INDUCED HYPOTHALAMIC ACTIVITY

BLANCA LIZARBE SERRA

MADRID, 2013

UNIVERSIDAD AUTÓNOMA DE MADRID

DEPARTAMENTO DE FÍSICA DE LA MATERIA CONDENSADA

MAGNETIC RESONANCE IMAGING OF APPETITE-INDUCED HYPOTHALAMIC ACTIVITY

BLANCA LIZARBE SERRA

Licenciada en Física

Directores

Dr. Sebastián Cerdán García-Esteller

Dra. Pliar López-Larrubia

Dr. Juan José Saenz

Tesis Doctoral realizada en el Instituto de Investigaciones Biomédicas "Alberto Sols"

Agradecimientos/Acknowledgements

Esta tesis se ha desarrollado a partir de un proyecto ideado por el Prof. Dr. Sebastián Cerdán. A mi llegada al laboratorio, él me transmitió las herramientas y conocimientos necesarios para poder desenvolverme en el trabajo. En este sentido, mi primer agradecimiento es para el Dr. Sebastián Cerdán. Por el tiempo dedicado a contarme, escucharme, responderme, y por darme la libertad de equivocarme. Por la confianza y el respeto; en definitiva, por ser mi profesor y vivir la ciencia con dedicación verdadera.

A la Dra. Pilar López Larrubia, por ayudarme sin vacilación en las distintas etapas que he pasado como estudiante pre-doctoral. Por prestarse a soluciones desde el móvil, desde el fijo, desde una escalera o desde debajo de toneladas de magnetismo. Y, siempre con un sitio para mí en su despacho, por su claridad en la resolución de mis dudas.

Al Dr. Juan José Saenz, por ser el contacto académico –e imprescindible- con la Física, con la Universidad, por su disponibilidad y optimismo, gracias.

Debo agradecer al Prof. Jimmy Bell, del laboratorio Molecular and Metabolic Imaging Group, del Imperial College London, por dirigir mi estancia breve en su grupo. Thanks for all the efforts made for my integration in the group, for the scientific dedication in the development of my little DWI project in London. Special thanks to Jelena Anastasovksa, my –almost- own guide in Hammersmith, to Gina Sánchez-Canon, Meliz Sahuri, Sarah Schofield, Margena Wylezinska-Arridge and Jordi Lopez-Tremoleda. For all the time and efforts dedicated to me and my project.

Gracias a los miembros de la Unidad de Cirugía Experimental de La Paz, a la Dra. Carlota Largo, Dra. María Tabernero y el Dr. Víctor Caz, por su colaboración en el estudio de la obesidad inducida por administración de dietas hipercalóricas. Además, han realizado todas las medidas de hormonas en sangre que se presentan en esta tesis.

Quiero agradecer a la Dra. María Luisa García-Martín, su ayuda –y disponibilidad- en la realización de los experimentos piloto en sujetos humanos, y a los médicos del servicio de resonancia y neuroradiología de la Clínica del Rosario. Gracias a los voluntarios del estudio, por comer, por no comer, y por las horas de resonancias. Gracias al Dr. Juan Antonio Hernández-Tamames, al Dr. Pablo Serrano-Balazote, y al equipo de Neuroendocrinas del hospital universitario de Fuenlabrada, por intentar llevar a cabo un proyecto conjunto.

Al grupo del Dr. Mario Vallejo, en especial al Dr. Mario Vallejo y al Dr. Antonio Fernández, quiero agradecer su ayuda en la interpretación de las mediciones en las Jaulas Metabólicas, y por realizar los análisis de activación de c-fos en hipotálamo.

A los miembros del SIERMAC, el servicio de resonancia, así como a los compañeros que primero me vieron llegar, gracias por ayudarme en todas aquellas tareas que yo, inexperta, no era capaz de realizar. Sin Teresa Navarro, Rocío Pérez, Patricia Sánchez, y Daniel Calle me hubiera sido imposible comenzar a trabajar con animales. A los miembros del SIERMAC, los fijos y los temporales (o con regreso, María Rodríguez) gracias por el apoyo técnico en las jornadas *de máquina*, por intentar ayudarme y por conseguirlo.

Quiero dar un agradecimiento explícito a mi compañero Daniel Calle, con quien he compartido el trabajo diario durante los últimos cuatro años: gracias Dani por tu ayuda constante e incondicional. También he compartido trabajo con Ania Benítez, quien ha desarrollado el software de clasificación de sujetos ayunados o alimentados, que se publicó en un artículo y se describe en esta tesis. Además, Ania siempre ha tenido respuestas a mis preguntas de Matlab: gracias Ania, tus líneas están en mi código. En este sentido, la llegada de Gerardo Arturo Peláez ha supuesto un gran – y didáctico- apoyo informático para cualquiera que haya preguntado, como ha sido mi caso, así que se lo agradezco. A Patricia Sánchez quiero darle las gracias por su trabajo, con control y eficacia. Gracias otra vez, por todas las veces que te he dicho: gracias, Patri.

Al resto de compañeros, tanto del laboratorio del Dr. Sebastián Cerdán como el de la Dra. Pliar López y del SIERMAC, gracias por escucharme en los seminarios, por

darme los vuestros, por preguntar, por responder, por cambiarme las siempre ajustadas horas de máquina, por los congresos y por los consejos. En especial, gracias a Alexandra Borges, Jesús Pacheco, Ana Belén Martín Recuero, Tiago B. Rodrigues, Viviana Negri, Rocío Pérez, Ana Metelo, Miguel Martínez, Nuria Arias, Ana Amor, Eva Cañadillas y Santos Ángel de la Cuerda.

Gracias a Javier Pérez, el *dibujante de figuras* que además me enseñó Inskape sin saberlo, y a las personas de los servicios de animalario y de informática, cuyo trabajo diario permite y facilita el de los demás.

And the beat goes on.

A mis padres y a Antonio,

Por ser el tiempo que soy

Summary

Obesity is a pandemic syndrome that underlies the most morbid and prevalent diseases in developed countries. It results from an imbalance in appetite regulation and energy expenditure, two processes that are fundamentally controlled by the hypothalamus. Magnetic Resonance Imaging methods are excellently endowed to assess brain anatomy and function, under physiological and pathological conditions, providing an always increasing array of approaches. In this dissertation, I will introduce a collection of new strategies to evaluate non-invasively appetite regulation in the brain of mice and humans, based in the use of diffusion weighted magnetic resonance imaging methods. **Chapter 1** introduces general concepts on the magnetic resonance imaging phenomenon and its applications, reviewing the key physiological mechanisms supporting hypothalamic appetite regulation. A short compilation of the most common neuroimaging techniques used to evaluate appetite-related processes is also included. **Chapter 2** describes the development and implementation of a new functional diffusion weighted imaging method applied to the detection of hypothalamic activity by fasting in mice and humans. **Chapter 3** covers four different experimental manipulations designed to probe the role of specific hypothalamic nuclei in the regulation of appetite control and energy balance, under conditions where these are intentionally altered. Finally, **Chapter 4** compares the use of the methodology – analysed with different models of diffusion- with the results obtained with a more conventional functional imaging technique, both applied to the paradigm of glucose administration to fasting mice. In conclusion, this dissertation demonstrates that diffusion weighted magnetic resonance imaging methods provide a novel and useful approach to investigate appetite regulation non-invasively.

Resumen

La obesidad es un síndrome pandémico que subyace a las enfermedades más prevalentes y mórbidas en los países desarrollados. Es resultado de un desequilibrio en la regulación del apetito y del gasto energético; dos mecanismos que están fundamentalmente controlados por el hipotálamo. Las técnicas de imagen por resonancia magnética constituyen una herramienta excelente de evaluación anatómica y funcional del cerebro, en condiciones fisiológicas y patológicas, proporcionando un constante creciente tipo de aplicaciones. La tesis que aquí presento se ha centrado en el desarrollo de nuevas estrategias para evaluar de forma no invasiva los procesos de regulación cerebral del apetito en ratones y seres humanos, utilizando técnicas de resonancia magnética pesada en difusión. El **Capítulo 1** proporciona una introducción a los principios básicos de la imagen por resonancia magnética, así como alguna de sus aplicaciones, recopilando las principales nociones fisiológicas de los mecanismos hipotalámicos de la regulación del apetito. También incluye s una breve compilación de las técnicas de neuroimagen más utilizadas en la evaluación de procesos relacionados con el apetito. En el **Capítulo 2** describo el desarrollo y la implementación de una nueva técnica de imagen funcional basada en difusión para la detección de la actividad hipotalámica por apetito, en ratones y en seres humanos. El **Capítulo 3** está dedicado a la aplicación de esta técnica a cuatro situaciones experimentales distintas, diseñadas para evaluar la respuesta específica de los núcleos hipotalámicos en procesos en los que la regulación del apetito y el balance energético están alterados. Finalmente, en el **Capítulo 4** muestro la comparación del uso de la metodología –analizada con distintos modelos de difusión- con los resultados obtenidos mediante la aplicación de una técnica funcional más convencional, ambas aplicadas al estudio de los efectos hipotalámicos de la administración de glucosa a ratones ayunados. En conclusión, mi Tesis doctoral demuestra que la técnica de imagen de resonancia magnética pesada en difusión proporciona un instrumento nuevo y robusto para el estudio de la regulación del apetito de forma no invasiva.

Index

Figures

Tables

Abbreviations

ADC	Apparent Diffusion Coefficient
AgRP	Agouti Related Peptide
A-P	Antero-Posterior
AQP-4	AQuaPorin-4
ARC	ARCuate nucleus
ATP	Adenosine TriPhosphate
Av	Averaged
BBB	Blood Brain Barrier
BOLD	Blood Oxygenation Level Dependent
CART	Cocaine and Amphetamine Regulated Transcript
CBF	Cerebral Blood Flow
CCK	Colecystokinin
$CMRO_2$	Cerebral Metabolic Rate of Oxygen utilization
D_{FAST}	Fast Diffusion Coefficient
D	Diffusion Coefficient
DMN	DorsoMedial Nucleus
D_{SLOW}	Slow Diffusion Coefficient
DTI	Diffusion Tensor Imaging
DWI	Diffusion Weighted Imaging
EPI	Echo Plannar Imaging
ETL	Echo Train Length
FDP	Fast Diffusion Phase
fDWI	Functional Diffusion Weighted Imaging
FID	Free Induction Decay
fMRI	Functional Magnetic Resonance Imaging
FOV	Field Of View
FSE	Fast Spin-Echo
FT	Fourier Transform
GE	Glucose-Excited
GI	Glucose-Inhibited
GLAST/EAAT1	GLutamate ASpartate Transporter/ Excitatory Amino Acid Transporter 1

GLP-1	Glucagon Like Peptide 1
GLT-1/EAAT2	GLial Transporter/ Excitatory Amino Acid Transporter 2
HDL	High Density Lipoprotein
H-F	Head-Food
HFD	High Fat Diet
HR-MAS	High Resolution-Magic Angle Spinning
iFT	Inverse Fourier Transformation
IVIM	Intravoxel Incoherent Motion
LDA	Linear Discriminant Analysis
LDL	Low Density Lipoprotein
LH	Lateral Hypothalamus
L-R	Left-Right
MEMRI	Manganese-Enhanced MRI
MR	Magnetic Resonance
MRI	Magnetic Resonance Imaging
N(H)	Spin Density
N_{ex}	Number of Excitations
NMR	Nuclear Magnetic Resonance
N_P	Number of Phase Encoding steps
NPY	Neuropeptide Y
OXM	Oxyntomodulin
POMC	Pro-opiomelanocortin
PVN	ParaVentricular Nucleus
PYY	Peptide YY
RER	Respiration Exchange Rate
RF	Radiofrequency
ROI	Region Of Interest
SD	Standard Deviation
SDP	Slow Diffusion Phase
SE	Spin-Echo
SNR	Signal-to-Noise Ratio
SPM	Statistical Parametric Mapping
ST	Stejstal-Tanner

T1	Longitudinal Relaxation Time
T2	Transversal Relaxation Time
T2*	Observed Transversal Relaxation Time
T2*W	T2 star Weighted
T3	Triiodothyronine
T4	Thyroxine
TE	Echo Time
TE_{eff}	Effective Echo Time
TR	Repetition Time
TSH	Thyroid-Stimulating Hormone
VMN	VentroMedial Nucleus

Chapter 1

Magnetic Resonance Imaging Principles and Hypothalamic Control of Appetite

Chapter 1 provides a general overview to the main magnetic resonance imaging principles and applications, as well as to the key physiological mechanisms involved in cerebral appetite regulation. A short review of the most common neuroimaging techniques used to evaluate appetite is presented.

1.1 Magnetic Resonance Imaging Principles

Magnetic Resonance (MR) is a nuclear phenomenon involving the interaction between magnetic fields and radiofrequency (RF) electromagnetic waves. It was discovered in 1946, in parallel studies by Felix Bloch and co-workers [1] at Stanford University, and by Edward M. Purcell [2] at Harvard University. Magnetic resonance imaging (MRI) makes use of the property of nuclear magnetic resonance (NMR) to image the distribution of atomic nuclei inside the body, producing images with excellent contrast and very high spatial resolution. The first MR image was produced in 1972 by Paul Lauterbur, who obtained a 2D image of two water tubes. Soon after, he acquired the first image of a living animal [3]. The use of Fourier Zeugmatography [4] improved the results, removing the initial artifacts obtained in the projection-reconstruction algorithm. In the late 1970s, Peter Mansfield improved gradient selection and implemented the Echo Planar Imaging method, a technique that would allow scans to take seconds rather than hours, resulting in clearer images than Lauterbur had [5]. Subsequently, many groups began making contributions, and the technology blossomed. Since then, MRI has demonstrated a huge range of applications, including analytical chemistry and biochemistry, biomedical and clinical uses.

In the first part of the chapter, I present an outline of some of the basic MRI principles: from the nuclear magnetism, the resonance phenomenon and the relaxation properties to the main steps required for image formation. Additionally, I will introduce some of the most common imaging methods employed to obtain contrast and functional information in tissues. Some of the concepts presented here may be found more comprehensively described in the Magnetic Resonance Imaging monograph by Jellinger and co-workers [6].

1.1.1 Basic MRI principles

Nuclear Magnetism

Nuclei with an odd number of neutrons or protons show a non-zero spin-angular momentum, characterized by a nuclear magnetic moment μ. This magnetic moment

affects the magnetic fields surrounding the nuclei, being analogous to that of a dipole (Figure 1.1A).

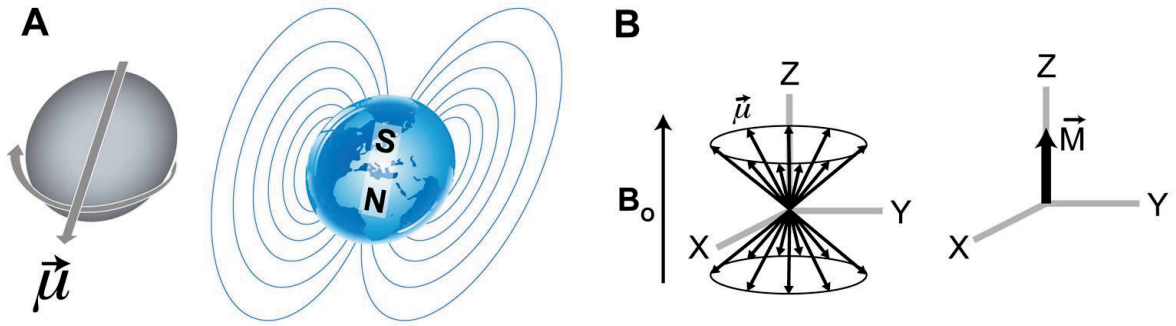

Figure 1.1. Magnetic moment of a nucleus and magnetization properties. A: Magnetic moment of a rotating proton (left) and magnetic field of a dipole (right). **B**: Orientation and precession of an ensemble of magnetic moments in the presence of an external magnetic field B_0 (left). Spins tend to orient in the less energetic, B_0 parallel direction, resulting in a net magnetization $\vec{M}$ (right).

The hydrogen atoms have a nuclear spin quantum number of m=1/2, meaning that when an external magnetic field B_0 is applied, it creates two possible energetically different states identified by the magnetic moments μ=±1/2 and energies $E = \pm {}^{\gamma h}/_{2\pi} mB_0$, where γ and h represent the gyromagnetic ratio (rad·s^{-1}T^{-1}) and the Plank constant (J·s), respectively. The state μ=+1/2, less energetic than the μ=-1/2, has a component of the magnetic moment parallel to the field, while the μ=-1/2 has a component antiparallel to the B_0 field. In a population of spins, a static magnetic field orients all spins and creates a net magnetization, resulting from the sum of the parallel and antiparallel individual magnetic moments:

$$M = \sum p_i \mu_i \qquad [1.1]$$

Where μ_i is the magnetic moment of the i_{th} state and p_i its population. The number of protons on each state is described by Boltzmann statistics, which in thermal equilibrium defines the relative populations of protons in the high or low energy states as

$${}^{p_{high}}/_{p_{low}} = e^{-{}^{\Delta E}/_{kT}} \qquad [1.2]$$

Where p_{high} and p_{low} are the populations of the upper and lower states respectively, $\Delta E = E_{high} - E_{low}$ is the energy difference between the two states, k is the Boltzmann constant and T (K) is the absolute temperature. Thus, in equilibrium, the lower energy levels will contain slightly more nuclei (arrows up) than higher levels (arrows down), as depicted in Figure 1.1B. At any state, however, the resulting magnetization experiences a torque from the static magnetic field that leads to the motion law

$$\frac{dM}{dt} = \gamma MxB \qquad [1.3]$$

Under these circumstances, M precesses clockwise around the magnetic field with a specific angular frequency $\omega_L = \gamma B$, known as the Larmor frequency.

Resonance

Resonance is a physical phenomenon consisting in inducing allowed transitions between states of different energy. In the process of MR imaging formation, transitions are induced between adjacent nuclear spin energy sates, and the energy change for a nucleus undergoing an MR transition is $\Delta E = E_{high} - E_{low} = \gamma hB$. Such transition depletes longitudinal magnetization, and constitutes the basic disturbances leading eventually to the NMR signal recording. More specifically, in the process of NMR imaging formation perturbations are applied in form of an RF pulse perpendicular to the main magnetic field and with amplitude B_1. This pulse rotates the original magnetization away from its equilibrium axis, switching it to the transversal plane. Once the RF is removed, the magnetization, still precessing at the Larmor frequency perpendicular to the B_0 field, decays exponentially with a time-constant known as transversal relaxation time T2. This change in precessing magnetization can be detected as a time-varying electrical voltage V(t) in a coil wire placed in the transversal plane.

Relaxation

During the process of RF stimulation, nuclei absorb energy and promote to the excited state. The phenomenon of absorption of radio frequency waves by matter was characterized by Purcell and Bloch in the first half of the 20th century [1, 2]. They described how nuclei return to the equilibrium by dissipating energy into the surroundings through the so called *spin-lattice* relaxation, process in which the

longitudinal magnetization is recovered with a time constant T1 (longitudinal relaxation time). The energy loss corresponds to a transfer of population from anti-parallel spins (with higher energy) to parallel spins, and the relaxation time depends on the ability of molecules from the lattice to translate and rotate; the smaller the molecules are, the shorter the magnetization recovery time is; and the closer the rotation frequency to the Larmor frequency is, the shorter the magnetization recovery time becomes. Hence, the relaxation time T1 can be interpreted as the average lifetime of anti-parallel spins.

Transverse magnetization, on the other hand, decays because its component magnetic moments dephase as a result of their mutual interaction. The T2 relaxation time, which differs between tissues, characterizes the rate at which the transverse magnetization shrinks. During this period, no energy is transferred from the nuclei to the tissue, and nuclei in the excited and ground states can exchange energy with each other. The main contribution to T2 decay in biological tissues comes from the magnetic fields of neighboring protons, and larger molecules, which tend o to reorient slowly, promote T2 relaxation and have shorter T2. However, the experimentally observed transverse magnetization decreases more rapidly than expected from the T2 relaxation alone, due to the presence of magnetic field inhomogeneities accelerating the dephasing between protons. This shorter time is characterized by the T2* constant and it is expressed as

$$1/T2^{*} = 1/T2 + \gamma\pi\Delta B \qquad [1.4]$$

Where γ is the gyromagnetic ratio (rad·s^{-1}T^{-1}) and ΔB (T) the field inhomogeneity. When incorporating the relaxation effects to the time dependence of magnetization described in Equation [1.3], it results

$$\frac{\overrightarrow{dM}}{dt} = \gamma\overrightarrow{M}x\overrightarrow{B} - \frac{M_x\vec{i}+M_y\vec{j}}{T2} - \frac{(M_z+M_0)\vec{k}}{T1} \qquad [1.5]$$

Equation 1.5 describes the evolution of magnetization with time and is known as the Bloch equation [1].

Most MR techniques tip the magnetization repeatedly by using a train of RF excitation pulses separated by a *repetition time (*TR). Under steady state conditions, the longitudinal magnetization recovers between RF pulses approximately to a fraction $1 - e^{TR/T1}$ of its equilibrium value. In that sense, longer values of TR allow more longitudinal relaxation to occur, and this can be manipulated to enhance the contrast between tissues with different T1. Additional RF pulses may be also applied to enhance contrast in T2. In that case, at a time τ after the initial 90º excitation pulse, a 180º RF refocusing pulse is applied to reestablish phase coherence after time τ, as represented schematically in Figure 1.2.

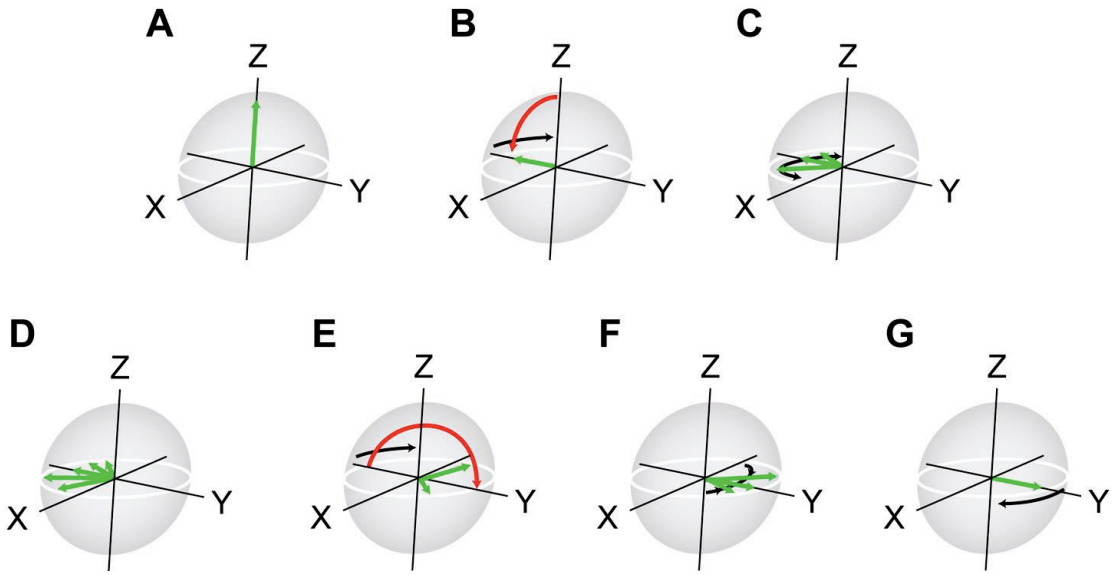

Figure 1.2. Evolution of magnetization during a spin-echo (SE) sequence. Spins at equilibrium (green arrow) are oriented in the direction of the static field (A). The RF pulse (red arrow) flips 90º the magnetization (B). Spins dephase due to local field inohomogenities (C, D). A 180º pulse re-orientates magnetization (E). Spins start recovering coherence (F). At TE/2 time after the 180º pulse, spins recover totally their coherence and an echo appears (G).

The time from the center of the initial RF pulse to the center of the echo –the moment in which the signal recovers its coherence- is the echo time (TE). The amplitude of the transverse magnetization depends on the TE and T2, proportional to $e^{-TE/T2}$. Sequences using this mechanistic are known as *spin echo* (SE) sequences.

Detecting and imaging magnetization

MR images are presented as 2D planes divided into picture elements (pixels), or voxels (considering the slice thickness), and the intensity of these elements represents the strength of the MR signal. These spatial maps are reconstructed from the MR measurements through the *phase encoding* concept, introduced by Laterbur in the early 70s [3]. It is based on the idea of exploiting orthogonal magnetic field gradients in order to express the magnetization as a bidimensional Fourier transformation (FT). Figure 1.3 illustrates a schematic representation of an MRI acquisition sequence.

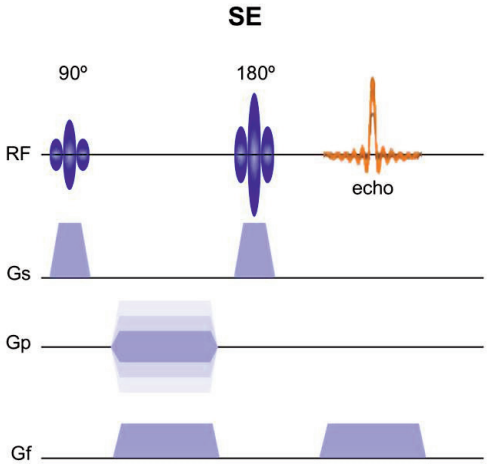

Figure 1.3. Schematic representation of a spin-echo (SE) imaging experiment. During the activation of the 90ºRF pulse, a slice-selection gradient is turned on (G_s). The phase-encoding gradients (G_p) change the phase of magnetization in the selected slice, and the frequency-encoding gradients (G_f) allocate specific frequencies. The signal echo is received at the same time the G_f is activated.

The process begins by briefly activating pulsed magnetic field gradients, at carefully timed moments during MRI acquisition. The first applied gradient, the slice-selection gradient (Gs), is switched in combination with the RF pulse in order to restrict the resonance to a specific slice. The applied magnetic field gradient spreads out the spin's precession frequency; in this situation, frequencies contained in the RF pulse affect only a specific slice. Shortly after the RF pulse has been turned off, a phase-encoding gradient (Gp) is pulsed perpendicular to the slice-selection gradient, thus making the Larmor frequency depend further on spatial position (now on the phase encoding direction). At that point, magnetization components in the same slice regain

the same Larmor frequency, and their phase varies along the phase-encoding direction. The final step in spatial encoding is applying a frequency-encoding gradient in the third orthogonal direction, at the same time that the signal is received. This modifies the Larmor frequencies and creates proton columns with identical frequencies. In general, the steeper the applied gradients are, the greater degree of achievable separation of spin systems (resolution) is possible. Strong gradients are necessary to seek out high spatial frequencies, whereas less steep gradients bring out lower spatial frequencies.

The resulting MR signal can be decomposed into thousands of sine and cosine waves of different frequency and orientation, depending on their position in the imaged volumes. Fourier transformations are mathematical tools that express complicated functions as distributions of cosine and sine waves of different amplitudes and frequencies. A FT of a continuous function *f(x)* is

$$\mathrm{F(k)} = \int_{-\infty}^{+\infty} \mathrm{f(x)e^{-i2\ k}}\ \mathrm{dx} \qquad [1.6]$$

Where, *k* represents the coordinates of the *spatial frequency space* or *k-space.* In MRI, the signal that is aimed to decompose is the final MR echo, the free induction decay (FID), which expresses, for each voxel, the variation of the received MR signal with time. The FID contains the frequency-encoded and phase-encoded spatial information, and a FT of the signal (using Equation 1.6) can reveal this information. If this transformation is applied to all pixels, and inverse Fourier Transform (iFT) of all the k-space combines all the frequency information and results in the image we see [7].

1.1.2 Image Contrast

The primary sources of inherent tissue contrast in MRI are the hydrogen spin densities (N[H]), longitudinal relaxation times (T1), and transverse relaxation times (T2). Other sources, such as flow, magnetic susceptibility inhomogeneity and chemical shift, affect also image contrast, but to a lesser extent. Contrast between two tissues A and B is expressed as $C_x = \frac{X_B - X_A}{X_B + X_A}$, where x represents the parameter of evaluation. In general, inherent tissue properties remain unchanged regardless of the

imaging method, but properties like T1 or T2 can change with increasing magnetic fields. Image contrast between two tissues is analogously defined as the difference of received MR signal (S) from the two tissues, divided into the total signal registered. More specifically, the MR signal in a spin echo (SE) sequence (the most commonly used pulse sequence in clinical MRI) depends on tissue parameters as described in Equation 1.7.

$$S(TE, TR) = N[H][1 - 2e^{-\frac{TR - TE/2}{T2}} + e^{-\frac{TR}{T1}}]e^{-TE/T2} \qquad [1.7]$$

Using different TE and TR times, a SE sequence can be used to highlight T1, T2 or spin-density differences between regions. Figure 1.4A depicts the MR signal intensity (in %) of a SE sequence depending on the TR used, in two tissues (A and B) with different T1 properties. Using a short-medium repetition time TR_1, the signal contrast obtained between the tissues A and B is the maximum. For longer times, like TR_2, longitudinal magnetization is almost recovered in both tissues and the signal contrast is very low. Figure 1.4B shows the signal decay with increasing TE of a SE sequence in two tissues with different T2 relaxation times. At short and medium TE times, like TE_1, the signal difference between tissues is very appreciable, while at long echo times, like TE_2, the signal received is almost zero for both tissues.

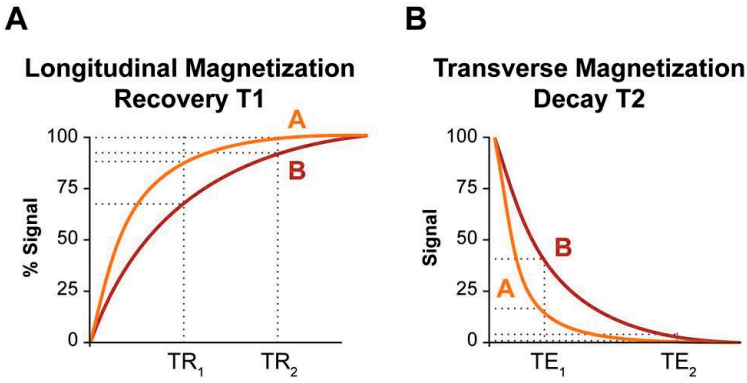

Figure 1.4. T1 and T2 factors contributing to the measured signal intensity in a SE sequence. **A**: Signal intensities from two tissues with different T1, as function of the applied TR. **B**: Signal values of two tissues with different T2 relaxation times in terms of the TE used. Values are expressed in % of the signal corresponding to the total magnetization recovery in A.

Other imaging techniques, like gradient-echo imaging, provide methods of accumulating images in much shorter times than conventional pulse sequences. Basically, it consists in replacing the 180º pulse of a SE with gradient reversals, in particular reversing the frequency-encoding gradient. Without the application of the 180º pulse, this technique does not eliminate the dephasing effects of magnetic field inhomogeneity. Consequently, signal decays depend on T2 and T2* relaxation times, as expressed in Equation 1.8.

$$S(\theta, TE, TR) = N[H]e^{-TE/T2^*} \frac{\left[1-e^{-\frac{TR}{T1}}\right]\sin\theta}{[1-e^{-\frac{TR}{T1}}e^{-\frac{TR}{T2}}-(e^{-\frac{TR}{T1}}-e^{-\frac{TR}{T2}})\cos\theta} \qquad [1.8]$$

Filling the k-space: Fast Spin Echo and Echo-Planar Reading

Big efforts have been dedicated since the late 1970s to decrease the acquisition times in MRI techniques, without concomitant loss of signal properties or contrast. In that sense, revolutionary changes arrived with the improvement of technical acquisition strategies of Fast Spin Echo (FSE) [8] and echo-planar imaging (EPI) [9]. To understand how these techniques work, it is convenient to recall some important features of the Fourier analysis.

During the process of reading a conventional SE signal, and in order to provide information along the phase-encoding axis, the phase-encoding gradient is activated once between the 90º and 180º pulses (Figure 1.3). To distinguish 256 points (typical image resolution), 256 values of the phase-encoding gradient are required on 256 different passes (or *Ky* lines), each taking a TR time. In the reading process, each gradient-pass of SE is sampled in 256 parts of a single frequency. Hence, in conventional SE techniques, all echoes are preceded by a single-value of the phase-encoding value. In FSE sequences, several echoes are collected after one excitation RF pulse. As a result, more than one line of the *k*-space can be covered in the same TR, decreasing considerably the acquisition time. The new parameters necessary to describe FSE sequences are the echo train length (ETL, number of echoes per 90º RF pulse), number of phase encoding steps (N_p) and number of excitations (N_{ex}). An effective echo time (TE_{eff}) is defined as the echo time to of the echo that is used to fill the center line of k-space in a multiecho sequence.

EPI techniques fill the whole *k*-space after a single RF pulse (Figure 1.5). To do so, the readout gradient is reversed rapidly from maximum positive to maximum negative as much times as *k*-space lines have to be collected during a single T2* decay. The total numbers of lobes of the readout gradient are the number of phase encoding steps. In multishot EPI techniques, the coverage of the *k*-space is divided into steps, mainly in order to avoid signal loss in using a unique pulse. Additionally, there are more advanced techniques of filling the *k-space* that present, in general, improvements regarding the acquisition time or exposition to MR artifacts [10-12]. In the present work presented we have used basically single- and multishot EPI-readout methods.

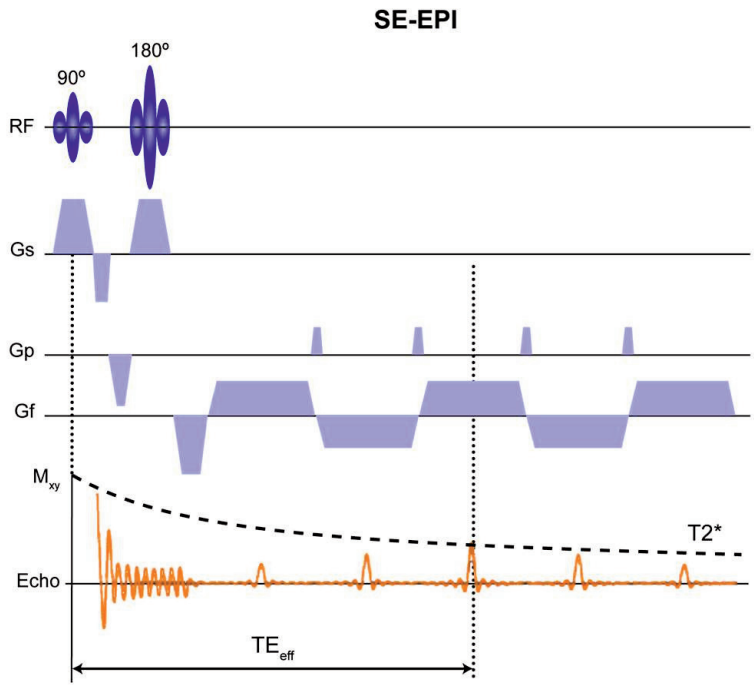

Figure 1.5. EPI readout added onto a conventional SE pulse sequence. The RF line depicts the 90º excitation pulse and the 180º refocusing pulse. In the G_s,G_p and G_f lines are represented the slice selection, phase and frequency gradients, and the echo line groups the echo signals recaptured. After one single excitation pulse, five MRI signals are phase and frequency encoded, and measured during the decay time T2*.

1.1.3 Diffusion Weighted Imaging

The concept of molecular diffusion

Molecular diffusion denotes to the random translational motion of molecules resulting from their thermal energy. It is also known as Brownian motion, and it was first investigated systematically by A. Einstein in the beginnings of the last century [13]. In a free medium, and during a given time interval, molecular displacements follow a Gaussian distribution and travel randomly over a distance, well described by a diffusion coefficient (D). This coefficient depends on the mass of the molecules, the temperature and the viscosity of the medium. A water molecule diffusing in water at 37 °C has a diffusion coefficient of 3×10^{-9} m^2/s, which means that travels, on average, 17 μm during 50 ms. During their diffusion-driven displacements, molecules probe tissue structure on a microscopic scale: they cross or interact with cell membranes, macromolecules or fibers, that modify the water molecule diffusion properties, reducing the expected diffusion time and definitely altering the Gaussian distribution. On these grounds, the non-invasive quantification of water diffusion distributions *in vivo* provides unique evidences in the definition of structural and geometric characteristics of tissues. Moreover, diffusion measurements are also perfectly endowed to probe potential changes in physiological or pathological states [14].

Diffusion Weighted MRI

The MRI methodology used to evaluate diffusion of water molecules in biological tissues is known as Diffusion Weighted Imaging (DWI). It was first proposed by Le Bihan and co-workers [15] and has emerged since then in one of the most used MRI protocols in clinic [16, 17]. The sequence is based on the Stejskal-Tanner (ST) method [18], which introduces a couple of magnetic field gradients at both sides of the 180º pulse in a SE technique. Those gradients are capable of encoding water molecules in such a way that the final echo received will be lower if water molecules have moved in-between the application of the phase gradients, or higher if those molecules have not moved –or have moved in a coherent manner. A diagram of a DWI sequence and water molecule encoding is presented in Figure 1.6.

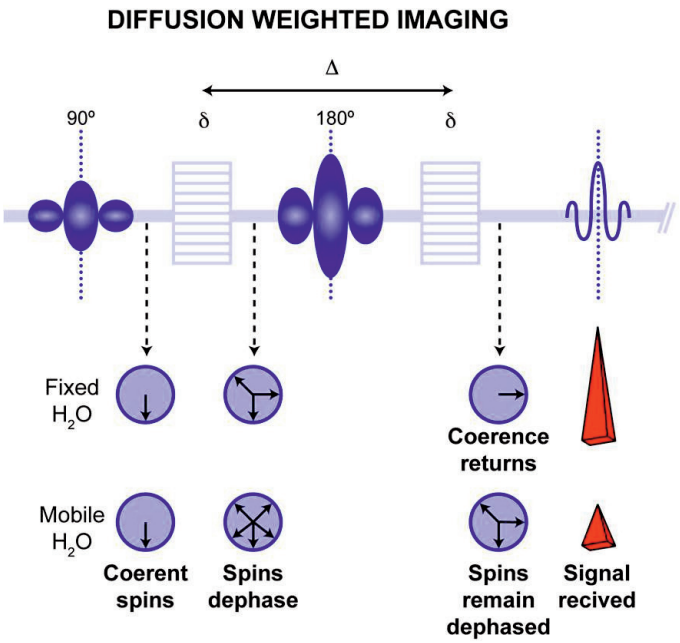

Figure 1.6. Representation of a DWI sequence and water molecule encoding processes. After the 90º RF pulse, a magnetic field gradient is applied during a specific time (δ) and spins in water molecules experience a specific dephasing. After a time (Δ), a second, and exactly opposite gradient is applied behind de 180ºpulse. If molecules in a voxel have moved incoherently, spins will not be able to recover the same phase and the total magnetization in a voxel will loss coherence, hence signal. Conversely, if motion is coherent, all spins will experience the same rephasing and final coherence will not change.

The sensitivity of a DWI acquisition depends on the gradient duration (δ), gradient separation (Δ) and strength (G). The imaging protocol typically consists in applying a series of magnetic field gradients with different diffusion sensitivity, and fitting the MRI signal obtained to an appropriate diffusion model of water in biological tissues.

Diffusion MRI models

The signal observed in each DW image voxel, at a millimetric or submillimetric resolution, results from the combination of all the microscopic displacements of water molecules in the voxel. The first attempt to describe the MRI-detected diffusion changes consisted in taking the expression of the freely-moving water in tissues, the Gaussian distribution, but replacing the diffusion coefficient D, with a global, statistical parameter, the apparent diffusion coefficient (ADC) [15]. The ADC has

since been largely used in the literature, and it is related with the MRI signal decay as described by Equation [1.8].

$$\frac{S(\delta,\Delta,G)}{S(0)} = e^{-\gamma^2\delta^2G^2(\Delta-\delta/3)ADC} \qquad [1.8]$$

Where S(0) represents the signal value without the application of diffusion gradients, γ is the gyromagnetic ratio of the proton, Δ the time between the application of the diffusion gradients, δ the duration of the diffusion gradients and G their strength. In fact, the expression $\gamma^2\delta^2G^2(\Delta-\delta/3)$ is normally referred to as the *b* value (from Le Bihan) of a DWI sequence, and defines the degree of sensitivity of the method; high *b* values –with high gradient intensities and long periods of gradient evaluation- probe low movements, while low *b* ranges encode faster diffusions. The diffusion time normally refers to the $(\Delta-\delta/3)$ value, and this model of diffusion is known as the monoexponential model.

The interpretation of the biophysical models underlying diffusion changes observed in physiological or pathological states, however, has been a matter of debate in the last decades. Indeed, further investigations demonstrated that the signal decay of diffusion weighted acquisitions, principally at high b values, was not monoexponential [19]. Several models have been proposed describing this behavior, like biexponential models [20] kurtosis imaging [21] or q-ball imaging [22]. From these models, the one that is of greatest interest here is the biexponential approach, which describes the signal decay as

$$\frac{S(b)}{S(0)} = SDP \cdot e^{-bD_{slow}} + FDP \cdot e^{-bD_{fast}} \qquad [1.9]$$

Where SDP and FDP represent the slow and fast phases of diffusion, respectively, with D_{slow} and D_{fast} their corresponding diffusion coefficients. The slow diffusing phase is supposed to account for those water molecules moving in the vicinities of cellular membranes, while the fast phase expresses those molecules diffusing relatively far away from these structures [23]. This conception of molecular phases has steered to the use of DWI techniques with functional applications [24]. Notably, some other studies have described DWI-detected changes during activation

processes with decreases in the ADC [25, 26]. In general, functional DWI (fDWI) changes are explained under the assumption that neuronal activation induces cellular swelling in the astrocytes (or even neurons) participating in the activation processes, an event that has been demonstrated using other techniques [27-29] and that has leaded to an important number of fDWI studies [30-32]. Moreover, these diffusion changes seem to occur closer to the activated areas -temporally and spatially- than the physiological events detected with blood oxygen level dependent (BOLD) contrast fMRI [33], although other explanations than swelling-detection effects have been reported [34]. An example of the use of DWI methods to detect activation-related process is depicted in Figure 1.7 [24]. Figure 1.7 depicts activation maps of three subjects after receiving visual activation impulses, as measured with fDWI, and more conventional functional MRI techniques.

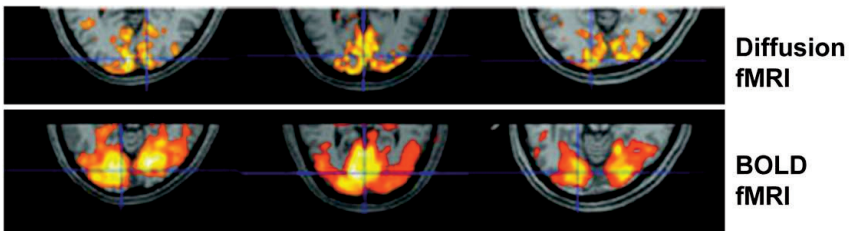

Figure 1.7. fMRI activation maps after visual stimuli in human patients. **Upper panels**: voxels detected as activated using diffusion fMRI techniques in three subjects, well located along the cortical visual ribbon. **Lower panels**: BOLD fMRI maps showing activated visual areas, located in large subcortical areas beyond the cortex.

The application of the low b values weighting range in DWI sequences, on the other hand, encodes incoherent movements of water perfusion in the microvasculature [15], as described by the intravoxel incoherent motion (IVIM) theory. IVIM methods have been used to detect changes in the brain microcapillary perfusion [35], and its application on body diffusion weighted MRI, especially in prostate tumors [36], breast tumors [37] and in liver diseases [38] has increased very substantially during the last years. The use of the IVIM approach, however, can cause systematic over- or under-estimation of coefficients due to the difficulty of defining appropriate diffusion and perfusion models, and their corresponding challenging methods of data fitting [39, 40]. In fact, almost all studies performed so far have relied on biexponential diffusion

models that account for perfusion and Gaussian-diffusion phases, and only very recent studies are starting to take into account that diffusion, even at low b values, might have non-Gaussian behaviors [41, 42].

1.1.4 Functional MRI

Functional MRI techniques are dedicated to measure brain activity. In humans, the most widely extended approach is the blood oxygen level dependent contrast fMRI, discovered in the early 90s by Ogawa and co-workers [43], and nowadays with more than 3000 papers with the keyword "fMRI" published annually [44]. It is based on detecting increases in oxygen delivery and associated hemodynamic responses during neuronal activation processes, although the exact relationship between BOLD signals and underlying neural activity is still a matter of debate [44, 45]. The neuronal activation process starts with increased neural activity, a process increasing flux of Na^+, K^+, and Ca^{2+}, and ATP production via enhanced glucose consumption. These changes induce astrocytes and neuronal cells to send vasoactive signals into nearby arterioles and capillaries, hence dilating the arterial vessels. Notably, there is a reported localized increase in cerebral blood flow (CBF) that is considered a direct consequence of this neuronal activity and the coupling between glucose metabolism and CBF changes [46]. This increase, however, exceeds the rise in cerebral metabolic rate of oxygen utilization ($CMRO_2$) [47], inducing increases in the capillary and venous oxygenation levels. Oxygen is carried in the blood bound to hemoglobin, and a change in oxygenation varies the ratio between deoxyhemoglobin (paramagnetic) and oxyhemoglobin (diamagnetic), and by studying this ratio, BOLD images map brain activity. More specifically, oxyhemoglobin, the main hemoglobin component of arterial blood, has no significant effects on magnetic properties, while deoxyhemoglobin, present in the draining veins after the oxygen has been delivered to the tissues, is strongly paramagnetic [48]. Consequently, the activation-induced decreases in deoxyhemoglobin, if detected using T2* weighted gradient echo EPI sequences, which are highly susceptibility-sensitive and relatively fast, will highlight activated areas with an increase in signal intensity. However, these effects are small, making mandatory the use of very refined methodology, paradigms and data analysis techniques to consistently demonstrate the effect. In fact, conventional functional

studies using BOLD techniques evaluate brain activity by repeating several times the same activation paradigm and calculating average values of the brain responses. There are some studies, however, that have used similar acquisition protocols (T2*W images) to detect functionality as a consequence of local changes in blood flow, without taking into account oxygenation differences. These sequences are normally longer because there is no need of detecting the rapid changes in oxygenation levels, and the activation paradigm is normally performed only once, with the flow effects lasting longer. This is the case of some studies evaluating appetite-related activations in which the response to the administration of appetite-inducing or inhibiting substances was investigated [49, 50]. Some of these studies, however, use the terminology BOLD fMRI to refer to the functional technique used, presumably because similar techniques are applied and correlated effects are studied. Hereafter, we will refer to both types of studies as BOLD fMRI techniques, although the specific physiological event assessed will be clarified when necessary.

Manganese-Enhanced MRI (MEMRI) is an imaging technique capable of monitoring neural activity using the divalent manganese ion, Mn^{2+}, as a surrogate measure of calcium influx [51]. The major advantage of using Mn^{2+} is that the contrast obtained is directly related to the accumulation of the ion in activated cells. Thereafter, the contrast in MEMRI is more directly related to neural activity than hemodynamic-based fMRI techniques. In fact, it is currently thought to directly reflect the neuronal accumulation of Mn^{2+} through voltage dependent calcium channels in stimulated brain areas, an event that is transynaptically extendable and enables MEMRI to map neuronal connectivities [52]. Mn^{2+} accumulation, in fact, can exceed the neuronal tracts and extend to surrounding astrocytes and astrocytic networks through the abundant gap junctions between astrocytes [53]. Moreover, neuronal activation has shown to elicit astrocytic ntracellular and intercellular Ca^{2+} waves [54-56]. Hydrated Mn^{2+} ions are classically known to induce a strong reduction in the T1 of water, resulting in bright contrast in T1 weighted images in those activated areas accumulating Mn^{2+} [57]. However, MEMRI is not devoid of limitations, since Mn^{2+} administration is known to become neurotoxic, competing with endogenous Ca^{2+} fluxes, pertubing levels of metabolites and interfering with the operation of vital

metabolic pathways as the tricarboxylic acid cycle and neurotransmitter cycles [58, 59].

Despite these limitations, MEMRI has been successfully used to detect brain activity [60] and neuronal architecture [61] in rodents. An example of MEMRI application for the study of obesity in mice is shown in Figure 1.8 [62]. In the figure, hyperintense areas of the T1 weighted image reflect the accumulation of Mn^{2+}, and signal intensity values in the areas of interest can be quantified.

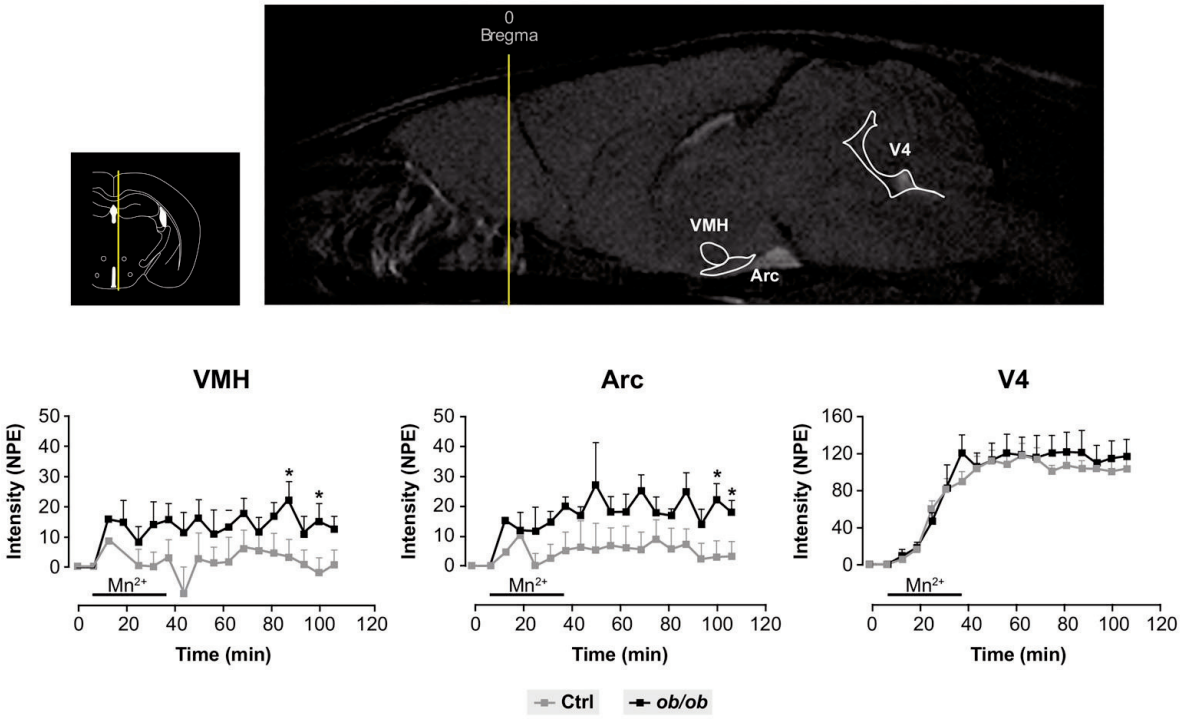

Figure 1.8. Representative MEMRI response in obese and control mice. Insert upper left: Localization of the hypothalamus, third and fourth ventricles in an anatomical atlas (Paxinos, 2001). Upper right: Mn^{2+} induced increase in MR signal intensity in the acuate nucleus (Arc), ventromedial nucleus (VMH) and the fourth ventricle (V4). Lower panels: Kinetics of MEMRI increase in VMH, ARC and V4 during and after Mn^{2+} infusion. Note that the obese animals (black squares) show a larger increase in MEMRI than the controls (grey squares) in VMH and Arc, but not in V4, revealing a specific obesity effect in these hypothalamic nuclei.

1.2 Hypothalamic control of appetite

1.2.1 Systemic and intrahypothalamic mechanisms of appetite regulation and energy balance

The hypothalamus is a small cerebral structure responsible for the integral homeostasis of vital systemic functions including global energy metabolism, appetite, thirst and osmoregulation, thermoregulation, circadian rhythms and some other fundamental survival responses such as aggressiveness [63-65]. It operates as a highly sophisticated neuroendocrine transducer, sensing peripheral endocrine signals and transforming them in intracerebral excitatory or inhibitory neurotransmitter events that deliver the homeostatic response back to the periphery [66, 67]. Hypothalamic function involves frequently the operation of highly elaborated feed-back control loops (Figure 1.9). Activation of the hypothalamic interface during appetite regulation processes is thought to proceed essentially in two steps, an initial endocrine activation, involving the receptor-mediated interaction of the hormone (or neuropeptide) with the presynaptic terminal, followed either by the activation of excitatory or inhibitory neurotransmitter release at the postsynaptic cleft. In this process, the neurotransmitters glutamate and GABA play a central role mediating glutamatergic [68] or GABAergic [69] neurotransmissions through specific neuronal pathways of the hypothalamus; pathways that eventually trigger the release of hypothalamic neuropeptides (or hormones) to the blood stream or to other hypothalamic structures to maintain systemic homeostasis [70]. Recent years have witnessed an important development in the understanding of the specific hypothalamic mechanisms involved in appetite control and global energy homeostasis [71]. Appetite control operates on the balance of positive and negative peripheral signals from the adipose tissue, the pancreas and the gastrointestinal tract, modulating intrahypothalamic and brain stem autonomic activities that determine the early hunger or satiety responses and the long term body weight and energy balance [72]. Peripheral signals from the gut include mainly peptide YY (PYY), oxyntomodulin (OXM), ghrelin, glucagon like peptide 1 (GLP-1) and colecystokinin (CCK).

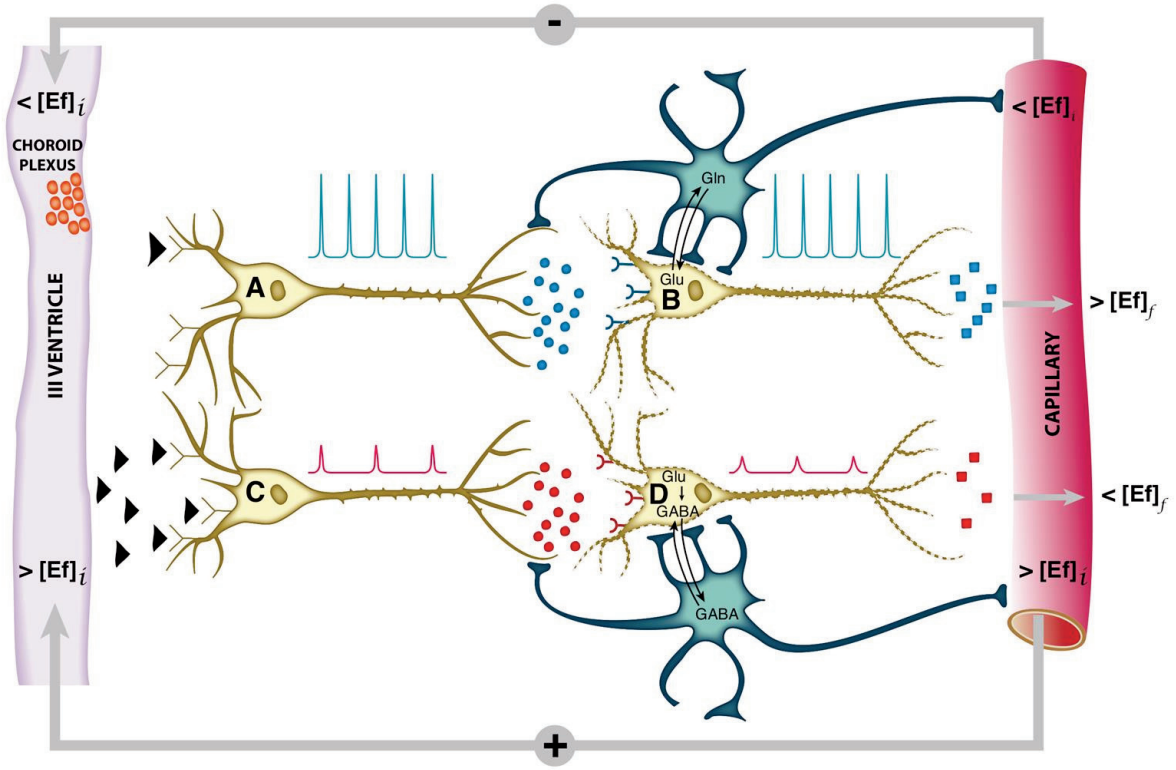

Figure 1.9. Representation of the neuroendocrine interface and feed-back control loops. Neuroendocrine integration involve neurons receiving endocrine signals and releasing neurotransmitters (A, C) or neurons receiving neurotransmitter signals and releasing neuropeptides or hormones (B, D). The initial decrease in plasma concentration of an endocrine inhibitory effector (<[Ef]i), passes the blood brain barrier, releasing the inhibition of neuron A and triggering action potentials (blue spikes) and the synaptic release of an excitatory neurotransmitter as glutamate (blue circles). This activates neuron B and triggers the release of an endocrine signal resulting eventually in an increase in the final plasma concentration of the effector (>[Ef]f). The initial increase in the plasma concentration of the effector (>[Ef]i) inhibits neuron C, decreasing the frequency and amplitude of the action potentials and triggering the release of an inhibitory neurotransmitter as GABA (red circles). This causes neuron D to reduce or suspend the release of the effector Ef, resulting eventually in an homeostatic reduction in the plasma concentration of (<[Ef]f). Both negative and positive feed-back loops tend to maintain the plasma concentration of the effector Ef. Glu: glutamate, Gln: glutamine, GABA: γ-aminobutyric acid.

Adipose tissue, pancreatic and gut derived peptides influence the hypothalamic circuitry providing short term hunger or satiety signals and resulting in the long term in anabolic (-) or catabolic (+) effects in energy expenditure, increasing or decreasing body weight. In particular, these mediators modulate the activation of the arcuate (ARC), paraventricular (PVN), dorsomedial nuclei (DMN) and ventromedial nuclei (VMN) of the hypothalamus which control food intake through a delicate balance of orexigenic and anorexigenic pathways operated by specific neurons and

neuropeptides [73]. Figure 1.10 [74] illustrates the current views on the mechanism of appetite control within the hypothalamus.

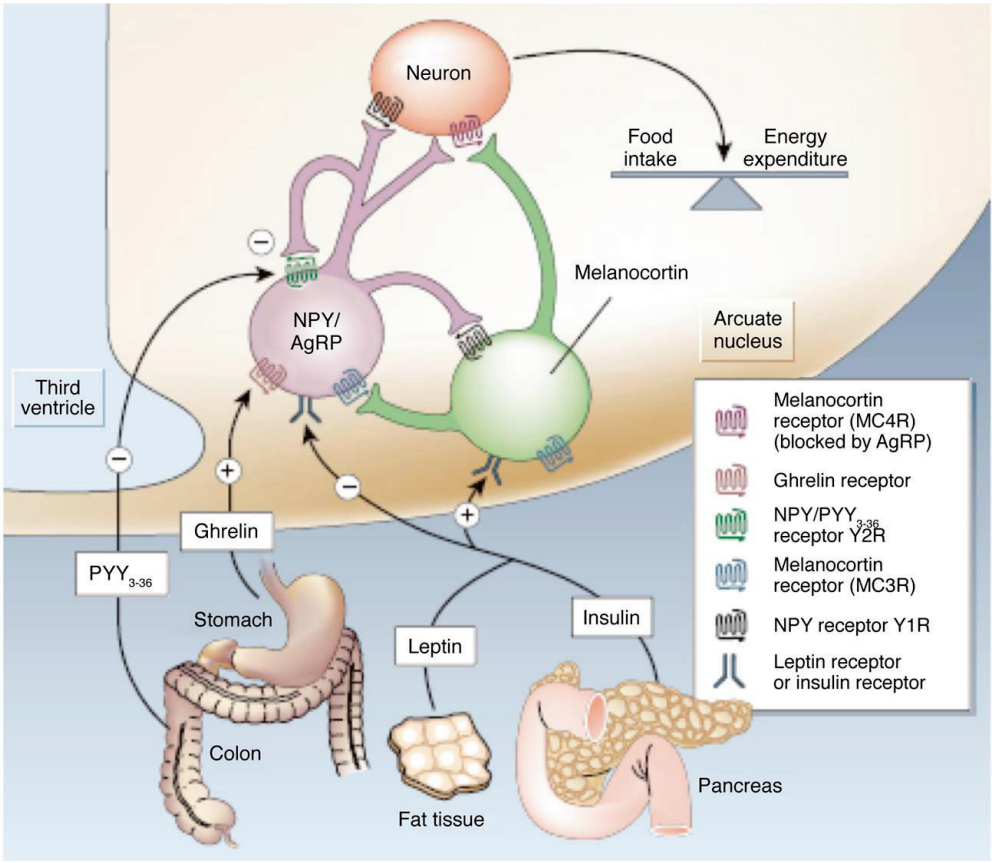

Figure 1.10. Hypothalamic control of global energy balance. Appetite is regulated by a complex feed-back loop involving endocrine signals originated in peripheral tissues and intrahypothalamic peptides. Leptin and insulin inhibit the orexigenic NPY/AgRP neurons (purple) and stimulate the anorexigenic melanocortin neurons (green), resulting in a reduction of food intake. Ghrelin or PYY_{3-36} activate or inhibit the NPY/AgRP neurons resulting in orexigenic or anorexigenic responses, respectively.

Hypothalamic control of energy homeostasis involves the modulation of orexigenic (stimulation of food intake) and anorexigenic (satiety signals) pathways, that determine the positive or negative balance between food intake and energy expenditure [71, 75]. Briefly, leptin and insulin produced by fat tissues and pancreas, circulate in blood in amounts proportional to body fat and blood glucose. These long term systemic effectors reach easily the hypothalamic ARC nucleus, an area of relatively permeable blood brain barrier (BBB) and thus highly accessible to activation by systemic effectors. Insulin and leptin, inhibit the orexigenic neuropeptide

Y (NPY) and agouti related peptide neurons (purple) activate the anorexigenic neurons (green) of the melanocortin (α-MSH)/cocaine and amphetamine regulated transcript (CART) pathways, resulting in decreased food intake and increased energy expenditure. Long term increases in leptin or insulin lead to receptor desensitization and insulin or leptin "resistance", increasing plasma glucose levels and fat accumulation and eventually producing obesity and diabetes. Ghrelin and peptide PYY_{3-36}, released by the stomach and the colon, respectively, provide the arcuate with positive or negative short term signals of appetite or satiety through the selective activation or inhibition of the NPY/ AgRP neurons, resulting in hunger or satiety, respectively [76].

Progress has been slower, however, in the characterization of the neurotransmitter events underlying the neuroendocrine response. In this respect, early interpretations conceived the hypothalamic response as a neuronal only event. The evolution of the tripartite synapse concept, however, revealed the essential role of astroglia in the modulation of synaptic neurotransmission [77, 78]. Furthermore, glutamatergic or GABAergic neurotransmissions involve necessarily the operation of transcellular cycles of glutamate and GABA between neurons and astrocytes [79]. In fact, important evidence supports the crucial role of glutamatergic or GABAergic neurotransmissions on hypothalamic function [80, 81]. In particular, intracerebral glutamate administration is known to elicit an intense orexigenic response [82] while knock out mice in glutamate or GABA vesicular transporters are known to exhibit altered feeding behavior [69]. However, further improvements in our understanding of the role of metabolic compartmentation in neuroendocrine function have been often hampered by the limited accessibility of sufficiently robust noninvasive methods to monitor neuronal activation and transcellular neurotransmitter cycling in the hypothalamus in vivo. In that sense, MRI approaches are known to be well endowed to observe hypothalamic morphology and function. Briefly, MEMRI techniques allow to monitor neuronal activation through the accumulation of Mn^{2+} and its effects in T1 weighted images [51], BOLD methods detect cerebral activation through associated increase in the oxihemoglobin/deoxihemoglobin ratio and perfusion changes [83] and

DWI visualizes microstructural changes in the diffusion coefficient of water [14], reflecting most probably activation induced neurocellular swelling events.

1.2.2 MRI of hypothalamic regulation

Manganese Enhanced Magnetic Resonance Imaging

The first MEMRI study of hypothalamic activation associated with feeding appeared in the last decade [84]. Authors infused intravenously $MnCl_2$ during an MRI acquisition and compared signal enhancement in the hypothalamus of fed or overnight-fasted mice, obtaining significant differences in different hypothalamic nuclei. This revealed for the first time that region-specific Mn^{2+} enhancement in the mouse brain could be modulated by fasting. Since then, several MEMRI studies have focused on the hypothalamic functionality associated to feeding, by studying the effect of peptide administration and its pathways of activation [85-87], cerebral activation in transgenic mice [62] and hypothalamic response to alterations of food intake [88, 89]. Moreover, recent years have witnessed growing interest on MEMRI applications, geared to a better understanding of the molecular mechanisms by which Mn^{2+} produces alterations of the hypothalamic physiological processes. In particular, a significant number of publications focused on studies combing MEMRI with other imaging or spectroscopic techniques [62, 90, 91], or have used information provided by MEMRI approaches to understand other functional techniques [92].

Blood Oxygenation Level Dependent contrast

The use of BOLD fMRI in the study of appetite regulation started in the late nineties, with the monitorization of the hypothalamic response to glucose uptake in obese and lean humans [49]. Authors found different hypothalamic signal responses in both groups, with lower signal attenuation in obese subjects. The signal attenuation in the hypothalamus was associated to an initial increased orexeginic-induced blood flow that diminished after the administration of the anorexigenic agent glucose, and the reduced attenuation in obese subjects was explained as a lower “satiety” response to glucose. Almost at the same time, BOLD imaging was used to detect hypothalamic functionality in normal rats following intraperitoneal glucose administration [93], and recorded similar significant decreases of the MRI signal in the hypothalamic region

after the injection. Since then, BOLD-detected activity in rats after the administration of orexigenic or anorexigenic agents has been correlated with c-fos neuronal expression in the activated areas [94, 95], and its use for the study of appetite regulation in animals has generated an important number of contributions [96]. Current studies are basically related to the effects on hypothalamic activation after the administration of different diets or peptides to rats [97, 98] and its correlation with endogenous levels of neuropeptides.

In humans, early fMRI studies started investigating cerebral activation with food pictures [99], and the hypothalamic response to different tastes and calories [100]. It soon became clear that appetite in humans was the result of complex and interrelated neuronal circuits, including not only hypothalamus and brainstem, the principal homeostatic brain areas regulating body weight, but also corticolimbic and higher cortical regions. Consequently, different authors investigated the neuronal networks that responded to specific orexigenic or anorexigenic signals [101-103]. Currently, the applications of BOLD fMRI on studies of appetite regulation are dedicated either to the study of hypothalamic response to glucose [104, 105], to the establishment of differences between fMRI responses in obese and non-obese humans [106], or to the evaluation of the effects of appetite modulating hormones derived from the gastrointestinal tract and adipose tissue, mainly ghrelin [107], insulin [108] and leptin [109, 110].

Diffusion Weighted Imaging

DWI techniques –using monoexponential models of diffusion- have been used to characterize human brain microstructures of obese subjects, as compared to non-obese [111] The apparent diffusion coefficient values in the hypothalamus (and other brain regions) of obese subjects were found to be significantly higher than in non-obese patients, and results were associated to an obesity-related vasogenic edema. In fact, the relationship between hypothalamic inflammation and obesity has become a matter of study and debate in the recent years [112, 113]. It seems clear that the consumption of fat-rich diets activates proinflammatory responses in the rat hypothalamus [114, 115], and that the ability of high fat diets to induce obesity seems to depend upon the neuronal expression of mediators of inflammatory signaling in

mice [116]. On these grounds, DWI is ideally endowed to evaluate the potential inflammation changes in vivo in both animals and men [117].

Some years ago, water diffusion behavior in biological tissues was suggested to represent slow and fast diffusion phases, as explained in detail in the MRI principles part of this chapter. Since then, several contributions have used this biphasic model to detect and describe brain activation using functional DWI (fDWI) in humans and in vitro [30, 33, 118], although studies regarding appetite-related processes have not yet been reported. In fact, fDWI is a high demanding technique that requires strong magnetic field values and gradients, and the anatomical resolution is limited by the signal to noise ratio obtainable, a fact that challenges the study of hypothalamic regulation in both men and small animals.

On these grounds, the development of fDWI strategies for the evaluation of hypothalamic activity, improving the spatial and temporal resolution of BOLD fMRI and avoiding the use of the potentially toxic doses of manganese could represent an important contribution in the study of hypothalamic functionality and dis-functionality. Besides, the possibility of using fDWI to detect directional differences through the implementation of diffusion tensor imaging (DTI) approaches [119, 120] may allow the investigation of neuronal tracts and their potential alterations under different kinds of appetite-related disturbances.

Chapter 2

Imaging hypothalamic activity in mice and humans using fDWI

Chapter 2 describes the setup of functional DWI methods for the detection of hypothalamic activation by fasting in mice and humans. Diffusion -and data analysis- models are proposed and detected changes are on agreement with activation-induced cellular swelling, in the individual nuclei of mice and in the entire hypothalamic structure in humans.

2.1 Introduction

Hypothalamic appetite regulation is a vital homeostatic process underlying global energy balance in animals and humans, its disturbances resulting in feeding disorders with high morbidity and mortality. The objective evaluation of appetite remains difficult, as described earlier in more detail in Chapter I.

A variety of neuroimaging tools, including mainly positron emission tomography (PET) and fMRI methods, have been proposed to evaluate appetite functionality [121]. PET studies provide information on cerebral activation by detecting the emitted positrons derived from the increased uptake of 18F-deoxiglucose, an event revealing the metabolic coupling between glucose uptake, blood flow and neuronal activity in the hypothalamus during feeding-related stimuli [122, 123]. BOLD fMRI infers regional neuronal activity from the changes in magnetic susceptibility occurring after increased oxygen delivery to activated neurons in the hypothalamus of rats and humans [93]. Furthermore, other studies using MEMRI techniques have revealed the time course of hypothalamic activation as a response to the systemic administration of different orexigenic or anorexigenic peptides [86]. These previous approaches are not devoid of limitations to investigate hypothalamic physiology in animals and man, mainly derived from their reduced spatial and temporal resolution in the PET and BOLD fMRI approaches, and the potential neurotoxicity of Mn^{2+}, in the MEMRI technique.

To overcome these limitations, we propose here, the direct, non-invasive visualization of hypothalamic activation by fasting using diffusion weighted magnetic resonance imaging [14], in the mouse brain as well as in a preliminary study in the human brain; improving the spatial and temporal resolution provided earlier by PET or BOLD and avoiding the use of the potentially toxic doses of manganese precluding its use of MEMRI in humans. The brain of fed or fasted mice or humans were imaged at 7 or 1.5 Tesla, respectively, by DW MRI using a complete range of b values ($10<b<2000$ $s.mm^{-2}$), and the diffusion weighted image data sets were registered and analyzed pixel by pixel using a biexponential model of diffusion, or a

model-free Linear Discriminant Analysis (LDA) approach. Our results demonstrate that fDWI is excellently endowed to investigate appetite regulation and its disorders.

2.2 Materials and methods

2.2.1 Experimental models

The experimental protocols used in this study were approved by the ethical committee of our institution (Instituto de Investigaciones Biomédicas "Alberto Sols") and met the guidelines of the national (R.D. 53/2013) and the European Community (2010/62/UE) guidelines for care and management of experimental animals. Animals were housed in the animal premises of our institution (Reg. No. ES280790000188) and cared by specialized personnel. Experiments with animals were carried out using healthy adult male C57BL/6 mice (n=12) aged nine weeks. Each animal was investigated in two successive experimental conditions both receiving drinking water ad libitum; "fed"; receiving normal mice chow diet (A04 http://www.safe-diets.com/eng/home/home.html, SAFE Augy, France, 2900 kcal/kg), and "fasted"; following either 48 h (group 1, n=6, 25±4 g) or 16 h (group 2, n=6, 26±2 g) after complete food removal. In all small animal imaging experiments, anesthesia was initiated in a methacrylate induction box (isofluorane 2% 1 L/min O_2) and maintained during the imaging time with a nose mask (isofluorane 1% 1 L/min O). Anesthetized animals were placed in a water heated probe, which maintained the core body temperature at approximately 37 °C during scanning. The physiological state of the animal during the imaging process was monitored by the respiratory rate and body temperature using a Biotrig physiological monitor (Bruker Biospin, Ettlingen, Germany). We performed a pilot study with human subjects to illustrate the potentialities of the proposed methodology in a routine clinical environment. Human participants in the study were six healthy male volunteers, aged 24–33. Conditions for the participation were: (1) healthy clinical trajectory without familiar history of obesity, diabetes or other endocrine disorders; (2) Body Mass Index (BMI) of 18.5–25, corresponding to normal body weight; and (3) volunteers were required to follow a balanced diet (2000–2500 Cal/day) during seven days prior to the basal image

acquisitions, with no drinks other than water ad libitum, no medication or abnormal exercise. Specific instructions to follow a balanced diet were provided for each individual at the beginning of the study and the degree of compliance with these was obtained individually before the imaging sessions. All individuals adhered correctly to the outlined protocol. Each volunteer was imaged in two successive conditions; first, “fed”, after one week of a balanced diet and second “fasted”, 24 h after food deprivation. Blood samples from the median cubital vein were drained before the “fed” and “fasted” image acquisitions and analyzed for routine biochemical parameters, T3, T4, TSH and insulin levels.

2.2.2 MRI sequences

The magnetic resonance imaging experiments with mice were performed on a 7.0-T horizontal-bore (16 cm) superconducting magnet equipped with a 1H selective birdcage resonator of 23 mm and a 90 mm diameter gradient insert (36 G/cm). Imaging data were acquired using Hewlett-Packard console running Paravision 4.0 software (Bruker Medical Gmbh, Ettlingen, Germany). Figure 2.1 provides an overview of the acquisition and image analysis approaches implemented in this study and the regions of interest investigated, as illustrated for the mouse brain. A collection of DWI of the fed and fasted mouse brain was obtained (left panel) and analyzed using either a biexponential diffusion model (upper right panels) or a model-independent Linear Discriminant Analysis approach (lower right panels). The set of DWI was acquired with the conditions indicated below, across an axial plane containing the hypothalamus [124] with the diffusion gradient oriented along three orthogonal directions; Left–Right (L–R), Antero-Posterior (A–P) and Head–Feet (H–F). This structure was localized using a sagittal section showing the pituitary gland and selecting after the first axial section rostral to it, as indicated in Figure 2.1A. This section is located anatomically as Bregma −1.46 mm. In the six mice of group 1, acquisition parameters (in a console Bruker Pharmascan, Bruker Medical Gmbh, Ettlingen, Germany) were: repetition time (TR)=3000 ms, echo time (TE)=51 ms, four shot EPI, averages (Av)=3, Δ= 20 ms, δ=4 ms, field of view (FOV)=35x35 mm^2, acquisition matrix (Mtx)= 128×128, corresponding to an in-plane resolution of

296×296 μm^2, slice thickness of 1.5 mm, number of slices=3, using a collection of five low b values (10<b<100 s.mm−2) and six high b values (200<b<1800 s.mm^{-2}).

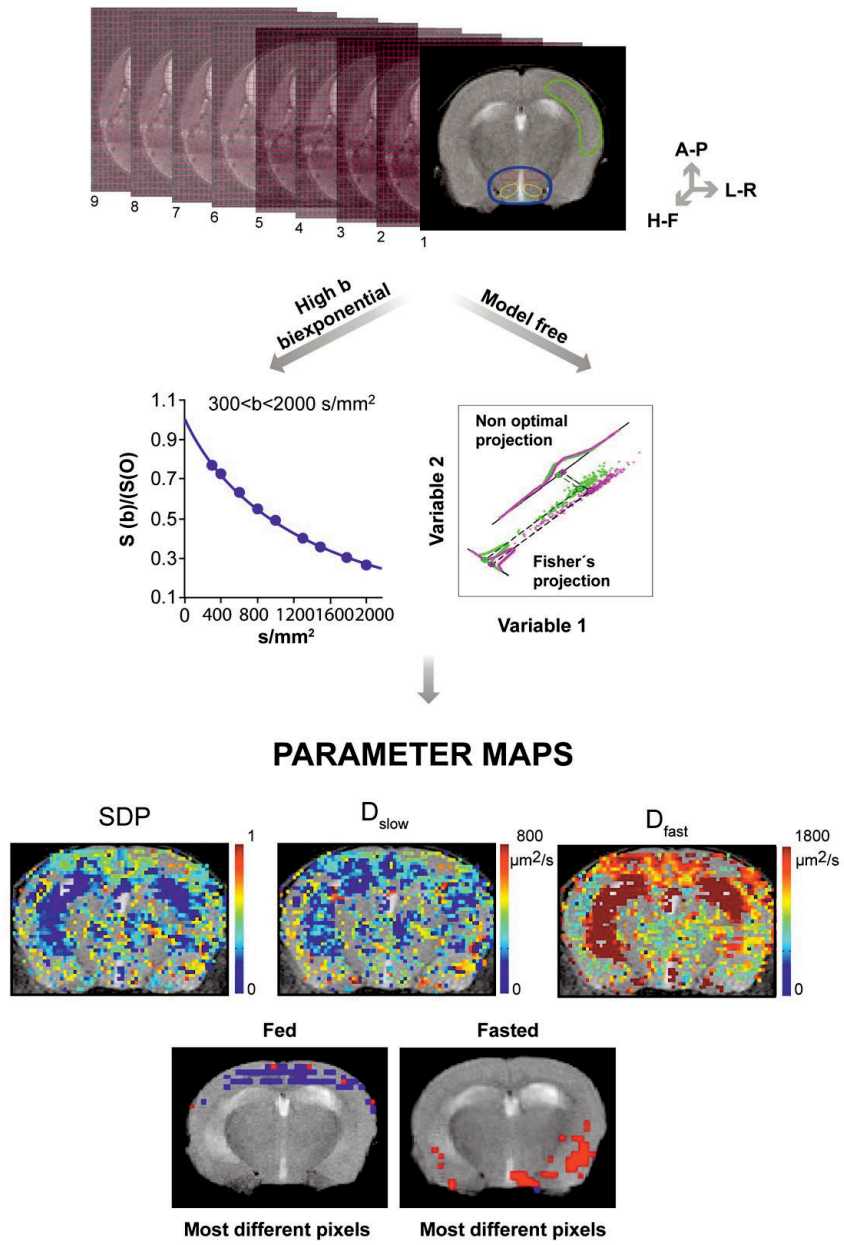

Figure 2.1. Overview of the fDWI methodology. Diffusion weighted images (10<b< 2000 s.mm^{-2}) are acquired consecutively in the same slice, in three diffusion directions A-P, L-R and H-F. The diffusion set is analysed with two independent approaches: a biexponential model fit and a Fisher LDA. From the biphasic model, coloured maps of the independent parameters fitted are obtained, (SDP, D_{slow}, D_{fast}). Investigated areas were the hypothalamus (circled dark blue, excluding the third ventricle) and its substructures and the somatosensory cortex (circled in green). Individual hypothalamic nuclei investigated are depicted in light blue (ARC), yellow (VMN) and red (DMN). Using Fisher LDA, the entire DWI data set can be classified between the two feeding sates, with the most different pixels from the fed or fasted represented in blue and red, respectively.

The six mice of group 2, were investigated using nine diffusion weighted images acquired along the axial plane containing the hypothalamus, with b values ($300<b<2000$ s.mm^{-2}). Acquisition parameters were (in a console Bruker AVANCE III, Bruker Medical Gmbh, Ettlingen, Germany): repetition time (TR=3000 ms, TE=31 ms, four shot EPI readout, Av=3, Δ=20 ms, δ=4 ms, FOV=21x21 mm^2, Mtx=128×128, corresponding to an in-plane resolution of 164×164 μm^2, slice thickness of 1.25 mm and number of slices=3. In both cases, T2 weighted (T2W) spin echo anatomical images were acquired previous to the DWI with improved resolution to localize and resolve precisely the hypothalamic region in every mouse. Axial T_2W images across the section containing the hypothalamus were acquired using the rapid acquisition with relaxation enhancement (RARE) sequence with the following parameters: TR=3200 ms, TE=60 ms, RARE factor=8, Av=3, FOV=38x38 mm^2 (Pharmascan console), 21x21 mm^2 (AVANCE III console), Mtx=256×256 corresponding to an in-plane resolution of 148×148 μm2 (Pharmascan console) or 80×80 μm2 (AVANCE III console), number of slices=3 and slice thickness=1.5 mm (Pharmascan console), or 1.25 mm (AVANCE III console).

The magnetic resonance imaging experiments with human volunteers were performed in the Magnetic Resonance Unit of the Hospital Nuestra Señora del Rosario (Madrid, Spain), using a GE Medical Systems 1.5-T horizontal-bore superconducting magnet, equipped with a ^{1}H quadrature head resonator. Prior to the imaging experiments, volunteers signed up an informed consent and confidentiality document. Image acquisitions were medically supervised by the neuroradiologist and clinical laboratory staff of the clinic. Multi b-value diffusion weighted images were acquired using 6 b values ($200<b<1200$ s.mm^{-2}). T_2W spin echo anatomical images were acquired in every subject in the same plane as the DWI, using a rapid acquisition with a Fast Relaxation Fast Spin Echo (FRFSE) sequence in coronal orientations. Acquisition parameters were: TR=3200 ms, TE=90 ms, Echo Train Length=8, Av=4, FOV=240x240 mm^2, Matrix size= 512×512, corresponding to an in-plane resolution of 468.7×468.7 μm^2, and slice thickness=3 mm.

2.2.3 Image analysis

Images acquired with the small animal or human scanners were transformed in DICOM format and exported to external HP Z-400 Workstations. Image analysis was performed as described below, using Statistical Parametric Mapping Software (SPM, http://www.fil.ion.ucl.ac.uk/spm/software) and a collection of in-house developed programs (Matlab v7, The Mathworks, Nattick, MA, USA) for nonlinear model fitting and classification of diffusion weighted images using Linear Discriminant Analysis.

2.2.4 Selection of ROIs

In the mouse brain, the cortical area, the hypothalamus and the hypothalamic nuclei ARC, DMN and VMN, were selected manually based on the anatomical descriptions given by the mouse brain atlas [124]. Figure 2.1 (leftmost panels) illustrates the localization of the different ROIs in a representative mouse brain. In the human images, hypothalamic and cortical ROIs were selected with the assistance of experienced clinical neuroradiologists (Fig. 2.1A).

2.2.5 Diffusion model

We used the biexponential model of attenuation of the DWI signal [20], as described by the expression;

$$\frac{S(b)}{S(0)} = SDP \cdot e^{-bD_{slow}} + FDP \cdot e^{-bD_{fast}} \qquad [2.1]$$

where, S (b) and S (0) represent the individual pixel intensities in the presence and absence of diffusion gradient, b indicates the diffusion weighting factor ($s.mm^{-2}$), SDP represents the slow diffusion phase containing water molecules moving with a slow diffusion coefficient D_{slow}, and FDP refers to the fast diffusion phase containing the water molecules moving with a fast diffusion coefficient D_{fast}. The addition of diffusion phases represents the total water molecules contributing to the signal decay (SDP+FDP=1).

2.2.6 Parameter fitting and statistical analysis

Parameters of the biexponential model were determined independently for each voxel and direction in the two feeding states, using the non-linear least-squares fitting Trust-Region algorithm, customized to limit parameter ranges and optimize the

goodness of fit. In particular, the goodness of fit (r^2) was restricted to be higher than 0.8 to guarantee an optimal fitting. Parameters are presented as mean±standard deviation within the considered ROIs in each animal or human. Statistical comparisons between the fed and fasted conditions were made constructing a cumulative, representative ROI that grouped the contributions of the individual ROIs selected from each mouse or human. The statistical analysis was made first using unpaired Student's t test, comparing each pair of fed and fasted cumulative ROIs. Further differences were assessed using a multiple linear regression model with the generalized estimating equation (GEE), a process that uses robust standard error estimates taking into account within-subjects correlations [125]. All statistical analyses were performed using SPSS (*IBM Statistical package for the social sciences,* 2000, http://www-01.ibm.com/software/analytics/spss/).

2.2.7 Model-free DWI analyses

We also implemented a model-free classification algorithm, based on Fisher Linear Discriminant Analysis (Fisher LDA), [126]. This model-free approach, allowed to investigate whether the DWI images could be automatically classified into the “fed” and “fasted” groups, without constrains imposed by the biexponential model. LDA constructs a projection of the original data onto a low dimensional subspace trying to maximize the separation amongst the different classes. When there are only two classes, as in the present case (fed/fasted), this subspace is one-dimensional. Hence, the projection may be interpreted as an Appetite Index that can be used to discriminate between the two conditions (see Figure 2.1).

2.3 Results

2.3.1 The effects of fasting in the mouse brain using DWI

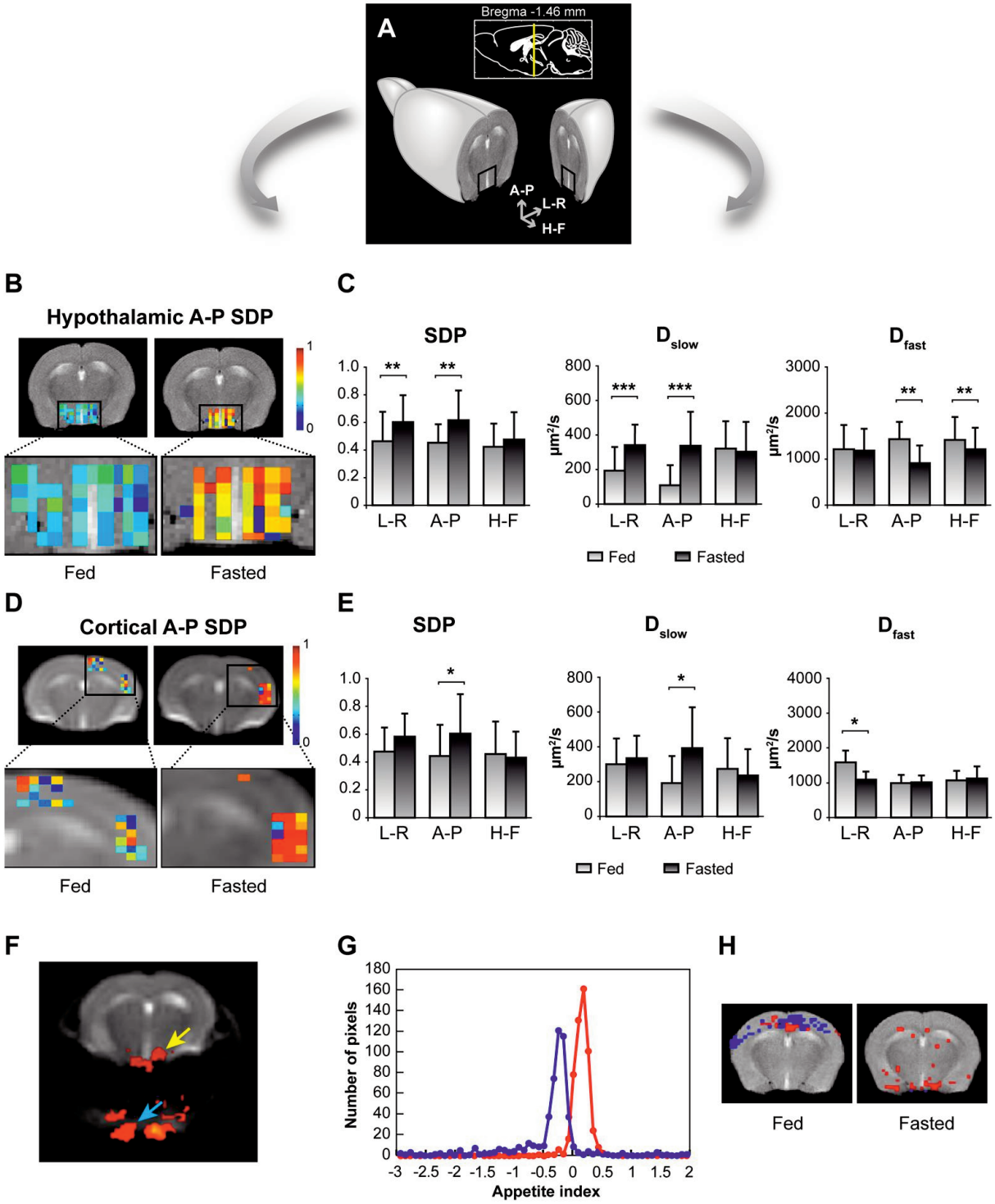

Figure 2.2. Imaging appetite by fDWI in the mouse brain. A: Axial and coronal MRI sections containing the hypothalamus in a representative mouse brain model and in a brain atlas (insert). **B**: Hypothalamic A-P SDP colour maps obtained from the DWI of fed or fasted animals (upper panels), superimposed to the corresponding T2W anatomical brain images. The hypothalamus is shown enlarged in the lower panels. **C:** Values of hypothalamic SDP, D_{slow} and D_{fast} parameters (mean ± SD) in the L-R, A-P and H-F directions. **D**: Cortical areas investigated from a representative mouse brain, in the fed and fasted states (upper images). Values are shown superimposed to anatomical T2W images and enlarged below. **E**: SDP, D_{slow} and D_{fast} values (mean ± SD) of six mice in the fed and fasted conditions (*$p<0.05$, **$p<0.005$, ***$p<0.001$, t student test). **F**: SPM analysis of the areas that best differentiate the fed and fasted hypothalamus in a representative mouse brain. Note the hypothalamic (yellow arrow) and vascular (blue arrow) activations. **G**: "Appetite Index" histogram of the fed (blue) and fasted (red) pixels as projected over calculated the LDA vector. Note the resolution of fed and fasted histograms. **H**: Panels that illustrate the localization in the mouse brain image of the 5% lowest (fed) and highest (fasted) points located at each end of the appetite index.

Figure 2.2A shows the anatomical localization of MRI sections used to localize the hypothalamus in the mouse brain and the directions of diffusion measurements. Hypothalamic activation after 48 h of fasting is conveniently detected by fDWI as a shift to red in the fasted condition, in the diffusion maps shown in Figure 2.2B. The upper panels show the hypothalamic SDP maps (A–P direction) in the fed and fasted conditions, superimposed on the corresponding anatomical T_2W images from the whole brain. These hypothalamic SDP maps are shown enlarged in the corresponding lower panels. The shift from blue to orange and red, revealing increased SDP, is clearly detected in the fasted condition. Artworks in Figure 2.2C summarize the mean values, standard deviations and comparative statistical significances of the diffusion parameters (SDP, D_{slow} and D_{fast}), from six mice under the fed and fasted conditions, investigated in three orthogonal directions (L–R, A–P and H–F). SDP and D_{slow} increased significantly with fasting in the L–R and A–P directions, whereas D_{fast} decreased in the A–P and H–F orientations. The impact of this fasting paradigm was investigated additionally in the cerebral somatosensory cortex of the same animals, obtaining a different, albeit significant, diffusion response (Figure 2.2D). In particular, subsidiary effects of fasting become significant as reflected by the red-shift in the A–P SDP parameter of fasted animals (2.2D, upper right panels), indicating most probably, motor activations related to the feeding impulse. Enlarged SDP maps with improved resolution in this region are shown below (2D, lower panels). Mean values, standard deviations and statistical significance of the different diffusion parameters are shown in the corresponding bar graphs of the panels in Figure 2.2E. SDP and D_{slow} increase significantly in the A–P direction and D_{fast} decreases in the L–R measurements. Notably, the model independent analysis of the diffusion weighted data sets using LDA (Figures 2.2F–H) was also able to classify successfully all mice investigated between the fed and fasted states. This indicates that the intrinsic differences between fed and fasted brains may be detected even automatically, independently of the diffusion model used. Figure 2.2F shows how SPM processing detected, as activated areas by the fasting paradigm, an area including the hypothalamus (yellow arrow) and an area of subsidiary vascular activation with the carotid arteries and the jugular veins (blue arrow). Taken together these evidences reveal a highly complex cerebrovascular

response to the fasting paradigm involving not only a hypothalamic activation but also an additional vascular adaptation. LDA was applied to detect the most different pixels between the fed and fasted image data sets of every mouse. Results from a representative mouse are illustrated in Figures 2.2G and H. The Fisher LDA projection (Appetite Index, Figure 2.2G) separates optimally the pixels of the fed (blue) and fasted (red) states. The pixels that are most representative of each state, located at the edges of the histogram (<5% or >95%), are shown in Figure 2.2H, superimposed on the corresponding T2W images. Using a leave one out cross validation strategy, it was possible to classify correctly, as fed or fasted, the image data sets from all mice investigated, when using the diffusion data sets acquired with the whole range of b values (six high b and five low b). However, using only the six highest b value data sets, only five mice out of the six mice investigated were classified correctly between fed and fasted states. This suggests that the microvascular contributions emphasized by the low b values are needed to obtain the optimal discriminant power required to classify correctly the images of every mouse between the fed and fasted states.

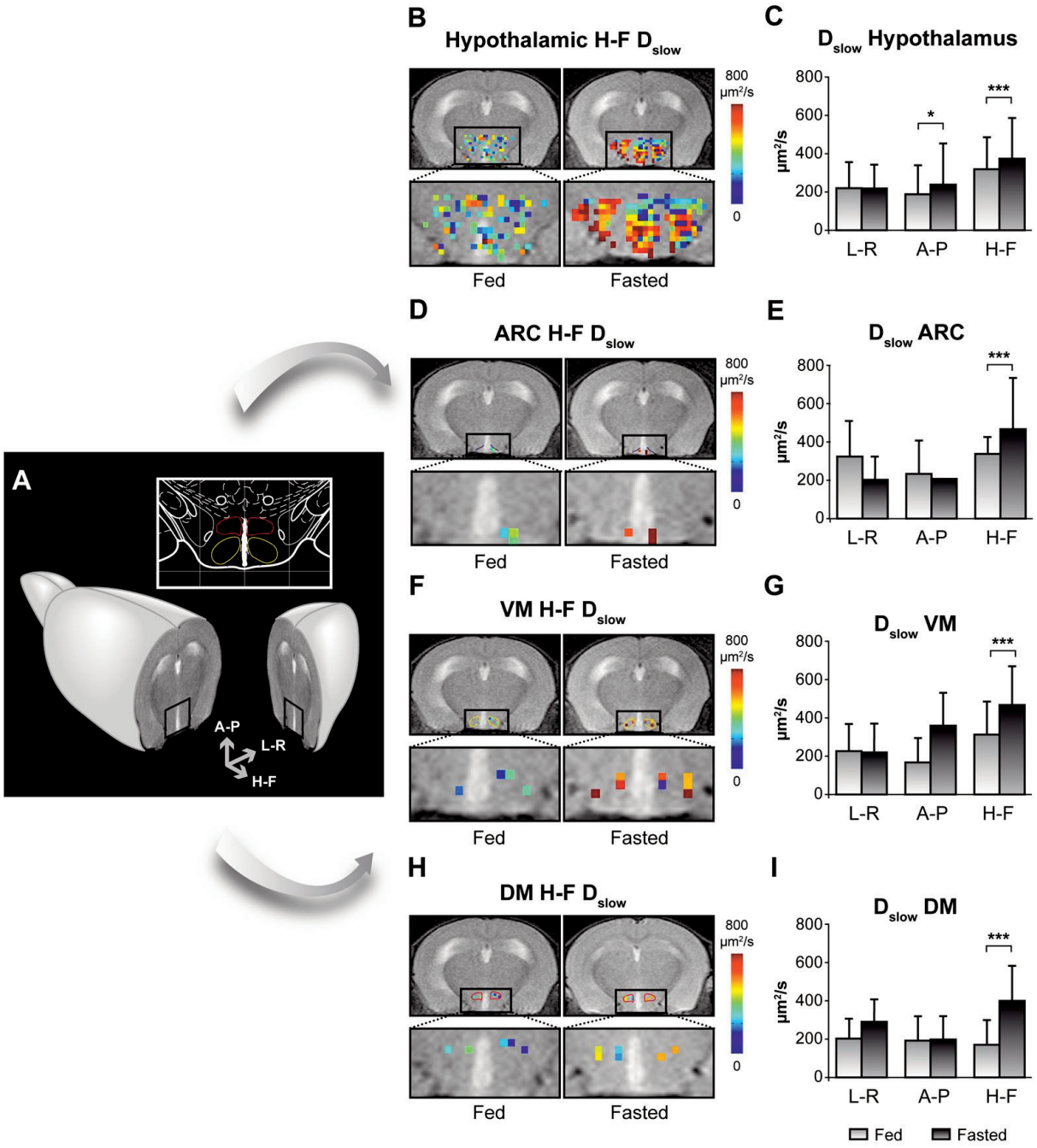
A
A-P
L-R
H-F
B
Hypothalamic H-F D slow
800 µm²/s
0
Fed
Fasted
C
D slow Hypothalamus
µm²/s
800
600
400
200
0
*
***
L-R
A-P
H-F
D
ARC H-F D slow
E
D slow ARC
F
VM H-F D slow
G
D slow VM
H
DM H-F D slow
I
D slow DM
Fed
Fasted

Figure 2.3. Imaging appetite by fDWI in hypothalamic nuclei of the mouse brain. **A**: axial MRI section containing the hypothalamus in a representative mouse brain and in a brain atlas (Insert) showing the localization of the main periventricular hypothalamic nuclei: DMN (red), VMN (yellow) and ARC (light blue). **B**: Hypothalamic H-F D_{slow} colour maps from fed or fasted mice, superimposed to T_{2w} images. The hypothalamic region is depicted enlarged in the lower panels. **C**: Values of hypothalamic D_{slow} (mean ± SD) in the L-R, A-P and H-F directions for 6 mice in the fed state and after 16 hours of fasting, and statistical differences (*$p<0.05$, **$p<0.005$, ***$p<0.001$, t student test). D: H-F D_{slow} parameter maps of the ARC in the fed (left) or fasted (right) states in a representative mouse, superimposed to T_{2w} images. The region is shown enlarged in the bottom panels. **E**: D_{slow} values (mean ± SD) of the ARC of six mice in the fed state and after 16 hours of fasting in the three directions of measurement and statistical differences between states ($p<0.001$, using GEE statistic methods) in the H-F direction. **F**: H-F D_{slow} parameter maps of VMN in the fed (left) or fasted (right) states for a representative mouse, superimposed to T2W images. The hypothalamic region is shown enlarged in the bottom panels. **G**: D_{slow} values (mean ± SD) of the VMN of six mice in the fed state and after 16 hours of fasting, in the three directions of measurement, and statistical differences between states (H-F direction $p<0.001$, t student test). **H**: H-F D_{slow} parameter maps of the DMN of a representative mouse, superimposed to T2W images of the mouse brain (upper panels) and with the hypothalamic area enlarged (bottom panels). **I**: D_{slow} values (mean ± SD) of the DMN of six mice in the fed or fasted states in the three directions, with statistical differences ($p<0.001$) in the H-F direction.

We investigated then the possibilities to resolve the effects of fasting in individual hypothalamic nuclei with shorter fasting times (16 h) and increased image resolution obtainable after a console upgrade. Figure 2.3A shows the anatomical localization of MRI sections used to identify the hypothalamus in the mouse brain and the directions of diffusion measurements. The inset on the top shows the anatomical localization of the hypothalamic nuclei: DMN (in red), VMN (in yellow) and ARC (in light blue). Hypothalamic activation after 16 h of fasting is revealed by fDWI as an increment of D_{slow} coefficients in the fasted condition depicted in the diffusion maps and bar graphs of Figures 2.3B and C. The upper panels of Figure 2.3B show the hypothalamic D_{slow} maps (H–F direction) in the fed and fasted conditions of a representative mouse, superimposed on the corresponding anatomical T2W images from the whole brain. The lower panels in Figure 2.3B show the hypothalamic D_{slow} maps with augmented resolution, depicting clearly a shift to the red that reveals an increase in D_{slow}. Figure 2.3C summarizes the mean values, standard deviations and comparative statistical significances of the slow diffusion parameters in the L–R, A–P and H–F directions from the six mice under the fed and fasted conditions. D_{slow} increased significantly with fasting in the A–P and H–F directions. Figures 2.3D–I show the effects of the 16 h fasting in the Arcuate Nucleus, the Ventromedial Nucleus and the Dorsomedial Nucleus, respectively. The upper panels of Figures 2.3D, F and H depict the D_{slow} maps (H–F direction) in the fed and fasted conditions of a representative mouse, superimposed on co-localized T2W images. The lower panels depict enlarged corresponding D_{slow} maps showing very significant increases in the H–F direction. The bar graphs of Figures 3E–I show the mean±SD of D_{slow} values from the six mice of group 2 for each investigated nucleus. Significant increases in D_{slow} were detected in all nuclei in the H–F direction. The DMN and VMN nuclei showed also significantly increased SDP.

2.3.2 The effects of fasting in the human brain using DWI

Table 2.1 shows the results for the blood samples taken from the cubital vein of the human volunteers before the “fed” (black) and “fasted” (grey) image acquisitions. Blood samples were analyzed for routine biochemical and endocrine parameters including; glucose, cholesterol, triglycerides, HDL, LDL, T3, T4, TSH and insulin.

Table 2.1. Blood concentrations of relevant biochemical parameters in each one of the six human volunteers, determined before each imaging session

	1		2		3		4		5		6	
Glucose **(mg/dL)**	**98**	88	**87**	79	**90**	79	**95**	77	**88**	83	**86**	80
Cholesterol **(mg/dL)**	**190**	175	**161**	162	**112**	126	**131**	125	**155**	162	**219**	227
Triglycerides **(mg/dL)**	**97**	47	**63**	45	**32**	41	**51**	47	**67**	35	**129**	87
HDL **(mg/dL)**	**63**	58	**42**	43	**40**	43	**48**	46	**36**	39	**36**	37
LDL **(mg/dL)**	**108**	108	**106**	110	**66**	75	**73**	70	**106**	116	**157**	173
T3 **(ng/ml)**	**1.1**	1	**1**	0.9	**1.2**	1.1	**1.**	0.9	**1**	1	**1.3**	1.2
T4 **(mcg/dl)**	**6.3**	7.6	**7.9**	8.9	**7.8**	9.3	**7.6**	7.7	**7.6**	7.7	**7.6**	7.8
TSH **(mcUl/mL)**	**1.4**	0.6	**0.7**	0.6	**2**	1.9	**1.6**	0.9	**0.7**	0.4	**1.2**	0.8
Insulin **(mcUl/mL)**	**6.2**	3.1	**5.5**	<3	**3.7**	<3	**<3**	<3	**3**	<3	**3.6**	<3

Glucose, cholesterol, triglycerides, HDL, LDL, T3, T4, TSH and Insulin values in the fed (black) and fasted (grey) conditions for the six volunteers.

Determinations were performed using clinically validated protocols by Analitical Biochemistry Laboratory Services of the Clinica Nuestra Sra. Del Rosario (Madrid). Glucose was measured using the glucose oxidase method (One touch Ultra, Lifescan, Johnson and Johnson, Issy-les-Moulineaux, FR). Total serum cholesterol, triglycerides were measured enzymatically using a CHOD-PAP test (Boehringer-Mannheim, DE), T3, T4 and TSH determination used the Accubind-ELISA kit and insulin with the insulin ELISA kit (Millipore, Billerica, MA, USA). Values of all parameters fell within the normal clinical range both in the “fed” and “fasted” conditions for every individual. Mean values of all volunteers and reference values are shown in table 2.2.

Figure 2.4A shows the localization of MRI sections containing the hypothalamus in a human brain model and the directions of our DWI measurements. The diffusion maps shown in Figure 2.4B show that fDWI visibly detects the hypothalamic activation induced by 24 h of fasting.

Table 2.2. Mean values of blood concentrations of relevant biochemical parameters in all volunteers and reference values.

	Mean volunteer values[a]		Reference values[a]
Glucose **(mg/dL)**	90.7	81	65-105
Cholesterol **(mg/dL)**	161.3	162.8	130-240
Triglycerides **(mg/dL)**	73.2	50.3	35-155
HDL **(mg/dL)**	44.2	44.3	> 32
LDL **(mg/dL)**	102.7	108.7	< 180
T3 **(ng/ml)**	1.1	1	0.75-1.78
T4 **(mcg/dl)**	7.5	8.2	6.09-12.23
TSH **(mcUl/mL)**	1.3	0.9	0.34-5.6
Insulin **(mcUl/mL)**	4.4	<3	<25

Mean values of glucose, cholesterol, triglycerides, HDL, LDL, T3, T4, TSH and Insulin in the fed (black) and fasted (grey) conditions for all six volunteers and reference values.

The upper images show the hypothalamic SDP maps (H–F direction) in the fed and fasted conditions, superimposed on the corresponding anatomical T_2W images from the whole brain. Hypothalamic diffusion maps are shown enlarged in the corresponding lower images. The fasted condition is clearly detected by a shift to orange and red of the SDP color map, revealing a significant increase in SDP. Bar graphs in Figure 2.4C summarize the mean values, standard deviations and comparative statistical significances of the diffusion parameters (SDP, D_{slow} and D_{fast}) fitted as described in the materials and methods section. We investigated six healthy volunteers under the fed and fasted conditions, monitoring the diffusion of water molecules in three orthogonal directions (L–R, A–P and H–F). As in the mouse brain, we found a significant increase of SDP and D_{slow} (H–F; with fasting. However, the human brain did not show a significant cortical activation associated with the fasting paradigm (Figures 2.4D and E).

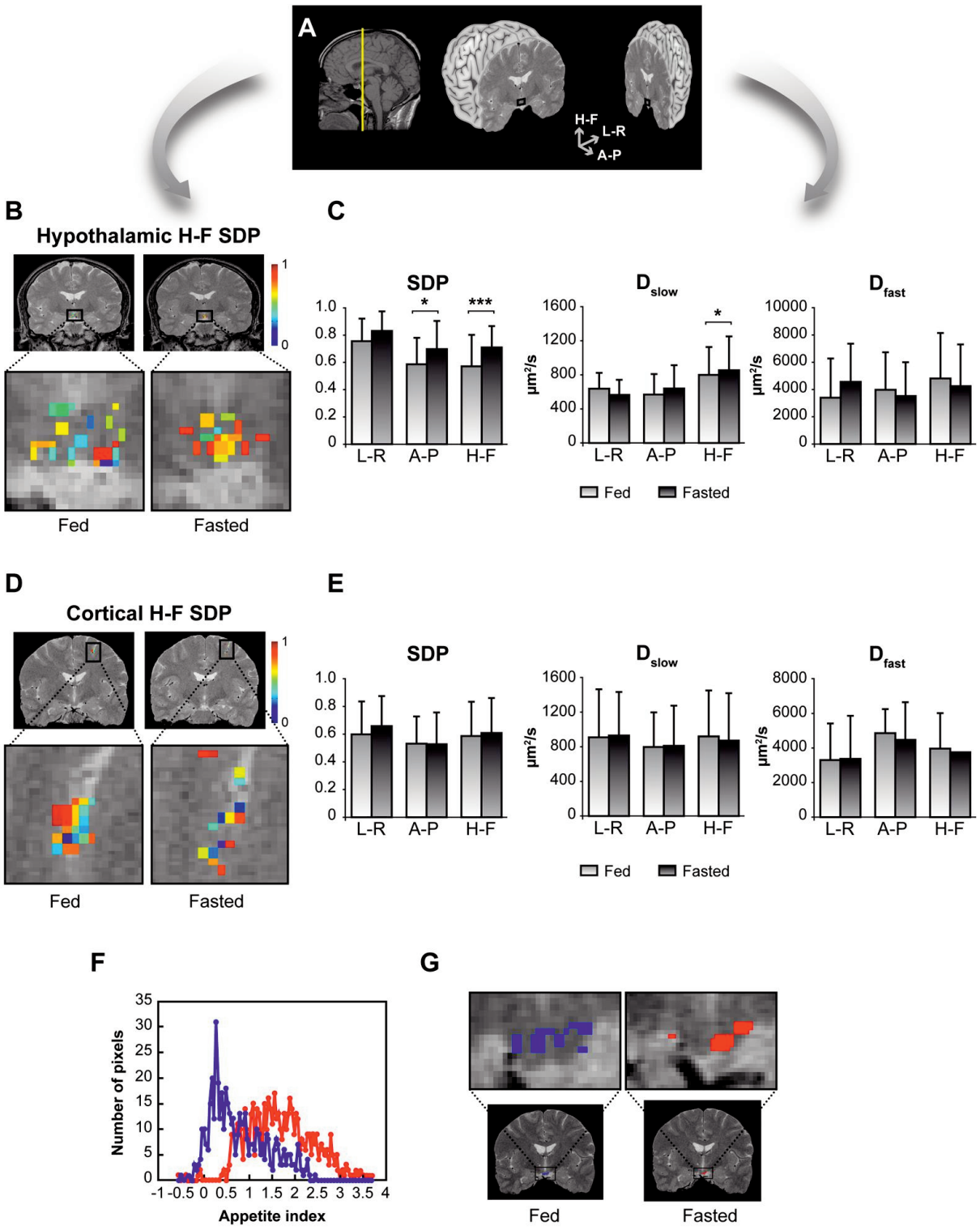
A
H-F
L-R
A-P
B
Hypothalamic H-F SDP
1
0
Fed
Fasted
C
SDP
1.0
0.8
0.6
0.4
0.2
0
*
***
L-R
A-P
H-F
D slow
1600
1200
800
400
0
*
µm²/s
D fast
10000
8000
6000
4000
2000
0
Fed
Fasted
D
Cortical H-F SDP
1
0
Fed
Fasted
E
SDP
1.0
0.8
0.6
0.4
0.2
0
L-R
A-P
H-F
D slow
1600
1200
800
400
0
µm²/s
D fast
8000
6000
4000
2000
0
Fed
Fasted
F
Number of pixels
35
30
25
20
15
10
5
0
-1 -0.5 0 0.5 1 1.5 2 2.5 3 3.5 4
Appetite index
G
Fed
Fasted

Figure 2.4. Imaging appetite in the human brain. A: Coronal and sagital sections containing the hypothalamus in a representative human brain. **B**: Parameter maps showing the H-F SDP pixel values from six volunteers in the fed and fasted conditions, superimposed to anatomical T2w images (upper panels). The lower panels show enlarged hypothalamic maps. **C**: Bar graphs of SDP, D_{slow} and D_{fast} parameters (mean ± SD) of six human subjects in the fed and fasted conditions. Significant increases in A-P ($p<0.05$) and H-F ($p<0.001$) SDP and H-F ($p<0.05$) D_{slow}, (GEE protocol). **D**: Cortical areas analyzed in the human brain, in the fed and fasted conditions (upper panels), with H-F SDP values superimposed to anatomical T2w images. The corresponding enlargements of the cortical areas are shown below. **E**: Bar graphs of SDP, D_{slow} and D_{fast} values (mean ± SD) in the fed and fasted states. **F**: "Appetite Index" histogram for the fed (blue) and fasted (red) human hypothalamus calculated using LDA. **G**: Identification of the areas representing the position of the 5% of the points located in the lower (fed) and upper (fasted) extremes of the Appetite Index histogram.

The resolution of individual hypothalamic substructures was not possible when using the clinical 1.5 T scanner. Even under these unfavorable field conditions, our results show that the detection of hypothalamic activation is feasible by DWI, becoming most probably much improved at higher magnetic fields of 3 T and 7 T.

LDA of the human hypothalamic data set was also able to separate successfully the diffusion weighted images from the fasted and fed conditions (Figures 2.4F and 2.4G), implying again that the intrinsic differences between fDWI data sets in the two feeding conditions, are independent of the diffusion model used. A distribution of the fed and fasted projections from the hypothalamus of a representative subject is illustrated in the histogram (Appetite Index, Figure 2.4F). In Figure 2.4G, the upper images show enlarged hypothalamic areas that best discriminate the fed (blue pixels) and fasted (red pixels) groups and the corresponding localizations in the anatomical T2W images of the human brain (lower panels). An evaluation of the accuracy of classifications between fed and fasted states, as performed with the leave one out strategy, classified correctly the imaging data sets of five out of the six subjects, the same percentage obtained in the mouse brain images acquired with six b values under similar conditions.

2.4 Discussion

We report here that fasting results in significant changes in the diffusion parameters of cerebral water molecules in mice and humans providing a novel approach for the objective, non-invasive, fully translational evaluation of the feeding impulse in vivo. Our data are consistent with previous applications of fDWI to cerebral activation studies, in particular of visual activation in humans [24] and with DWI measurements *in vitro* of induced neuronal activity [30]. In these cases, neuronal activation was associated to increments of the slow diffusion parameters in the activated areas, a finding proposed to reveal a relative redistribution of water molecules between the fast (FDP) and slow (SDP) diffusion phases, most probably reflecting, activation-induced increases in neurocellular volume (swelling) [24].

The interpretation of the physiological or pathological changes in water diffusion parameters in the in vivo brain has been a matter of debate in the last decades.

Early physiological interpretations described the existence of two dynamically different diffusion phases, fast and slow, attributed initially to the extracellular and intracellular environments, respectively. Further studies showed that the volume fractions of the intra- and extracellular phases predicted by DWI did not match those determined histologically [20, 127], implying that factors additional to morphological compartmentalization contributed appreciably to the diffusion environments detected by MRI in the brain [128]. More recently, the slow diffusion phase, containing the water molecules with slow diffusion coefficient, has been suggested to represent dynamically restricted water molecules associated with membranes and cytoskeleton structures. Conversely, the fast diffusion phase, containing the water molecules with a fast diffusion coefficient, has been proposed to represent the remaining, freely moving, solvent water molecules [20] (Figure 4, upper panels). On these grounds, increases in SDP detected by MRI upon neural activation [129] reveal a relative increment of water molecules diffusing in the vicinity of the membrane and cytoskeleton structures. This is consistent with the large increments in monovalent and divalent cation transport occurring during the action potentials, thought to be localized initially in the vicinity of the neural membranes. The redistribution may also reflect the concomitant increment of glial volume reported to occur during neuronal activation [27, 129, 130]. In our case, the increase in diffusion parameters detected during fasting, might reveal the osmotic swelling of glial cells in the vicinity of stimulated orexigenic synapses, as expected to occur during increased glutamatergic neurotransmission [29, 131] (Figure 2.5, lower panels). Importantly, these changes become detectable even after sixteen hours fasting in mice and may be even localized within subhypothalamic regions as the ARC nucleus, the VMN and the DMN.

More specifically, under fasting conditions, excess glutamate released to the orexigenic cleft is recaptured by surrounding astrocytes, by Na^+ dependent cotransport mainly through the GLAST/EAAT1 and GLT-1/EAAT2 transporters, with a $3Na^+$ per glutamate stoichiometry [132]. The three sodium ions incorporated in this way, are extruded to the extracellular space, in exchange with two potassium ions through the Na^+/K^+ ATPase. Astrocytic ATP required for the operation of the Na^+/K^+

ATP-ase and glutamine synthesis during activation by fasting, is thought to be derived from increased glucose consumption and metabolism by oxidative and glycolytic pathways [133] . This increased metabolic demand results in an increased hypothalamic microvascular blood flow, a circumstance consistent with the changes detected here by SPM and LDA under low b weightings (Figure 2.5D). Additional K^+ ions accumulated in the extracellular space during orexigenic firing, may enter the astrocyte by stimulation of the $Na^+/K^+/2Cl^-$ cotransporter [130]. Indeed, increased K^+ concentrations are known to be tightly coupled to neuronal activation, and have been detected using metallographic microscopic imaging approaches [134].

Taken together, these processes lead to intracellular potassium accumulation during activation, a circumstance triggering a concomitant water influx and volume increase of the astrocytes, mainly mediated through the highly abundant aquaporin AQP-4 [135] and mediated by astrocytic swelling processes [28, 136]. The osmotic swelling response associated to orexigenic stimulation, is proposed to occur initially in few astrocytes, those surrounding the orexigenic clefts, but can be rapidly extended to a plethora of neighbouring astrocytes, through the numerous interconnecting gap junctions of the network arrangement [137]. This increases significantly the spatial distribution of the orexigenic activation and makes it MRI detectable.

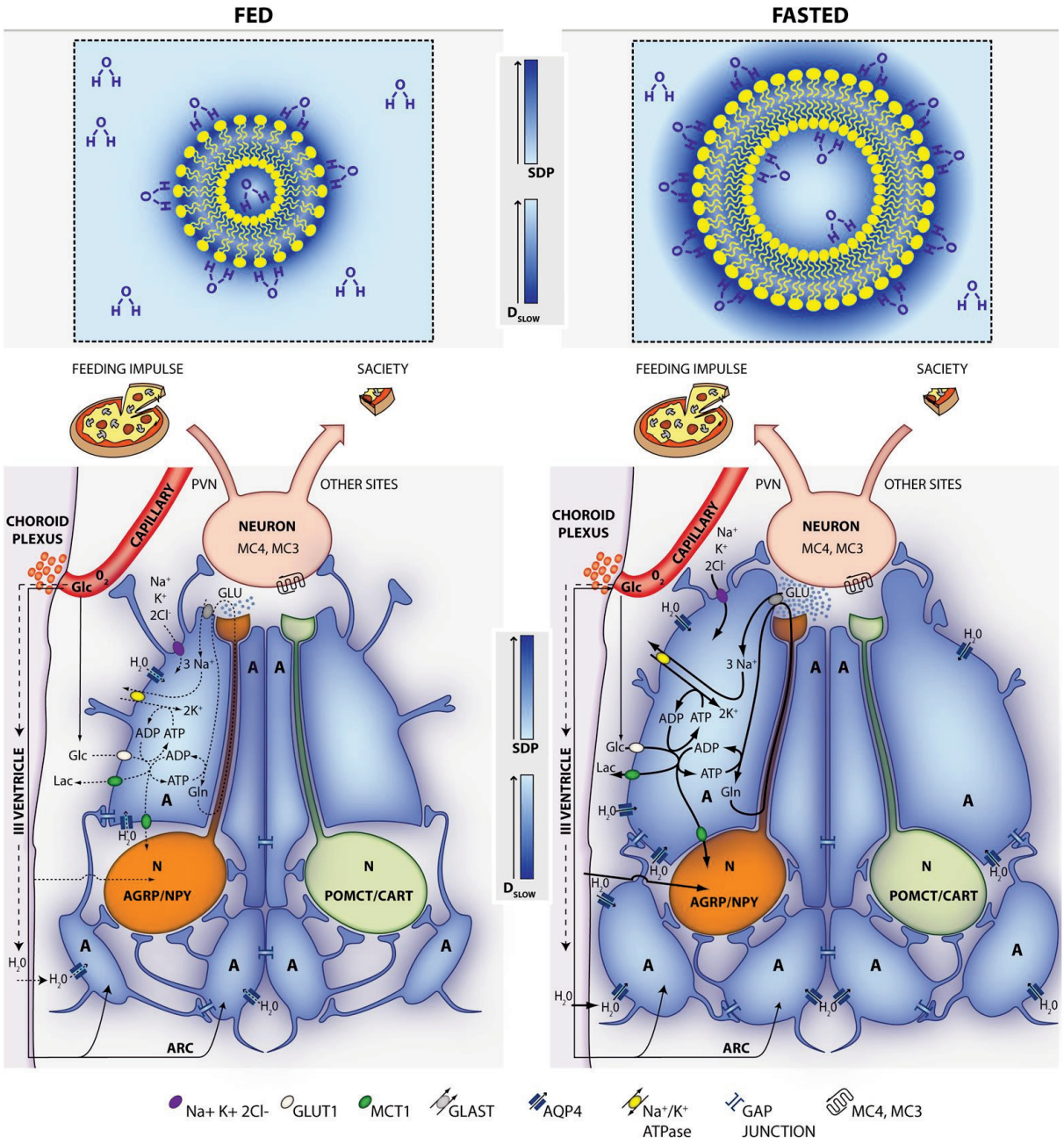

Figure 2.5. Neuroglial metabolic coupling and astrocytic volume changes underlie the orexigenic hypothalamic activation as detected by fDWI. The upper panels illustrate the effects of volume changes in the phase distribution (SDP) and dynamics (Dslow) of water molecules around the plasma membrane, under the fed (left) and fasted (right) conditions. Water molecules close to the plasma membrane (dark blue) experience more restricted diffusional motions than those far apart (light blue). The lower panels illustrate the neuroglial metabolic coupling mechanisms and associated volume responses in the fed (left) and fasted (right) hypothalamus.. The central colour coded bar graphs, represent variations of SDP (increase as dark blue) and Dslow (increase as light blue), as detected by fDWI. A: Astrocyte, ARC: Arcuate Nucleus, PVN: Paraventricular Nucleus, MC4, MC3: Melanocortin receptors, N: Neuron, AGRP/NPY: Agouti Related Protein/NeuroPeptideY, POMPCT/CART: Proopiomielanocortin transcript/Cocaine and Amphetamine Regulated Transcript. Mechanisms are shown only in one astrocyte for simplicity.

The osmotic swelling response associated to hypothalamic fasting appears not to be isotropic, suggesting smaller anatomical restrictions to volume increase in the directions where the increase in diffusion parameters is observed.

The fDWI approach to the fasting paradigm explored here is not devoid of limitations. In particular, a higher anatomical resolution is desirable, but limited at this field by the signal to noise ratio (SNR) obtainable, particularly at high b values. This may be improved by increasing the number of averages, at the compromise of augmenting linearly the image acquisition time. In this respect, the use of single shot EPI readout may help to decrease the acquisition time. However, this is a very demanding technique at high fields, leading frequently to distorted hypothalamic geometry, making difficult in our hands an adequate pixel by pixel analysis of the hypothalamus and its substructures. Additional limitations may derive from constrains imposed by the biexponential model, in particular by the potential influence of microvascular flow on the diffusion coefficient measurements [34, 138]. On these grounds, the implementation of integral dynamic model considering diffusion and flow would represent a considerable improvement [139]. In any case, model imposed limitations may be overcome through the use of a model-free approach, as the LDA strategy proposed here. Finally, despite its inherent limitations, fDWI presents valuable advantages over other non-invasive methods of investigating hypothalamic physiology. fDWI provides improved anatomical resolution over the PET FDG method, highlights diffusion alterations, an event not detectable by fMRI BOLD and avoids the use of potentially toxic Mn^{2+} doses required by MEMRI, becoming then fully translational to the clinic.

Chapter 3

fDWI evaluation of hypothalamic appetite regulation pathways

In Chapter 3 I describe fDWI results on the response of individual hypothalamic nuclei to four different experimental manipulations of global energy balance; NPY-null mice, leptin-deficient mice, rats subjected to high fat diets and fasting mice receiving ghrelin administration.

3.1 Introduction

The success of the fDWI methodology in evaluating hypothalamic activity opened the possibility of investigating, more specifically, the role of individual hypothalamic nuclei and associated signaling and communication pathways during appetite regulation. With this aim, we selected four conditions encompassing different perturbations of the molecular events underlying appetite regulation, and investigated them with fDWI methods.

The first perturbation explored was the effect of the genetic ablation of the Neuropeptide Y on fDWI of hypothalamic appetite regulation. NPY is an orexigenic peptide present in the neuronal groups of the ARC, DMN and VMN nuclei [140]. Indeed, genetically modified mice that contain a specific mutation inactivating the NPY gene, lack NPY expression and show reduced food intake in response to fasting, relative to wild type controls [141]. Hence, NPY-lacking mice are expected to show altered hypothalamic activity in response to fasting, although this has not been proved yet. On these grounds, we implemented fDWI studies to characterize the hypothalamic response to feeding paradigms in this genetically modified mouse model (*129S-Npy^{tm1Rpa}/J)* (http://jaxmice.jax.org).

The second approach investigated the effects of leptin deficiency on hypothalamic activity. Leptin is a hormone secreted by the adipose tissue that acts as an anorexigenic signal, reducing food intake and promoting energy expenditure [71]. In fact, mice or humans with low levels of leptin are obese and show hyperphagia [142]. Notably, recent findings demonstrate that obese mice show higher levels of orexigenic activity in the hypothalamus [62], and that obesity development activates inflammatory pathways [116, 143, 144]. Taken together, these evidences suggest that fDWI methods could provide a powerful tool to study hypothalamic regulation of obese individuals and help to develop more appropriate therapies. To this end, we designed a new collection of fDWI experiments using B6.V-*Lep^{ob}*/J mice (ob/ob,

jaxmice.jax.org). These mice are leptin-deficient genetically, and are characterized by very low or absent leptin levels in blood, high body weight and hyperphagia [145].

In the third perturbation, we investigated further the development of obesity by studying the effects of high fat diet (HFD) feeding on fDWI-observed hypothalamic activity. Indeed, obesity development in humans is very often associated to the ingestion of diets with high caloric content, and with the ability of the hypothalamus to regulate body weight in these over-eating environments [146]. Moreover, a huge number of studies in the last decades have been focused in developing HFD-induced obese animal models to understand the hypothalamic regulation during high caloric intake [147, 148]. Notably, two recent studies using MRI techniques reported HFD-induced astrogliosis in the hypothalamus [149], and changes in the ADC values in brain structures involved in reward and feeding behaviors [117]. The model of HFD in rats is particularly relevant in this respect, since not all rats subjected to the same HFD develop obesity, for as yet unknown mechanism. We hypothesized then that the HFD model in rats in conjunction with fDWI of the hypothalamus could provide important clues on the mechanisms of obesity development.

Finally, to complete the characterization of the DWI properties of the hypothalamus during appetite regulation processes, we investigated the effects of the administration of ghrelin to normal mice. Ghrelin is a peptide secreted in the stomach that acts as a peripheral signal increasing food intake in rodents and humans [150, 151]. Its action in the hypothalamus has been widely studied [152-154] as well as his role on the appetite regulation pathways [155], providing an already validated frame for fDWI studies. The ARC nuclei seems to be the first site of action for ghrelin, but the role of the other hypothalamic structures, and the specific characterization of the ghrelin regulation of appetite and energy balance remains still under investigation [156]. To study the effects of ghrelin administration on fDWI-detected activity, I performed a short project in the Biological Imaging Centre in London (BIC) in collaboration with the Metabolic and Molecular Imaging Group of the Imperial College, under the coverage of a short term fellowship associated to my PhD program. We applied fDWI techniques to mice before and after the i.p. administration

of ghrelin in a in a high field system, a 9.4 T magnet. With this increase in magnetic field strength, as compared to the fMRI evaluations performed so far, we expected to improve the signal to noise ratio and obtain improved quality images in the individual hypothalamic nuclei and their response to ghrelin.

3.2 Materials and Methods

3.2.1 fDWI evaluation of hypothalamic activity in NPY-lacking mice

Animal Model

A total of 34 *129S-Npy^{tm1Rpa}/J* mice were used for the characterization of the hypothalamic activity of NPY-lacing mice. For measurements in the metabolic cages (n=11), blood hormonal tests (n=17) and imaging experiments (n=17). Three of the animals that underwent the imaging experiments were used, after one week of recovery, for measurements in the metabolic cages, and the rest of mice investigated in the metabolic cages were used for the blood hormones analyses after recovering for a week.

Physiological characterization

Prior to the imaging experiments, we performed a phenotypic characterization of this strain by measuring the food and drink intake in metabolic cages (Phenomaster, TSE Systems GmbH) of 11 NPY-lacking mice (23±3g, 8-13 weeks old), in comparison with the intake of 13 wild-type C57BL/6J mice (23±1.5g, 8-12 weeks old). Metabolic cages allow for an individual automatic evaluation of drinking and feeding behavior, with an on-line monitorization of periodic measurements (every 13 minutes). Prior to the Phenomaster measurements, all animals were placed for 72 hours adaptation, in training cages equipped with the same drinking and feeding devices of the metabolic cages. Training is recommended to ensure an optimal adaptation to the Phenomaster environment before the quantitative measurements [157]. After the training period, animals were moved to the metabolic cages and food and water intake were measured first during 24 hours (*ad libitum* drinking and feeding) under regular food chow diet (2900 Kcal/Kg, A04 SAFE Augy, France), second during 48

hours of fasting and third 24 hours immediately after the fasting period. An illustrative scheme is presented in Fig. 3.1.

Figure 3.1. Measurements of food and water intake in C57BL6/J and NPY-lacking mice with the Phenomaster. Image of a representative metabolic cage and schematic representation of the experimental protocol followed inthe measurements of food and water intake, with consecutive periods of 24h fed *ad libitum*, 48h fasting and 24h of

Hormonal profiles in blood

Blood samples of 17 NPY-lacking mice (8-13 weeks old) were collected in a fed *ad libitum* state (n=6, 26.5±1.4g), after 16h of fasting (n=6, 25±1g before, 22±0.7g after) and after 48h of fasting (n=5, 29±3g before, 24.3±2.7g). Besides, blood samples of 22 wild type C57BL6/J mice (8-12 weeks old) were extracted in the *fed ad libitum* state (n=7, 24.7±0.5g), after 16h of fasting (n=8, 26.4±3g before, 23.9±3.2 after) and after 48h of fasting (n=7,24.8±1.9g before, 20±1.8g after). The contents of insulin, leptin, ghrelin and peptide YY (PYY) of all the samples were analyzed using a Mouse Metabolic Hormone Magnetic Bead Panel (Millipore MMHMAG-44K, http://www.millipore.com). For each animal, a total of 0.8±1 mL of blood was extracted from the heart while the animals were anesthetized with 2%

isofluorane/oxygen. All mice were sacrificed after the blood extractions. Experimental protocols for the sample collection, storage, preparation of reagents for immunoassay and immunoassay procedure, followed specific the instructions of the MMHMAG-44K mouse panel protocols. The immunoassay procedure was carried out by the Experimental Surgery Department group of the Hospital La Paz Health Research Institute in Madrid, using the Luminex system (Luminex 200™ xPONENT® 3.1 System with MILLIPLEX® Analyst 5.1, Millipore, www.millipore.com). For the data analyses, mean values of the peptides and hormones detected were calculated for each group of mice and feeding condition. In order to perform robust statistical comparisons, we eliminated the outlier values of each subgroup. Outlier values were considered those exceeding the range between (Q1-1.5*IQR<value<Q3+1.5*IQR); where Q_1 and Q_3 are the upper and lower quartiles values (25% lowest and highest range of data values, respectively) and IQR is the inter quartile range (the difference between Q_3 and Q_1) and represents a measure of the statistical dispersion [158]. Finally, we performed one-way ANOVA tests between values the experimental conditions in the two animal populations, with post-hoc Bonferroni corrections attending for the feeding conditions. Additional one-way ANOVA analyses were performed between feeding states of each mice population, and two-tailed impaired t student tests were performed between mice types in specific feeding conditions.

MRI

Ten NPY-lacking mice (group 1, 27±3g, 8-13 weeks old) underwent the same imaging protocol either under fed *ad libitum* conditions or after 48h of fasting. Seven different NPY-lacking mice (group 2, 26±3g, 8-12 weeks old) were imaged in a fed *ad libitum* state and after an overnight-fasting (16±1 h, 24±2g after the fasting. Starting at 9 a.m., 2 animals per day were transported from the animal facilities to the MRI lab, were mice were imaged in a 7T Bruker Biospec scanner (90mm gradient coil, 36G/cm, mouse head resonator) under the effects of anesthesia (1% isofluorane, 1L/min O_2). T_2W spin echo anatomical images and DWI sequences for group 1 were acquired in the same conditions of previous experiments with C57BL/6J animals (group 1), as described in Figure 1.1, characterized by a an in-plane resolution of 296x296 μm^2. For group 2, sequences were acquired with the settings used for C57BL6/J (group 2) that underwent the overnight-fasting experiments, and

characterized by an in-plane resolution of 164x164 μm^2. Diffusion model and data analyses were also carried out under the same conditions and restrictions described for the C57BL/6J study.

3.2.2 fDWI evaluation of hypothalamic activity in leptin-deficient mice

Animal Model

A total of 25 B6.V-*Lep*^{ob}/J mice were used for the evaluation of the hypothalamic activity of leptin-deficient mice. We used (n=8) in the metabolic cages, (n=14) in the blood hormonal tests and (n=10) in the imaging experiments. Seven of the animals that underwent the imaging experiments were used, after one week of recovery, for measurements of blood hormones, with four of them included in the fed group and three in the fasted.

Physiological characterization

The drinking and feeding behavior of B6.V-*Lep*^{ob}/J mice was evaluated in fed *ad libitum* conditions and after fasting, performing a new set of tests using the metabolic cages system (Phenomaster, TSE Systems GmbH) described earlier. Additionally, we incorporated evaluations of locomotor activity and indirect calorimetry [159, 160], to assess estimations of the metabolic substrates utilization of obese mice. Particularly, we measured the ratio between delivered CO_2 and consumed O_2, the respiratory exchange rate (RER). Differences in RER values can reveal differences in energy metabolism: while the oxidation of glucose leads to RER values equal to 1 ($6O_2+C_6H_{12}O_6 \rightarrow 6CO_2+6H_2O+32$ ATP), in the oxidation of a fatty acid molecule (e.g. palmitic acid) the RER coefficient is equal to 0.7 ($23O_2+C_{16}H_{32}O_2 \rightarrow 16CO_2+16H_2O+129$ ATP). The experimental setup consisted in isolating 8 ob/ob mice (43±2 g, 8-11 weeks old) and 8 C57BL/6J mice (27±3 g, 8-11 weeks old) during 72 hours, in the following consecutive conditions: 28h of free access to food and water sources, 16 hours without food and 28 hours of *ad libitum* feeding and drinking. Like in experiments with NPY-lacking mice, all animals spent 48 hours in the *training* cages before the measurements.

Hormonal profiles in blood

Blood samples of 14 ob/ob mice (8-12 weeks old) were collected in a fed *ad libitum* state (n=7, 43±5g) and after 16h of fasting (n=7, 46±4g before fasting, 43±4g after fasting). Sample extraction, storage, and immunoassay protocols were carried out as described above for the NPY-lacking mice, as well as the data analyses and statistical calculations. In fact, data from the C57BL6/J mice in the *fed ad libitum* and 16h of fasting conditions presented and described earlier is used here to evaluate its difference with obese mice.

MRI

In the imaging tests, leptin-deficient mice (n=10, 42±5g, 8-11 weeks old) underwent the same MRI study in two feeding conditions: fed *ad libitum* and after an overnight fasting (16±1 h, 39±4g). The experimental protocol followed for the same animal handling, image acquisition and data analyses than for the NPY-null mice and for group 2 of C57BL6/J mice in Chapter 2.

3.2.3 Correlation between high fat diet-induced obesity development and fDWI-detected hypothalamic activity

Animal Model

Sixteen male Wistar rats were fed *ad libitum* during 6 months with high-fat diet (purified diet 17.4% proteins, 35.8% lipids, 35% carbohydrates, 230 HF SAFE, Augy, France, www.safe-diets.com). Animals were housed in the Experimental Surgery Department animal facilities of the Hospital La Paz Health Research Institute. At the age of 6 months, animals were distributed in different groups according to its body weight, into obese rats (n=4; body weigh over 550g), moderately obese (n=8; body weigh between 450 and 550g) and non-obese rats (n=4; body weight under 450g)

MRI

The hypothalamic activity of the obese and non-obese groups was evaluated with fDWI in a fed *ad libitum* condition and after an overnight fasting (16±1h). Imaging protocols were similar than those carried out with the NPY-null and ob/ob mice, with an adapted field of view (38 mm), in-plane resolution of 0.296 mm/pixel and slice thickness of 1.5 mm. The DWI acquisitions were performed with 8 b values in the

range 300<b<1800 s/mm^2 in three orthogonal directions (L-R, A-P and H-F). Diffusion data obtained were fitted to the biexponential model, and coefficients of hypothalamus of obese rats were statistically compared to values in the non-obese group, in the two feeding conditions evaluated (Figure 3.9). In addition, we analyzed independently the response to fasting in both animal groups (Figure 3.10).

3.2.4 Hypothalamic nuclei fDWI-changes after ghrelin administration to fasted mice

Animal Model

Thirteen C57BL6/J mice (8–12 weeks old weighing 20–29 g, Harlan, UK) were imaged before and after an i.p. administration of the ghrelin peptide (0.3nmol/g). For all the experiments, animals were fasted the night before to homogenize the endogenous levels of ghrelin across individuals.

MRI

Acquisitions were performed between 9 and 11 a.m., and animals were anaesthetized using a 2.0% isofluorane-oxygen mixture for induction and 1.5% for maintenance (flow rate 1.0 L/min) during imaging protocols. An intraperitoneal catheter was placed on each mouse with the ghrelin solution (100μL) while animals were asleep. The head was centrally located inside a quadrature mouse head coil with an internal diameter of 25 mm (Magnetic Resonance Laboratories, Oxford, UK) and scanned in a 9.4 T horizontal-bore MR scanner (Varian, Palo Alto, CA). DWI imaging acquisitions consisted in 4 shot EPI readout sequence with TR=2000ms, TE=33ms, Av=3, Δ=20ms, δ=4ms, FOV=30x30mm2, Mtx=128x128, corresponding to an in-plane resolution of 234.4 x 234.4 μm^2, slice thickness=1.5 mm and number of slices 3. Images were acquired in three orthogonal directions (L-R, A-P and H-F) and with 8 b values 250<b<2000 s/mm^2, and each sequence lasted 13min. Note that de diffusion times Δ and δ and the b values are the same as in the experiments performed in the 7T Bruker scanner in order to consider the same diffusion range. A total of 3 sequences were acquired per animal, one before the ghrelin administration (basal condition), one immediately after the i.p. administration (ghrelin) and the third 20 min after the insult (20 min after ghrelin).

3.3 Results

3.3.1 fDWI evaluation of hypothalamic activity in NPY-lacking mice

Physiological characterization

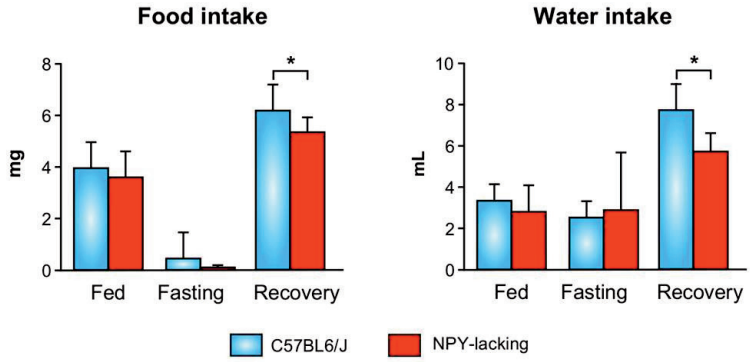

Figure 3.2. Food and water intake measurements of C57BL6/J and NPY-lacking mice. Mean values (±SD) of the food (left) and water (right) intake of n=12 NPY-lacking (red) and n=13 C57BL6/J (blue) mice in fed *ad libitum,* fasting and recovery conditions (*p<0.05, two-tailed unpaired T student tests). Note the decrease in food and water intake in the mutant mice in the recovery period.

Figure 3.2 shows the mean values (±SD) of the food consumed (g) and water drunk (mL) by the control (blue) and the NPY-lacking (red) mice in the fed *ad libitum*, fasting and recovery conditions. With unrestricted access to food, these mice did not show significant differences in food or water consumption. In the recovery phase after fasting, however, NPY mice showed significantly reduced food and drink intake.

Hormonal Profiles

Bar graphs in Figure 3.3 illustrate mean (±SD) values of the peptides and hormones analyzed of the C57BL6/J mice (in blue bars) and of the NPY-lacking mice (red bars), in the different feeding conditions evaluated. One-way ANOVA tests between values in C57BL6/J and *129S-Npy^{tm1Rpa}/J* mice showed that insulin levels in mutated mice are significantly lower in the fed *ad libitum* and 16h of fasting conditions, as compared to control mice. On the contrary, ghrelin and PYY plasma levels in the fed *ad libitum* state are significantly higher in the NPY-lacking mice. Additionally, results in the control mice showed that insulin and leptin levels decreased significantly from the fed *ad libitum* state to the 16h and 48h of fasting conditions (Table 3.1).

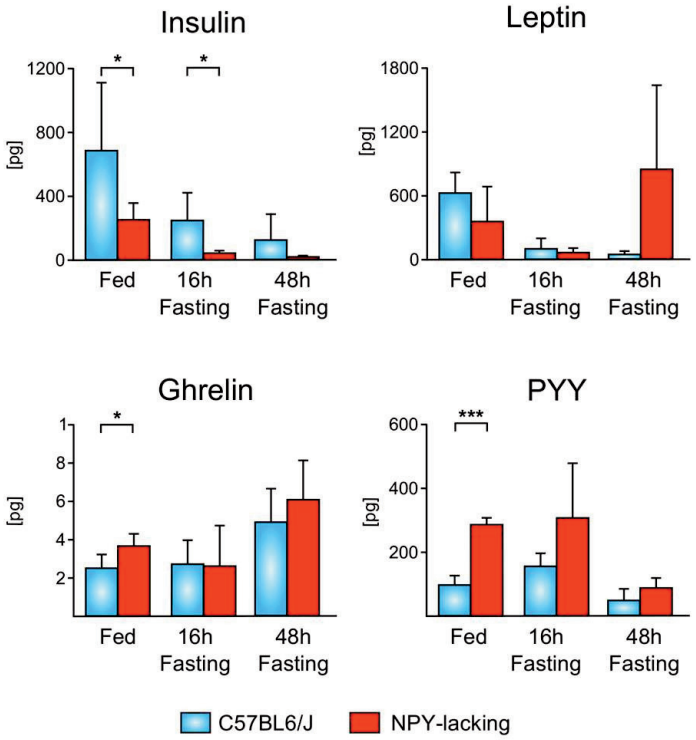

Figure 3.3. Blood Analyses of NPY-lacking mice and C57BL6/J mice. Insulin, Leptin, Ghrelin and PYY mean values (±SD) of NPY-lacking (red) and C57BL6/J (blue) mice in the fed, 16h of fasting and 48h of fasting conditions, with n_{fed}=6,$n_{16h\ fasting}$=6,$n_{48h\ of\ fasting}$=5 NPY-lacking animals and n_{fed}=7,$n_{16h\ fasting}$=8,$n_{48h\ of\ fasting}$=7 C57BL6/J mice (*p<0.05, ***p<0.001, two-tailed unpaired T student tests).

PYY increased in the overnight fasting and decreased in the longer fasting period, and ghrelin decreased in the 48h of fasting state. In NPY-lacking mice, insulin decreased also in both periods fasting but leptin increased in the 48h. PYY decreased only in the longer fasting and ghrelin levels only changes significantly in the 16h and 48h of fasting comparison.

Table 3.1. Ghrelin, insulin, leptin and PYY ANOVA tests between feeding conditions in NPY-lacking and C57BL6/J mice

	Grhelin		Insulin		Leptin	PYY	
	C57BL6/J	NPY	C57BL6/J	NPY	C57BL6/J	C57BL6/J	NPY
fed Vs 16h fasted			*	***	***	*	
fed Vs 48h fasted	*		*	***	***	*	***
16h Vs 48h fasted	*	*				***	*

Significant differences between mice in fed *ad libitum*, 16h of fasting and 48h of fasting conditions, with n_{fed}=6, $n_{16hfasted}$=6,$n_{48hfasted}$=5 for mutant mice and n_{fed}=7, $n_{16hfasted}$=8,$n_{48hfasted}$=7 for control animals (*p<0.05, **p<0.005,***p<0.001, ANOVA tests with Bonferroni corrections).

fDWI

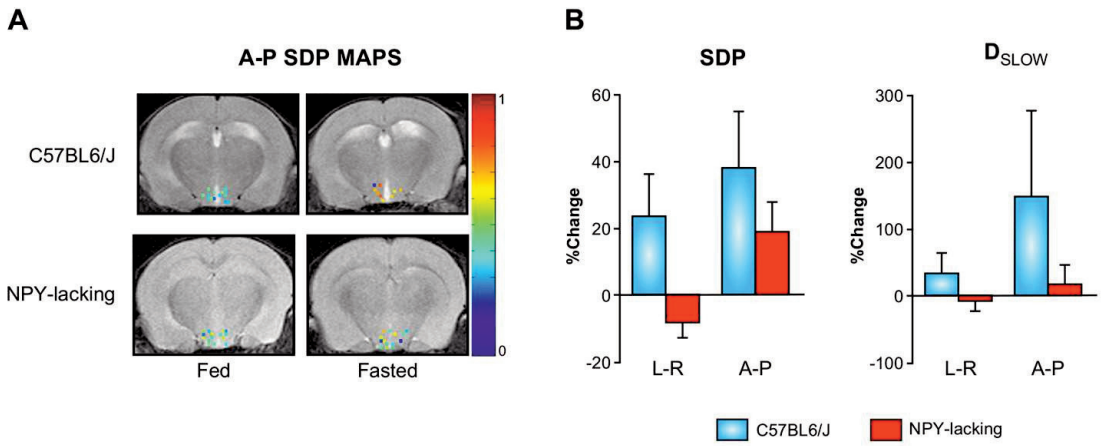

Figure 3.4. fDWI detection of hypothalamic activation by 48h of fasting in NPY-lacking mice. **A:** A-P SDP color maps of representative C57BL6/J (upper panels) and NPY-lacking (lower panels) mice, in the fed (left) or fasted states (right). Pixels in the hypothalamus are shown superimposed to a T2W image. **B**: Relative SDP and D_{slow} mean (±SD) changes (in %) between feeding conditions, for the C57BL6/J (blue) and NPY-lacking (red) animals, in the L-R and A-P directions. Note that increases in control mice are more pronounced.

Figure 3.4A shows A-P SDP parameter maps in the hypothalamus of representative C57BL6/J (upper panels) and NPY-lacking mice (lower panels) in the fed and 48 hours of fasting states. In the A-P direction, SDP values in the mutant mice increase with fasting, as depicted with a slight turn from green to green-yellow pixels. This increase is lower, however, than the SDP change in non-mutated mice, as illustrated by a turn from blue to orange in the upper panels. Figure 3.4B shows % of change of SDP and D_{slow} values from the fed to the 48 of fasting state in NPY-lacking mice (red) and control mice (blue). In the L-R direction, values of hypothalamic SDP and D_{slow} decrease with fasting in the mutant mice, although the difference is not significant. In the A-P orientation, slow diffusion values increase significantly with fasting ($p<0.05$), but to a lesser extent than normal mice.

In the overnight fasting evaluation of NPY-lacking mice, results depicted no significant differences between de fed and fasted conditions, neither in SDP nor in D_{slow} or D_{fast}. Statistical comparisons were performed independently between fed and fasted voxels in the ARC, DMN, VMN hypothalamic nuclei and whole hypothalamus in the three orthogonal directions, but no significant changes were found.

In summary, NPY deficiency reduced significantly the orexigenic stimulation, resulted in reductions in food and drink intake in *129S-Npy^{tm1Rpa}/J* mice and these circumstances were reflected by small or undetectable changes on fDWI parameters.

3.3.2 fDWI evaluation of hypothalamic activity in leptin-deficient mice

Physiological characterization

Figure 3.5 depicts the water and food intake, RER and locomotor activity values of C57BL/6J mice (blue) and ob/ob mice (red), during the 72 hours period spent in the metabolic cages. Left panels illustrate mean values at each time point measured, and bars graphs on the right depict mean values (±SD) of the accumulated measurements during the Fed, Fasting and Recovery conditions. Results show that in a fed *ad libitum* situation, obese mice consume higher quantities of water and food chow, as represented with higher red bars in panels A-B. RER values in obese mice are significantly higher than in control animals, and spontaneous activity counts are lower (bar graphs in panels C-D). In the fasting period, the ratio between delivered CO_2 and consumed O_2 slowly decreased in both groups, reaching its minimum mean value (0.77) at the end of the fasting, consistent with a shift from glucose to lipid metabolism. Activity measurements in this period are higher in the control mice, and food and water intake do not show statistical differences. In the recovery period, C57BL6/J mice rapidly recuperate from the fasting by consuming higher quantities of food during a short time, (depicted in figure 3.5B with a peak exceeding the 1 g height). In fact mice, their amount of chow consumed per day increases from around 3g under *fed ad libitum* conditions to 4.6 after the fasting. On the contrary, obese animals show a fasting-induced response spread along the recovery time, with no differences between amounts of food consumed in the fed *ad libitum* or recovery conditions. This is reflected with a significant decrease in body weight of obese mice during the whole protocol, and non-changing body weights in control mice. Spontaneous activity shows a peak right after the food refilling, decreasing in both strains for the rest of the light period (08:00-20:00h), recovering only the higher values during the dark cycle. Finally, light cycles play an important role in both types

of mice increasing the spontaneous activity counts in the dark cycle (20:00-08:00 h, Figure 3.5D).

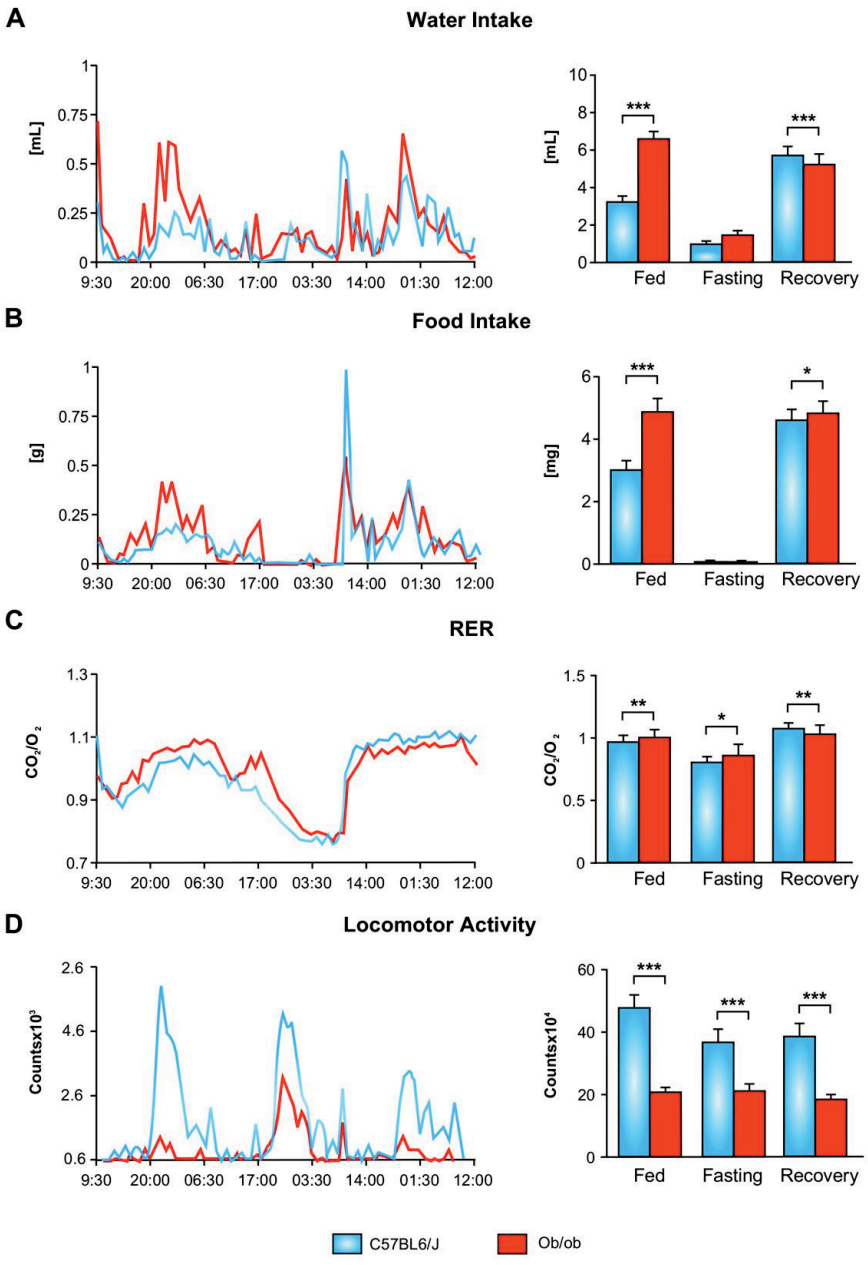

Figure 3.5. Indirect calorimetry measurements in ob/ob and C57BL6/J mice. A,C,E,G: Water, Food, RER and locomotor activity mean values of 8 C57BL6/J mice (blue lines) and 8 ob/ob animals (red lines) as a function of time. **B,D,F,H**: Water, Food, RER and spontaneous activity mean (±SD) values of the same mice averaged during the fed, fasting and recovery periods, and statistical significances between animal groups in the same feeding condition (*p<0.05,**p<0.005,*p<0.001).

Hormonal Profiles in blood

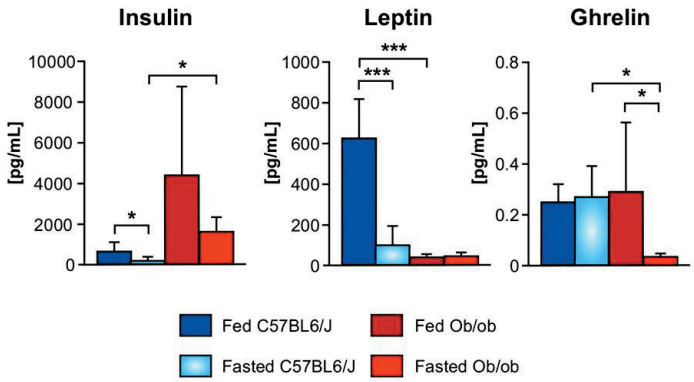

Figure 3.6. Blood Analyses of ob/ob mice and C57BL6/J mice. Mean values (±SD) of insulin, leptin and ghrelin measured in C57BL6/J (blue) and in ob/ob (red) mice in fed (dark colors) and 16h of fasting (light colors) conditions, with n_{fed}=7,$n_{16h\ fasting}$=7 obese animals and n_{fed}=8,$n_{16h\ fasting}$=7 C57BL6/J mice (*p<0.05,**p<0.005,***p<0.0001).

Mean values (±SD) of circulating levels of insulin, leptin and ghrelin of C57BL6/J (blue bars) and ob/ob (red bars) mice are depicted in Figure 3.6. Insulin levels decreased with fasting in both kinds of mice and are, in the two feeding states, higher in the obese animals. Leptin levels decrease with fasting in the control mice, but do not change in the obese mice, with very low levels in both states. Ghrelin levels decrease significantly with fasting in the obese mice, but are almost constant in C57BL6/J mice.

fDWI

Panel A in Figure 3.7 shows the anatomical localization of the hypothalamus and the orientation of the diffusion directions evaluated. The hypothalamic nuclei ARC, VMN and DMN are highlighted in blue, yellow and red, respectively, to favor identification (panel A, insert). Panel B shows SDP color maps of representative C57BL6/J (left) and ob/ob (right) mice in the fed. SDP values in the VMN and DMN hypothalamus of obese mice are higher than in control mice, as depicted by a turn to orange in the SDP maps. Mean values (±SD) of SDP and D_{slow} of obese and non-obese mice in the hypothalamic nuclei, in the fed (panel C) or fasting (panel D) conditions. SDP and D_{slow} values in the DMN and VMN are higher in the obese mice (Figure 3.7C).

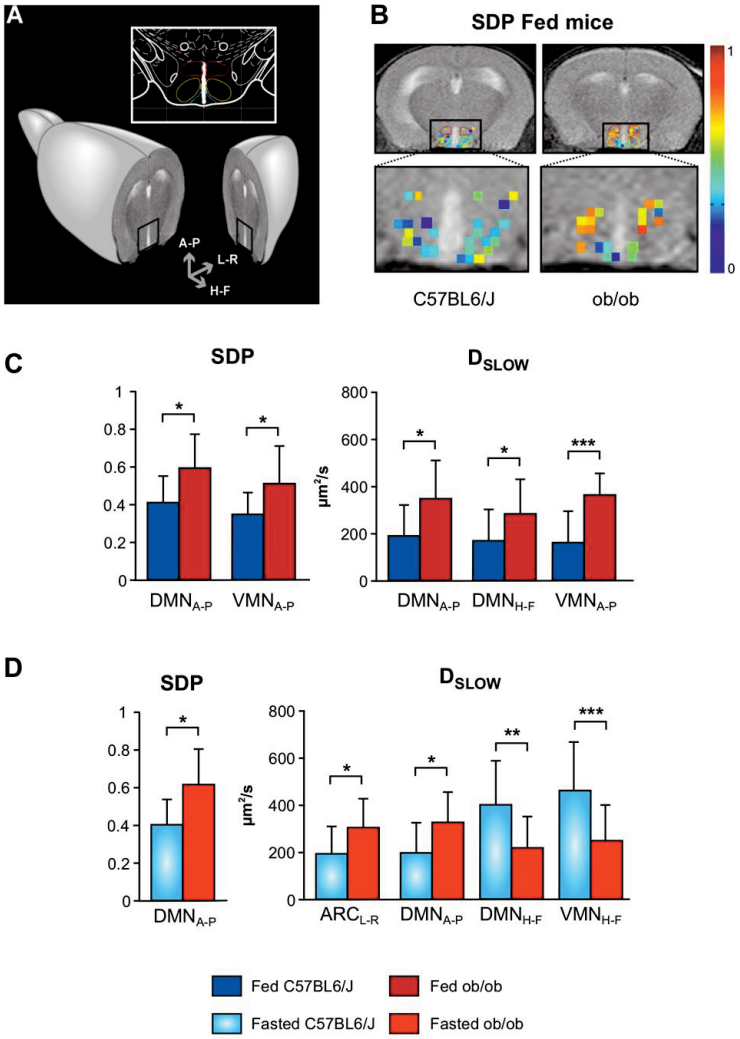

Figure 3.7. fDWI parameters in individual hypothalamic nuclei of ob/ob mice and control mice under the fed and fasting conditions. **A**: Localization of the hypothalamus, directions of diffusion measurements and localization of hypothalamic nuclei in a mouse brain atlas (insert). **B**: SDP parameter maps of representative C57BL6/J (left) and obese (right) animals in the fed "*ad libitum*" condition. The hypothalamic areas are shown enlarged in the lower panels. Note the turn from blue colors in the control animals to the orange tones in obese mice. **C**: Mean values (±SD) of SDP and D_{slow} coefficients diffusion of 6 C57BL6/J mice (blue) and 10 ob/ob mice (red), in fed (left) and 16h of fasting (right) conditions, in the L-R, A-P and H-F directions (*p<0.05, **p<0.05,***p<0.001).

In fasting conditions, obese mice show significantly higher SDP and D_{slow} values in the ARC and DMN, but lower in the H-F measurements of the DMN and VMN, as shown in bar graphs of Figure 3.7D. In the fed state, D_{fast} values in obese mice are higher than in control animals, in the DMN and VMN (H-F direction), and in the fasted state are higher in the H-F direction of the ARC (data not shown).

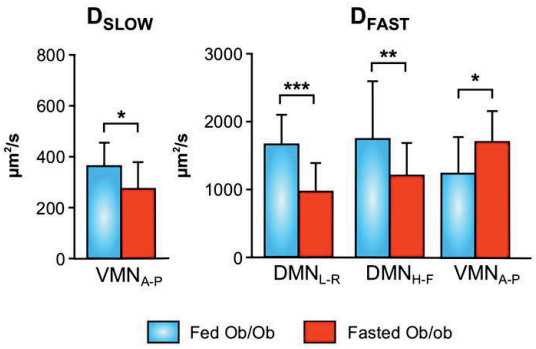

Figure 3.8. Fasting-induced significant changes of fDWI parameters of hypothalamic nuclei in ob/ob mice. Mean values (±SD) of diffusion coefficients of 10 ob/ob mice in the fed (dark red) or fasting (light red) conditions with significant changes between the feeding states (*p<0.05, **p<0.005, ***p<0.001).

Figure 3.8 shows mean (±SD) diffusion coefficients values of ob/ob mice in those hypothalamic nuclei that show significant changes between the fed (dark red bars) and overnight fasting conditions (light red). In the DMN, values of D_{fast} coefficients decrease significantly with fasting in the L-R and H-F orientations. In the VMN, D_{slow} values decrease significantly after the overnight fasting, and D_{fast} increase in the A-P direction.

Summarizing, leptin deficiency increases significantly the orexigenic stimulation in the fed "*ad libitum*" conditions. This stimulation was measured with increases in food and drink intake, altered metabolic substrate utilization and lower locomotor activity. These circumstances are reflected with significantly higher fDWI coefficients in the hypothalamus of fed *ad libitum* obese mice.

3.3.3 Correlation between high fat diet-induced obesity development and fDWI-detected hypothalamic activity

fDWI

Hypothalamic SDP color maps of representative obese and non-obese rats are shown in Figure 3.9A in the fed (left) and in the fasting (right) states. The area of the hypothalamic nuclei is drawn superimposed to the color map to facilitate identification; the DMN nuclei area is highlighted with an orange line, the VMN with yellow curves, and the ARC and third ventricle are indicated with pink lines. In the DMN, obese rats in the fed state show higher H-F SDP pixel values than non-obese

rats in the same feeding condition, as depicted with a shift from blue pixel colors in the non-obese rat panel (lowest left panel) to yellow/orange in the obese representation (upper left panel). In fasting obese rats, the ARC nucleus shows higher SDP values than in fasting non-obese rats, as illustrated by the shift from blue in the non-obese rat (lower right panel) to light blue/yellow pixel colors in the obese rat (upper right panel). SDP Mean values (±SD) of obese and non-obese rats that show significant differences between obesity conditions, either in the fed or fasting states, are represented in the bar graphs in Figure 3.9B.

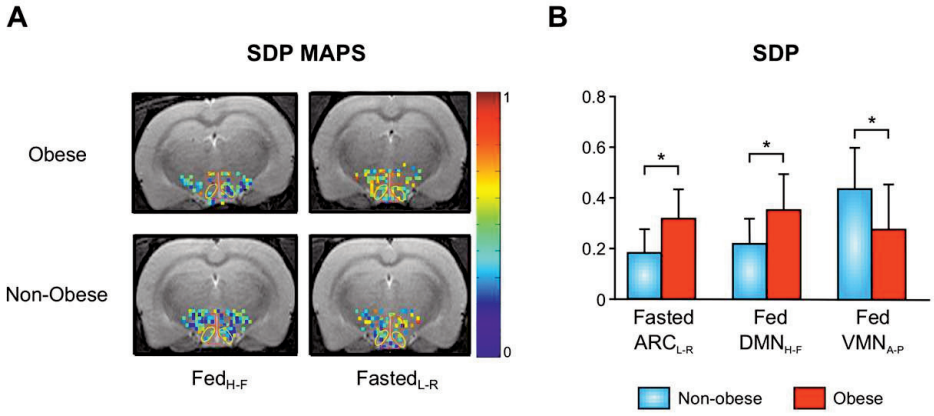

Figure 3.9. fDWI detection of activation in the hypothalamic nuclei of HFD rats. **A**: SDP parameter maps of obese (upper panels) and non-obese (lower panels) rats, in the fed (left) and fasting (right) conditions. Color maps are shown superimposed to T2W images. The hypothalamic nuclei ARC (pink), VMN (yellow) and DMN (red) are shown superimposed. Note the increase in SDP in fasted conditions from non-obese to obese rats, illustrated as a turn from dark blue to green in the color maps. In the fed state, note a similar increase in the DMN nuclei. **B**: Bar graphs of SDP mean values (±SD) changing significantly between the 4 non-obese (blue) and 4 obese (red) animals (*$p<0.05$).

In the fasting state, obese rats show significantly higher values of SDP in the ARC nuclei, in the L-R direction of measurement ($p<0.05$). In the fed condition, obese rats show higher values of SDP in the DMN in the H-F direction ($p<0.05$), and lower SDP coefficients in the A-P VMN ($p<0.05$). Besides, D_{slow} coefficients changed significantly between obesity groups in the A-P measurements in the fed VMN, with lower values for the obese rats ($p<0.05$). D_{fast} did not vary between groups in any of the conditions evaluated. Bar graphs in Figure 3.10 show mean (±SD) diffusion coefficient values that change significantly after fasting, in obese rats (upper panels)

and in non-obese rats (lower panel). In the obese group, SDP values increase significantly with fasting in the ARC H-F and VMN A-P directions, while values in the DMN A-P decrease. Besides, obese rats showed increased D_{slow} values with fasting in in the H-F orientation in the ARC nuclei and the A-P and H-F directions of the VMN. D_{fast} decreases in the L-R measurements in the ARC and on A-P direction in the DMN. For non-obese rats, SDP L-R values in the ARC decrease in a significant manner, and no other significant changes with fasting are detected in the D_{slow} or D_{fast} coefficient values.

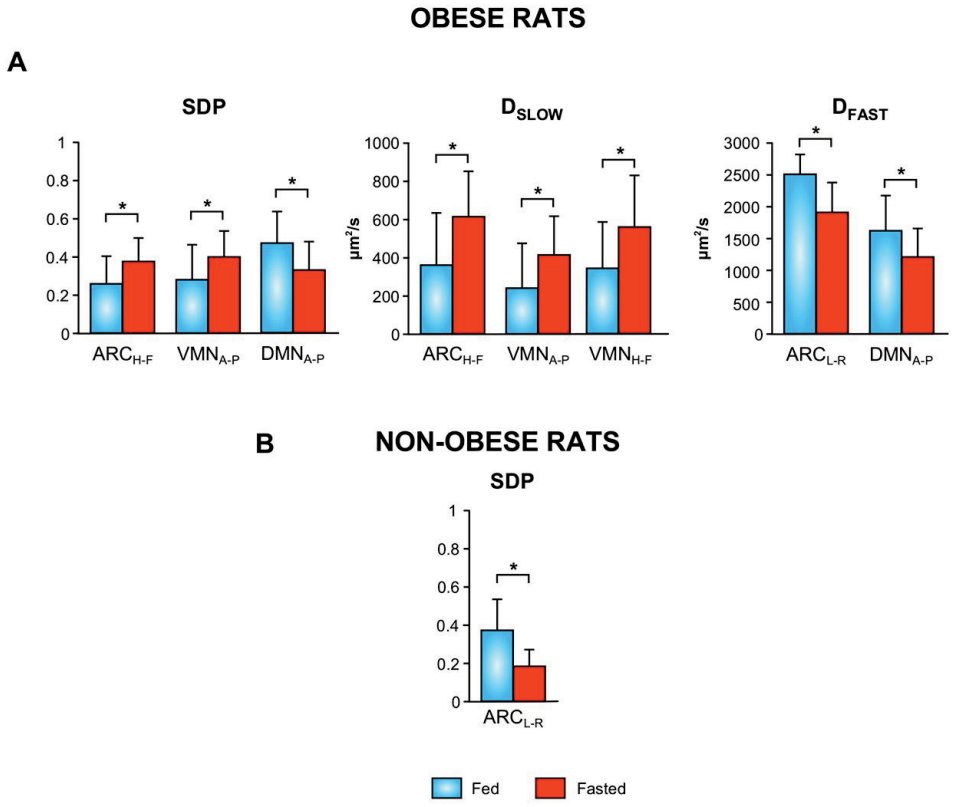

Figure 3.10. Activation by fasting in hypothalamic nuclei of HFD-obese and HFD-non-obese rats. Mean values (±SD) of fDWI hypothalamic nuclei parameters that reach statistical significance between states in HFD-induced obese (**A**) and HFD-administered non-obese (**B**) rats

In summary, HFD-induced obesity development increases significantly the fDWI parameters in the ARC and DMN. On the contrary, non-obesity development appears to be associated to an inability to modify the diffusion parameters in the ARC.

3.3.4 Hypothalamic nuclei fDWI-changes after ghrelin administration to fasted mice

fDWI

Figure 3.11A shows the anatomical localization of the hypothalamic nuclei investigated before and after the administration of the peptide. Representative D_{slow} maps in the Basal, Ghrelin and 20 min after ghrelin conditions are shown in the three images in panel B. The ARC nuclei shows decreases in the D_{slow} values in the H-F direction, as depicted with a turn to from orange (Basal panel) to blue (20 min after ghrelin image). Bar graphs in panel C illustrate mean values (±SD) and statistical differences between conditions of the diffusion parameters of all mice in the hypothalamic. Between the basal and the ghrelin states, SDP decreases significantly in the DMN, D_{slow} decreases in the ARC and D_{fast} values decrease in the VMN. Between the initial state and 20min after ghrelin, SDP decreases significantly in the ARC, D_{slow} decreases in the DMN, and D_{fast} decreases significantly in the VMN. In the ghrelin and 20min after ghrelin comparisons, D_{slow} values increase in the VMN.

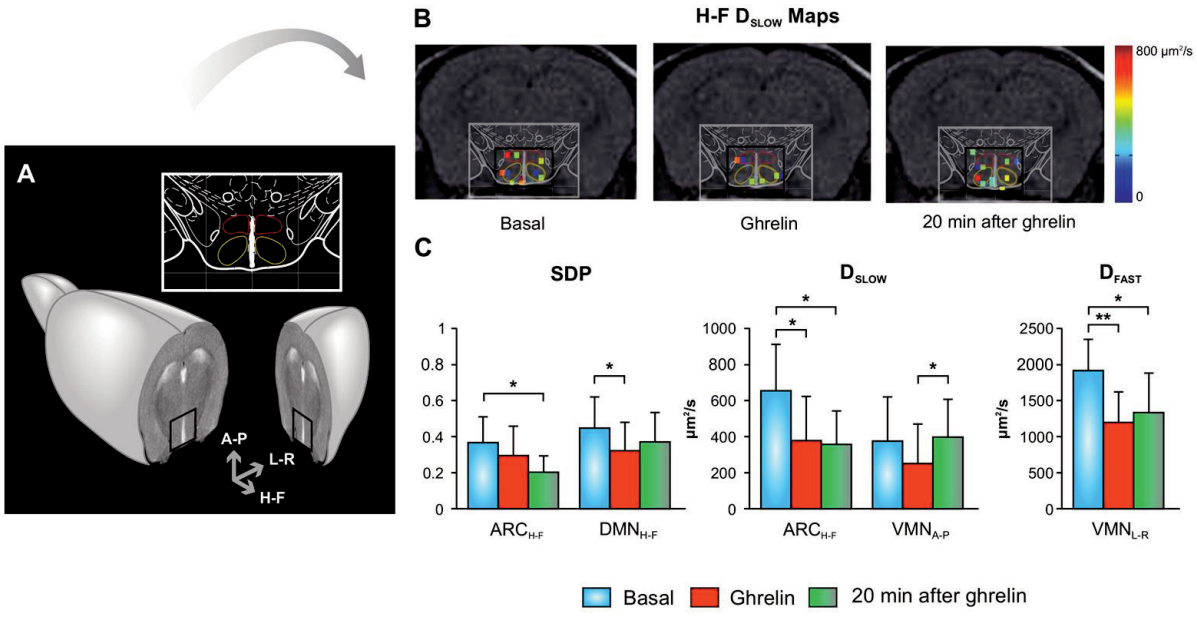

Figure 3.11. fDWI parameters of hypothalamic nuclei during the ghrelin administration paradigm in C57BL6/J fasted mice. **A**: Anatomical localization of the mouse hypothalamus and directions of DWI measurements. The localizations of the ARC (in light blue), VMN (in yellow) and DMN (in red) are shown in the inserted anatomical atlas. **B**: D_{slow} parameter maps in the basal (left), ghrelin (center) and 20 min after ghrelin (right) states. **C**: Bar graphs with mean (±SD) values of all mice investigated (n=13). Only values reaching statistical significance are depicted (*p<0.05, **p<0.001).

Results of diffusion mean values in the entire hypothalamus are shown in Table 3.2. Hypothalamic mean values of SDP and D_{slow} decrease significantly from the basal to the ghrelin sates (H-F direction), while D_{fast} increases (A-P orientation). In the basal to 20 min after ghrelin period, SDP and D_{slow} decrease in the H-F direction. Finally, in the ghrelin to 20 min after ghrelin condition, D_{slow} and D_{fast} values decrease (L-R and A-P, respectively).

Table 3.2. Whole-hypothalamus diffusion values between conditions in the ghrelin administration experiments

	SDP_{H-F}	$D_{slow\ H-F}$ [$\mu m^2/s$]	$D_{slow\ L-R}$ [$\mu m^2/s$]	$D_{FAST\ A-P}$ [$\mu m^2/s$]
Basal	0.36±0.15	445±241	294±199	1248±454
Ghrelin	0.30±0.15	354±232	309±201	1357±449
20 min after ghrelin	0.32±0.15	388±238	258±199	1264±466
Basal Vs Ghrelin	***	***	>0.05	*
Basal Vs 20 min after Ghrelin	*	*	>0.05	>0.05
Ghrelin Vs 20 min after Ghrelin	>0.05	>0.05	*	*

SDP, D_{slow} and D_{fast} mean values (±SD) of all voxels in the hypothalamus of C57BL6/J mice (n=13) that show significant differences between states (*p<0.05, **p<0.005, ***p<0.001, T student tests).

Summarizing, ghrelin administration to fasting mice elicited fDWI decreases in the ARC, DMN, and increases or decreases in the VMN and whole hypothalamus, depending on the direction investigated.

3.4. Discussion

The hypothalamus is a complex structure containing highly specific neuronal groups organized in subhypothalamic nuclei that control, among other functions, appetite and global energy balance [64]. Alterations in this balance can lead to obesity or weight loss processes [75], as described in more detail in the first chapter of this work. Here, we have evaluated the effect of different manipulations of the

hypothalamic neuronal pathways using fDWI tools, providing an ample frame for the validation for our methodology.

Genetically modified *129S-Npy^{tm1Rpa}/J* mice, which do not express the orexigenic peptide NPY, show a weaker response to fasting than that found in unmodified C57BL6/J mice. This weaker response is characterized by lower levels of food intake, higher levels of PYY in the basal state, and almost unvarying leptin levels and fDWI values between feeding conditions. The lack (or small) fDWI-detected orexigenic changes induced by fasting, either after 16h or 48h of food deprivation, suggests that changes in diffusion parameters are good indicators of the decreased physiological response to the fasting stimulus. The reduced response to fasting detected is most probably caused by the deficient orexigenic activation of NPY-null mice, being detected here for the first time, as a lower activation-induced cellular swelling process in the hypothalamus.

On the contrary, B6.V-*Lep^{ob}*/J mice, the obese mice, show very high slow diffusion coefficients in the fed *ad libitum* conditions, greater amounts of food and water consumption, increased body weights and a hormonal profile that promotes enhanced orexigenic behavior, even in the fed *ad libitum* conditions. More specifically, the fDWI data in the fed *ad libitum* state reveal increased SDP and D_{slow} values in the DMN and VMN nuclei (Figure 3.7C), as compared to values of C57BL6/J mice. Higher slow diffusion coefficients agree with the reported greater astrocytic volumes in the hypothalamic nuclei of obese mice [143], and indicate higher functional activity [24, 161]. D_{fast} values in the DMN and VMN nuclei of mutant mice are also larger, a circumstance that could reveal increased residual microvascular contributions [34]. In fact, the reactive astrogliosis in the hypothalamus of obese mice [144], is linked to a large number of microvessels supporting the higher number and volumes of peripheral astrocytes. Taken together, our results indicate increased neurocellular swelling and augmented microvascular contributions, consistent with the higher orexigenic activity observed in obesity. Moreover, the fDWI-detected increased hypothalamic functionality is well supported by the physiological changes measured, being a direct consequence of the absence of the anorexigenic agent leptin [162]. Indeed, leptin-deficient mice have been

demonstrated to have increased hypothalamic activity even in fed *ad libitum* conditions [62].

Ob/ob mice, however, show a relatively poor activation by fasting, as compared to activation in C57BL6/J mice. In the ARC and DMN nuclei, L-R and A-P diffusion measurements in the fasting condition suggest higher activity in obese mice than in the controls. On the contrary, values in in the ARC in the H-F orientation suggest the opposite. This lack of generalized higher activity during fasting in obese animals is in agreement with the food intake measurements during the recovery period: while C57BL6/J mice respond to fasting increasing rapidly their food intake, obese animals eat similarly to the pre-fasting conditions. Furthermore, the decrease in RER values detected in the recovery period for the ob/ob group, indicate an increased lipid metabolism that is coupled with the decreased necessity of activating the orexigenic pathways promoting food intake.

The effects of obesity development in the hypothalamic activity are investigated in more detail in the HFD-administration experiments. Our results point towards positive correlations between obesity development and hypothalamic nuclei hiperactivation -thus astrocytic inflammation- in the DMN and ARC nuclei. In contrast, non-obese rats show a lack of fDWI-detected orexigenic response. These results are in agreement with recent immunohistochemical evidences revealing that mice under HFD show increased number and size of microglial cells, specifically in the ARC [143] and in the DMN [144], thus suggesting that different hypothalamic nuclei may have distinct inflammatory responses. Moreover, our results are supported by recent MRI approaches investigating diet-induced obesity models in rodents [149]. Authors reported an increase in T2 relaxation times in the hypothalamus of diet-induced obese mice, as compared to controls, that was positively correlated with increased astrocyte density (detected histologically). They failed, however, in detecting changes in diffusion parameters arguing that either the small ROIs used or the small number and range of b values assayed (only 0 and 1000 s/mm^2) could be hampering the information obtained, a circumstance that in our study has been extensively improved.

The administration of ghrelin to fasting mice gave rise to generally decreased slow diffusion fractions and slow coefficients in all nuclei investigated, lasting along all the acquisition time in the ARC. Decreased slow diffusion fractions are normally associated to cellular shrinking [24], and cellular shrinking is associated to decreased neurocellular activity [27, 163, 164], as reported in the rest of the experiments presented herein. On these grounds, these results suggest that ghrelin deactivates the hypothalamic nuclei, a concept apparently in conflict with the reported orexigenic effects of this peptide [150, 165]. In fact, ghrelin has shown to act specifically in the hypothalamus [166], where MEMRI methods have been used to detect activations in the ARC and VMN nuclei of fed *ad libitum* mice [154]. In our study, however, mice were imaged in a fasted state, a condition that could hinder the orexigenic effects of the exogenous administration of ghrelin, at least at the same dose used in studies with fed mice. In fact, another study using ^{13}C high resolution magic angle spinning (HR-MAS) techniques failed to detect regional alterations in the metabolism of [1-^{13}C] Glc after the administration of similar doses of ghrelin to fed mice, but detected alterations in the hypothalamic metabolism between the fed or fasted mice [133]. Authors concluded that the signaling network involved in the fasting process was not mimicked adequately by ghrelin administration only, while additional signals would be required to elicit the complete orexigenic hypothalamic effect.

Additionally to the dose-dependent effects, the different experimental conditions in the ghrelin administration experiment, in comparison with the rest of the fDWI approaches described here, could represent an additional difficulty in the combined interpretation of the results. Ghrelin experiments were performed with a higher field scanner, which involves different acquisition protocols, experimental setup and imaging artifacts. High magnetic fields, even though producing higher values of the SNR, are associated to higher field inhomogeneity, hence prone to produce increased geometric distortion and susceptibility artifacts. Susceptibility effects limit, at the same time, the SNR, causing signal loss at relatively long echo times and limiting eventually the spatial resolution. Notably, being the ROIs investigated here very small, it is highly probable that the geometric distortions, the signal loss or the

limited spatial resolution may have hampered the detection of ghrelin fDWI effects on hypothalamic nuclei.

Summarizing, our results with NPY-lacking animals, leptin-deficient mice, HFD-induced obese rats, and ghrelin- administration experiments, show that fDWI can be used as a marker of neuronal activity during hypothalamic performance. Generally, increases in orexigenic activity and associated hormonal responses, lead to increases in SDP and D_{slow}. In contrast, decreases in orexigenic activity and concomitant hormonal profiles are paralleled by lower SDP and D_{slow}. It appears then to exist a close relationship between the diffusion parameters and their physiological determinants. In this sense, it should be noted that we introduced here specific genetic deletions in the orexigenic and anorexigenic pathways and showed that these selective modifications result in the expected fDWI effects. This reveals that stimulation or inhibition of the feeding impulse proceeds through different hypothalamic pathways, activate different subhypothalamic nuclei and may be adequately visualized by fDWI.

Chapter 4

Glucose sensing in the hypothalamus as detected by fDWI and T2*W methods. A comparative study.

*I report on the effects of glucose administration on the activity of hypothalamic nuclei, as detected with fDWI and T2*W imaging techniques. Comparisons between the fMRI results obtained by both methodologies provided information the physiological events underlying the glucose sensing mechanisms in the hypothalamus.*

4.1 Introduction

Glucose is the primary source of energy in the adult mammalian brain [167]. While hypoglycemic conditions cause cerebral energy failure, coma or even death [168], hyperglycemia can lead to excitotoxic damage by glutamate, reduced cerebral blood flow, vascular reactivity and dementia [169]. Thus, the regulation of extracellular glucose levels entails, vital importance to ensure satisfactory cerebral energetics [170]. Glucose sensing is achieved by some specialized neuronal groups in the hypothalamus, which exhibit excitatory or inhibitory responses to acute changes of extracellular glucose levels [171]. Glucose-excited neurons (GE) increase their action potential frequency with increased glucose levels, while glucose-inhibited neurons (GI) decrease it [172, 173]. The VMN and lateral hypothalamus (LH) are known to exhibit GI and GE neurons [68, 174-178]. In the ARC, however, although the contribution of pro-opiomelanocortin (POMC) and NPY neurons in the stimulation or inhibition of appetite is quite established [72], its role in the glucose homeostasis process remains unclear [179, 180]. Moreover, the ultimate function of the glucose sensing mechanisms in the brain and their integration with systemic regulation by pancreatic hormones, remains insufficiently understood.

The use of non-invasive evaluation methods may favor a better understanding of these processes. Notably, neuroimaging techniques like PET or fMRI are well endowed to detect glucose-induced changes by detecting variations in neuronal activity. PET studies provide functional information from the increase in glucose uptake and blood flow in activated areas [122]. BOLD fMRI infers functional information from activity-induced variations of magnetic susceptibility, as detected with T2*W imaging methods, reflecting changes in the oxyhemoglobin/deoxyhemoglobin ratio and blood flow [83]. Indeed, BOLD fMRI and PET studies have been used previously to investigate hypothalamic responses to the administration of glucose [93, 181-184]. However, the use BOLD fMRI in hypothalamic activity through T2*W imaging methods, has been mainly limited by the high spatial and temporal resolutions required. Furthermore, the physiological origins of the BOLD contrast effect remain unclear [185]. PET imaging is also limited by the

spatial resolution requirements and its use is restricted because of the large amounts of radiation involved.

Notably, functional diffusion weighted imaging has recently emerged as a new methodology to evaluate cerebral activation [24] and hypothalamic responses to fasting [186]. This technique identifies cerebral functionality by detecting activation-induced water diffusion changes, and is inherently endowed with higher spatial and temporal resolution than BOLD or PET imaging approaches, but the biophysical events underlying the fDWI-observed variations demand further substantiation [34, 129]. On these grounds, it would become advisable to evaluate the glucose sensing process using two independent techniques as fDWI and T2*W, to be able to extract common features and differences between these methods and elaborate a unifying interpretation. Here, we address this topic by providing an fDWI and T2*W evaluation of hypothalamic activity after the administration of glucose to fasting mice. We analyzed the fDWI data by performing monoexponetial and biexponential diffusion models –at high b and low b values- and compared the results obtained with the fMRI T2*W observations. The comparison allowed an integrative interpretation of the different biophysical events underlying functional MRI detection and provided a more comprehensive view of the glucose-sensing process in the individual hypothalamic nuclei.

4.2 Materials and Methods

4.2.1 Animals and experimental design

C57BL6/J mice (n=22, 8-11 weeks, 24±1.3g) were fasted overnight and imaged in a 7T Bruker Biospec scanner, before and after the i.p. administration of glucose (8mL/Kg at a dose of 16.6mM/Kg) or saline (8mL/Kg). Animals were divided in four experimental groups: group 1 (fDWI/glucose administration, n=7), group 2 (fDWI/saline administration n=4), group 3 (T2*W/glucose administration, n=7), group 4 (T2*W/saline administration, n=4).

The fDWI protocol consisted in acquiring two consecutive sequences (low and high b) before the glucose/saline administration ("basal"), either immediately after the substrate bolus ("glucose" or "saline") or 35 min after ("recovery"). The T2*W procedure entailed a similar set of sequences acquired before and after the glucose/saline administration, with the "basal", "glucose"/"saline" and "recovery" conditions defined as in fDWI protocol. Immediately after the imaging sessions, we performed blood glucose tests, while blood samples were stored for posterior analyses of insulin, leptin and ghrelin. A general overview of the methodology implemented is depicted in Figure 4.1.

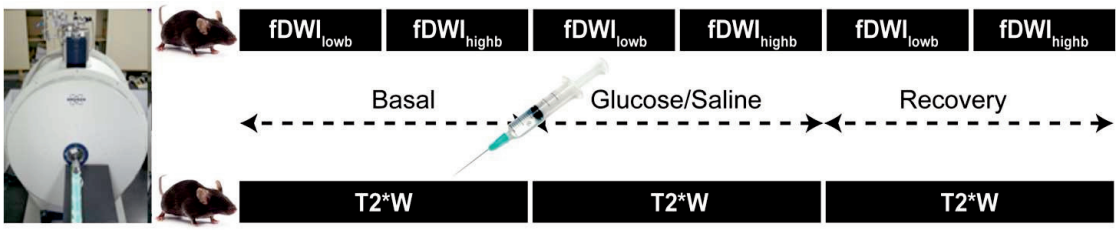

Figure 4.1. Overview of the methodology implemented in the fMRI evaluation of hypothalamic glucose sensing. C57BL6/J mice (n=22) were imaged in a 7T scanner (left image) using either fDWI (upper sequence) or T2*W protocols (lower sequence). Glucose or saline were administered 35 min after starting imaging session, and acquisitions were divided into "basal", previous to substrate administration, "glucose/saline" obtained during the 35 min following the injections, and "recovery", obtained the last 35 min of acquisition.

4.2.2 Imaging protocols

All imaging experiments started at 9 a.m. Two animals were examined per morning to minimize uncertainties derived from significantly different durations in the circadian rhythms [187]. During image acquisition protocols, animals were anesthetized with 1.5% isofluorane/oxygen, maintaining constant the tempetarure of the animalwas kept constant at 37 degrees with a recirculating water circuit. The physiological state during the imaging process was further monitored by the respiratory rate and body temperature using an ECGT/Temperature device (Model 1025, Small Animal Monitoring and Gating System, SA Instruments, Inc., NY). Animals were weighted the night before fasting and just before starting the imaging protocols.

All images were acquired with a 7T Bruker AVANCE III magnet equipped with a 1H selective birdcage resonator of 23 mm and a 90 mm diameter gradient insert (36G/cm). Imaging data were acquired using Hewlett-Packard console console running Paravision 5.1 software (Bruker Medical Gmbh, Ettlingen, Germany).

fDWI protocols consisted in serial consecutive DWI acquisitions with "high diffusion weighting" (high b) and "low diffusion weighting" (low b). "High b" images were acquired using the following parameters; TR/TE=3000/31ms; δ=4*ms,* Δ=20ms and nine b values in the range 300<b<2000 s/mm^2. "Low b" images were acquired under similar TR/TE conditions and diffusion times, but using eight low b values in the interval 10<b<600 s/mm^2. In-plane resolution was 0.165 μm^2/pixel and the voxel height was 1.125 mm in both cases.

The T2*W protocol consisted in consecutive gradient-echo sequences (TR/TE=182/4ms) of 1 min and 20 s of duration each, and similar spatial resolution to that obtained in the DWI sequences. The "basal", "glucose/saline" and "recovery" states consisted, then, in eighteen consecutive T2*W image acquisitions.

4.2.3 Image analyses

DWI results were analyzed using monoexponetial and biexponential models for the "high b", and biexponetial fittings for the "low b" datasets. Home-made MATLAB libraries were used for this purpose, in a similar manner to that described in Chapter 2. T2*W values in each scan, were normalized to the maximum value inside the brain. The "basal", "glucose/saline" or "recovery" conditions were subdivided in three consecutive subsets of six scans each. Voxels showing unstable behavior, with intensity variations larger than 15%, within each subset, were not further considered. ROI's for the hypothalamic nuclei, ARC, DMN, VMN, LH and a control area in the hippocampus, were manually selected for each animal. Each pixel from each nuclei and animal could be then be defined by specific "low b" (SDP, D_{slow}, D_{fast}) and "high b" (ADC, SDP, D_{slow} and D_{fast}) coefficients for the "basal", "glucose/saline" and "recovery" conditions, or by a collection of normalized T2*W values in each condition. Statistical evaluations were performed independently for each coefficient and area, comparing values of all animals in the different functional conditions evaluated with

one-way ANOVA tests, and corrected with Bonferroni tests to account for the different states evaluated.

4.2.4 Blood tests

After imaging sessions, blood glucose levels in all animals were measured with a glucometer (One touch Ultra, Lifescan, Johnson and Johnson, Issy-les-Moulineaux, FR) in blood drained from the tail vein. Immediatelly after, while mice were still anesthetized, blood samples of seven glucose-administered and six saline-administered mice were extracted from the heart and stored for the subsequent analyses of ghrelin, insulin, and leptin, using a Mouse Metabolic Hormone Magnetic Bead Panel and following the same procedures described in the *Hormonal profiles in blood* part in Chapter 3.

4.3 Results

4.3.1 Physiology

We evaluated the body weights of the animals in the different groups before the imaging experiments. Body weights of the animals that underwent the glucose-administration (24.2±1.3g) decreased significantly ($p<0.001$) during the overnight-fasting preceding the imaging session. The decrease was, on average, of an 11±2% of their initial body weight. Animals that underwent the saline administration procedures (24.9±1.4g) lost, on average, a significant ($p<0.001$) 11±1% of their body weight. In this respect, no significant differences are found between the glucose and saline treated animal groups. Rectal-temperature measurements did not show significant differences between the different animal groups.

4.3.2 fDWI

Figure 4.2 shows the mean values of ADC coefficients (±SD) determined at high b in the glucose (left) and saline (right panel) groups under the different functional states investigated, “basal” (blue), “glucose/saline” (red/white) and “recovery” (green). Mice receiving glucose depict significant increases in the L-R ADC in the DMN, VMN, LH and hippocampus after the bolus administration. In the recovery period, L-R ADC values decrease significantly in all nuclei investigated and also in the hippocampus. Besides, L-R ADC decreases significantly in the DMN when comparing values in the

basal and recovery periods. No significant changes are found in the saline-administered group in the hypothalamic diffusion coefficients evaluated, but H-F ADC values in the hippocampus increased significantly after the glucose administration, decreasing in the recovery period.

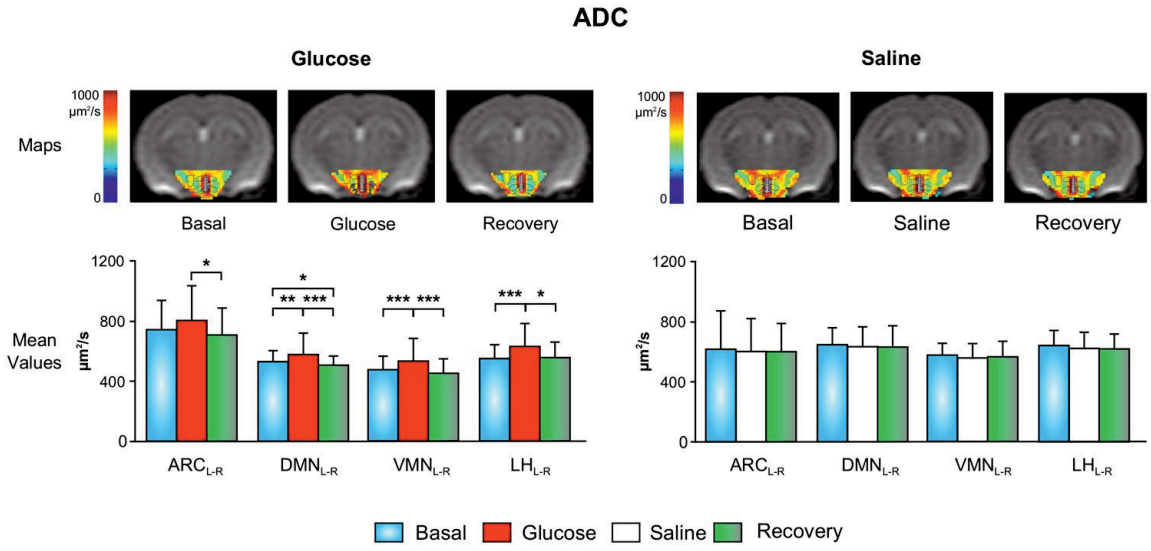

Figure 4.2. ADC changes in hypothalamic nuclei after the administration of glucose or saline to fasted mice. **Left panels**: ADC color maps of a representative mouse before the administration of glucose (basal), after (glucose) and in a recovery (recovery) phase (upper images). Pixel values in the hypothalamus are shown superimposed to a T2 image, and ROI's of the hypothalamic nuclei ARC, VMN, DMN and LH are circled in black to favor identification. Mean ADC values (± SD) of all mice from the glucose group in the basal (blue), glucose (red) and recovery (green) periods are depicted in the lower bar graphs. **Right panels**: ADC parameter maps of a representative mouse before and after the administration of saline, in the basal, saline and recovery states. ADC pixel values in the hypothalamus are shown in colors superimposed to a T2W image. ADC mean values (±SD) of all animals from the saline group in the basal (blue), saline (white) and recovery (green) conditions. (*p<0.05, **p<0.005,***p<0.001, ANOVA tests with Bonferroni corrections). ADC: Apparent Diffusion Coefficient; ARC: Arcuate Nucleus; DMN: Dorsomedial Nucleus; VMN: Ventromedial Nucleus; LH: Lateral Hypothalamus; L-R: Left-Right.

Mean values (±SD) of high b SDP coefficients for the glucose and in saline groups are shown in Figure 3. Mice receiving glucose show significant decreases of SDP after the administration of the bolus in the A-P values of the ARC and in the L-R and H-F directions of the DMN. In the recovery period, values increase although these changes do not reach statistical significance. The saline-injected mice show decreased values of SDP in the DMN in the basal-to-saline transition, and decreased values of SDP in the hippocampus in the saline-recovery process. Additional significant changes in the D_{slow} and D_{fast} coefficients are presented in table 4.1.

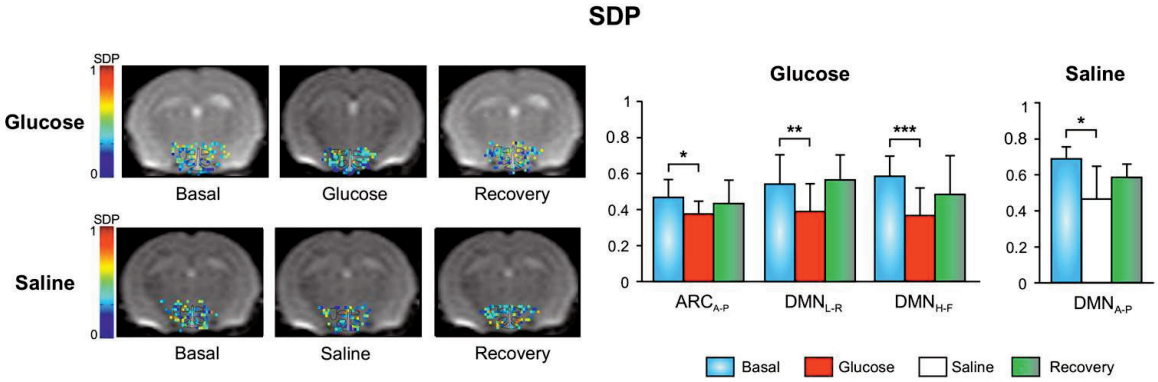

Figure 4.3. SDP changes in the hypothalamic nuclei after the administration of glucose or saline to fasting mice. Left panels: hypothalamic SDP maps of a representative mouse administered with glucose (upper images) or saline (lower images), in the basal, glucose ore saline and recovery conditions. ROI's of hypothalamic nuclei of ARC, DMN, VMN and LH are circled in black to favor identification. **Right panels**: show bar graphs of mean SDP values (SD) of voxels in the hypothalamic nuclei of mice in administered with glucose (left) or saline (right). For simplicity, only values that show significant differences between conditions are depicted (*p<0.05,**p<0.005,***p<0.001, ANOVA tests with Bonferroni corrections).

Table 4.1 shows mean values of hypothalamic D_{slow} and D_{fast} coefficients in mice receiving glucose (left panels) or saline (right panels), in the basal (B), glucose (G) and recovery (R) conditions. Values reaching statistical significance between states are highlighted in black. Mice showed significant decreases in D_{slow} coefficients in the ARC and DMN after glucose administration. The recovery process is characterized by the return to initial D_{slow} values in the ARC, in the A-P and H-F directions. In the VMN and hippocampus, the recovery phase reflects decreases in D_{slow} and D_{fast}, as well as values in the L-R orientation in the ARC. The comparisons between the basal and recovery conditions show increases in L-R D_{fast} values in the VMN and hippocampus and decreases in the H-F only in hippocampus. Mice treated with saline show changes in the DMN and hippocampus. The saline bolus elicits decreases of D_{slow} in the DMN. In the recovery phase, slow coefficients decrease in the hippocampus, and comparisons between the "basal" and "recovery" phases indicate increases in D_{fast} in the DMN. The lateral hypothalamus does not show any significant changes in diffusion coefficients.

Table 4.1. Significant changes of high b biexponential diffusion coefficients

Glucose effects

ARC			
	B	**G**	**R**
D_{S1}	**275±121**	**282±198**	**146±87**$^{++*}$
D_{S2}	200± 50	**129±61**	**275±131***
D_{S3}	**316±125**	**243±163**	**449±226**$^{**+}$

VMN			
	B	**G**	**R**
D_{S1}	292±106	**360±108**	**258±94***
D_{F1}	**881±302**	847±393	**1186±367**$^{+}$

DMN			
	B	**G**	**R**
D_{S3}	**460±120**	**178±107**$^{###}$	357±208

Hippocampus			
	B	**G**	**R**
D_{S1}	**256±113**	**253±147**	**189±126**$^{*++}$
D_{F1}	1322±293	**1259±287**	**1397±334***
D_{F2}	**1042±302**	**1040±290**	**844±341**$^{+*}$
D_{F3}	**1374±455**	**1218±288**$^{#}$	1287±335

Saline effects

DMN			
	B	**S**	**R**
D_{S2}	**371±80**	**174±124****	292±52
D_{F2}	**830±342**	1032±474	**1506±220**$^{+}$

Hippocampus			
	B	**S**	**R**
D_{S2}	**315±92**	339±133	**183±89**$^{+++}$

Mean values (±SD) of slow (D_S) and fast (D_F) diffusion coefficients from mice receiving glucose (left) or saline (right) administrations. Results are given for the L-R (1), A-P (2) and H-F (3) directions in the ARC, DMN, VMN and Hippocampus, and for the basal (B), glucose/saline (G/S) and recovery (R) periods. For simplicity, only ROI's and directions with significant changes are given. ($^{\#}$, $^{\#\#}$, $^{\#\#\#}$, *, **, ***, $^{+}$, $^{++}$, $^{+++}$ indicate, respectively, statistical significances with $p<0.05$, $p<0.005$ and $p<0.001$ in basal vs glucose comparisons, glucose vs recovery, and basal vs recovery, using one-way ANOVA tests with Bonferrroni corrections).

Fitting the low b DWI data to the biexponential model yielded relatively poor results, with roughly 50% of the pixels fitting the model with $r^2>0.8$, as compared to the results obtained in the high b range. In spite of this, some mean values depict significant differences between physiological states (Table 4.2).

Table 4.2. Significant changes of low b biexponential diffusion parameters

Glucose effects

ARC			
	B	**G**	**R**
D_{F1}	**3055±1632**	**926±253**$^{\#}$	2110±1174

VMN			
	B	**G**	**R**
SDP_1	0.80±0.10	**0.75±0.12**	**0.89±0.02***
SDP_3	**579±138**	**118±83**$^{\#\#\#}$	**387±227***
D_{F2}	1854±1300	**2695±1154**	**1266±568***

LH			
	B	**G**	**R**
SDP_2	0.8±0.1	**0.68±0.21**	**0.89±0.01***
SDP_3	**0.78±0.10**	0.6±0.30	**0.6±0.16**$^{+}$
D_{S2}	317±186	**299±186**	**470±36***
D_{F2}	**2548±1606**	1841±1280	**715±91**$^{+}$

Hippocampus			
	B	**G**	**R**
D_{F2}	**1443±852**	**2353±1161**$^{\#}$	2182±1331
D_{F3}	2554±1097	**3265±1653**	**2071±758***

Saline effects

DMN			
	B	**S**	**R**
D_{F3}	2028±1299	**5160±828***	**3428±1810**

Hippocampus			
	B	**S**	**R**
D_{S2}	1858±812	**2710±1359**	**1706±904***

Mean values (±SD) of slow diffusion phase (SDP), slow diffusion coefficients (D_S) and fast diffusion coefficients (D_F) from mice receiving glucose (left) or saline (right) administrations. Values are given for the L-R (1), A-P (2) and H-F (3) measurements in the ARC, VMN, DMN, LH and hippocampus, for the basal (B), glucose/saline (G/S) and recovery (R) periods, For simplicity, only ROI's and directions with significant changes are depicted. ($^{\#}$, $^{\#\#}$, $^{\#\#\#}$, *, **, ***, $^{+}$, $^{++}$, $^{+++}$ express, respectively, statistical significances with $p<0.05$, $p<0.005$ and $p<0.001$ in basal vs glucose comparisons, glucose vs recovery, and basal vs recovery, using one-way ANOVA tests with Bonferrroni corrections).

Table 4.2 depicts the low b mean (±SD) values in mice receiving glucose (left) or saline (right) administrations, with parameters showing significant differences highlighted in black. Mice administered with glucose show decreases in the D_{fast} coefficient in the ARC and VMN after the glucose bolus, and increased D_{fast} values in

the hippocampus. In the recovery phase, SDP and D_{slow} values increase in the VMN and LH nuclei. Additionally, D_{fast} coefficients decrease in the VMN and hippocampus. Comparisons between basal and fasting conditions indicate that in the LH, H-F SDP and A-P D_{fast} values decrease significantly. Saline-administered mice report increases in the D_{fast} coefficients in the basal-to-saline transition, and D_{fast} decreases in the hippocampus in the saline-to-recovery change.

4.3.3 T2*W approach

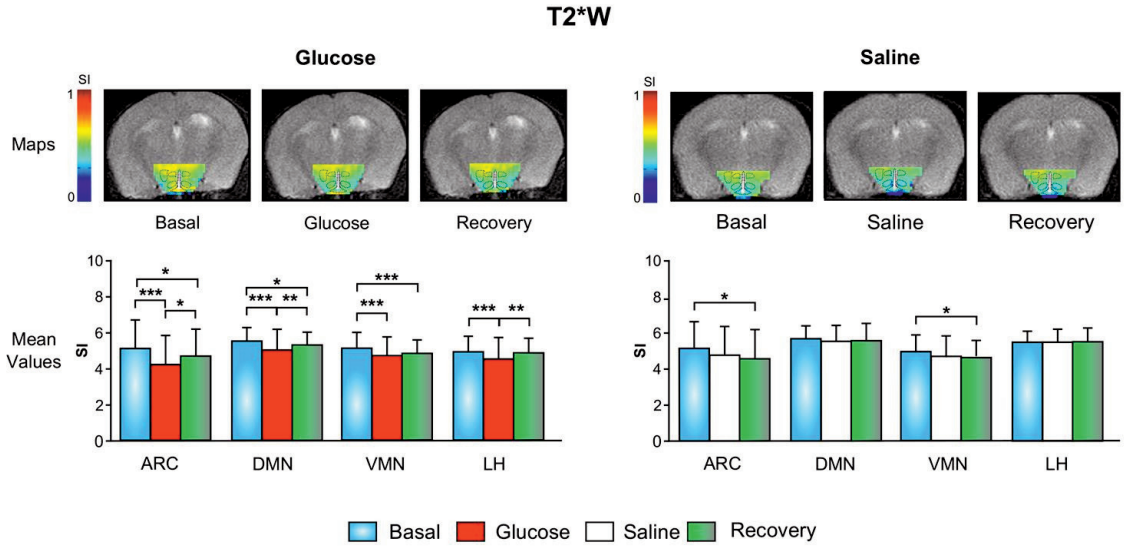

Figure 4.4. T2*W signal changes in the hypothalamic nuclei after the administration of glucose or saline to fasting mice. **Left panels**: T2*W signal intensity color maps of a representative mouse before the administration of glucose (basal), right after (glucose) and in the recovery (recovery) period (upper images). Pixel values in the hypothalamus are shown superimposed to a T2W image, and ROI's of the hypothalamic nuclei ARC, VMN, DMN and LH are circled in black to favor identification. Mean signal intensity values (± SD) of all mice from the glucose group in the basal (blue), glucose (red) and recovery (green) periods are depicted in the lower bar graphs. **Right panels**: T2*W signal intensity maps before and after the administration of saline, in the basal, saline and recovery states. Pixel values in the hypothalamus are colored superimposed to a T2W image. Signal intensity mean values (±SD) of all animals from the saline group in the basal (blue), saline (white) and recovery (green) conditions. (*p<0.05, **p<0.005, ***p<0.001, ANOVA tests with Bonferroni corrections). SI: Signal Intensity; ARC: Arcuate Nucleus; DMN: Dorsomedial Nucleus; VMN: Ventromedial Nucleus; LH: Lateral Hypothalamus.

Figure 4.4 summarizes the mean values (±SD) of the T2*W signal in all areas and conditions investigated for the glucose (left) and saline (right) treated groups. All hypothalamic nuclei show significant differences between the basal and glucose periods and mean values increase in the glucose-recovery shift in the ARC, in the DMN and in the LH. Notably, the ARC, DMN and VMN depict significant decreases in

the basal-recovery comparisons. The hippocampal area does not show any significant changes in the acquired T2*W signal mean values during the glucose administration tests. In the saline imaging experiments, the ARC and the VMN areas reveal significant decreases of the signal from the basal to the recovery states ($p<0.05$ in both cases), while no other changes are detected in the saline protocol.

4.3.4 Blood tests results

Figure 4.5 shows the mean values (±SD) of blood glucose and plasma insulin and leptin, measured 70 minutes after the administration of either saline or glucose to fasting mice. The figure also shows values from overnight-fasting and *fed ad libitum* mice to favor the comparisons. Mice administered with glucose showed significantly increased levels of glucose, leptin and insulin, as compared to mice receiving saline. Notably, mice receiving glucose administrations depict significantly lower levels of leptin than fed *ad libitum* mice (panel B) and significantly higher insulin levels than fasting mice. Mice receiving saline depict lower levels of plasma leptin than fed ad *libitum* mice and similar values to fasting mice. Measurements of ghrelin content did not show significant changes between conditions (not shown).

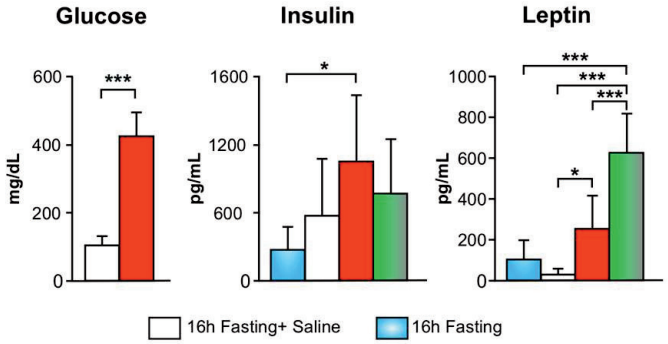

Figure 4.5. Blood tests in glucose or saline-administered mice. **A**: Mean values (±SD) after the imaging sessions, of blood glucose in mice receiving glucose (n=14, red bar) or saline (n=8, white bar) administrations. Glucose levels are significantly higher in the glucose group (***$p<0.001$, t student test). **B, C**: Mean values (±SD) of insulin and leptin in mice after 16h hours of fasting (n=7, blue bar), in mice administered with saline and after an imaging session (n=6, white bar), mice administered with glucose and after the imaging session (n=7, red bar), and mice in fed *ad libitum* conditions (n=7, green bar) (*$p<0.05$, **$p<0.005$,***$p<0.001$, ANOVA tests with Bonferroni corrections).

In summary, the increases in blood glucose and plasma leptin or insulin confirm that the glucose i.p. administration to mice has been successfully accomplished, eliciting the expected hormonal response [188, 189].

4.4 Discussion

In this Chapter, I evaluated the information provided by fDWI and T2*W as functional neuroimaging approaches to investigate the glucose sensing mechanisms of the hypothalamus. I used four different functional non-invasive MRI approaches; fDWI acquisitions with mono and biexponential fittings, low b DWI with biexponential fittings and T2*W imaging. The results obtained allow for an integrative interpretation of the biophysical events underlying fMRI detection of neuronal activation and the specific role of individual hypothalamic nuclei during the glucose sensing paradigm.

4.4.1 Physiological interpretation of the functional models

The monoexpoential high b value approach observes ADC changes compatible with a glucose inhibitory response in all nuclei. This initial glucose-inhibiting response elicits increases in the ADC, reflecting most probably cellular shrinking or a decrease of the intracellular-to-extracellular volume ratio in the observed voxels (α). The recovery reaction proceeds with ADC decrease, reflecting cellular swelling and the return to the equilibrium value of intracellular-to-extracellular volumes. ADC values, however, are known to depend not only on the relative intra-and extracellular volumes but also on tortuosity (λ), a parameter revealing the obstacles to water movements during the diffusion time [190]. Indeed, both α and λ have been proposed to change during cell swelling and shrinking processes [191, 192]. Consequently, the detected ADC changes in the hypothalamus after glucose administrations could involve not only relative volume changes but additional variations in λ.

The results obtained by the high b biexponential model are consistent with a GI response in the ARC and DMN nuclei, as characterized with a cellular shrinking reaction to glucose administration. This shrinking process is evidenced by significant decreases in the SDP and D_{slow} values. SDP represents the fraction of water

molecules diffusing close to cell membranes [20, 25] and therefore, a decrease in SDP is consistent with a decrease in cellular volume. D_{slow} and D_{fast} account for the corresponding diffusion coefficients of the slow and fast phases, and our results show that these coefficients change significantly upon neuronal activation. Indeed, cellular volume changes have been shown to modify the viscosity of extracellular space (ECS) [193] by compressing or decompressing it, a circumstance that can affect diffusion coefficients. In this situation, even small activated-induced volume changes could induce variations in the ECS and alter diffusion values of the water molecules [191, 194]. Moreover, our results in the VMN and hippocampus indicate that the shrinking process slightly increases the slow diffusion coefficients, while the swelling response decreases it. This, however, differs from previous investigations by other authors, who assumed that the diffusion coefficients were constant during neuronal activation processes [24, 30].

The biexponential analyses of the low b value data sets lead to relatively poor fittings. Coefficients lead, however, to some significant changes between states. The IVIM approach defines the D_{fast} coefficients as a *pseudodiffusion* coefficient that may reveal changes in the microvasculature during the neuronal activation processes [139]. In this range of low b values, D_{slow} may reflect, similarly to the ADC, the Brownian diffusion, and SDP should account for the diffusion fraction contributing to the signal decay. In our results, mice administered with glucose show a glucose-induced decrease in D_{fast} in the ARC and LH that is consistent with a decreased local blood flow associated to decreased neuronal activity. This finding suggests that the ARC and LH have GI neurons. On the contrary, changes in the VMN and hippocampus are consistent with a GE response, while the DMN does not show significant variations.

T2*W imaging results are consistent with a GI response in all nuclei that recovers in the recovery period, and no changes in the hippocampus. Our results are consistent with previous studies evaluating the hypothalamic response to glucose in rats [93, 181] and in humans [49, 50, 182, 183], and changes have been associated to decreases in neuronal activity of glucose-sensing neurons. In our experiments, we found additional significant drops of the signal from the initial basal state to the

recovery period in the ARC, DMN and VMN nuclei. This signal decay can be caused by an inevitable loss of field homogeneity during acquisition time, or reveal that values do not recover completely during the recovery period.

In summary, our results provide an integrative interpretation of fDWI and T2W changes during hypothalamic activation. Firstly, while high b DWI approaches appear to reflect volume regulatory process during activation, while low b DWI and T2*W methods seem to reveal changes in the microvascular blood flow. Secondly, our findings suggest that while ADC reflects changes including cellular volume and extracellular space composition variations, SDP changes reflect more specifically the swelling and shrinking processes. Third, D_{slow} and D_{fast} can change upon neuronal firings and, although normally correlated with SDP changes, they may present dependence on the composition and properties of the extracellular matrix. Fourth, the biexponential model seems not to be the optimal model for low b fittings, with approximately half pixels yielding good fittings only. A triexponential model that accounted for the non-Gaussian diffusion could, most probably, improve this approach. Finally, IVIM results are in good agreement with T2*W-detected blood flow changes and include directional information of the activation-induced changes.

4.4.2 Summary of findings in the individual hypothalamic nuclei

The results obtained for the ARC reveal that this nucleus expresses GI neurons, as detected by the generalized cell shrinking effect that increases ADC values, decreases SDP high b, D_{fast}-IVIM and T2*W signal. In the recovery period, cells swell to recover initial values, as expressed with decreasing ADC values, increasing SDP and T2*W imaging signal. These findings agree well with the reported glucose-induced deactivation of the ARC nucleus [179, 195], although our conclusion is derived from a fully non-invasive method. Notably, the administration of saline does not affect the ARC nucleus.

In the DMN, fMRI-detected effects indicate that this nuclei express GI neurons, as observed by the increases in the ADC, decreases in high b SDP and D_{slow} and T2*W signal, that recover to basal values in the recovery phase. Glucose effects in the DMN are less covered in the literature, but the orexigenic role of NPY

neurotransmitters in the DMN [196] is in agreement with a GI response. However, the DMN responds clearly to the administration of saline, in agreement with cellular shrinking and increased blood flow. This response suggests an important involvement of the DMN in the regulation of fluid homeostasis as a response to changes in osmolality.

In the Ventromedial nucleus (VMN), glucose-induced changes are consistent with the presence of both GI and GE neurons, in agreement with findings of subpopulations of GI and GE neurons [175]. More specifically, our results show that diffusion changes in the VMN are directionally dependent, with L-R detected inhibiting responses and A-P and H-F changes are in agreement with a GE reaction. Mice administered with saline do not show changes in the VMN.

The lateral hypothalamus responds to glucose and saline administrations similarly as the VMN nuclei; expresses GI neurons, detected in the L-R measurements and GE neurons, detected in the A-P and H-F. Results are in agreement with recent findings describing the existence of GI and GE neurons in this area of the hypothalamus [171], revealing for the first time a different spatial orientation for these axons. Saline administration does not induce any response in the LH area.

The hippocampal region is affected almost equally by glucose or saline administrations. Results suggest that the hippocampus experiences an initial vasodilation process, as detected with increased IVIM-D_{fast} coefficients after either glucose or saline administrations, and a final increase of the cellular-to-extracellular volume ratio with simultaneous vasoconstriction. These changes are in agreement with a fluid homeostasis regulatory response [197]. In fact, the hippocampus has been identified as a site of action of vasopressin, a hormone participating in the fluid homeostasis and electrolyte processes [198, 199].

In summary, both fDWI and T2*W methodologies succeeded in detecting changes in the hypothalamic nuclei after the administration of glucose. Glucose induced a temporal inhibition of orexigenic activity in the ARC and DMN nuclei of fasting mice, as detected with high b and low b DWI and T2*W methods. In the LH and VMN areas, both inhibition and excitation responses were detected.

Conclusions

1. Our work has demonstrated that hypothalamic activation by fasting in mice or humans can be detected non-invasively by functional diffusion weighted magnetic resonance imaging methods. Activation can be identified through changes in the water diffusion parameters, in agreement with activation-induced astrocytic swelling processes. These results validate the use of fDWI as a very promising tool in the global understanding of appetite and body weight regulation processes in mammals.

2. The application of fDWI methodology to mice lacking NPY showed that 48 hours of fasting trigger a weaker hypothalamic orexigenic response, as compared to activity in control mice. Moreover, 16 hours of fasting do not elicit any significant changes in the hypothalamic nuclei. Results prove the sensibility of the technique to the lack of the orexigenic neuropeptide Y, and evidence the importance of the neurotransmitter in the activation processes. The interpretation of the MRI approach is supported by the results showing lower food and drink intake of 129S-Npy^{tm1Rpa}/J in response to fasting, probably consequence of a smaller orexigenic impulse and linked to the up regulation of the anorexigenic signals PYY and leptin.

3. In this work, we have been able to demonstrate that ob/ob mice in *fed ad libitum* conditions show higher fDWI activation parameters in the hypothalamic nuclei, as compared to wild type mice. Results are consistent with a generally greater asctrocytic swelling produced by the lack of the anorexigenic signal leptin, which should inhibit the activation of orexigenic pathways. MRI observations are on agreement with the higher food intake of obese mice, body weight, indirect calorimetry, locomotor activity and blood tests measurements.

4. The fDWI implementation to leptin-deficient mice showed that fasting increases selectively hypothalamic activity, and that this response is less acute and less generalized than it is in C57BL6/J control mice. MRI-detected effects are in agreement with physiological measurements

indicating a less acute response to fasting. The physiological results indicate, basically: a lack of increase in food intake after the fasting period, a loss on body weight at the end of the procedure and higher uses of lipids as metabolic substrate. In this case, fDWI proves a different activation pattern in obese mice evidencing the consequences of leptin deficiency in both the anorexigenic and orexigenic pathways.

5. Our evaluation of hypothalamic activity in diet-induced obesity development showed that obesity is correlated with diffusion changes in the ARC and DMN hypothalamic nuclei. These changes indicate higher astrocytic swelling and/or astrogliosis processes, in fed and fasting conditions. On the contrary, non-obesity development during the exposure to high fat diets is linked to a failure in orexegenic activation in the ARC. Results are consistent with recent findings of inflammatory processes in the hypothalamus of obese subjects, specifically affecting astrocytes. Furthermore, these results open the possibility of using fDWI methods in the evaluation of diet composition effects in hypothalamic activity and the prognosis of obesity.

6. The implementation of the fDWI approach in a 9.4 T magnet did not succeed in detecting the orexigenic effects of the administration of ghrelin to fasting mice. This suggests that high fields are more difficult to harmonize with a robust detection of brain activity using the described fDWI techniques, at least with similar acquisition characteristics than those used in a 7T system. This, however, should be validated using different ghrelin doses to increase the orexigenic effect.

7. The combination of fDWI and T2*W imaging techniques revealed that while DWI high b reflect activation-induced cellular volume regulations, low b DWI and T2*W changes detect activation-induced blood flow fluctuations. Cellular volume regulations are observed through changes in the SDP and FDP coefficient values of the biexponential model of diffusion. Variations in ADC,

D_{slow} and D_{fast} can include, additionally to cell volume regulations, activation-induced changes in the extracellular space composition and properties.

8. Parallel fDWI and T2*W evaluations of glucose sensing in the hypothalamus revealed the presence of glucose-inhibiting neurons in the ARC and the DMN nuclei. The LH and the VMN depict directional-dependent excitatory or inhibitory responses. Additionally, the hippocampus and DMN showed responses to volume regulations. Inhibitory responses elicit cellular shrinking processes (increased ADC, decreased SDP), potential tortuosity decreases (decreased D_{slow} and D_{fast}) and local blood flow decreases (decreased IVIM D_{fast} and T2*W signal intensities). Excitatory responses prompt cellular swelling reactions (decreased ADC, increased SDP), possible tortuosity decreases (increased D_{slow} and D_{fast}) and increases in blood flow (increases in IVIM D_{fast} values and T2*W signal values).

Conclusiones

1. Nuestro trabajo ha demostrado que la activación hipotalámica en condiciones de ayuno puede ser detectada de forma no invasiva con métodos de imagen funcional pesada en difusión. Esta activación se identifica mediante cambios en los parámetros de difusión del agua, que están de acuerdo con una respuesta a la activación caracterizada por aumentos de volumen de los astrocitos. Estos primeros resultados nos condujeron a tratar de aplicar la misma técnica a otras evaluaciones del funcionamiento hipotalámico, como en ratones con alteraciones en las principales rutas del control del apetito y de la regulación del balance energético. Además, nuestros resultados validan el uso de fDWI como una herramienta muy prometedora en la compresión global de los procesos de regulación del apetito y peso corporal en mamíferos.

2. La aplicación de la metodología fDWI a ratones carentes de NPY demostró que 48 horas de ayuno provocan una respuesta orexigénica débil en el hipotálamo. Más aún, 16 horas de ayuno no provocan ningún cambio significativo en los núcleos hipotalámicos de los ratones 129S-Npy^{tm1Rpa}/J. Estos resultados prueban la sensibilidad de la técnica a la deficiencia del neuropéptido Y, y ponen en evidencia la importancia de este neuropeptido en los procesos de activación. Esta interpretación del abordaje MRI está respaldada por los resultados que muestran una menor ingesta de comida y bebida de los ratones 129S-Npy^{tm1Rpa}/J en respuesta al ayuno, lo que puede ser consecuencia de un menor impulso orexigénico y está relacionado con un aumento de las señales anorexigénicas PYY y leptina.

3. Con este trabajo hemos podido demostrar que los ratones ob/ob presentan, en condiciones de alimentación *ad libitum,* parámetros de activación fDWI en hipotálamo muy elevados, en relación a los valores en animales control. Estos resultados están de acuerdo con un incremento generalizado de volumen de los astrocitos, producido por la falta de señalización anorexigénica de la leptina, cuya función principal es inhibir la activación de las rutas orexigénicas. Estas observaciones están en acuerdo con el

incremento en ingesta de comida de los ratones obesos, las medidas de calorimetría indirecta, actividad locomotora y análisis de sangre.

4. La implementación de la técnica fDWI a ratones deficientes en leptina ha demostrado que el ayuno aumenta de forma selectiva la actividad hipotalámica, pero la respuesta es menos aguda y menos generalizada que en los ratones control C57BL6/J. La interpretación de los resultados de MRI está en consonancia con las medidas de parámetros fisiológicos, que indican una respuesta al ayuno más débil que en los ratones control. Los indicadores fisiológicos son, básicamente: falta de incremento en la ingesta después del ayuno, pérdida de peso al final del protocolo, y elevado uso de lípidos como sustrato metabólico. En este caso, el uso de fDWI prueba un patrón de activación distinto en ratones obesos, evidenciando las consecuencias de la deficiencia en leptina en las rutas de activación orexigénicas y anorexigénicas.

5. Nuestra evaluación de la activación hipotalámica en el desarrollo de obesidad inducida por la administración de dietas de alto contenido en grasa, muestra que la obesidad está correlacionada con cambios en los parámetros de difusión en los núcleos ARC y DMN. Estos cambios indican incrementos de volumen de los astrocitos y/o proliferación de los mismos, en condiciones ayuno y alimentación. La falta de desarrollo de obesidad aparece asociada con falta de activación del núcleo ARC con el ayuno. Los resultados son consistentes con recientes hallazgos de procesos inflamatorios en el hipotálamo de sujetos obesos, que específicamente a los astrocitos. Además, abren las puertas al uso de la metodología fDWI en la evaluación de los efectos de dietas con distinta composición a la actividad hipotalámica y al desarrollo de obesidad.

6. La implementación de la metodología fDWI a un imán de 9.4 T no resultó eficaz en la detección de los efectos orexigéncos producidos por la administración de grelina a ratones ayunados. Estos resultados sugieren

que el uso de fDWI en imanes de alto campo no es compatible con una detección robusta de la actividad cerebral, al menos bajo mismas características de adquisición de un imán de 7T. Esto debería der validado utilizando otras dosis de grelina que aumenten el efecto orexigénico.

7. La combinación de las técnicas fDWI y T2*W ha revelado que, mientras que DWI a alto b refleja la regulación de volúmenes celulares que ocurre durante la activación neuronal, los cambios de DWI a bajo b y T2*W detectan fluctuaciones de flujo inducidas también por la actividad. Las regulaciones de volumen se observan mediante cambios en las fracciones SDP y FDP del modelo biexponencial de difusión. Las variaciones en los coeficientes ADC, D_{slow} y D_{fast} pueden incluir, además de efectos de regulación de volumen, cambios en la composición y propiedades del espacio extracelular.

8. La aplicación de fDWI y T2*W de forma paralela en la detección de glucosa, revela la presencia de neuronas inhibidas por glucosa en los núcleos ARC y DMN. El LH y VMN muestran respuestas inhibitorias y excitadoras en función de la dirección valorada. La zona de hipocampo y el núcleo DMN presentan, además, repuestas a la regulación de volumen. Las respuestas inhibitorias conllevan procesos de deshinchamiento celular (aumentos de ADC, disminuciones en SDP), posible disminución de tortuosidad (disminuciones de D_{slow} y D_{fast}) y un bajada de flujo sanguíneo local (IVIM D_{fast} disminuidos, disminuciones en la intensidad de señal T2*W). Las respuestas excitatorias impulsan aumentos de volumen celular (ADC disminuidos, SDP crecientes), posibles cambios en tortuosidad (disminución de los coeficientes D_{slow} y D_{fast}) e incrementos de flujo sanguíneo (IVIM D_{fast} y T2*W aumentados).

Bibliography

1. Bloch, F., *Nuclear Induction.* Physical Review, 1946. **70**(7-8): p. 460-474.
2. Purcell, E.M., H.C. Torrey, and R.V. Pound, *Resonance Absorption by Nuclear Magnetic Moments in a Solid.* Physical Review, 1946. **69**(1-2): p. 37-38.
3. Lauterbur, P.C., *Image formation by induced local interactions. Examples employing nuclear magnetic resonance. 1973.* Clin Orthop Relat Res, 1989(244): p. 3-6.
4. Kumar, A., D. Welti, and R.R. Ernst, *Imaging of macroscopic objects by NMR Fourier zeugmatography.* Naturwissenschaften, 1975. **62**(1): p. 34-34.
5. Mansfield, P. and A.A. Maudsley, *Medical imaging by NMR.* Br J Radiol, 1977. **50**(591): p. 188-94.
6. Jellinger, K.A., *Magnetic Resonance Imaging, 3rd edition. David D. Stark and William G. Bradley, Jr (eds). Volumes I–III. Mosby, St. Louis, MO, USA, 1999. 1936 + ≈100 pp. ISBN 0-8151-8518-9; 28607.* European Journal of Neurology, 2001. **8**(1): p. 96-97.
7. Gallagher, T.A., A.J. Nemeth, and L. Hacein-Bey, *An introduction to the Fourier transform: relationship to MRI.* AJR Am J Roentgenol, 2008. **190**(5): p. 1396-405.
8. Hennig, J., A. Nauerth, and H. Friedburg, *RARE imaging: a fast imaging method for clinical MR.* Magn Reson Med, 1986. **3**(6): p. 823-33.
9. Mansfield, P., *Real-time echo-planar imaging by NMR.* Br Med Bull, 1984. **40**(2): p. 187-90.
10. Paschal, C.B. and H.D. Morris, *K-space in the clinic.* J Magn Reson Imaging, 2004. **19**(2): p. 145-59.
11. Pruessmann, K.P., *Encoding and reconstruction in parallel MRI.* NMR Biomed, 2006. **19**(3): p. 288-99.
12. Breuer, F.A., et al., *Controlled aliasing in parallel imaging results in higher acceleration (CAIPIRINHA) for multi-slice imaging.* Magn Reson Med, 2005. **53**(3): p. 684-91.
13. Einstein, A., *Investigations on the Theory of Brownian Motion, reprint of the 1st English edition (1926)*, 1956, Dover, New-York.
14. Le Bihan, D., *Looking into the functional architecture of the brain with diffusion MRI.* Nat Rev Neurosci, 2003. **4**(6): p. 469-80.
15. Le Bihan, D., et al., *MR imaging of intravoxel incoherent motions: application to diffusion and perfusion in neurologic disorders.* Radiology, 1986. **161**(2): p. 401-7.
16. Sotak, C.H., *The role of diffusion tensor imaging in the evaluation of ischemic brain injury - a review.* NMR Biomed, 2002. **15**(7-8): p. 561-9.
17. Mayer, A.R., et al., *A prospective diffusion tensor imaging study in mild traumatic brain injury.* Neurology, 2010. **74**(8): p. 643-50.

18. Stejskal, E.O., *Use of Spin Echoes in a Pulsed Magnetic-Field Gradient to Study Anisotropic, Restricted Diffusion and Flow.* The Journal of Chemical Physics, 1965. **43**(10): p. 3597-3603.
19. Alexander, D.C., G.J. Barker, and S.R. Arridge, *Detection and modeling of non-Gaussian apparent diffusion coefficient profiles in human brain data.* Magn Reson Med, 2002. **48**(2): p. 331-40.
20. Niendorf, T., et al., *Biexponential diffusion attenuation in various states of brain tissue: implications for diffusion-weighted imaging.* Magn Reson Med, 1996. **36**(6): p. 847-57.
21. Jensen, J.H., et al., *Diffusional kurtosis imaging: the quantification of non-gaussian water diffusion by means of magnetic resonance imaging.* Magn Reson Med, 2005. **53**(6): p. 1432-40.
22. Perrin, M., et al., *Validation of q-ball imaging with a diffusion fibre-crossing phantom on a clinical scanner.* Philos Trans R Soc Lond B Biol Sci, 2005. **360**(1457): p. 881-91.
23. Le Bihan, D., *Diffusion, confusion and functional MRI.* Neuroimage, 2012. **62**(2): p. 1131-6.
24. Le Bihan, D., et al., *Direct and fast detection of neuronal activation in the human brain with diffusion MRI.* Proc Natl Acad Sci U S A, 2006. **103**(21): p. 8263-8.
25. Darquie, A., et al., *Transient decrease in water diffusion observed in human occipital cortex during visual stimulation.* Proc Natl Acad Sci U S A, 2001. **98**(16): p. 9391-5.
26. Yacoub, E., et al., *Decreases in ADC observed in tissue areas during activation in the cat visual cortex at 9.4 T using high diffusion sensitization.* Magn Reson Imaging, 2008. **26**(7): p. 889-96.
27. Andrew, R.D. and B.A. MacVicar, *Imaging cell volume changes and neuronal excitation in the hippocampal slice.* Neuroscience, 1994. **62**(2): p. 371-83.
28. Neprasova, H., et al., *High extracellular K(+) evokes changes in voltage-dependent K(+) and Na (+) currents and volume regulation in astrocytes.* Pflugers Arch, 2007. **453**(6): p. 839-49.
29. Hansson, E., et al., *Astroglia and glutamate in physiology and pathology: aspects on glutamate transport, glutamate-induced cell swelling and gap-junction communication.* Neurochem Int, 2000. **37**(2-3): p. 317-29.
30. Flint, J., et al., *Diffusion weighted magnetic resonance imaging of neuronal activity in the hippocampal slice model.* Neuroimage, 2009. **46**(2): p. 411-8.
31. Aso, T., et al., *An intrinsic diffusion response function for analyzing diffusion functional MRI time series.* Neuroimage, 2009. **47**(4): p. 1487-95.
32. Tirosh, N. and U. Nevo, *Neuronal activity significantly reduces water displacement: DWI of a vital rat spinal cord with no hemodynamic effect.* Neuroimage, 2013. **76**: p. 98-107.

33. Kohno, S., et al., *Water-diffusion slowdown in the human visual cortex on visual stimulation precedes vascular responses.* J Cereb Blood Flow Metab, 2009. **29**(6): p. 1197-207.
34. Miller, K.L., et al., *Evidence for a vascular contribution to diffusion FMRI at high b value.* Proc Natl Acad Sci U S A, 2007. **104**(52): p. 20967-72.
35. Federau, C., et al., *Quantitative measurement of brain perfusion with intravoxel incoherent motion MR imaging.* Radiology, 2012. **265**(3): p. 874-81.
36. Riches, S.F., et al., *Diffusion-weighted imaging of the prostate and rectal wall: comparison of biexponential and monoexponential modelled diffusion and associated perfusion coefficients.* NMR Biomed, 2009. **22**(3): p. 318-25.
37. Sigmund, E.E., et al., *Intravoxel incoherent motion imaging of tumor microenvironment in locally advanced breast cancer.* Magn Reson Med, 2011. **65**(5): p. 1437-47.
38. Taouli, B. and D.M. Koh, *Diffusion-weighted MR imaging of the liver.* Radiology, 2010. **254**(1): p. 47-66.
39. Koh, D.M., D.J. Collins, and M.R. Orton, *Intravoxel incoherent motion in body diffusion-weighted MRI: reality and challenges.* AJR Am J Roentgenol, 2011. **196**(6): p. 1351-61.
40. Neil, J.J. and G.L. Bretthorst, *On the use of Bayesian probability theory for analysis of exponential decay data: an example taken from intravoxel incoherent motion experiments.* Magn Reson Med, 1993. **29**(5): p. 642-7.
41. Lu, Y., et al., *Extension of the intravoxel incoherent motion model to non-gaussian diffusion in head and neck cancer.* J Magn Reson Imaging, 2012. **36**(5): p. 1088-96.
42. Iima, M., et al., *Potential of perfusion and diffusion IVIM MRI in a rat brain 9L glioma model.* Proc. Intl. Soc. Mag. Reson. Med. 21, 2013.
43. Ogawa, S., et al., *Brain magnetic resonance imaging with contrast dependent on blood oxygenation.* Proc Natl Acad Sci U S A, 1990. **87**(24): p. 9868-72.
44. Kim, S.G. and S. Ogawa, *Biophysical and physiological origins of blood oxygenation level-dependent fMRI signals.* J Cereb Blood Flow Metab, 2012. **32**(7): p. 1188-206.
45. Logothetis, N.K., *What we can do and what we cannot do with fMRI.* Nature, 2008. **453**(7197): p. 869-78.
46. Raichle, M.E., *Circulatory and Metabolic Correlates of Brain Function in Normal Humans*, in *Comprehensive Physiology*. 2011, John Wiley & Sons, Inc.
47. Fox, P.T. and M.E. Raichle, *Focal physiological uncoupling of cerebral blood flow and oxidative metabolism during somatosensory stimulation in human subjects.* Proc Natl Acad Sci U S A, 1986. **83**(4): p. 1140-4.

48. Pauling, L. and C.D. Coryell, *The Magnetic Properties and Structure of Hemoglobin, Oxyhemoglobin and Carbonmonoxyhemoglobin.* Proc Natl Acad Sci U S A, 1936. **22**(4): p. 210-6.
49. Matsuda, M., et al., *Altered hypothalamic function in response to glucose ingestion in obese humans.* Diabetes, 1999. **48**(9): p. 1801-6.
50. Smeets, P.A., et al., *Oral glucose intake inhibits hypothalamic neuronal activity more effectively than glucose infusion.* Am J Physiol Endocrinol Metab, 2007. **293**(3): p. E754-8.
51. Koretsky, A.P. and A.C. Silva, *Manganese-enhanced magnetic resonance imaging (MEMRI).* NMR Biomed, 2004. **17**(8): p. 527-31.
52. Pautler, R.G., *In vivo, trans-synaptic tract-tracing utilizing manganese-enhanced magnetic resonance imaging (MEMRI).* NMR Biomed, 2004. **17**(8): p. 595-601.
53. Andrew, R.D., et al., *Dye transfer through gap junctions between neuroendocrine cells of rat hypothalamus.* Science, 1981. **211**(4487): p. 1187-9.
54. Jaffe, L., *The discovery of calcium waves.* Semin Cell Dev Biol, 2006. **17**(2): p. 229.
55. Jaffe, L.F., *Calcium waves.* Philos Trans R Soc Lond B Biol Sci, 2008. **363**(1495): p. 1311-6.
56. Jaffe, L.F., *Fast calcium waves.* Cell Calcium, 2010. **48**(2-3): p. 102-13.
57. Lee, J.H., et al., *Manganese-enhanced magnetic resonance imaging of mouse brain after systemic administration of MnCl2: dose-dependent and temporal evolution of T1 contrast.* Magn Reson Med, 2005. **53**(3): p. 640-8.
58. Zwingmann, C., D. Leibfritz, and A.S. Hazell, *Energy metabolism in astrocytes and neurons treated with manganese: relation among cell-specific energy failure, glucose metabolism, and intercellular trafficking using multinuclear NMR-spectroscopic analysis.* J Cereb Blood Flow Metab, 2003. **23**(6): p. 756-71.
59. Zwingmann, C., D. Leibfritz, and A.S. Hazell, *Brain energy metabolism in a sub-acute rat model of manganese neurotoxicity: an ex vivo nuclear magnetic resonance study using [1-13C]glucose.* Neurotoxicology, 2004. **25**(4): p. 573-87.
60. Aoki, I., et al., *Dynamic activity-induced manganese-dependent contrast magnetic resonance imaging (DAIM MRI).* Magn Reson Med, 2002. **48**(6): p. 927-33.
61. Aoki, I., et al., *In vivo detection of neuroarchitecture in the rodent brain using manganese-enhanced MRI.* Neuroimage, 2004. **22**(3): p. 1046-59.
62. Delgado, T.C., et al., *Neuroglial metabolic compartmentation underlying leptin deficiency in the obese ob/ob mice as detected by magnetic resonance*

imaging and spectroscopy methods. J Cereb Blood Flow Metab, 2011. **31**(12): p. 2257-66.
63. Lin, D., et al., *Functional identification of an aggression locus in the mouse hypothalamus.* Nature, 2011. **470**(7333): p. 221-6.
64. Swaab, D.F., Hofman, M.A., Mirmiran, M., Ravid, R., van Leewen, F.W. Eds., *The Human Hypothalamus in Health and Disease*. Prog Brain Res. Vol. 93. 1992: Elsevier.
65. Ganong, W.F., *Central Regulation of Visceral Function*, in *Review of Medical Physiology*. 1993, Appleton & Lange: Connecticut. p. 208-230.
66. Levin, B.E., et al., *Metabolic sensing and the brain: who, what, where, and how?* Endocrinology, 2011. **152**(7): p. 2552-7.
67. McEwen, B.S., *Endocrine effects on the brain and their relationship to behavior*, in *Basic Neurochemistry*, G. Siegel, Agranoff, B., Albers, R.W., Molinoff, P., Editor. 1989, Raven Press: New York. p. 893-913.
68. Tong, Q., et al., *Synaptic glutamate release by ventromedial hypothalamic neurons is part of the neurocircuitry that prevents hypoglycemia.* Cell Metab, 2007. **5**(5): p. 383-93.
69. Xu, Y., et al., *Role of GABA release from leptin receptor-expressing neurons in body weight regulation.* Endocrinology, 2012. **153**(5): p. 2223-33.
70. Delgado, T.C., *Glutamate and GABA in Appetite Regulation.* Front Endocrinol (Lausanne), 2013. **4**: p. 103.
71. Coll, A.P., I.S. Farooqi, and S. O'Rahilly, *The hormonal control of food intake.* Cell, 2007. **129**(2): p. 251-62.
72. Morton, G.J., et al., *Central nervous system control of food intake and body weight.* Nature, 2006. **443**(7109): p. 289-95.
73. Stanley, S., et al., *Hormonal regulation of food intake.* Physiol Rev, 2005. **85**(4): p. 1131-58.
74. Schwartz, M.W. and G.J. Morton, *Obesity: keeping hunger at bay.* Nature, 2002. **418**(6898): p. 595-7.
75. Schwartz, M.W., et al., *Central nervous system control of food intake.* Nature, 2000. **404**(6778): p. 661-71.
76. Tang-Christensen, M., et al., *Central administration of ghrelin and agouti-related protein (83-132) increases food intake and decreases spontaneous locomotor activity in rats.* Endocrinology, 2004. **145**(10): p. 4645-52.
77. Halassa, M.M., T. Fellin, and P.G. Haydon, *The tripartite synapse: roles for gliotransmission in health and disease.* Trends Mol Med, 2007. **13**(2): p. 54-63.
78. Araque, A., et al., *Tripartite synapses: glia, the unacknowledged partner.* Trends Neurosci, 1999. **22**(5): p. 208-15.
79. Hertz, L., *Intercellular metabolic compartmentation in the brain: past, present and future.* Neurochem Int, 2004. **45**(2-3): p. 285-96.

80. Hentges, S.T., et al., *GABA release from proopiomelanocortin neurons.* J Neurosci, 2004. **24**(7): p. 1578-83.
81. Collin, M., et al., *Plasma membrane and vesicular glutamate transporter mRNAs/proteins in hypothalamic neurons that regulate body weight.* Eur J Neurosci, 2003. **18**(5): p. 1265-78.
82. Stanley, B., Ha, L., Spears. L., Dee, M.,, *Lateral hypothalamic injections of glutamate, kainic acid, D,L-alpha-amino-3-hydroxy--5-methyl-isoxazole propionic acid or N-methyl-D-aspartic acid rapidly elicit transient eating in rats.* Brain Res., 1993. **613:88-95**.
83. Logothetis, N.K. and B.A. Wandell, *Interpreting the BOLD signal.* Annu Rev Physiol, 2004. **66**: p. 735-69.
84. Kuo, Y.T., et al., *Manganese-enhanced magnetic resonance imaging (MEMRI) without compromise of the blood-brain barrier detects hypothalamic neuronal activity in vivo.* NMR Biomed, 2006. **19**(8): p. 1028-34.
85. Chaudhri, O.B., et al., *Differential hypothalamic neuronal activation following peripheral injection of GLP-1 and oxyntomodulin in mice detected by manganese-enhanced magnetic resonance imaging.* Biochem Biophys Res Commun, 2006. **350**(2): p. 298-306.
86. Parkinson, J.R., O.B. Chaudhri, and J.D. Bell, *Imaging appetite-regulating pathways in the central nervous system using manganese-enhanced magnetic resonance imaging.* Neuroendocrinology, 2009. **89**(2): p. 121-30.
87. Hankir, M.K., et al., *Peptide YY 3-36 and pancreatic polypeptide differentially regulate hypothalamic neuronal activity in mice in vivo as measured by manganese-enhanced magnetic resonance imaging.* J Neuroendocrinol, 2011. **23**(4): p. 371-80.
88. Just, N. and R. Gruetter, *Detection of neuronal activity and metabolism in a model of dehydration-induced anorexia in rats at 14.1 T using manganese-enhanced MRI and 1H MRS.* NMR Biomed, 2011. **24**(10): p. 1326-36.
89. Anastasovska, J., et al., *Fermentable carbohydrate alters hypothalamic neuronal activity and protects against the obesogenic environment.* Obesity (Silver Spring), 2012. **20**(5): p. 1016-23.
90. Just, N., et al., *Effect of manganese chloride on the neurochemical profile of the rat hypothalamus.* J Cereb Blood Flow Metab, 2011. **31**(12): p. 2324-33.
91. Gutman, D.A., et al., *Mapping of the mouse olfactory system with manganese-enhanced magnetic resonance imaging and diffusion tensor imaging.* Brain Struct Funct, 2012.
92. Silva, A.C., *Using manganese-enhanced MRI to understand BOLD.* Neuroimage, 2012. **62**(2): p. 1009-13.

93. Mahankali, S., et al., *In vivo fMRI demonstration of hypothalamic function following intraperitoneal glucose administration in a rat model.* Magn Reson Med, 2000. **43**(1): p. 155-9.
94. Stark, J.A., et al., *Functional magnetic resonance imaging and c-Fos mapping in rats following an anorectic dose of m-chlorophenylpiperazine.* Neuroimage, 2006. **31**(3): p. 1228-37.
95. Dodd, G.T., S.R. Williams, and S.M. Luckman, *Functional magnetic resonance imaging and c-Fos mapping in rats following a glucoprivic dose of 2-deoxy-D-glucose.* J Neurochem, 2010. **113**(5): p. 1123-32.
96. De Silva, A., et al., *The use of functional MRI to study appetite control in the CNS.* Exp Diabetes Res, 2012. **2012**: p. 764017.
97. Zhang, L., et al., *NPY modulates PYY function in the regulation of energy balance and glucose homeostasis.* Diabetes Obes Metab, 2012. **14**(8): p. 727-36.
98. Min, D.K., et al., *Changes in differential functional magnetic resonance signals in the rodent brain elicited by mixed-nutrient or protein-enriched meals.* Gastroenterology, 2011. **141**(5): p. 1832-41.
99. Killgore, W.D., et al., *Cortical and limbic activation during viewing of high- versus low-calorie foods.* Neuroimage, 2003. **19**(4): p. 1381-94.
100. Smeets, P.A., et al., *Functional magnetic resonance imaging of human hypothalamic responses to sweet taste and calories.* Am J Clin Nutr, 2005. **82**(5): p. 1011-6.
101. Batterham, R.L., et al., *PYY modulation of cortical and hypothalamic brain areas predicts feeding behaviour in humans.* Nature, 2007. **450**(7166): p. 106-9.
102. Miller, J.L., et al., *Enhanced activation of reward mediating prefrontal regions in response to food stimuli in Prader-Willi syndrome.* J Neurol Neurosurg Psychiatry, 2007. **78**(6): p. 615-9.
103. Malik, S., et al., *Ghrelin modulates brain activity in areas that control appetitive behavior.* Cell Metab, 2008. **7**(5): p. 400-9.
104. Vidarsdottir, S., et al., *Glucose ingestion fails to inhibit hypothalamic neuronal activity in patients with type 2 diabetes.* Diabetes, 2007. **56**(10): p. 2547-50.
105. Purnell, J.Q., et al., *Brain functional magnetic resonance imaging response to glucose and fructose infusions in humans.* Diabetes Obes Metab, 2011. **13**(3): p. 229-34.
106. Tomasi, D., et al., *Association of body mass and brain activation during gastric distention: implications for obesity.* PLoS One, 2009. **4**(8): p. e6847.
107. Jones, R.B., et al., *Functional neuroimaging demonstrates that ghrelin inhibits the central nervous system response to ingested lipid.* Gut, 2012. **61**(11): p. 1543-51.

108. Guthoff, M., et al., *Insulin modulates food-related activity in the central nervous system.* J Clin Endocrinol Metab, 2010. **95**(2): p. 748-55.
109. Farooqi, I.S., et al., *Leptin regulates striatal regions and human eating behavior.* Science, 2007. **317**(5843): p. 1355.
110. Baicy, K., et al., *Leptin replacement alters brain response to food cues in genetically leptin-deficient adults.* Proc Natl Acad Sci U S A, 2007. **104**(46): p. 18276-9.
111. Alkan, A., et al., *Diffusion-weighted imaging features of brain in obesity.* Magn Reson Imaging, 2008. **26**(4): p. 446-50.
112. Wisse, B.E. and M.W. Schwartz, *Does hypothalamic inflammation cause obesity?* Cell Metab, 2009. **10**(4): p. 241-2.
113. Thaler, J.P. and M.W. Schwartz, *Minireview: Inflammation and obesity pathogenesis: the hypothalamus heats up.* Endocrinology, 2010. **151**(9): p. 4109-15.
114. De Souza, C.T., et al., *Consumption of a fat-rich diet activates a proinflammatory response and induces insulin resistance in the hypothalamus.* Endocrinology, 2005. **146**(10): p. 4192-9.
115. Velloso, L.A., E.P. Araujo, and C.T. de Souza, *Diet-induced inflammation of the hypothalamus in obesity.* Neuroimmunomodulation, 2008. **15**(3): p. 189-93.
116. Kleinridders, A., et al., *MyD88 signaling in the CNS is required for development of fatty acid-induced leptin resistance and diet-induced obesity.* Cell Metab, 2009. **10**(4): p. 249-59.
117. Cazettes, F., et al., *Obesity-mediated inflammation may damage the brain circuit that regulates food intake.* Brain Res, 2011. **1373**: p. 101-9.
118. Aso, T., et al., *Comparison of diffusion-weighted fMRI and BOLD fMRI responses in a verbal working memory task.* Neuroimage, 2013. **67**: p. 25-32.
119. Ahn, S. and S.K. Lee, *Diffusion tensor imaging: exploring the motor networks and clinical applications.* Korean J Radiol, 2011. **12**(6): p. 651-61.
120. Le Bihan, D., et al., *Diffusion tensor imaging: concepts and applications.* J Magn Reson Imaging, 2001. **13**(4): p. 534-46.
121. Carnell, S., et al., *Neuroimaging and obesity: current knowledge and future directions.* Obes Rev, 2012. **13**(1): p. 43-56.
122. Gautier, J.F., et al., *Differential brain responses to satiation in obese and lean men.* Diabetes, 2000. **49**(5): p. 838-46.
123. Tataranni, P.A., et al., *Neuroanatomical correlates of hunger and satiation in humans using positron emission tomography.* Proc Natl Acad Sci U S A, 1999. **96**(8): p. 4569-74.
124. *Paxinos, G., Franklin, K.B.J. , The Mouse Brain in Stereotaxic Coordinates*. 2001, *New York Academic Press*.

125. Burton, P., L. Gurrin, and P. Sly, *Extending the simple linear regression model to account for correlated responses: an introduction to generalized estimating equations and multi-level mixed modelling.* Stat Med, 1998. **17**(11): p. 1261-91.
126. Hastie, T., R. Tibshirani, and J. Friedman, *The elements of statistical learning: Data Mining, Inference and Prediction*. 2001, New York: Springer Series in Statistics.
127. Sehy, J.V., J.J. Ackerman, and J.J. Neil, *Evidence that both fast and slow water ADC components arise from intracellular space.* Magn Reson Med, 2002. **48**(5): p. 765-70.
128. Garcia-Martin, M.L., Ballesteros,P., Cerdan,S., *The metabolism of water in cells and tissues as detected by NMR methods.* Progress in Nuclear Magnetic Resonance Spectroscopy, 2001. **39**(1): p. 41-77.
129. Le Bihan, D., *The 'wet mind': water and functional neuroimaging.* Phys Med Biol, 2007. **52**(7): p. R57-90.
130. Hertz, L., L. Peng, and G.A. Dienel, *Energy metabolism in astrocytes: high rate of oxidative metabolism and spatiotemporal dependence on glycolysis/glycogenolysis.* J Cereb Blood Flow Metab, 2007. **27**(2): p. 219-49.
131. Simard, M. and M. Nedergaard, *The neurobiology of glia in the context of water and ion homeostasis.* Neuroscience, 2004. **129**(4): p. 877-96.
132. Anderson, C.M. and R.A. Swanson, *Astrocyte glutamate transport: review of properties, regulation, and physiological functions.* Glia, 2000. **32**(1): p. 1-14.
133. Violante, I.R., et al., *Cerebral activation by fasting induces lactate accumulation in the hypothalamus.* Magn Reson Med, 2009. **62**(2): p. 279-83.
134. Goldschmidt, J., W. Zuschratter, and H. Scheich, *High-resolution mapping of neuronal activity by thallium autometallography.* Neuroimage, 2004. **23**(2): p. 638-47.
135. Badaut, J., et al., *Aquaporins in brain: distribution, physiology, and pathophysiology.* J Cereb Blood Flow Metab, 2002. **22**(4): p. 367-78.
136. Florence, C.M., L.D. Baillie, and S.J. Mulligan, *Dynamic volume changes in astrocytes are an intrinsic phenomenon mediated by bicarbonate ion flux.* PLoS One, 2012. **7**(11): p. e51124.
137. Halassa, M.M. and P.G. Haydon, *Integrated brain circuits: astrocytic networks modulate neuronal activity and behavior.* Annu Rev Physiol, 2010. **72**: p. 335-55.
138. Autio, J.A., et al., *High b-value diffusion-weighted fMRI in a rat forepaw electrostimulation model at 7 T.* Neuroimage, 2011. **57**(1): p. 140-8.
139. Le Bihan, D., *Intravoxel incoherent motion perfusion MR imaging: a wake-up call.* Radiology, 2008. **249**(3): p. 748-52.

140. Beck, B., *Neuropeptide Y in normal eating and in genetic and dietary-induced obesity.* Philos Trans R Soc Lond B Biol Sci, 2006. **361**(1471): p. 1159-85.
141. Bannon, A.W., et al., *Behavioral characterization of neuropeptide Y knockout mice.* Brain Res, 2000. **868**(1): p. 79-87.
142. Clement, K., et al., *A mutation in the human leptin receptor gene causes obesity and pituitary dysfunction.* Nature, 1998. **392**(6674): p. 398-401.
143. Thaler, J.P., et al., *Obesity is associated with hypothalamic injury in rodents and humans.* J Clin Invest, 2012. **122**(1): p. 153-62.
144. Buckman, L.B., et al., *Regional astrogliosis in the mouse hypothalamus in response to obesity.* J Comp Neurol, 2013. **521**(6): p. 1322-33.
145. Ewart-Toland, A., et al., *Effect of the genetic background on the reproduction of leptin-deficient obese mice.* Endocrinology, 1999. **140**(2): p. 732-8.
146. Berthoud, H.R., *The neurobiology of food intake in an obesogenic environment.* Proc Nutr Soc, 2012. **71**(4): p. 478-87.
147. Rothwell, N.J. and M.J. Stock, *The development of obesity in animals: the role of dietary factors.* Clin Endocrinol Metab, 1984. **13**(3): p. 437-49.
148. Williams, L.M., *Hypothalamic dysfunction in obesity.* Proc Nutr Soc, 2012. **71**(4): p. 521-33.
149. Lee, D., et al., *Longer T2 relaxation time is a marker of hypothalamic gliosis in mice with diet-induced obesity.* Am J Physiol Endocrinol Metab, 2013.
150. Wren, A.M., et al., *Ghrelin causes hyperphagia and obesity in rats.* Diabetes, 2001. **50**(11): p. 2540-7.
151. Wren, A.M., et al., *Ghrelin enhances appetite and increases food intake in humans.* J Clin Endocrinol Metab, 2001. **86**(12): p. 5992.
152. Kohno, D., et al., *Ghrelin directly interacts with neuropeptide-Y-containing neurons in the rat arcuate nucleus: Ca2+ signaling via protein kinase A and N-type channel-dependent mechanisms and cross-talk with leptin and orexin.* Diabetes, 2003. **52**(4): p. 948-56.
153. Kageyama, H., et al., *Visualization of ghrelin-producing neurons in the hypothalamic arcuate nucleus using ghrelin-EGFP transgenic mice.* Regul Pept, 2008. **145**(1-3): p. 116-21.
154. Kuo, Y.T., et al., *The temporal sequence of gut peptide CNS interactions tracked in vivo by magnetic resonance imaging.* J Neurosci, 2007. **27**(45): p. 12341-8.
155. Chaudhri, O., C. Small, and S. Bloom, *Gastrointestinal hormones regulating appetite.* Philos Trans R Soc Lond B Biol Sci, 2006. **361**(1471): p. 1187-209.
156. Fry, M. and A.V. Ferguson, *Ghrelin: central nervous system sites of action in regulation of energy balance.* Int J Pept, 2010. **2010**.

157. Tschop, M.H., et al., *A guide to analysis of mouse energy metabolism.* Nat Methods, 2012. **9**(1): p. 57-63.
158. Upton, G. and I.T. Cook, *Understanding statistics*. 1996: Oxford University Press.
159. Ferrannini, E., *The theoretical bases of indirect calorimetry: a review.* Metabolism, 1988. **37**(3): p. 287-301.
160. Speakman, J.R., *Measuring energy metabolism in the mouse - theoretical, practical, and analytical considerations.* Front Physiol, 2013. **4**: p. 34.
161. Hsuchou, H., et al., *Obesity induces functional astrocytic leptin receptors in hypothalamus.* Brain, 2009. **132**(Pt 4): p. 889-902.
162. Jequier, E., *Leptin signaling, adiposity, and energy balance.* Ann N Y Acad Sci, 2002. **967**: p. 379-88.
163. Federico, P., et al., *Mapping patterns of neuronal activity and seizure propagation by imaging intrinsic optical signals in the isolated whole brain of the guinea-pig.* Neuroscience, 1994. **58**(3): p. 461-80.
164. Pal, I., et al., *Neuronal and astroglial correlates underlying spatiotemporal intrinsic optical signal in the rat hippocampal slice.* PLoS One, 2013. **8**(3): p. e57694.
165. Toshinai, K., et al., *Ghrelin-induced food intake is mediated via the orexin pathway.* Endocrinology, 2003. **144**(4): p. 1506-12.
166. Olszewski, P.K., et al., *Neural basis of orexigenic effects of ghrelin acting within lateral hypothalamus.* Peptides, 2003. **24**(4): p. 597-602.
167. Sokoloff, L., *The brain as a chemical machine.* Prog Brain Res, 1992. **94**: p. 19-33.
168. Suh, S.W., A.M. Hamby, and R.A. Swanson, *Hypoglycemia, brain energetics, and hypoglycemic neuronal death.* Glia, 2007. **55**(12): p. 1280-6.
169. Laakso, M., *Hyperglycemia and cardiovascular disease in type 2 diabetes.* Diabetes, 1999. **48**(5): p. 937-42.
170. Marty, N., M. Dallaporta, and B. Thorens, *Brain glucose sensing, counterregulation, and energy homeostasis.* Physiology (Bethesda), 2007. **22**: p. 241-51.
171. Burdakov, D., S.M. Luckman, and A. Verkhratsky, *Glucose-sensing neurons of the hypothalamus.* Philos Trans R Soc Lond B Biol Sci, 2005. **360**(1464): p. 2227-35.
172. Song, Z., et al., *Convergence of pre- and postsynaptic influences on glucosensing neurons in the ventromedial hypothalamic nucleus.* Diabetes, 2001. **50**(12): p. 2673-81.
173. Yang, X.J., et al., *Metabolic pathways that mediate inhibition of hypothalamic neurons by glucose.* Diabetes, 2004. **53**(1): p. 67-73.

174. Zhang, R., et al., *Selective inactivation of Socs3 in SF1 neurons improves glucose homeostasis without affecting body weight.* Endocrinology, 2008. **149**(11): p. 5654-61.
175. Routh, V.H., *Glucose sensing neurons in the ventromedial hypothalamus.* Sensors (Basel), 2010. **10**(10): p. 9002-25.
176. de Lecea, L., et al., *The hypocretins: hypothalamus-specific peptides with neuroexcitatory activity.* Proc Natl Acad Sci U S A, 1998. **95**(1): p. 322-7.
177. Sakurai, T., et al., *Orexins and orexin receptors: a family of hypothalamic neuropeptides and G protein-coupled receptors that regulate feeding behavior.* Cell, 1998. **92**(5): p. 1 page following 696.
178. Burdakov, D., O. Gerasimenko, and A. Verkhratsky, *Physiological changes in glucose differentially modulate the excitability of hypothalamic melanin-concentrating hormone and orexin neurons in situ.* J Neurosci, 2005. **25**(9): p. 2429-33.
179. Muroya, S., et al., *Glucose-sensitive neurons in the rat arcuate nucleus contain neuropeptide Y.* Neurosci Lett, 1999. **264**(1-3): p. 113-6.
180. Claret, M., et al., *AMPK is essential for energy homeostasis regulation and glucose sensing by POMC and AgRP neurons.* J Clin Invest, 2007. **117**(8): p. 2325-36.
181. Chen, M., et al., *Functional magnetic resonance imaging and immunohistochemical study of hypothalamic function following oral glucose ingestion in rats.* Chin Med J (Engl), 2007. **120**(14): p. 1232-5.
182. Smeets, P.A., et al., *Functional MRI of human hypothalamic responses following glucose ingestion.* Neuroimage, 2005. **24**(2): p. 363-8.
183. Liu, Y., et al., *The temporal response of the brain after eating revealed by functional MRI.* Nature, 2000. **405**(6790): p. 1058-62.
184. Gautier, J.F., et al., *Effect of satiation on brain activity in obese and lean women.* Obes Res, 2001. **9**(11): p. 676-84.
185. Moraschi, M., M. DiNuzzo, and F. Giove, *On the origin of sustained negative BOLD response.* J Neurophysiol, 2012. **108**(9): p. 2339-42.
186. Lizarbe, B., et al., *Imaging hypothalamic activity using diffusion weighted magnetic resonance imaging in the mouse and human brain.* Neuroimage, 2013. **64**: p. 448-57.
187. Firsov, D., N. Tokonami, and O. Bonny, *Role of the renal circadian timing system in maintaining water and electrolytes homeostasis.* Mol Cell Endocrinol, 2012. **349**(1): p. 51-5.
188. Ma, X., L. Zubcevic, and F.M. Ashcroft, *Glucose regulates the effects of leptin on hypothalamic POMC neurons.* Proc Natl Acad Sci U S A, 2008. **105**(28): p. 9811-6.

189. Mueller, W.M., et al., *Evidence that glucose metabolism regulates leptin secretion from cultured rat adipocytes.* Endocrinology, 1998. **139**(2): p. 551-8.
190. Nicholson, C. and J.M. Phillips, *Ion diffusion modified by tortuosity and volume fraction in the extracellular microenvironment of the rat cerebellum.* J Physiol, 1981. **321**: p. 225-57.
191. Kume-Kick, J., et al., *Independence of extracellular tortuosity and volume fraction during osmotic challenge in rat neocortex.* J Physiol, 2002. **542**(Pt 2): p. 515-27.
192. Sykova, E. and C. Nicholson, *Diffusion in brain extracellular space.* Physiol Rev, 2008. **88**(4): p. 1277-340.
193. Rusakov, D.A. and D.M. Kullmann, *Geometric and viscous components of the tortuosity of the extracellular space in the brain.* Proc Natl Acad Sci U S A, 1998. **95**(15): p. 8975-80.
194. Sykova, E., et al., *Glial swelling and astrogliosis produce diffusion barriers in the rat spinal cord.* Glia, 1999. **25**(1): p. 56-70.
195. Becskei, C., T.A. Lutz, and T. Riediger, *Glucose reverses fasting-induced activation in the arcuate nucleus of mice.* Neuroreport, 2008. **19**(1): p. 105-9.
196. Yang, L., et al., *Role of dorsomedial hypothalamic neuropeptide Y in modulating food intake and energy balance.* J Neurosci, 2009. **29**(1): p. 179-90.
197. Szczepanska-Sadowska, E., *Interaction of vasopressin and angiotensin II in central control of blood pressure and thirst.* Regul Pept, 1996. **66**(1-2): p. 65-71.
198. Buijs, R.M., *Intra- and extrahypothalamic vasopressin and oxytocin pathways in the rat. Pathways to the limbic system, medulla oblongata and spinal cord.* Cell Tissue Res, 1978. **192**(3): p. 423-35.
199. Muhlethaler, M., J.J. Dreifuss, and B.H. Gahwiler, *Vasopressin excites hippocampal neurones.* Nature, 1982. **296**(5859): p. 749-51.

Appendix I: MATLAB Functions

Content

I. Fed and Fasted Diffusion Analyses

1. Analysis

```
%In this function, the pathways to the of the animal's data to analyze are entered ("var").
Afterwards, The DICOM reading function and image analyses function are called, and
information concerning the state of the animal (fed or fasted), image coordinates of the
data to analyze (center and ratio), and diffusion model must be given.

var='C:\\Users\\Blanca\\Documents\\MATLAB\\ob_ob\\Ob_1\\E11';

%"lectura_9b_1a0" is the function that reads the DICOM data stored in "var", normalizes it
and creates matrixes with the information of all pixel values for all the b values, in the
d1, d2 and d3 directions
[d1,d2,d3]=lectura_9b_1a0(var);

%image reading(animal,condition,sequence,pixel values d1,pixel values d2,pixel values
d3,xcentre,ycentre,Rx,Ry,diffusion model)calls all the functions to proceed with the
biexponential analyses
image_reading(1,0,11,d1,d2,d3,12.28,9.18,4.5,3.8,'biexp');
clear all

%%%%%%%%%
var='C:\\Users\\Blanca\\Documents\\MATLAB\\ob_ob\\Ob_1_fasted\\E11';
[d1,d2,d3]=lectura_9b_1a0(var);
image_reading(1,1,11,d1,d2,d3,12.28,9.18,4.5,3.8,'biexp');
clear all
```

2. Reading 9b 1a0

```
%This functions reads the DICOM data from the desired animal

function [d1,d2,d3]=lectura_9b_1a0(path)

    bas1=dicomread(sprintf('%s\\MRIm02', path));bas1_vector=reshape(bas1,16384,1);
 %d1 images, vectors and normalized to basal vectors
    b1d1=dicomread(sprintf('%s\\MRIm05',
path));b1d1_vector=reshape(b1d1,16384,1);b1d1_vector_nor=double(b1d1_vector(:,:))./double(ba
s1_vector);
    b2d1=dicomread(sprintf('%s\\MRIm08',
path));b2d1_vector=reshape(b2d1,16384,1);b2d1_vector_nor=double(b2d1_vector(:,:))./double(ba
s1_vector);
    b3d1=dicomread(sprintf('%s\\MRIm11',
path));b3d1_vector=reshape(b3d1,16384,1);b3d1_vector_nor=double(b3d1_vector(:,:))./double(ba
s1_vector);
    b4d1=dicomread(sprintf('%s\\MRIm14',
path));b4d1_vector=reshape(b4d1,16384,1);b4d1_vector_nor=double(b4d1_vector(:,:))./double(ba
s1_vector);
    b5d1=dicomread(sprintf('%s\\MRIm17',
path));b5d1_vector=reshape(b5d1,16384,1);b5d1_vector_nor=double(b5d1_vector(:,:))./double(ba
s1_vector);
    b6d1=dicomread(sprintf('%s\\MRIm20',
path));b6d1_vector=reshape(b6d1,16384,1);b6d1_vector_nor=double(b6d1_vector(:,:))./double(ba
s1_vector);
    b7d1=dicomread(sprintf('%s\\MRIm23',
path));b7d1_vector=reshape(b7d1,16384,1);b7d1_vector_nor=double(b7d1_vector(:,:))./double(ba
s1_vector);
    b8d1=dicomread(sprintf('%s\\MRIm26',
path));b8d1_vector=reshape(b8d1,16384,1);b8d1_vector_nor=double(b8d1_vector(:,:))./double(ba
s1_vector);
    b9d1=dicomread(sprintf('%s\\MRIm29',
path));b9d1_vector=reshape(b9d1,16384,1);b9d1_vector_nor=double(b9d1_vector(:,:))./double(ba
s1_vector);
```

```
%d2 images, vectors and normalized to basal vectors
    b1d2=dicomread(sprintf('%s\\MRIm32',
path));b1d2_vector=reshape(b1d2,16384,1);b1d2_vector_nor=double(b1d2_vector(:,:))./double(ba
s1_vector);
    b2d2=dicomread(sprintf('%s\\MRIm35',
path));b2d2_vector=reshape(b2d2,16384,1);b2d2_vector_nor=double(b2d2_vector(:,:))./double(ba
s1_vector);
    b3d2=dicomread(sprintf('%s\\MRIm38',
path));b3d2_vector=reshape(b3d2,16384,1);b3d2_vector_nor=double(b3d2_vector(:,:))./double(ba
s1_vector);
    b4d2=dicomread(sprintf('%s\\MRIm41',
path));b4d2_vector=reshape(b4d2,16384,1);b4d2_vector_nor=double(b4d2_vector(:,:))./double(ba
s1_vector);
    b5d2=dicomread(sprintf('%s\\MRIm44',
path));b5d2_vector=reshape(b5d2,16384,1);b5d2_vector_nor=double(b5d2_vector(:,:))./double(ba
s1_vector);
    b6d2=dicomread(sprintf('%s\\MRIm47',
path));b6d2_vector=reshape(b6d2,16384,1);b6d2_vector_nor=double(b6d2_vector(:,:))./double(ba
s1_vector);
    b7d2=dicomread(sprintf('%s\\MRIm50',
path));b7d2_vector=reshape(b7d2,16384,1);b7d2_vector_nor=double(b7d2_vector(:,:))./double(ba
s1_vector);
    b8d2=dicomread(sprintf('%s\\MRIm53',
path));b8d2_vector=reshape(b8d2,16384,1);b8d2_vector_nor=double(b8d2_vector(:,:))./double(ba
s1_vector);
    b9d2=dicomread(sprintf('%s\\MRIm56',
path));b9d2_vector=reshape(b9d2,16384,1);b9d2_vector_nor=double(b9d2_vector(:,:))./double(ba
s1_vector);

   %d3 images, vectors and normalized to basal vectors
    b1d3=dicomread(sprintf('%s\\MRIm59',
path));b1d3_vector=reshape(b1d3,16384,1);b1d3_vector_nor=double(b1d3_vector(:,:))./double(ba
s1_vector);
    b2d3=dicomread(sprintf('%s\\MRIm62',
path));b2d3_vector=reshape(b2d3,16384,1);b2d3_vector_nor=double(b2d3_vector(:,:))./double(ba
s1_vector);
    b3d3=dicomread(sprintf('%s\\MRIm65',
path));b3d3_vector=reshape(b3d3,16384,1);b3d3_vector_nor=double(b3d3_vector(:,:))./double(ba
s1_vector);
    b4d3=dicomread(sprintf('%s\\MRIm68',
path));b4d3_vector=reshape(b4d3,16384,1);b4d3_vector_nor=double(b4d3_vector(:,:))./double(ba
s1_vector);
    b5d3=dicomread(sprintf('%s\\MRIm71',
path));b5d3_vector=reshape(b5d3,16384,1);b5d3_vector_nor=double(b5d3_vector(:,:))./double(ba
s1_vector);
    b6d3=dicomread(sprintf('%s\\MRIm74',
path));b6d3_vector=reshape(b6d3,16384,1);b6d3_vector_nor=double(b6d3_vector(:,:))./double(ba
s1_vector);
    b7d3=dicomread(sprintf('%s\\MRIm77',
path));b7d3_vector=reshape(b7d3,16384,1);b7d3_vector_nor=double(b7d3_vector(:,:))./double(ba
s1_vector);
    b8d3=dicomread(sprintf('%s\\MRIm80',
path));b8d3_vector=reshape(b8d3,16384,1);b8d3_vector_nor=double(b8d3_vector(:,:))./double(ba
s1_vector);
    b9d3=dicomread(sprintf('%s\\MRIm83',
path));b9d3_vector=reshape(b9d3,16384,1);b9d3_vector_nor=double(b9d3_vector(:,:))./double(ba
s1_vector);

 %     d1,d2,d3 group in the first column pixels from b1 in the corresponding direction. The
last column (9) corresponds to the b9 diffusion data. In the DICOM Reading process, values
from the first image column (and 128 rows) are first written in the new matrix, below values
from the second image column are written…till achieving a vector (1 column x 16384 rows) for
each b value.

n=128; m=128;l=n*m;d1=zeros(l,9);d2=zeros(l,9);d3=zeros(l,9);
    d1(:,:)=[b1d1_vector_nor b2d1_vector_nor b3d1_vector_nor b4d1_vector_nor b5d1_vector_nor
b6d1_vector_nor b7d1_vector_nor b8d1_vector_nor b9d1_vector_nor];
    d2(:,:)=[b1d2_vector_nor b2d2_vector_nor b3d2_vector_nor b4d2_vector_nor b5d2_vector_nor
b6d2_vector_nor b7d2_vector_nor b8d2_vector_nor b9d2_vector_nor];
    d3(:,:)=[b1d3_vector_nor b2d3_vector_nor b3d3_vector_nor b4d3_vector_nor b5d3_vector_nor
b6d3_vector_nor b7d3_vector_nor b8d3_vector_nor b9d3_vector_nor];
```

```
end
```

3. Image reading

```
function image_reading(animal,state,sequence,d1,d2,d3,x,y,Rx,Ry,ajuste)
%calls all the functions to proceed with the analyses and the storage of results

coordinates_128=load('coordinates_128');
char(double(ajuste));
char(ajuste)
tf=strcmp(ajuste,'biexp');

        [coefficients]=diffusion_3d(animal,sequence,x,y,Rx,Ry,d1,d2,d3,coordinates_128,tf);
        coefficients_filtered=filtering_mono(coefficients);

[hypothalamus_data,nuclei_data]=hypothalamus_grouping(coefficients_filtered,animal,state);
        if tf==1
        results_folders_biexp;
        else
        results_folders_monoexp;
        end
        if sequence==12
        save coefficients_filtered_2 coefficients_filtered -ascii
        save hypothalamus_data_2 hypothalamus_data -ascii
        save nuclei_data_2 nuclei_data -ascii
        else
        save coefficients_filtered_rois coefficients_filtered -ascii
        save hypothalamus_data_rois hypothalamus_data -ascii
        save nuclei_data_rois nuclei_data -ascii
        end
cd ('C:\Users\aborges\Documents\MATLAB\Ejecucion_ob_ob_difusion')
end
```

4. Diffusion 3d

```
function coefficients=diffusion_3d(animal,sequence,x,y,Rx,Ry,d1,d2,d3,coordinates_128,tf)
%This function specifies the area of analyses, the b parameters, and calls the fitting
functions

if sequence==10
    b_values=[18;29;40;61;93;134;165];num_b=7;
else
    b_values=[320;422;626;930;1234;1538;1634;1841;2043]; num_b=9;
end
%
n=128;m=128;
switch animal
    case {(1),(2)}
    rx=Rx*n/25; ry=Ry*m/25;
    xcentre=x*n/25;ycentre=y*m/25;                  %expressing coordinates as pixels
    otherwise
    rx=Rx*n/21; ry=Ry*m/21;
    xcentre=x*n/21;ycentre=y*m/21;
end
fila_min=ycentre-ry;columna_min=xcentre-rx;
fila_max=ycentre+ry;columna_max=xcentre+rx;

%to calculate the transformation from matrix coordinates(x,y) to vector coordinates(l) it
%must be taken into account how the "reshape" function puts the data
l_min=floor(columna_min-1)*128+floor(fila_min);
l_max=ceil(columna_max-1)*128+ceil(fila_max);
k=0;
for i=l_min:l_max
     r1(i)=((xcentre-coordinates_128(i,1))^2);%
     r2(i)=((ycentre-coordinates_128(i,2))^2);
     frac1(i)=r1(i)/(rx^2);
     frac2(i)=r2(i)/(ry^2);
     elipse(i)=frac1(i)+frac2(i);
```

```
     if elipse(i)<1
         k=k+1;
         roi_pixel=[coordinates_128(i,1),coordinates_128(i,2)];
         if tf==1
         coefficients_results
=single_nonlinear_fitting_3d_r08(num_b,b_values,d1(i,1:9),d2(i,1:9),d3(i,1:9));
         else
         coefficients_results
=single_monoexponential_fitting_3d_r08(num_b,b_values,d1(i,1:9),d2(i,1:9),d3(i,1:9));
         end
         coefficients(k,:)=[roi_pixel coefficients_results];

     end
end
```

5. Single nonlinear fitting 3d r08

```
function [results,phases]=single_nonlinear_fitting_3d_r08(num_b,b_values,d1,d2,d3)
%This function proceeds to fit non-linearly the diffusion data

switch num_b
    case (7)
    options=fitoptions('Normalize','off','method','NonlinearLeastSquares','Robust','off','d
    isplay','off','startpoint',[0.5 0.0015 0.005], 'upper',[1 0.004 0.04],'lower',[0 0
    0],'algorithm','Trust-Region','MaxIter',600,'MaxFuneval',600);
     case(9)
    options=fitoptions('Normalize','off','method','NonlinearLeastSquares','Robust','off','d
    isplay','off','startpoint',[0.3 0.0003 0.0013],'upper',[1 0.001 0.004],'lower',[0 0
    0],'algorithm','Trust-Region','MaxIter',600,'MaxFuneval',600);
end

s=fittype('A*exp(-x*dslow)+(1-A)*exp(-
x*dfast)','coefficients',{'A','dslow','dfast'},'options',options);

    [c1,min_percent,max_percent,phase1]=fitting(num_b,b_values,d1',s);
            if (c1(4)>0.65 && c1(2)>10^-5 && c1(3)/c1(2)>1.1 && min_percent>5 &&
max_percent<95 )
                result(1:4)=[c1(1,1),c1(1,2)*10^6, c1(1,3)*10^6,c1(1,4)];
                phase(1:3)=[phase1 min_percent max_percent];
            else
                result(1:4)=NaN;
                phase(1:3)=NaN;
            end

    [c2,min_percent2,max_percent2,phase2]=fitting(num_b,b_values,d2',s);
              if (c2(4)>0.65 && c2(2)>10^-5 && c2(3)/c2(2)>1.1&& min_percent2>5 &&
max_percent2<95)
                  result(5:8)=[c2(1,1),c2(1,2)*10^6, c2(1,3)*10^6,c2(1,4)];
                  phase(4:6)=[phase2 min_percent2 max_percent2];
              else
                  result(5:8)=NaN;
                  phase(4:6)=NaN;
              end

    [c3,min_percent3,max_percent3,phase3]=fitting(num_b,b_values,d3',s );
             if (c3(4)>0.65 && c3(2)>10^-5 && c3(3)/c3(2)>1.1 && min_percent3>5 &&
max_percent3<95)
                 result(9:12)=[c3(1,1),c3(1,2)*10^6, c3(1,3)*10^6,c3(1,4)];
                 phase(7:9)=[phase3 min_percent3 max_percent3];
             else
                 result(9:12)=NaN;
                 phase(7:9)=NaN;
             end

 results=result;
 phases=phase;

end
```

6. Filtering mono

```
function [results_filtered]=filtering_mono(results)
%This function filters the data with NAN values

dimen1=size(results(:,1),1);
dimen2=size(results(1,:),2);
j=0;
    for  i=1:dimen1
        x=isnan(results(i,3:dimen2));
        if x==1;
        else
        j=j+1;
        results_filtered(j,:)=results(i,:);
        end
    end
end
```

7. Hypothalamus grouping

```
function [hypothalamus_data,Nuclei_data]=hypothalamus_grouping(coefficients,animal,state)
%This function identifies the hypothalamic and subhypothalamic regions for all animals

switch animal
case (1)
        if state==0
        cd('C:\\Users\\aborges\\Documents\\MATLAB\\ob_ob_images_revisted_230513\Ob_1\E4')
        else
cd('C:\\Users\\aborges\\Documents\\MATLAB\\ob_ob_images_revisted_230513\Ob_1_fasted\E4')
        end
    case(2)
        if state==0
        cd('C:\\Users\\aborges\\Documents\\MATLAB\\ob_ob_images_revisted_230513\Ob_2\E4')
        else
cd('C:\\Users\\aborges\\Documents\\MATLAB\\ob_ob_images_revisted_230513\Ob_2_fasted\E4')
        end
    case(3)
        if state==0
        cd('C:\\Users\\aborges\\Documents\\MATLAB\\ob_ob_images_revisted_230513\Ob_3\E4')
        else
cd('C:\\Users\\aborges\\Documents\\MATLAB\\ob_ob_images_revisted_230513\Ob_3_fasted\E4')
        end
   case(4)
        if state==0
        cd('C:\\Users\\aborges\\Documents\\MATLAB\\ob_ob_images_revisted_230513\Ob_4\E4')
        else
cd('C:\\Users\\aborges\\Documents\\MATLAB\\ob_ob_images_revisted_230513\Ob_4_fasted\E4')
        end
   case(5)
        if state==0
        cd('C:\\Users\\aborges\\Documents\\MATLAB\\ob_ob_images_revisted_230513\Ob_5\E4')
        else
cd('C:\\Users\\aborges\\Documents\\MATLAB\\ob_ob_images_revisted_230513\Ob_5_fasted\E4')
        end
   case(6)
        if state==0
        cd('C:\\Users\\aborges\\Documents\\MATLAB\\ob_ob_images_revisted_230513\Ob_6\E4')
        else
cd('C:\\Users\\aborges\\Documents\\MATLAB\\ob_ob_images_revisted_230513\Ob_6_fasted\E4')
        end
   case(7)
        if state==0
        cd('C:\\Users\\aborges\\Documents\\MATLAB\\ob_ob_images_revisted_230513\Ob_7\E4')
        else
cd('C:\\Users\\aborges\\Documents\\MATLAB\\ob_ob_images_revisted_230513\Ob_7_fasted\E4')
        end
   case (8)
        if state==0
        cd('C:\\Users\\aborges\\Documents\\MATLAB\\ob_ob_images_revisted_230513\Ob_8\E4')
```

```
        else
cd('C:\\Users\\aborges\\Documents\\MATLAB\\ob_ob_images_revisted_230513\Ob_8_fasted\E4')
        end
    case(9)
        if state==0
        cd('C:\\Users\\aborges\\Documents\\MATLAB\\ob_ob_images_revisted_230513\Ob_9\E4')
        else
cd('C:\\Users\\aborges\\Documents\\MATLAB\\ob_ob_images_revisted_230513\Ob_9_fasted\E4')
        end
    case(10)
        if state==0
        cd('C:\\Users\\aborges\\Documents\\MATLAB\\ob_ob_images_revisted_230513\Ob_10\E4')
        else
cd('C:\\Users\\aborges\\Documents\\MATLAB\\ob_ob_images_revisted_230513\Ob_10_fasted\E4')
        end
end

hypo_coordinates=load('hypothalamic_coordinates.txt');
%in this file, column 1 is 'x', column 2 is 'y'
ventricle_coordinates=load('ventricle.txt','txt');
ARC=load('ARC.txt');
LDM=load('Left DM.txt');LVM=load('Left VM.txt');
RDM=load('Right DM.txt');RVM=load('Right VM.txt');
LH=load('Lateral H.txt');

%files sizes
s_coef=size(coefficients(:,1));
s_hypo=size(hypo_coordinates(:,1));
s_ven=size(ventricle_coordinates(:,1));
s_ARC=size(ARC(:,1),1);one=ones(s_ARC,1);
s_LDM=size(LDM(:,1),1);two=ones(s_LDM,1)+1;
s_LVM=size(LVM(:,1),1);three=ones(s_LVM,1)+2;
s_RDM=size(RDM(:,1),1);four=ones(s_RDM,1)+3;
s_RVM=size(RVM(:,1),1);five=ones(s_RVM,1)+4;
s_LH=size(LH(:,1),1);six=ones(s_LH,1)+5;

DM_Nuclei=[two LDM ;four RDM]; VM_Nuclei=[three LVM;five RVM];LH_Nuclei=[six LH];
Nuclei=[one ARC;DM_Nuclei;VM_Nuclei;LH_Nuclei];

%hypothalamic área selection. I sum 1 because the coordinates info comes from Image J,
%which starts counting at (0,0), while my coefficients begin in (1,1)
hypothalamus_coord=[hypo_coordinates(:,1)+ones(s_hypo,1),hypo_coordinates(:,2)+ones(s_hypo,1
)];
ventricle_coord=[ventricle_coordinates(:,1)+ones(s_ven,1),ventricle_coordinates(:,2)+ones(s_
ven,1)];
hypothalamus_nv=setdiff(hypothalamus_coord(:,1:2),ventricle_coord(:,1:2),'rows');
s_hypo_nv=size(hypothalamus_nv(:,1),1);
s_column=size(coefficients(1,:),2);

l=0;
for i=1:s_hypo_nv
     for j=1:s_coef
        if coefficients(j,1)==hypothalamus_nv(i,1) &&
coefficients(j,2)==hypothalamus_nv(i,2)
          l=l+1;
          hypothalamus_data(l,:)=[animal state hypothalamus_nv(i,1:2)
coefficients(j,3:s_column)];

        end
     end
end

 %nuclei selection
 n=0;
 ll=0;
 s_hypo_data=size(hypothalamus_data(:,1),1);
 for n=1:size(Nuclei(:,1),1)
          for m=1:s_hypo_data
               if Nuclei(n,2)+1==hypothalamus_data(m,3) &&
Nuclei(n,3)+1==hypothalamus_data(m,4)
               ll=ll+1;
```

```
                Nuclei_data(ll,:)=[Nuclei(n,1) hypothalamus_data(m,:)];
                end
            end
 end
 cd('C:\Users\aborges\Documents\MATLAB\Ejecucion_ob_ob_difusion')
end
```

8. Results folders biexp

```
%This function creates folders to save the new data
cd('C:\Users\aborges\Documents\MATLAB\ob_ob_revisted220513')
switch animal
    case (1)
        if state==0
        mkdir('Ob_1');cd('Ob_1');
        else
        mkdir('Ob_1_fasted');cd('Ob_1_fasted');
        end
     case (2)
        if state==0
        mkdir('Ob_2');cd('Ob_2');
        else
        mkdir('Ob_2_fasted');cd('Ob_2_fasted');
        end
     case (3)
        if state==0
        mkdir('Ob_3');cd('Ob_3');
        else
        mkdir('Ob_3_fasted');cd('Ob_3_fasted');
        end
     case (4)
        if state==0
        mkdir('Ob_4');cd('Ob_4');
        else
        mkdir('Ob_4_fasted');cd('Ob_4_fasted');
        end
     case (5)
        if state==0
        mkdir('Ob_5');cd('Ob_5');
        else
        mkdir('Ob_5_fasted');cd('Ob_5_fasted');
        end
     case (6)
        if state==0
        mkdir('Ob_6');cd('Ob_6');
        else
        mkdir('Ob_6_fasted');cd('Ob_6_fasted');
        end
     case (7)
        if state==0
        mkdir('Ob_7');cd('Ob_7');
        else
        mkdir('Ob_7_fasted');cd('Ob_7_fasted');
        end
     case (8)
        if state==0
        mkdir('Ob_8');cd('Ob_8');
        else
        mkdir('Ob_8_fasted');cd('Ob_8_fasted');
        end
     case (9)
        if state==0
        mkdir('Ob_9');cd('Ob_9');
        else
        mkdir('Ob_9_fasted');cd('Ob_9_fasted');
        end
     case (10)
        if state==0
        mkdir('Ob_10');cd('Ob_10');
        else
```

```
        mkdir('Ob_10_fasted');cd('Ob_10_fasted');
        end

end
```

9. All Nuclei

```
%This function groups the nuclei data for all the fed and fasted mice
cd('C:\Users\aborges\Documents\MATLAB\ob_ob_revisted220513\Ob_1')
nucleos=load('nuclei_data_rois','ascii');size2=size(nucleos(:,1),1);
cd('C:\Users\aborges\Documents\MATLAB\ob_ob_revisted220513\Ob_1_fasted')
nucleos_fasted=load('nuclei_data','ascii');size2f=size(nucleos_fasted(:,1),1);
agrupacion_nucleoss(1:size2,:)=nucleos;
agrupacion_nucleoss_fasted(1:size2f,:)=nucleos_fasted;

cd('C:\Users\aborges\Documents\MATLAB\ob_ob_revisted220513\Ob_2')
nucleos=load('nuclei_data_rois','ascii');size3=size(nucleos(:,1),1);
cd('C:\Users\aborges\Documents\MATLAB\ob_ob_revisted220513\Ob_2_fasted')
nucleos_fasted=load('nuclei_data_rois','ascii');size3f=size(nucleos_fasted(:,1),1);
old_total_size=size2;new_total_size=size2+size3;
old_total_sizef=size2f;new_total_sizef=size2f+size3f;
agrupacion_nucleoss(old_total_size+1:new_total_size,:)=nucleos;
agrupacion_nucleoss_fasted(old_total_sizef+1:new_total_sizef,:)=nucleos_fasted;

cd('C:\Users\aborges\Documents\MATLAB\ob_ob_revisted220513\Ob_3')
nucleos=load('nuclei_data_rois','ascii');size4=size(nucleos(:,1),1);
cd('C:\Users\aborges\Documents\MATLAB\ob_ob_revisted220513\Ob_3_fasted')
nucleos_fasted=load('nuclei_data','ascii');size4f=size(nucleos_fasted(:,1),1);
old_total_size=new_total_size;new_total_size=old_total_size+size4;
old_total_sizef=new_total_sizef;new_total_sizef=old_total_sizef+size4f;
agrupacion_nucleoss(old_total_size+1:new_total_size,:)=nucleos;
agrupacion_nucleoss_fasted(old_total_sizef+1:new_total_sizef,:)=nucleos_fasted;

cd('C:\Users\aborges\Documents\MATLAB\ob_ob_revisted220513\Ob_4')
nucleos=load('nuclei_data_rois','ascii');size5=size(nucleos(:,1),1);
cd('C:\Users\aborges\Documents\MATLAB\ob_ob_revisted220513\Ob_4_fasted')
nucleos_fasted=load('nuclei_data','ascii');size5f=size(nucleos_fasted(:,1),1);
old_total_size=new_total_size;new_total_size=old_total_size+size5;
old_total_sizef=new_total_sizef;new_total_sizef=old_total_sizef+size5f;
agrupacion_nucleoss(old_total_size+1:new_total_size,:)=nucleos;
agrupacion_nucleoss_fasted(old_total_sizef+1:new_total_sizef,:)=nucleos_fasted;

cd('C:\Users\aborges\Documents\MATLAB\ob_ob_revisted220513\Ob_5')
nucleos=load('nuclei_data_rois','ascii');size6=size(nucleos(:,1),1);
cd('C:\Users\aborges\Documents\MATLAB\ob_ob_revisted220513\Ob_5_fasted')
nucleos_fasted=load('nuclei_data','ascii');size6f=size(nucleos_fasted(:,1),1);
old_total_size=new_total_size;new_total_size=old_total_size+size6;
old_total_sizef=new_total_sizef;new_total_sizef=old_total_sizef+size6f;
agrupacion_nucleoss(old_total_size+1:new_total_size,:)=nucleos;
agrupacion_nucleoss_fasted(old_total_sizef+1:new_total_sizef,:)=nucleos_fasted;

cd('C:\Users\aborges\Documents\MATLAB\ob_ob_revisted220513\Ob_6')
nucleos=load('nuclei_data_rois','ascii');size7=size(nucleos(:,1),1);
cd('C:\Users\aborges\Documents\MATLAB\ob_ob_revisted220513\Ob_6_fasted')
nucleos_fasted=load('nuclei_data','ascii');size7f=size(nucleos_fasted(:,1),1);
old_total_size=new_total_size;new_total_size=old_total_size+size7;
old_total_sizef=new_total_sizef;new_total_sizef=old_total_sizef+size7f;
agrupacion_nucleoss(old_total_size+1:new_total_size,:)=nucleos;
agrupacion_nucleoss_fasted(old_total_sizef+1:new_total_sizef,:)=nucleos_fasted;

cd('C:\Users\aborges\Documents\MATLAB\ob_ob_revisted220513\Ob_7')
nucleos=load('nuclei_data_rois','ascii');size8=size(nucleos(:,1),1);
cd('C:\Users\aborges\Documents\MATLAB\ob_ob_revisted220513\Ob_7_fasted')
nucleos_fasted=load('nuclei_data','ascii');size8f=size(nucleos_fasted(:,1),1);
old_total_size=new_total_size;new_total_size=old_total_size+size8;
old_total_sizef=new_total_sizef;new_total_sizef=old_total_sizef+size8f;
agrupacion_nucleoss(old_total_size+1:new_total_size,:)=nucleos;
agrupacion_nucleoss_fasted(old_total_sizef+1:new_total_sizef,:)=nucleos_fasted;

cd('C:\Users\aborges\Documents\MATLAB\ob_ob_revisted220513\Ob_8')
```

```
nucleos=load('nuclei_data_rois','ascii');size9=size(nucleos(:,1),1);
cd('C:\Users\aborges\Documents\MATLAB\ob_ob_revisted220513\Ob_8_fasted')
nucleos_fasted=load('nuclei_data','ascii');size9f=size(nucleos_fasted(:,1),1);
old_total_size=new_total_size;new_total_size=old_total_size+size9;
old_total_sizef=new_total_sizef;new_total_sizef=old_total_sizef+size9f;
agrupacion_nucleoss(old_total_size+1:new_total_size,:)=nucleos;
agrupacion_nucleoss_fasted(old_total_sizef+1:new_total_sizef,:)=nucleos_fasted;

cd('C:\Users\aborges\Documents\MATLAB\ob_ob_revisted220513\Ob_9')
nucleos=load('nuclei_data_rois','ascii');size10=size(nucleos(:,1),1);
cd('C:\Users\aborges\Documents\MATLAB\ob_ob_revisted220513\Ob_9_fasted')
nucleos_fasted=load('nuclei_data','ascii');size10f=size(nucleos_fasted(:,1),1);
old_total_size=new_total_size;new_total_size=old_total_size+size10;
old_total_sizef=new_total_sizef;new_total_sizef=old_total_sizef+size10f;
agrupacion_nucleoss(old_total_size+1:new_total_size,:)=nucleos;
agrupacion_nucleoss_fasted(old_total_sizef+1:new_total_sizef,:)=nucleos_fasted;

cd('C:\Users\aborges\Documents\MATLAB\ob_ob_revisted220513\Ob_10')
nucleos=load('nuclei_data_rois','ascii');size11=size(nucleos(:,1),1);
cd('C:\Users\aborges\Documents\MATLAB\ob_ob_revisted220513\Ob_10_fasted')
nucleos_fasted=load('nuclei_data','ascii');size11f=size(nucleos_fasted(:,1),1);
old_total_size=new_total_size;new_total_size=old_total_size+size11;
old_total_sizef=new_total_sizef;new_total_sizef=old_total_sizef+size11f;
agrupacion_nucleoss(old_total_size+1:new_total_size,:)=nucleos;
agrupacion_nucleoss_fasted(old_total_sizef+1:new_total_sizef,:)=nucleos_fasted;

cd('C:\Users\aborges\Documents\MATLAB\ob_ob_revisted220513')
save agrupacion_nucleos  agrupacion_nucleoss -ascii
save agrupacion_nucleos_fasted  agrupacion_nucleoss_fasted -ascii
```

II. Glucose Effects Diffusion Analyses

1. Analysis

```
%In this function, the pathways to the of the animal's data to analyze are entered ("var").
Afterwards, The DICOM reading function and image analyses function are called, and
information concerning the state of the animal (basal, glucose or recovery), image
coordinates of the data to analyze (center and ratio), and diffusion model must be given.

var='C:\\Users\\aborges\\Documents\\MATLAB\\Glucose_admin_difu\\5\\E4';

%"lectura_9b" is a function that reads the DICOM data, normalizes it and creates matrixes
with the information of all pixel values for all the b values, in the d1, d2 and d3
directions
[d1,d2,d3]=lectura_9b_1a0(var);

%image reading(animal,condition,sequence,pixel values d1,pixel values d2,pixel values
d3,xcentre,ycentre,Rx,Ry,diffusion model)calls all the functions to proceed the analyses
image_reading(5,0,4,d1,d2,d3,9.6,4.9,2,0.75,'monoexp');
clear all

var='C:\\Users\\aborges\\Documents\\MATLAB\\Glucose_admin_difu\\5\\E5';
[d1,d2,d3]=lectura_9b_1a0(var);
image_reading(5,0,5,d1,d2,d3,9.6,4.9,2,0.75,'monoexp');
clear all

var='C:\\Users\\aborges\\Documents\\MATLAB\\Glucose_admin_difu\\5\\E6';
[d1,d2,d3]=lectura_9b_1a0(var);
image_reading(5,1,6,d1,d2,d3,9.6,4.9,2,0.75,'monoexp');
clear all

var='C:\\Users\\aborges\\Documents\\MATLAB\\Glucose_admin_difu\\5\\E7';
[d1,d2,d3]=lectura_9b_1a0(var);
image_reading(5,1,7,d1,d2,d3,9.6,4.9,2,0.75,'monoexp');
clear all

var='C:\\Users\\aborges\\Documents\\MATLAB\\Glucose_admin_difu\\5\\E8';
[d1,d2,d3]=lectura_9b_1a0(var);
image_reading(5,2,8,d1,d2,d3,9.6,4.9,2,0.75,'monoexp');
clear all

var='C:\\Users\\aborges\\Documents\\MATLAB\\Glucose_admin_difu\\5\\E9';
[d1,d2,d3]=lectura_9b_1a0(var);
image_reading(5,2,9,d1,d2,d3,9.6,4.9,2,0.75,'monoexp');
clear all
%%%%%%%%%
 var='C:\\Users\\aborges\\Documents\\MATLAB\\Glucose_admin_difu\\5\\E4';
[d1,d2,d3]=lectura_9b_1a0(var);
image_reading(5,0,4,d1,d2,d3,9.6,4.9,2,0.75,'biexp');
clear all

var='C:\\Users\\aborges\\Documents\\MATLAB\\Glucose_admin_difu\\5\\E5';
[d1,d2,d3]=lectura_9b_1a0(var);
image_reading(5,0,5,d1,d2,d3,9.6,4.9,2,0.75,'biexp');
clear all

var='C:\\Users\\aborges\\Documents\\MATLAB\\Glucose_admin_difu\\5\\E6';
[d1,d2,d3]=lectura_9b_1a0(var);
image_reading(5,1,6,d1,d2,d3,9.6,4.9,2,0.75,'biexp');
clear all

var='C:\\Users\\aborges\\Documents\\MATLAB\\Glucose_admin_difu\\5\\E7';
[d1,d2,d3]=lectura_9b_1a0(var);
image_reading(5,1,7,d1,d2,d3,9.6,4.9,2.2,1,'biexp');
clear all

var='C:\\Users\\aborges\\Documents\\MATLAB\\Glucose_admin_difu\\5\\E8';
[d1,d2,d3]=lectura_9b_1a0(var);
image_reading(5,2,8,d1,d2,d3,9.6,4.9,2.2,0.75,'biexp');
```

```
clear all

var='C:\\Users\\aborges\\Documents\\MATLAB\\Glucose_admin_difu\\5\\E9';
[d1,d2,d3]=lectura_9b_1a0(var);
image_reading(5,2,9,d1,d2,d3,9.6,4.9,2.2,0.75,'biexp');
clear all
%%%%%%%%%%%%%%%%%%%%%%%%%%%%%%%%%%%%%%%%%%%%%%%%%%%%%%%%%%%%%%%%%%%%%%%
```

2. Reading 9b 1a0

```
function [d1,d2,d3]=lectura_9b_1a0(path)

%This functions reads all the DICOM data

b1d1_slice2=dicomread(sprintf('%s\\MRIm05', path));
b2d1_slice2=dicomread(sprintf('%s\\MRIm08', path));
b3d1_slice2=dicomread(sprintf('%s\\MRIm11', path));
b4d1_slice2=dicomread(sprintf('%s\\MRIm14', path));
b5d1_slice2=dicomread(sprintf('%s\\MRIm17', path));
b6d1_slice2=dicomread(sprintf('%s\\MRIm20', path));
b7d1_slice2=dicomread(sprintf('%s\\MRIm23', path));
b8d1_slice2=dicomread(sprintf('%s\\MRIm26', path));
b9d1_slice2=dicomread(sprintf('%s\\MRIm29', path));
b1d2_slice2=dicomread(sprintf('%s\\MRIm32', path));
b2d2_slice2=dicomread(sprintf('%s\\MRIm35', path));
b3d2_slice2=dicomread(sprintf('%s\\MRIm38', path));
b4d2_slice2=dicomread(sprintf('%s\\MRIm41', path));
b5d2_slice2=dicomread(sprintf('%s\\MRIm44', path));
b6d2_slice2=dicomread(sprintf('%s\\MRIm47', path));
b7d2_slice2=dicomread(sprintf('%s\\MRIm50', path));
b8d2_slice2=dicomread(sprintf('%s\\MRIm53', path));
b9d2_slice2=dicomread(sprintf('%s\\MRIm56', path));
b1d3_slice2=dicomread(sprintf('%s\\MRIm59', path));
b2d3_slice2=dicomread(sprintf('%s\\MRIm62', path));
b3d3_slice2=dicomread(sprintf('%s\\MRIm65', path));
b4d3_slice2=dicomread(sprintf('%s\\MRIm68', path));
b5d3_slice2=dicomread(sprintf('%s\\MRIm71', path));
b6d3_slice2=dicomread(sprintf('%s\\MRIm74', path));
b7d3_slice2=dicomread(sprintf('%s\\MRIm77', path));
b8d3_slice2=dicomread(sprintf('%s\\MRIm80', path));
b9d3_slice2=dicomread(sprintf('%s\\MRIm83', path));
bas1_slice2=dicomread(sprintf('%s\\MRIm02', path));


n=128;m=128;l=n*m;d1=zeros(l,9);d2=zeros(l,9);d3=zeros(1,9);k=0;
for i=1:n
        for j=1:m
            k=k+1;
%being first i fixed, and varying j, we are creating d1,d2 and d3 files
%with, first, 128 data from the first row,below the 128 data from the second row..

y_d1=[double(b1d1_slice2(i,j))  double(b2d1_slice2(i,j))  double(b3d1_slice2(i,j))
double(b4d1_slice2(i,j))  double(b5d1_slice2(i,j))  double(b6d1_slice2(i,j))
double(b7d1_slice2(i,j)) double(b8d1_slice2(i,j))
double(b9d1_slice2(i,j))]./double(bas1_slice2(i,j));

y_d2=[double(b1d2_slice2(i,j))  double(b2d2_slice2(i,j))  double(b3d2_slice2(i,j))
double(b4d2_slice2(i,j))  double(b5d2_slice2(i,j))  double(b6d2_slice2(i,j))
double(b7d2_slice2(i,j)) double(b8d2_slice2(i,j))
double(b9d2_slice2(i,j))]./double(bas1_slice2(i,j));

y_d3=[double(b1d3_slice2(i,j))  double(b2d3_slice2(i,j))  double(b3d3_slice2(i,j))
double(b4d3_slice2(i,j))  double(b5d3_slice2(i,j))  double(b6d3_slice2(i,j))
double(b7d3_slice2(i,j)) double(b8d3_slice2(i,j))
double(b9d3_slice2(i,j))]./double(bas1_slice2(i,j));

                d1(k,:)=double(y_d1(:));
                d2(k,:)=double(y_d2(:));
                d3(k,:)=double(y_d3(:));
            end
    end
```

```
    end
```

3. Image Reading

```
function image_reading(animal,state,sequence,d1,d2,d3,x,y,Rx,Ry,ajuste)
%calls all the functions to proceed with the analyses and the storage of results

coordinates_128=load('coordinates_128');
char(double(ajuste));
char(ajuste)
tf=strcmp(ajuste,'biexp');

    if sequence==4||sequence==6||sequence==8
        coefficients]=diffusion_3d(sequence,x,y,Rx,Ry,d1,d2,d3,coordinates_128,ajuste);
        coefficients_filtered=filtering_mono(coefficients);
       [hypothalamus_data,nuclei_data]=hypothalamus_grouping(coefficients_filtered,animal,s
       tate);
       hippocampus_data=hippocampus_grouping(coefficients_filtered,animal,state);
        if tf==1
            results_folders;
        else
            results_folders_monoexp;
        end
        if sequence==4||sequence==6||sequence==8
            save coefficients_filtered_flow_rois coefficients_filtered -ascii
            save hippocampus_data_flow hippocampus_data -ascii
            save hypothalamus_data_flow_rois hypothalamus_data -ascii
            save nuclei_data_flow_rois nuclei_data -ascii
        else
            save coefficients_filtered_hippocampus_area_flow coefficients_filtered -ascii
            save hippocampus_data_flow hippocampus_data -ascii
            save hypothalamus_data_rois hypothalamus_data -ascii
            save nuclei_data_rois nuclei_data -ascii
        end
    end

   cd ('C:\Users\aborges\Documents\MATLAB\Ejecucion_glucose_admin_difu')
end
```

4. Diffusion 3d

```
function [coefficients]=diffusion_3d(sequence,x,y,Rx,Ry,d1,d2,d3,coordinates_128,ajuste)
%This function specifies the area of analyses, the b parameters, and calls the fitting
functions


%The coordinates_128 file has 'x values' in the second column and 'y'in the first

if sequence==4||sequence==6||sequence==8
    b_values=[18;40;71;112;165;217;318;420;623];
else
    b_values=[320;422;626;930;1234;1538;1634;1841;2043];
end

n=128;m=128;
rx=Rx*n/21; ry=Ry*m/21;
xcentre=x*n/21;ycentre=y*m/21;
char(double(ajuste));
char(ajuste)
tf=strcmp(ajuste,'biexp');

fila_min=ycentre-ry;columna_min=xcentre-rx;
fila_max=ycentre+ry;columna_max=xcentre+rx;
l_min=floor(fila_min-1)*128+floor(columna_min);
l_max=ceil(fila_max-1)*128+ceil(columna_max);
k=0;
%we defiend l_min y l_max likwise because we are going to evaluate d1,d2,d3 files, which
have,first, the 128 values from the first imaging row, below the 128 from the first row…
for i=l_min:l_max
     r1=((xcentre-coordinates_128(i,2))^2)^0.5;%
```

```
     r2=((ycentre-coordinates_128(i,1))^2)^0.5;
     if r1<rx && r2<ry
         k=k+1;
         roi_pixel=[coordinates_128(i,1),coordinates_128(i,2)];
         if tf==1
         coefficients_results
=single_nonlinear_fitting_3d_r08(sequence,b_values,d1(i,1:9),d2(i,1:9),d3(i,1:9));
         else
         coefficients_results
=single_monoexponential_fitting_3d_r08(sequence,b_values,d1(i,1:9),d2(i,1:9),d3(i,1:9));
         end
         coefficients(k,:)=[roi_pixel coefficients_results];%The  coefficients files has 'x'
in the second column and y in the first.
         end
end
end
```

5. Single nonlinear fitting r08

```
function [results,phases]=single_nonlinear_fitting_3d_r08(sequence,b_values,d1,d2,d3)
%This function proceeds to fit non-linearly the diffusion data

switch sequence
    case {(4),(6),(8)}
    options=fitoptions('Normalize','off','method','NonlinearLeastSquares','display','off','
    startpoint',[0.5 0.0015 0.005],'upper',[1 0.005 0.05],'lower',[0 0
    0],'algorithm','Trust-Region','TolFun',10^-7,'TolX',10^-7);

    case{(5),(7),(9)}
    options=fitoptions('Normalize','off','method','NonlinearLeastSquares','display','off','
    startpoint',[0.5 0.0005 0.0015],'upper',[1 0.001 0.005],'lower',[0 0
    0],'algorithm','Trust-Region','TolFun',10^-7,'TolX',10^-7);
end

s=fittype('A*exp(-x*dslow)+(1-A)*exp(-
*dfast)','coefficients',{'A','dslow','dfast'},'options',options);

    [c1,min_percent,max_percent,phase1]=fitting(sequence,b_values,d1',s);

            if (c1(4)>0.75 && c1(2)>10^-5 && c1(3)/c1(2)>1.1 && min_percent>5 &&
max_percent<95)
                result(1:4)=[c1(1,1),c1(1,2)*10^6, c1(1,3)*10^6,c1(1,4)];
                phase(1:3)=[phase1 min_percent max_percent];
            else
                result(1:4)=NaN;
                phase(1:3)=NaN;
            end

    [c2,min_percent2,max_percent2,phase2]=fitting(sequence,b_values,d2',s);

              if (c2(4)>0.75 && c2(2)>10^-5 && c2(3)/c2(2)>1.1 && min_percent2>5 &&
max_percent2<95)
                  result(5:8)=[c2(1,1),c2(1,2)*10^6, c2(1,3)*10^6,c2(1,4)];
                  phase(4:6)=[phase2 min_percent2 max_percent2];
              else
                  result(5:8)=NaN;
                  phase(4:6)=NaN;
              end

    [c3,min_percent3,max_percent3,phase3]=fitting(sequence,b_values,d3',s);

             if (c3(4)>0.75 && c3(2)>10^-5 && c3(3)/c3(2)>1.1 && min_percent3>5 &&
max_percent3<95)
                 result(9:12)=[c3(1,1),c3(1,2)*10^6, c3(1,3)*10^6,c3(1,4)];
                 phase(7:9)=[phase3 min_percent3 max_percent3];
             else
                 result(9:12)=NaN;
                 phase(7:9)=NaN;
             end

 results=result;
```

```
 phases=phase;

end
```

6. Fitting

```
function [c1,min_percent,max_percent,phase]=fitting(sequence,b_values,d,s)
%calls the matlab library that fits the data with the customized conditions

 [fittedmodel1,gof]=fit(b_values,d,s);        % gof is goodness fit
 c1(1,:)=[coeffvalues(fittedmodel1),gof.rsquare];    % coefficient matrix for all pixels
 phase=(1-c1(1))*100/c1(1);

 switch sequence
     case {(5),(7),(9)}
 min_percent=(1-c1(1))/((1-c1(1))+c1(1)*exp((c1(3)-c1(2))*1800))*100;
 max_percent=(1-c1(1))/((1-c1(1))+c1(1)*exp((c1(3)-c1(2))*400))*100;
     case {(4),(6),(8)}
 min_percent=(1-c1(1))/((1-c1(1))+c1(1)*exp((c1(3)-c1(2))*400))*100;
 max_percent=(1-c1(1))/((1-c1(1))+c1(1)*exp((c1(3)-c1(2))*29))*100;
end
```

7. Single monoexponential fitting 3d r08

```
function results=single_monoexponential_fitting_3d_r08(sequence,b_values,d1,d2,d3)
%This function proceeds to fit monoexponentialy the diffusion data
  switch sequence
    case {(4),(6),(8)}
    ptions=fitoptions('Normalize','off','method','NonlinearLeastSquares','display','off','s
    tartpoint', 0.005,'upper',0.01 ,'lower',0 ,'algorithm','Trust-
    Region','MaxIter',600,'MaxFunEvals',600,'TolFun',10^-6,'TolX',10^-6);
    case{(5),(7),(9)}
    options=fitoptions('Normalize','off','method','NonlinearLeastSquares','display','off','
    startpoint', 0.001,'upper', 0.005 ,'lower',0,'algorithm','Trust-
    Region','MaxIter',600,'MaxFunEvals',600,'TolFun',10^-6,'TolX',10^-6);
  end
s=fittype('exp(-x*ADC)','coefficients','ADC','options',options);

    c1=monoexp_fitting(b_values,d1',s);
            if c1(2)>0.8
                result(1:2)=[c1(1,1)*10^6,c1(1,2)];

            else
                result(1:2)=NaN;

            end
    c2=monoexp_fitting(b_values,d2',s);
               if c2(2)>0.8
                   result(3:4)=[c2(1,1)*10^6,c2(1,2)];
               else
                   result(3:4)=NaN;

               end
    c3=monoexp_fitting(b_values,d3',s);
              if  c3(2)>0.8
                  result(5:6)=[c3(1,1)*10^6,c3(1,2)];

              else
                  result(5:6)=NaN;

              end
  results=result;
end
```

8. Monoexp fitting

```
function c1=monoexp_fitting(b_values,d,s)
 [fittedmodel1,gof]=fit(b_values,d,s);        % gof is goodness fit
 c1(1,:)=[coeffvalues(fittedmodel1),gof.rsquare];    % coefficient matrix for all pixels end
```

9. Filtering mono

```
    %This function filters the data with NAN values
function [results_filtered]=filtering_mono(results)

dimen1=size(results(:,1),1);
dimen2=size(results(1,:),2);
j=0;
    for  i=1:dimen1
        x=isnan(results(i,3:dimen2));
        if x==1;
        else
        j=j+1;
        results_filtered(j,:)=results(i,:);
        end
    end
end
```

10. Hypothalamus grouping

```
function [hypothalamus_data,Nuclei_data]=hypothalamus_grouping(coefficients,animal,state)
%This function identifies the hypothalamic and subhypothalamic regions for all animals


cd('C:\Users\Blanca\Documents\MATLAB\Glucose_admin_difu')
%reading of coordinates

switch animal
  case(5)
            cd('5\E4')
  case(6)
            cd('6\E4')
  case(7)
            cd('7\E4')
  case (8)
            cd('8\E4')
  case (9)
            cd('9\E4')
  case (10)
            cd('10\E4')
  case (11)
            cd('11\E4')
  case (100)
            cd('1_saline\E4')
  case (200)
            cd('2_saline\E4')
  case (300)
            cd('3_saline\E4')
  case (400)
            cd('4_saline\E4')
end

hypo_coordinates=load('hypothalamic_coordinates.txt');
ventricle_coordinates=load('ventricle.txt','txt');
ARC=load('ARC.txt');
LDM=load('Left DM.txt');LVM=load('Left VM.txt');
RDM=load('Right DM.txt');RVM=load('Right VM.txt');
LH=load('Lateral H.txt');

s_coef=size(coefficients(:,1));
s_hypo=size(hypo_coordinates(:,1));
s_ven=size(ventricle_coordinates(:,1));
s_ARC=size(ARC(:,1),1);one=ones(s_ARC,1);
s_LDM=size(LDM(:,1),1);two=ones(s_LDM,1)+1;
s_LVM=size(LVM(:,1),1);three=ones(s_LVM,1)+2;
s_RDM=size(RDM(:,1),1);four=ones(s_RDM,1)+3;
s_RVM=size(RVM(:,1),1);five=ones(s_RVM,1)+4;
s_LH=size(LH(:,1),1);six=ones(s_LH,1)+5;
DM_Nuclei=[two LDM ;four RDM]; VM_Nuclei=[three LVM;five RVM];
Nuclei=[one ARC;DM_Nuclei;VM_Nuclei;six LH];
```

```
%sleccion de area hipotalamo
hypothalamus_coord=[hypo_coordinates(:,1)+ones(s_hypo,1),hypo_coordinates(:,2)+ones(s_hypo,1
)];
ventricle_coord=[ventricle_coordinates(:,1)+ones(s_ven,1),ventricle_coordinates(:,2)+ones(s_
ven,1)];
hypothalamus_nv=setdiff(hypothalamus_coord(:,1:2),ventricle_coord(:,1:2),'rows');
s_hypo_nv=size(hypothalamus_nv(:,1),1);
s_column=size(coefficients(1,:),2);

n=0;
l=0;
for i=1:s_hypo_nv
     for j=1:s_coef
        if coefficients(j,1)==hypothalamus_nv(i,2) &&
coefficients(j,2)==hypothalamus_nv(i,1)
          l=l+1;
          hypothalamus_data(l,:)=[animal state hypothalamus_nv(i,1:2)
coefficients(j,3:s_column)];

        end
     end
end
%In the identification of the hypothalamic coordinates, I change the order of columns 1 and
%2 because the coefficients file has 'x' in the second column and y in the first, while in
files coming from Image J this is in the opposite order.

% nuclei selection
 ll=0;
 s_hypo_data=size(hypothalamus_data(:,1),1);
 for n=1:size(Nuclei(:,1),1)
          for m=1:s_hypo_data
                if Nuclei(n,2)+1==hypothalamus_data(m,3) &&
Nuclei(n,3)+1==hypothalamus_data(m,4)
                ll=ll+1;
                Nuclei_data(ll,:)=[Nuclei(n,1) hypothalamus_data(m,:)];
                end
          end
 end
 cd('C:\Users\Blanca\Documents\MATLAB\Ejecucion_Glucose_admin_difu')
end
```

11. Hippocampus grouping

```
function [hypocampus_data]=hippocampus_grouping(coefficients,animal,state)
%This function identifies the hippocampal regions for all animals


cd('C:\Users\aborges\Documents\MATLAB\Glucose_admin_difu')
%reading of coordinates

switch animal
  case(5)
            cd('5\E4')
  case(6)
            cd('6\E4')
  case(7)
            cd('7\E4')
  case (8)
            cd('8\E4')
  case (9)
            cd('9\E4')
  case (10)
            cd('10\E4')
  case (11)
            cd('11\E4')
  case (100)
            cd('1_saline\E4')
  case (200)
            cd('2_saline\E4')
```

```
  case (300)
            cd('3_saline\E4')
  case (400)
            cd('4_saline\E4')
  end
s_coef=size(coefficients(:,1));
s_column=size(coefficients(1,:),2);
hypocampus_coordinates=load('hippocampus_coordinates.txt');s_hypocampus=size(hypocampus_coor
dinates(:,1));
hypocampus_coord=[hypocampus_coordinates(:,1)+ones(s_hypocampus,1),hypocampus_coordinates(:,
2)+ones(s_hypocampus,1)];
llll=0;
for i=1:s_hypocampus
    for j=1:s_coef
       if coefficients(j,1)==hypocampus_coord(i,2)&&
coefficients(j,2)==hypocampus_coord(i,1)
           llll=llll+1;
           hippocampus_data(llll,:)=[animal state hippocampus_coord(i,1:2)
coefficients(j,3:s_column)];
       end
    end
end
cd('C:\Users\aborges\Documents\MATLAB\Ejecucion_Glucose_admin_difu')
end
```

12. Results folders

```
    %This function creates folders to save the new data
cd('C:\Users\aborges\Documents\MATLAB\Glucose_admin_difu')
switch animal
     case (5)
        mkdir('5_biexp_results_tol7');cd('5_biexp_results_tol7');
        if state==0
            mkdir('basal');cd('basal');
        end
        if state==1
            mkdir('glucose');cd('glucose');
        end
        if state==2
            mkdir('recovery');cd('recovery');
        end
     case (6)
        mkdir('6_biexp_results_tol7');cd('6_biexp_results_tol7');
        if state==0
            mkdir('basal');cd('basal');
        end
        if state==1
            mkdir('glucose');cd('glucose');
        end
        if state==2
            mkdir('recovery');cd('recovery');
        end
     case (7)
        mkdir('7_biexp_results_tol7');cd('7_biexp_results_tol7');
        if state==0
            mkdir('basal');cd('basal');
        end
        if state==1
            mkdir('glucose');cd('glucose');
        end
        if state==2
            mkdir('recovery');cd('recovery');
        end
     case (8)
        mkdir('8_biexp_results_tol7');cd('8_biexp_results_tol7');
        if state==0
            mkdir('basal');cd('basal');
        end
        if state==1
            mkdir('glucose');cd('glucose');
```

```
    end
    if state==2
        mkdir('recovery');cd('recovery');
    end
 case (9)
    mkdir('9_biexp_results_tol7');cd('9_biexp_results_tol7');
    if state==0
        mkdir('basal');cd('basal');
    end
    if state==1
        mkdir('glucose');cd('glucose');
    end
    if state==2
        mkdir('recovery');cd('recovery');
    end
case (10)
    mkdir('10_biexp_results_tol7');cd('10_biexp_results_tol7');
    if state==0
        mkdir('basal');cd('basal');
    end
    if state==1
        mkdir('glucose');cd('glucose');
    end
    if state==2
        mkdir('recovery');cd('recovery');
    end
case (11)
    mkdir('11_biexp_results_tol7');cd('11_biexp_results_tol7');
    if state==0
        mkdir('basal');cd('basal');
    end
    if state==1
        mkdir('glucose');cd('glucose');
    end
    if state==2
        mkdir('recovery');cd('recovery');
    end
 case (100)
    mkdir('1_saline_biexp_results_tol7');cd('1_saline_biexp_results_tol7');
    if state==0
        mkdir('basal');cd('basal');
    end
    if state==1
        mkdir('glucose');cd('glucose');
    end
    if state==2
        mkdir('recovery');cd('recovery');
    end
 case (200)
    mkdir('2_saline_biexp_results_tol7');cd('2_saline_biexp_results_tol7');
    if state==0
        mkdir('basal');cd('basal');
    end
    if state==1
        mkdir('glucose');cd('glucose');
    end
    if state==2
        mkdir('recovery');cd('recovery');
    end
 case (300)
    mkdir('3_saline_biexp_results_tol7');cd('3_saline_biexp_results_tol7');
    if state==0
        mkdir('basal');cd('basal');
    end
    if state==1
        mkdir('glucose');cd('glucose');
    end
    if state==2
        mkdir('recovery');cd('recovery');
    end
  case (400)
```

```
        mkdir('4_saline_biexp_results_tol7');cd('4_saline_biexp_results_tol7');
        if state==0
            mkdir('basal');cd('basal');
        end
        if state==1
            mkdir('glucose');cd('glucose');
        end
        if state==2
            mkdir('recovery');cd('recovery');
        end
end
```

13. Results folders monoexp

```
%This function creates folders to save the new monoexponential data

cd('C:\Users\aborges\Documents\MATLAB\Glucose_admin_difu')
switch animal
     case (5)
        mkdir('5_monoexp_results');cd('5_monoexp_results');
        if state==0
            mkdir('basal');cd('basal');
        end
        if state==1
            mkdir('glucose');cd('glucose');
        end
        if state==2
            mkdir('recovery');cd('recovery');
        end
     case (6)
        mkdir('6_monoexp_results');cd('6_monoexp_results');
        if state==0
            mkdir('basal');cd('basal');
        end
        if state==1
            mkdir('glucose');cd('glucose');
        end
        if state==2
            mkdir('recovery');cd('recovery');
        end
     case (7)
        mkdir('7_monoexp_results');cd('7_monoexp_results');
        if state==0
            mkdir('basal');cd('basal');
        end
        if state==1
            mkdir('glucose');cd('glucose');
        end
        if state==2
            mkdir('recovery');cd('recovery');
        end
     case (8)
        mkdir('8_monoexp_results');cd('8_monoexp_results');
        if state==0
            mkdir('basal');cd('basal');
        end
        if state==1
            mkdir('glucose');cd('glucose');
        end
        if state==2
            mkdir('recovery');cd('recovery');
        end
     case (9)
        mkdir('9_monoexp_results');cd('9_monoexp_results');
        if state==0
            mkdir('basal');cd('basal');
        end
        if state==1
            mkdir('glucose');cd('glucose');
        end
```

```
        if state==2
            mkdir('recovery');cd('recovery');
        end
    case (10)
        mkdir('10_monoexp_results');cd('10_monoexp_results');
        if state==0
            mkdir('basal');cd('basal');
        end
        if state==1
            mkdir('glucose');cd('glucose');
        end
        if state==2
            mkdir('recovery');cd('recovery');
        end
    case (11)
        mkdir('11_monoexp_results');cd('11_monoexp_results');
        if state==0
            mkdir('basal');cd('basal');
        end
        if state==1
            mkdir('glucose');cd('glucose');
        end
        if state==2
            mkdir('recovery');cd('recovery');
        end
    case (100)
        mkdir('1_saline_monoexp_results');cd('1_saline_monoexp_results');
        if state==0
            mkdir('basal');cd('basal');
        end
        if state==1
            mkdir('glucose');cd('glucose');
        end
        if state==2
            mkdir('recovery');cd('recovery');
        end
    case (200)
        mkdir('2_saline_monoexp_results');cd('2_saline_monoexp_results');
        if state==0
            mkdir('basal');cd('basal');
        end
        if state==1
            mkdir('glucose');cd('glucose');
        end
        if state==2
            mkdir('recovery');cd('recovery');
        end
    case (300)
        mkdir('3_saline_monoexp_results');cd('3_saline_monoexp_results');
        if state==0
            mkdir('basal');cd('basal');
        end
        if state==1
            mkdir('glucose');cd('glucose');
        end
        if state==2
            mkdir('recovery');cd('recovery');
        end
    case (400)
        mkdir('4_saline_monoexp_results');cd('4_saline_monoexp_results');
        if state==0
            mkdir('basal');cd('basal');
        end
        if state==1
            mkdir('glucose');cd('glucose');
        end
        if state==2
            mkdir('recovery');cd('recovery');
        end

end
```

14. All Nuclei

```
%This function groups the nuclei data for all the fed and fasted mice
cd('C:\Users\Blanca\Documents\MATLAB\Glucose_admin_difu\5_biexp_results_tol7\basal')
nucleos=load('nuclei_data_rois','ascii');size2=size(nucleos(:,1),1);unos2=ones(size2,1);
nucleos_flow=load('nuclei_data_flow_rois','ascii');size2f=size(nucleos_flow(:,1),1);unos2f=o
nes(size2f,1);
agrupacion_nucleoss(1:size2,:)=[unos2 nucleos];
agrupacion_nucleoss_flow(1:size2f,:)=[unos2f nucleos_flow];

cd('C:\Users\Blanca\Documents\MATLAB\Glucose_admin_difu\5_biexp_results_tol7\glucose')
nucleos=load('nuclei_data_rois','ascii');size3=size(nucleos(:,1),1);unos3=ones(size3,1);
nucleos_flow=load('nuclei_data_flow_rois','ascii');size3f=size(nucleos_flow(:,1),1);unos3f=o
nes(size3f,1);
old_total_size=size2;new_total_size=size2+size3;
old_total_sizef=size2f;new_total_sizef=size2f+size3f;
agrupacion_nucleoss(old_total_size+1:new_total_size,:)=[unos3 nucleos];
agrupacion_nucleoss_flow(old_total_sizef+1:new_total_sizef,:)=[unos3f nucleos_flow];

cd('C:\Users\Blanca\Documents\MATLAB\Glucose_admin_difu\5_biexp_results_tol7\recovery')
nucleos=load('nuclei_data_rois','ascii');size4=size(nucleos(:,1),1);unos4=ones(size4,1);
nucleos_flow=load('nuclei_data_flow_rois','ascii');size4f=size(nucleos_flow(:,1),1);unos4f=o
nes(size4f,1);
old_total_size=new_total_size;new_total_size=old_total_size+size4;
old_total_sizef=new_total_sizef;new_total_sizef=old_total_sizef+size4f;
agrupacion_nucleoss(old_total_size+1:new_total_size,:)=[unos4 nucleos];
agrupacion_nucleoss_flow(old_total_sizef+1:new_total_sizef,:)=[unos4f nucleos_flow];

cd('C:\Users\Blanca\Documents\MATLAB\Glucose_admin_difu\6_biexp_results_tol7\basal')
nucleos=load('nuclei_data_rois','ascii');size5=size(nucleos(:,1),1);unos5=ones(size5,1);
nucleos_flow=load('nuclei_data_flow_rois','ascii');size5f=size(nucleos_flow(:,1),1);unos5f=o
nes(size5f,1);
old_total_size=new_total_size;new_total_size=old_total_size+size5;
old_total_sizef=new_total_sizef;new_total_sizef=old_total_sizef+size5f;
agrupacion_nucleoss(old_total_size+1:new_total_size,:)=[unos5 nucleos];
agrupacion_nucleoss_flow(old_total_sizef+1:new_total_sizef,:)=[unos5f nucleos_flow];

cd('C:\Users\Blanca\Documents\MATLAB\glucose_admin_difu\6_biexp_results_tol7\glucose')
nucleos=load('nuclei_data_rois','ascii');size6=size(nucleos(:,1),1);unos6=ones(size6,1);
nucleos_flow=load('nuclei_data_flow_rois','ascii');size6f=size(nucleos_flow(:,1),1);unos6f=o
nes(size6f,1);
old_total_size=new_total_size;new_total_size=old_total_size+size6;
old_total_sizef=new_total_sizef;new_total_sizef=old_total_sizef+size6f;
agrupacion_nucleoss(old_total_size+1:new_total_size,:)=[unos6 nucleos];
agrupacion_nucleoss_flow(old_total_sizef+1:new_total_sizef,:)=[unos6f nucleos_flow];

cd('C:\Users\Blanca\Documents\MATLAB\glucose_admin_difu\6_biexp_results_tol7\recovery')
nucleos=load('nuclei_data_rois','ascii');size7=size(nucleos(:,1),1);unos7=ones(size7,1);
nucleos_flow=load('nuclei_data_flow_rois','ascii');size7f=size(nucleos_flow(:,1),1);unos7f=o
nes(size7f,1);
old_total_size=new_total_size;new_total_size=old_total_size+size7;
old_total_sizef=new_total_sizef;new_total_sizef=old_total_sizef+size7f;
agrupacion_nucleoss(old_total_size+1:new_total_size,:)=[unos7 nucleos];
agrupacion_nucleoss_flow(old_total_sizef+1:new_total_sizef,:)=[unos7f nucleos_flow];

cd('C:\Users\Blanca\Documents\MATLAB\Glucose_admin_difu\7_biexp_results_tol7\basal')
nucleos=load('nuclei_data_rois','ascii');size8=size(nucleos(:,1),1);unos8=ones(size8,1);
nucleos_flow=load('nuclei_data_flow_rois','ascii');size8f=size(nucleos_flow(:,1),1);unos8f=o
nes(size8f,1);
old_total_size=new_total_size;new_total_size=old_total_size+size8;
old_total_sizef=new_total_sizef;new_total_sizef=old_total_sizef+size8f;
agrupacion_nucleoss(old_total_size+1:new_total_size,:)=[unos8 nucleos];
agrupacion_nucleoss_flow(old_total_sizef+1:new_total_sizef,:)=[unos8f nucleos_flow];

cd('C:\Users\Blanca\Documents\MATLAB\glucose_admin_difu\7_biexp_results_tol7\glucose')
nucleos=load('nuclei_data_rois','ascii');size9=size(nucleos(:,1),1);unos9=ones(size9,1);
nucleos_flow=load('nuclei_data_flow_rois','ascii');size9f=size(nucleos_flow(:,1),1);unos9f=o
nes(size9f,1);
old_total_size=new_total_size;new_total_size=old_total_size+size9;
old_total_sizef=new_total_sizef;new_total_sizef=old_total_sizef+size9f;
agrupacion_nucleoss(old_total_size+1:new_total_size,:)=[unos9 nucleos];
```

```
agrupacion_nucleoss_flow(old_total_sizef+1:new_total_sizef,:)=[unos9f nucleos_flow];

cd('C:\Users\Blanca\Documents\MATLAB\glucose_admin_difu\7_biexp_results_tol7\recovery')
nucleos=load('nuclei_data_rois','ascii');size10=size(nucleos(:,1),1);unos10=ones(size10,1);
nucleos_flow=load('nuclei_data_flow_rois','ascii');size10f=size(nucleos_flow(:,1),1);unos10f
=ones(size10f,1);
old_total_size=new_total_size;new_total_size=old_total_size+size10;
old_total_sizef=new_total_sizef;new_total_sizef=old_total_sizef+size10f;
agrupacion_nucleoss(old_total_size+1:new_total_size,:)=[unos10 nucleos];
agrupacion_nucleoss_flow(old_total_sizef+1:new_total_sizef,:)=[unos10f nucleos_flow];

%%%%%%%%%%%%%%%%
cd('C:\Users\Blanca\Documents\MATLAB\Glucose_admin_difu\8_biexp_results_tol7\basal')
nucleos=load('nuclei_data_rois','ascii');size11=size(nucleos(:,1),1);unos11=ones(size11,1);
nucleos_flow=load('nuclei_data_flow_rois','ascii');size11f=size(nucleos_flow(:,1),1);unos11f
=ones(size11f,1);
old_total_size=new_total_size;new_total_size=old_total_size+size11;
old_total_sizef=new_total_sizef;new_total_sizef=old_total_sizef+size11f;
agrupacion_nucleoss(old_total_size+1:new_total_size,:)=[unos11 nucleos];
agrupacion_nucleoss_flow(old_total_sizef+1:new_total_sizef,:)=[unos11f nucleos_flow];

cd('C:\Users\Blanca\Documents\MATLAB\glucose_admin_difu\8_biexp_results_tol7\glucose')
nucleos=load('nuclei_data_rois','ascii');size12=size(nucleos(:,1),1);unos12=ones(size12,1);
nucleos_flow=load('nuclei_data_flow_rois','ascii');size12f=size(nucleos_flow(:,1),1);unos12f
=ones(size12f,1);
old_total_size=new_total_size;new_total_size=old_total_size+size12;
old_total_sizef=new_total_sizef;new_total_sizef=old_total_sizef+size12f;
agrupacion_nucleoss(old_total_size+1:new_total_size,:)=[unos12 nucleos];
agrupacion_nucleoss_flow(old_total_sizef+1:new_total_sizef,:)=[unos12f nucleos_flow];

cd('C:\Users\Blanca\Documents\MATLAB\glucose_admin_difu\8_biexp_results_tol7\recovery')
nucleos=load('nuclei_data_rois','ascii');size13=size(nucleos(:,1),1);unos13=ones(size13,1);
nucleos_flow=load('nuclei_data_flow_rois','ascii');size13f=size(nucleos_flow(:,1),1);unos13f
=ones(size13f,1);
old_total_size=new_total_size;new_total_size=old_total_size+size13;
old_total_sizef=new_total_sizef;new_total_sizef=old_total_sizef+size13f;
agrupacion_nucleoss(old_total_size+1:new_total_size,:)=[unos13 nucleos];
agrupacion_nucleoss_flow(old_total_sizef+1:new_total_sizef,:)=[unos13f nucleos_flow];

%%%%%%%%%%%%%%%%
cd('C:\Users\Blanca\Documents\MATLAB\Glucose_admin_difu\9_biexp_results_tol7\basal')
nucleos=load('nuclei_data_rois','ascii');size14=size(nucleos(:,1),1);unos14=ones(size14,1);
nucleos_flow=load('nuclei_data_flow_rois','ascii');size14f=size(nucleos_flow(:,1),1);unos14f
=ones(size14f,1);
old_total_size=new_total_size;new_total_size=old_total_size+size14;
old_total_sizef=new_total_sizef;new_total_sizef=old_total_sizef+size14f;
agrupacion_nucleoss(old_total_size+1:new_total_size,:)=[unos14 nucleos];
agrupacion_nucleoss_flow(old_total_sizef+1:new_total_sizef,:)=[unos14f nucleos_flow];

cd('C:\Users\Blanca\Documents\MATLAB\glucose_admin_difu\9_biexp_results_tol7\glucose')
nucleos=load('nuclei_data_rois','ascii');size15=size(nucleos(:,1),1);unos15=ones(size15,1);
nucleos_flow=load('nuclei_data_flow_rois','ascii');size15f=size(nucleos_flow(:,1),1);unos15f
=ones(size15f,1);
old_total_size=new_total_size;new_total_size=old_total_size+size15;
old_total_sizef=new_total_sizef;new_total_sizef=old_total_sizef+size15f;
agrupacion_nucleoss(old_total_size+1:new_total_size,:)=[unos15 nucleos];
agrupacion_nucleoss_flow(old_total_sizef+1:new_total_sizef,:)=[unos15f nucleos_flow];

cd('C:\Users\Blanca\Documents\MATLAB\glucose_admin_difu\9_biexp_results_tol7\recovery')
nucleos=load('nuclei_data_rois','ascii');size16=size(nucleos(:,1),1);unos16=ones(size16,1);
nucleos_flow=load('nuclei_data_flow_rois','ascii');size16f=size(nucleos_flow(:,1),1);unos16f
=ones(size16f,1);
old_total_size=new_total_size;new_total_size=old_total_size+size16;
old_total_sizef=new_total_sizef;new_total_sizef=old_total_sizef+size16f;
agrupacion_nucleoss(old_total_size+1:new_total_size,:)=[unos16 nucleos];
agrupacion_nucleoss_flow(old_total_sizef+1:new_total_sizef,:)=[unos16f nucleos_flow];

%%%%%%%%%%%%%%%%%%%%%%%%%%
cd('C:\Users\Blanca\Documents\MATLAB\Glucose_admin_difu\10_biexp_results_tol7\basal')
nucleos=load('nuclei_data_rois','ascii');size17=size(nucleos(:,1),1);unos17=ones(size17,1);
```

```
nucleos_flow=load('nuclei_data_flow_rois','ascii');size17f=size(nucleos_flow(:,1),1);unos17f
=ones(size17f,1);
old_total_size=new_total_size;new_total_size=old_total_size+size17;
old_total_sizef=new_total_sizef;new_total_sizef=old_total_sizef+size16f;
agrupacion_nucleoss(old_total_size+1:new_total_size,:)=[unos17 nucleos];
agrupacion_nucleoss_flow(old_total_sizef+1:new_total_sizef,:)=[unos16f nucleos_flow];

cd('C:\Users\Blanca\Documents\MATLAB\Glucose_admin_difu\10_biexp_results_tol7\glucose')
nucleos=load('nuclei_data_rois','ascii');size3=size(nucleos(:,1),1);unos3=ones(size3,1);
nucleos_flow=load('nuclei_data_flow_rois','ascii');size3f=size(nucleos_flow(:,1),1);unos3f=o
nes(size3f,1);
old_total_size=size2;new_total_size=size2+size3;
old_total_sizef=size2f;new_total_sizef=size2f+size3f;
agrupacion_nucleoss(old_total_size+1:new_total_size,:)=[unos3 nucleos];
agrupacion_nucleoss_flow(old_total_sizef+1:new_total_sizef,:)=[unos3f nucleos_flow];

cd('C:\Users\Blanca\Documents\MATLAB\Glucose_admin_difu\10_biexp_results_tol7\recovery')
nucleos=load('nuclei_data_rois','ascii');size4=size(nucleos(:,1),1);unos4=ones(size4,1);
nucleos_flow=load('nuclei_data_flow_rois','ascii');size4f=size(nucleos_flow(:,1),1);unos4f=o
nes(size4f,1);
old_total_size=new_total_size;new_total_size=old_total_size+size4;
old_total_sizef=new_total_sizef;new_total_sizef=old_total_sizef+size4f;
agrupacion_nucleoss(old_total_size+1:new_total_size,:)=[unos4 nucleos];
agrupacion_nucleoss_flow(old_total_sizef+1:new_total_sizef,:)=[unos4f nucleos_flow];

cd('C:\Users\Blanca\Documents\MATLAB\Glucose_admin_difu\11_biexp_results_tol7\basal')
nucleos=load('nuclei_data_rois','ascii');size5=size(nucleos(:,1),1);unos5=ones(size5,1);
nucleos_flow=load('nuclei_data_flow_rois','ascii');size5f=size(nucleos_flow(:,1),1);unos5f=o
nes(size5f,1);
old_total_size=new_total_size;new_total_size=old_total_size+size5;
old_total_sizef=new_total_sizef;new_total_sizef=old_total_sizef+size5f;
agrupacion_nucleoss(old_total_size+1:new_total_size,:)=[unos5 nucleos];
agrupacion_nucleoss_flow(old_total_sizef+1:new_total_sizef,:)=[unos5f nucleos_flow];

cd('C:\Users\Blanca\Documents\MATLAB\glucose_admin_difu\11_biexp_results_tol7\glucose')
nucleos=load('nuclei_data_rois','ascii');size6=size(nucleos(:,1),1);unos6=ones(size6,1);
nucleos_flow=load('nuclei_data_flow_rois','ascii');size6f=size(nucleos_flow(:,1),1);unos6f=o
nes(size6f,1);
old_total_size=new_total_size;new_total_size=old_total_size+size6;
old_total_sizef=new_total_sizef;new_total_sizef=old_total_sizef+size6f;
agrupacion_nucleoss(old_total_size+1:new_total_size,:)=[unos6 nucleos];
agrupacion_nucleoss_flow(old_total_sizef+1:new_total_sizef,:)=[unos6f nucleos_flow];

cd('C:\Users\Blanca\Documents\MATLAB\glucose_admin_difu\11_biexp_results_tol7\recovery')
nucleos=load('nuclei_data_rois','ascii');size7=size(nucleos(:,1),1);unos7=ones(size7,1);
nucleos_flow=load('nuclei_data_flow_rois','ascii');size7f=size(nucleos_flow(:,1),1);unos7f=o
nes(size7f,1);
old_total_size=new_total_size;new_total_size=old_total_size+size7;
old_total_sizef=new_total_sizef;new_total_sizef=old_total_sizef+size7f;
agrupacion_nucleoss(old_total_size+1:new_total_size,:)=[unos7 nucleos];
agrupacion_nucleoss_flow(old_total_sizef+1:new_total_sizef,:)=[unos7f nucleos_flow];

cd('C:\Users\Blanca\Documents\MATLAB\Glucose_admin_difu')

save agrupacion_nucleos_biexp_tol7 agrupacion_nucleoss -ascii
save agrupacion_nucleos_flow_biexp_tol7  agrupacion_nucleoss_flow -ascii

clear all
```

III. Glucose Effects T2*W Analyses

1. Analysis

```
%In this function, the pathways to the of the animal's data to analyze are entered ("var"),
as well as the pathways of the same animal in the basal state ("basal_var") because the
coordinates of the ROIS are stored in the basal state file. Afterwards, the signal change
analyses function are called, and information concerning the state of the animal (basal,
glucose or recovery), image coordinates of the data to analyze (center and ratio), and
diffusion model must be given.

var='C:\Users\aborges\Documents\MATLAB\Glucose_admin_BOLD\5\basal';
basal_var='C:\Users\aborges\Documents\MATLAB\Glucose_admin_BOLD\5\basal';

%"signal_change_T2_star_with_paths_3parts_normalized_to_maximum(data to analyze,basal_state
of the data to anayze,animal,condition,x,y,Rx,Ry)"
signal_change_T2_star_with_paths_3parts_normalized_to_maximum(var,basal_var,
5,0,10,7.8,5,2.25);
clear all

var='C:\Users\aborges\Documents\MATLAB\Glucose_admin_BOLD\5\glucose';
basal_var='C:\Users\aborges\Documents\MATLAB\Glucose_admin_BOLD\5\basal';
signal_change_T2_star_with_paths_3parts_normalized_to_maximum(var,basal_var,
5,1,10,7.8,5,2.25);
clear all

var='C:\Users\aborges\Documents\MATLAB\Glucose_admin_BOLD\5\recovery';
basal_var='C:\Users\aborges\Documents\MATLAB\Glucose_admin_BOLD\5\basal';
signal_change_T2_star_with_paths_3parts_normalized_to_maximum(var,basal_var,
5,2,9.8,7.8,5,2.25);
clear all
```

2. Signal change T2 star with 3parts normalized to maximum

```
function signal_change_T2_star_with_paths_3parts_normalized_to_maximum(var,basal_var,
animal,state,xc,yc,Rx,Ry)
%this function reads the data from all scans, normalizes it to the maximum values (inside
the brain), divides each condition in three parts, calls the function to eliminate those
pixels with high variaibility, calls to the area selection and stores the data.

coordinates_128=load('coordinates_128','txt');
directorio=dir(var);
cd(var);
s_directorio=size(directorio(:,1),1);

%brain coordinates
rx=Rx*128/21; ry=Ry*128/21;
xcentre=xc*128/21;ycentre=yc*128/21;
fila_min=ycentre-ry;columna_min=xcentre-rx;
fila_max=ycentre+ry;columna_max=xcentre+rx;
l_min=floor(columna_min-1)*128+floor(fila_min);
l_max=ceil(columna_max-1)*128+ceil(fila_max);

%reading of scans(the first two columns from the directory are empty, that's why we start
with 3.if state=0 directory 3 corresponds to scan 10,because it is written in alphabetical
order. We will rectify this for the calculations when necessary
for i=3:s_directorio
    cd(directorio(i).name)
    scan(:,:)=dicomread('MRIm2');
    reshaped_scan=double(reshape(scan,1,16384))';

%determination of the brain vector
    k=0;
     for j=l_min:l_max
```

```
     r1=((xcentre-coordinates_128(j,1))^2)^0.5;%
     r2=((ycentre-coordinates_128(j,2))^2)^0.5;
%coordinates puts in column 1 the indication of the column (x), and in column 2 the row
indication(y), to agree the reshaped_scan file.
        if r1<rx && r2<ry
         k=k+1;
         brain_vector(k)=reshaped_scan(j);
         brain_vector_with_coordinates(k,:)=[coordinates_128(j,1:2) reshaped_scan(j)];
        end
     end
    max_value(i-2)=max(brain_vector);
    max_value_coord(i-
2,:)=brain_vector_with_coordinates(brain_vector_with_coordinates(:,3)==max_value(i-2),:);
    all_scans_matrix(:,i-2)=reshaped_scan;
    all_scans_matrix_normalized(:,i-2)=reshaped_scan/max_value(i-2);
    cd(var)
end

%identification of the coordinates in all scans and order of scans for the basal state
k=0;
if state==0;
    scans_with_coord(:,:)=[coordinates_128 all_scans_matrix_normalized(:,13:s_directorio-2)
all_scans_matrix_normalized(:,1:12)];

%now files are organized by adquisition time (before they were in alphabetical order, 10
first to 21,afterwards from 4 to 9)
else
    scans_with_coord(:,:)=[coordinates_128 all_scans_matrix_normalized(:,1:s_directorio-2)];
end

%scan_with_coord contains the info from 18 scans, each column is one scan containing 16384
%rows

%division in 3 parts
first_half_scans(:,:)=scans_with_coord(:,3:8);
second_half_scans(:,:)=scans_with_coord(:,9:14);
third_half_scans(:,:)=scans_with_coord(:,15:20);

%with coordinates
first_half_scans_coordinates(:,:)=[coordinates_128(:,:) first_half_scans(:,:)];
second_half_scans_coordinates(:,:)=[coordinates_128(:,:) second_half_scans(:,:)];
third_half_scans_coordinates(:,:)=[coordinates_128(:,:) third_half_scans(:,:)];
cd('C:\Users\aborges\Documents\MATLAB\Ejecucion_glucose_admin_BOLD')

%mean between scans
for i=1:16384
mean_scans_part1(i,:)=mean(double(first_half_scans(i,:)));variability1(i,:)=double((first_ha
lf_scans(i,:)-mean_scans_part1(i,:))/mean_scans_part1(i,:));

mean_scans_part2(i,:)=mean(double(second_half_scans(i,:)));variability2(i,:)=double((second_
half_scans(i,:)-mean_scans_part2(i,:))/mean_scans_part2(i,:));

mean_scans_part3(i,:)=mean(double(third_half_scans(i,:)));variability3(i,:)=double((third_ha
lf_scans(i,:)-mean_scans_part3(i,:))/mean_scans_part3(i,:));

    sd_representative_scan_part1(i,:)=std(double(first_half_scans(i,:)));
    sd_representative_scan_part2(i,:)=std(double(second_half_scans(i,:)));
    sd_representative_scan_part3(i,:)=std(double(third_half_scans(i,:)));

%we will eliminate pixeles with variability higher tan the threshold (here the threshold in
15%)

[mean_scans1_corrected(i),first_half_scans_corrected(i,:),variability1_corrected(i,:),std_sc
ans1_corrected(i)]=variabilty_correction(first_half_scans(i,:),abs(variability1(i,:)),0.15);

[mean_scans2_corrected(i),second_half_scans_corrected(i,:),variability2_corrected(i,:),std_s
cans2_corrected(i)]=variabilty_correction(second_half_scans(i,:),abs(variability2(i,:)),0.15
);

[mean_scans3_corrected(i),third_half_scans_corrected(i,:),variability3_corrected(i,:),std_sc
ans3_corrected(i)]=variabilty_correction(third_half_scans(i,:),abs(variability3(i,:)),0.15);
```

```
end

representative_scan_part1(:,:)=[coordinates_128(:,:) mean_scans1_corrected(:)
std_scans1_corrected(:) double(std_scans1_corrected(:)./mean_scans1_corrected(:))*100];
representative_scan_part2(:,:)=[coordinates_128(:,:) mean_scans2_corrected(:)
std_scans2_corrected(:) double(std_scans2_corrected(:)./mean_scans2_corrected(:))*100];
representative_scan_part3(:,:)=[coordinates_128(:,:) mean_scans3_corrected(:)
std_scans3_corrected(:) double(std_scans3_corrected(:)./mean_scans3_corrected(:))*100];


cd('C:\Users\aborges\Documents\MATLAB\Ejecucion_glucose_admin_BOLD')

%hypothaalmus grouping gropus the data from all the areas
switch state
    case (0)
[hypothalamus_data_part1,nuclei_data_part1,ventricle_data_part1,hippocampus_data_part1]=hypo
thalamus_grouping(representative_scan_part1,animal,state,1,basal_var);

[hypothalamus_scans_part1,nuclei_scans_part1,ventricle_scans_part1,hippocampus_scans_part1]=
hypothalamus_grouping(first_half_scans_coordinates,animal,state,1,basal_var);

[hypothalamus_data_part2,nuclei_data_part2,ventricle_data_part2,hippocampus_data_part2]=hypo
thalamus_grouping(representative_scan_part2,animal,state,2,basal_var);

[hypothalamus_scans_part2,nuclei_scans_part2,ventricle_scans_part2,hippocampus_scans_part2]=
hypothalamus_grouping(second_half_scans_coordinates,animal,state,2,basal_var);

[hypothalamus_data_part3,nuclei_data_part3,ventricle_data_part3,hippocampus_data_part3]=hypo
thalamus_grouping(representative_scan_part3,animal,state,3,basal_var);

[hypothalamus_scans_part3,nuclei_scans_part3,ventricle_scans_part3,hippocampus_scans_part3]=
hypothalamus_grouping(third_half_scans_coordinates,animal,state,3,basal_var);

    case (1)
[hypothalamus_data_part1,nuclei_data_part1,ventricle_data_part1,hippocampus_data_part1]=hypo
thalamus_grouping(representative_scan_part1,animal,state,4,basal_var);

[hypothalamus_scans_part1,nuclei_scans_part1,ventricle_scans_part1,hippocampus_scans_part1]=
hypothalamus_grouping(first_half_scans_coordinates,animal,state,4,basal_var);

[hypothalamus_data_part2,nuclei_data_part2,ventricle_data_part2,hippocampus_data_part2]=hypo
thalamus_grouping(representative_scan_part2,animal,state,5,basal_var);

[hypothalamus_scans_part2,nuclei_scans_part2,ventricle_scans_part2,hippocampus_scans_part2]=
hypothalamus_grouping(second_half_scans_coordinates,animal,state,5,basal_var);

[hypothalamus_data_part3,nuclei_data_part3,ventricle_data_part3,hippocampus_data_part3]=hypo
thalamus_grouping(representative_scan_part3,animal,state,6,basal_var);

[hypothalamus_scans_part3,nuclei_scans_part3,ventricle_scans_part3,hippocampus_scans_part3]=
hypothalamus_grouping(third_half_scans_coordinates,animal,state,6,basal_var);

    case (2)
[hypothalamus_data_part1,nuclei_data_part1,ventricle_data_part1,hippocampus_data_part1]=hypo
thalamus_grouping(representative_scan_part1,animal,state,7,basal_var);

[hypothalamus_scans_part1,nuclei_scans_part1,ventricle_scans_part1,hippocampus_scans_part1]=
hypothalamus_grouping(first_half_scans_coordinates,animal,state,7,basal_var);

[hypothalamus_data_part2,nuclei_data_part2,ventricle_data_part2,hippocampus_data_part2]=hypo
thalamus_grouping(representative_scan_part2,animal,state,8,basal_var);

[hypothalamus_scans_part2,nuclei_scans_part2,ventricle_scans_part2,hippocampus_scans_part2]=
hypothalamus_grouping(second_half_scans_coordinates,animal,state,8,basal_var);

[hypothalamus_data_part3,nuclei_data_part3,ventricle_data_part3,hippocampus_data_part3]=hypo
thalamus_grouping(representative_scan_part3,animal,state,9,basal_var);

[hypothalamus_scans_part3,nuclei_scans_part3,ventricle_scans_part3,hippocampus_scans_part3]=
hypothalamus_grouping(third_half_scans_coordinates,animal,state,9,basal_var);
end
```

```
results_folders;

save hypothalamus_mean_T2_star_part1 hypothalamus_data_part1 -ascii
save hippocampus_mean_T2_star_part1 hippocampus_data_part1 -ascii
save nuclei_mean_T2_star_part1 nuclei_data_part1 -ascii
save ventricle_mean_T2_star_part1 ventricle_data_part1 -ascii

save hypothalamus_mean_T2_star_part2 hypothalamus_data_part2 -ascii
save hippocampus_mean_T2_star_part2 hippocampus_data_part2 -ascii
save nuclei_mean_T2_star_part2 nuclei_data_part2 -ascii
save ventricle_mean_T2_star_part2 ventricle_data_part2 -ascii

save hypothalamus_mean_T2_star_part3 hypothalamus_data_part3 -ascii
save hippocampus_mean_T2_star_part3 hippocampus_data_part3 -ascii
save nuclei_mean_T2_star_part3 nuclei_data_part3 -ascii
save ventricle_mean_T2_star_part3 ventricle_data_part3 -ascii
%%%%%%%%%%%%%%%%%%%%%%%%%%%%%%%%%%%%%%%%%%%%%%%%%%%%
save hypothalamus_scans_mean_T2_star_part1 hypothalamus_scans_part1 -ascii
save hippocampus_scans_mean_T2_star_part1 hippocampus_scans_part1 -ascii
save nuclei_scans_mean_T2_star_part1 nuclei_scans_part1 -ascii
save ventricle_scans_mean_T2_star_part1 ventricle_scans_part1 -ascii

save hypothalamus_scans_mean_T2_star_part2 hypothalamus_scans_part2 -ascii
save hippocampus_scans_mean_T2_star_part2 hippocampus_scans_part2 -ascii
save nuclei_scans_mean_T2_star_part2 nuclei_scans_part2 -ascii
save ventricle_scans_mean_T2_star_part2 ventricle_scans_part2 -ascii

save hypothalamus_scans_mean_T2_star_part3 hypothalamus_scans_part3 -ascii
save hippocampus_scans_mean_T2_star_part3 hippocampus_scans_part3 -ascii
save nuclei_scans_mean_T2_star_part3 nuclei_scans_part3 -ascii
save ventricle_scans_mean_T2_star_part3 ventricle_scans_part3 -ascii
cd('C:\Users\aborges\Documents\MATLAB\Ejecucion_glucose_admin_BOLD')
end
```

3. Variability correction

```
function
[mean_corrected,normalized_scans_corrected,variability_corrected,std_corrected]=variabilty_c
orrection(normalized_scans,variability,threshold)
%this function eliminates those pixels with higher variability than the desired threshold

%let's see how many scans we have to evaluate (num. of columns)
s=size(normalized_scans(1,:),2);k=0; kk=0;

%k will indicate the number of scans that have lower variability than the desired threshold
for l=1:s
    if variability(l)<=threshold
        k=k+1;
    end
end
switch k
    case (0)
        normalized_scans_corrected(1:6)=NaN;
        mean_corrected=NaN;
        variability_corrected(1:6)=NaN;
        std_corrected=NaN;
    case (1)
        for l=1:6
            if variability(l)<=threshold
                normalized_scans_corrected(l)=normalized_scans(l);
                non_NaN=normalized_scans(l);
                variability_corrected(l)=0;
            else
                normalized_scans_corrected(l)=NaN;
                variability_corrected(l)=NaN;
            end
        end
```

```
    mean_corrected=non_NaN;
    std_corrected=NaN;
case (2)
    for l=1:6
        if variability(l)<=threshold
            kk=kk+1;
           normalized_scans_corrected(l)=normalized_scans(l);
           non_NaN(kk)=normalized_scans(l);
        else
           normalized_scans_corrected(l)=NaN;
        end
    end
    mean_corrected=mean(non_NaN);
    std_corrected=std(non_NaN);
    variability_corrected(1:2)=double((non_NaN(:)-mean_corrected)/mean_corrected);
    normalized_scans_corrected(3:6)=NaN;
    variability_corrected(3:6)=NaN;
    kk=0;
case (3)
    for l=1:6
        if variability(l)<=threshold
            kk=kk+1;
           normalized_scans_corrected(l)=normalized_scans(l);
           non_NaN(kk)=normalized_scans(l);
        else
           normalized_scans_corrected(l)=NaN;
        end
    end
    mean_corrected=mean(non_NaN);
    std_corrected=std(non_NaN);
    variability_corrected(1:3)=double((non_NaN(:)-mean_corrected)/mean_corrected);
    normalized_scans_corrected(4:6)=NaN;
    variability_corrected(4:6)=NaN;
    kk=0;
case (4)
    for l=1:6
        if variability(l)<=threshold
            kk=kk+1;
           normalized_scans_corrected(l)=normalized_scans(l);
           non_NaN(kk)=normalized_scans(l);
        else
           normalized_scans_corrected(l)=NaN;
        end
    end
    mean_corrected=mean(non_NaN);
    std_corrected=std(non_NaN);
    variability_corrected(1:4)=double((non_NaN(:)-mean_corrected)/mean_corrected);
    normalized_scans_corrected(5:6)=NaN;
    variability_corrected(5:6)=NaN;
    kk=0;
case (5)
    for l=1:6
        if variability(l)<=threshold
            kk=kk+1;
           normalized_scans_corrected(l)=normalized_scans(l);
           non_NaN(kk)=normalized_scans(l);
        else
           normalized_scans_corrected(l)=NaN;
        end
    end
    mean_corrected=mean(non_NaN);
    std_corrected=std(non_NaN);
    variability_corrected(1:5)=double((non_NaN(:)-mean_corrected)/mean_corrected);
    normalized_scans_corrected(6)=NaN;
    variability_corrected(6)=NaN;
    kk=0;
case (6)
    normalized_scans_corrected(1:6)=normalized_scans(1:6);
    mean_corrected=mean(normalized_scans);
    std_corrected=std(normalized_scans);
    variability_corrected(1:6)=variability(1:6);
```

```
end
end
```

4. Hypothalamus grouping

```
function
[hypothalamus_data,Nuclei_data,ventricle_data,hypocampus_data]=hypothalamus_grouping(coeffic
ients,animal,state,part,basal_path)
%This function selects those pixels from the hypothalamus, hippocampus and subhypothalamic
structures

% coordinadates reading
directorio_basal=dir(basal_path);
var_E4=directorio_basal(15).name;
cd(basal_path);
hypocampus_coordinates=load(sprintf('%s\\hypocampus_coordinates.txt',var_E4));s_hypocampus=s
ize(hypocampus_coordinates(:,1));
hypo_coordinates=load(sprintf('%s\\hypothalamic_coordinates.txt',var_E4));%column 1 is 'x',
column 2 is 'y'

ventricle_coordinates=load(sprintf('%s\\ventricle.txt',var_E4));
ARC=load(sprintf('%s\\ARC.txt',var_E4));
LDM=load(sprintf('%s\\Left DM.txt',var_E4));LVM=load(sprintf('%s\\Left VM.txt',var_E4));
RDM=load(sprintf('%s\\Right DM.txt',var_E4));RVM=load(sprintf('%s\\Right VM.txt',var_E4));
LH=load(sprintf('%s\\Lateral H.txt',var_E4));

%files size
s_coef=size(coefficients(:,1));
s_hypo=size(hypo_coordinates(:,1));
s_ven=size(ventricle_coordinates(:,1));
s_ARC=size(ARC(:,1),1);one=ones(s_ARC,1);
s_LDM=size(LDM(:,1),1);two=ones(s_LDM,1)+1;
s_LVM=size(LVM(:,1),1);three=ones(s_LVM,1)+2;
s_RDM=size(RDM(:,1),1);four=ones(s_RDM,1)+3;
s_RVM=size(RVM(:,1),1);five=ones(s_RVM,1)+4;
s_LH=size(LH(:,1),1);six=ones(s_LH,1)+5;
DM_Nuclei=[two LDM ;four RDM]; VM_Nuclei=[three LVM;five RVM];
Nuclei=[one ARC;DM_Nuclei;VM_Nuclei;six LH];

%hypothalamic area selection
hypocampus_coord=[hypocampus_coordinates(:,1)+ones(s_hypocampus,1),hypocampus_coordinates(:,
2)+ones(s_hypocampus,1)];
hypothalamus_coord=[hypo_coordinates(:,1)+ones(s_hypo,1),hypo_coordinates(:,2)+ones(s_hypo,1
)];
ventricle_coord=[ventricle_coordinates(:,1)+ones(s_ven,1),ventricle_coordinates(:,2)+ones(s_
ven,1)];
hypothalamus_nv=setdiff(hypothalamus_coord(:,1:2),ventricle_coord(:,1:2),'rows');
s_hypo_nv=size(hypothalamus_nv(:,1),1);
s_column=size(coefficients(1,:),2);

n=0;
l=0;
for i=1:s_hypo_nv
    for j=1:s_coef
       if coefficients(j,1)==hypothalamus_nv(i,1) && coefficients(j,2)==hypothalamus_nv(i,2)
          l=l+1;
%As usual, hypothalamus has in the first column the "x",info(image column) and in the second
%the "y" info(image row).However, here, "coefficients" also have the info from the columns
in the first column, and the info from the rows in the second. In this situation, we do not
need to reverse the order in the area selection process
          hypothalamus_data(l,:)=[animal state part hypothalamus_nv(i,1:2)
coefficients(j,3:s_column)];

        end
     end
end

%seleccion núcleos
```

```
ll=0;s_hypo_data=size(hypothalamus_data(:,1),1);
for n=1:size(Nuclei(:,1),1)
       for m=1:s_hypo_data
          if Nuclei(n,2)+1==hypothalamus_data(m,4) && Nuclei(n,3)+1==hypothalamus_data(m,5)
                ll=ll+1;
                Nuclei_data(ll,:)=[Nuclei(n,1) hypothalamus_data(m,:)];
          end
       end
 end

lll=0;
%ventricle selection
 for i=1:s_ven
    for j=1:s_coef
       if coefficients(j,1)==ventricle_coord(i,1) && coefficients(j,2)==ventricle_coord(i,2)
         lll=lll+1;
         ventricle_data(lll,:)=[animal state part ventricle_coord(i,1:2)
coefficients(j,3:s_column)];

        end
    end
 end

llll=0;
for i=1:s_hypocampus
   for j=1:s_coef
      if coefficients(j,1)==hypocampus_coord(i,1)&& coefficients(j,2)==hypocampus_coord(i,2)
           llll=llll+1;
           hypocampus_data(llll,:)=[animal state part hypocampus_coord(i,1:2)
coefficients(j,3:s_column)];
      end
   end
end
 cd('C:\Users\aborges\Documents\MATLAB\Ejecucion_glucose_admin_BOLD')
end
```

5. Results folders

```
cd('C:\Users\aborges\Documents\MATLAB\Glucose_admin_BOLD')
switch animal
    case (1)
        mkdir('1_results_signal_change_variab15');cd('1_results_signal_change_variab15');
        if state==0
            mkdir('basal');cd('basal');
        end
        if state==1
            mkdir('glucose');cd('glucose');
        end
        if state==2
            mkdir('recovery');cd('recovery');
        end
     case (2)
        mkdir('2_results_signal_change_variab15');cd('2_results_signal_change_variab15');
        if state==0
            mkdir('basal');cd('basal');
        end
        if state==1
            mkdir('glucose');cd('glucose');
        end
        if state==2
            mkdir('recovery');cd('recovery');
        end
     case (3)
        mkdir('3_results_signal_change_variab15');cd('3_results_signal_change_variab15');
        if state==0
            mkdir('basal');cd('basal');
```

```
    end
    if state==1
        mkdir('glucose');cd('glucose');
    end
    if state==2
        mkdir('recovery');cd('recovery');
    end
case (4)
    mkdir('4_results_signal_change_variab15');cd('4_results_signal_change_variab15');
    if state==0
        mkdir('basal');cd('basal');
    end
    if state==1
        mkdir('glucose');cd('glucose');
    end
    if state==2
        mkdir('recovery');cd('recovery');
    end
case (5)
    mkdir('5_results_signal_change_variab15');cd('5_results_signal_change_variab15');
    if state==0
        mkdir('basal');cd('basal');
    end
    if state==1
        mkdir('glucose');cd('glucose');
    end
    if state==2
        mkdir('recovery');cd('recovery');
    end
case (6)
    mkdir('6_results_signal_change_variab15');cd('6_results_signal_change_variab15');
    if state==0
        mkdir('basal');cd('basal');
    end
    if state==1
        mkdir('glucose');cd('glucose');
    end
    if state==2
        mkdir('recovery');cd('recovery');
    end
case (7)
    mkdir('7_results_signal_change_variab15');cd('7_results_signal_change_variab15');
    if state==0
        mkdir('basal');cd('basal');
    end
    if state==1
        mkdir('glucose');cd('glucose');
    end
    if state==2
        mkdir('recovery');cd('recovery');
    end
case (8)
    mkdir('8_results_signal_change_variab15');cd('8_results_signal_change_variab15');
    if state==0
        mkdir('basal');cd('basal');
    end
    if state==1
        mkdir('glucose');cd('glucose');
    end
    if state==2
        mkdir('recovery');cd('recovery');
    end
case (9)
    mkdir('9_results_signal_change_variab15');cd('9_results_signal_change_variab15');
    if state==0
        mkdir('basal');cd('basal');
    end
    if state==1
        mkdir('glucose');cd('glucose');
    end
    if state==2
```

```
            mkdir('recovery');cd('recovery');
        end
    case (10)
        mkdir('10_results_signal_change_variab15');cd('10_results_signal_change_variab15');
        if state==0
            mkdir('basal');cd('basal');
        end
        if state==1
            mkdir('glucose');cd('glucose');
        end
        if state==2
            mkdir('recovery');cd('recovery');
        end
    case (11)
        mkdir('11_results_signal_change_variab15');cd('11_results_signal_change_variab15');
        if state==0
            mkdir('basal');cd('basal');
        end
        if state==1
            mkdir('glucose');cd('glucose');
        end
        if state==2
            mkdir('recovery');cd('recovery');
        end
    case (100)

mkdir('1_saline_results_signal_change_variab15');cd('1_saline_results_signal_change_variab15
');
        if state==0
            mkdir('basal');cd('basal');
        end
        if state==1
            mkdir('glucose');cd('glucose');
        end
        if state==2
            mkdir('recovery');cd('recovery');
        end
    case (200)

mkdir('2_saline_results_signal_change_variab15');cd('2_saline_results_signal_change_variab15
');
        if state==0
            mkdir('basal');cd('basal');
        end
        if state==1
            mkdir('glucose');cd('glucose');
        end
        if state==2
            mkdir('recovery');cd('recovery');
        end
    case (300)

mkdir('3_saline_results_signal_change_variab15');cd('3_saline_results_signal_change_variab15
');
        if state==0
            mkdir('basal');cd('basal');
        end
        if state==1
            mkdir('glucose');cd('glucose');
        end
        if state==2
            mkdir('recovery');cd('recovery');
        end
    case (400)

mkdir('4_saline_results_signal_change_variab15');cd('4_saline_results_signal_change_variab15
');
        if state==0
            mkdir('basal');cd('basal');
        end
        if state==1
```

```
            mkdir('glucose');cd('glucose');
        end
        if state==2
            mkdir('recovery');cd('recovery');
        end
end
```

6. All nuclei 3 parts

```
cd('C:\Users\aborges\Documents\MATLAB\Glucose_admin_BOLD\5_results_signal_change_variab15\ba
sal')
nuclei1=load('nuclei_mean_T2_star_part1','ascii');size1=size(nuclei1(:,1),1);
nuclei2=load('nuclei_mean_T2_star_part2','ascii');size1b=size(nuclei2(:,1),1);
nuclei3=load('nuclei_mean_T2_star_part3','ascii');size1c=size(nuclei3(:,1),1);sizeN1=size1+s
ize1b+size1c;
hypothalamus1=load('hypothalamus_mean_T2_star_part1','ascii');sizeh1=size(hypothalamus1(:,1)
,1);
hypothalamus2=load('hypothalamus_mean_T2_star_part2','ascii');sizeh1b=size(hypothalamus2(:,1
),1);
hypothalamus3=load('hypothalamus_mean_T2_star_part3','ascii');sizeh1c=size(hypothalamus3(:,1
),1);sizeH1=sizeh1+sizeh1b+sizeh1c;
agrupacion_nucleos(1:sizeN1,:)=[nuclei1;nuclei2;nuclei3];
agrupacion_hipotalamos(1:sizeH1,:)=[hypothalamus1;hypothalamus2;hypothalamus3];

cd('C:\Users\aborges\Documents\MATLAB\Glucose_admin_BOLD\5_results_signal_change_variab15\gl
ucose')
nuclei1=load('nuclei_mean_T2_star_part1','ascii');size2=size(nuclei1(:,1),1);
nuclei2=load('nuclei_mean_T2_star_part2','ascii');size2b=size(nuclei2(:,1),1);
nuclei3=load('nuclei_mean_T2_star_part3','ascii');size2c=size(nuclei3(:,1),1);sizeN2=size2+s
ize2b+size2c;
hypothalamus1=load('hypothalamus_mean_T2_star_part1','ascii');sizeh2=size(hypothalamus1(:,1)
,1);
hypothalamus2=load('hypothalamus_mean_T2_star_part2','ascii');sizeh2b=size(hypothalamus2(:,1
),1);
hypothalamus3=load('hypothalamus_mean_T2_star_part3','ascii');sizeh2c=size(hypothalamus3(:,1
),1);sizeH2=sizeh2+sizeh2b+sizeh2c;
old_total_size=sizeN1;new_total_size=sizeN1+sizeN2;
old_total_sizeH=sizeH1;new_total_sizeH=sizeH1+sizeH2;
agrupacion_nucleos(old_total_size+1:new_total_size,:)=[nuclei1;nuclei2;nuclei3];
agrupacion_hipotalamos(old_total_sizeH+1:new_total_sizeH,:)=[hypothalamus1;hypothalamus2;hyp
othalamus3];

cd('C:\Users\aborges\Documents\MATLAB\Glucose_admin_BOLD\5_results_signal_change_variab15\re
covery')
nuclei1=load('nuclei_mean_T2_star_part1','ascii');size2=size(nuclei1(:,1),1);
nuclei2=load('nuclei_mean_T2_star_part2','ascii');size2b=size(nuclei2(:,1),1);
nuclei3=load('nuclei_mean_T2_star_part3','ascii');size2c=size(nuclei3(:,1),1);sizeN2=size2+s
ize2b+size2c;
hypothalamus1=load('hypothalamus_mean_T2_star_part1','ascii');sizeh2=size(hypothalamus1(:,1)
,1);
hypothalamus2=load('hypothalamus_mean_T2_star_part2','ascii');sizeh2b=size(hypothalamus2(:,1
),1);
hypothalamus3=load('hypothalamus_mean_T2_star_part3','ascii');sizeh2c=size(hypothalamus3(:,1
),1);sizeH2=sizeh2+sizeh2b+sizeh2c;
old_total_size=new_total_size;new_total_size=old_total_size+sizeN2;
old_total_sizeH=new_total_sizeH;new_total_sizeH=old_total_sizeH+sizeH2;
agrupacion_nucleos(old_total_size+1:new_total_size,:)=[nuclei1;nuclei2;nuclei3];
agrupacion_hipotalamos(old_total_sizeH+1:new_total_sizeH,:)=[hypothalamus1;hypothalamus2;hyp
othalamus3];
%%%
```

```
hypothalamus2=load('hypothalamus_mean_T2_star_part2','ascii');sizeh2b=size(hypothalamus2(:,1
),1);
hypothalamus3=load('hypothalamus_mean_T2_star_part3','ascii');sizeh2c=size(hypothalamus3(:,1
),1);sizeH2=sizeh2+sizeh2b+sizeh2c;
old_total_size=new_total_size;new_total_size=old_total_size+sizeN2;
old_total_sizeH=new_total_sizeH;new_total_sizeH=old_total_sizeH+sizeH2;
agrupacion_nucleos(old_total_size+1:new_total_size,:)=[nuclei1;nuclei2;nuclei3];
agrupacion_hipotalamos(old_total_sizeH+1:new_total_sizeH,:)=[hypothalamus1;hypothalamus2;hyp
othalamus3];


cd('C:\Users\aborges\Documents\MATLAB\Glucose_admin_BOLD\6_results_signal_change_variab15\gl
ucose')
nuclei1=load('nuclei_mean_T2_star_part1','ascii');size2=size(nuclei1(:,1),1);
nuclei2=load('nuclei_mean_T2_star_part2','ascii');size2b=size(nuclei2(:,1),1);
nuclei3=load('nuclei_mean_T2_star_part3','ascii');size2c=size(nuclei3(:,1),1);sizeN2=size2+s
ize2b+size2c;
hypothalamus1=load('hypothalamus_mean_T2_star_part1','ascii');sizeh2=size(hypothalamus1(:,1)
,1);
hypothalamus2=load('hypothalamus_mean_T2_star_part2','ascii');sizeh2b=size(hypothalamus2(:,1
),1);
hypothalamus3=load('hypothalamus_mean_T2_star_part3','ascii');sizeh2c=size(hypothalamus3(:,1
),1);sizeH2=sizeh2+sizeh2b+sizeh2c;
old_total_size=new_total_size;new_total_size=old_total_size+sizeN2;
old_total_sizeH=new_total_sizeH;new_total_sizeH=old_total_sizeH+sizeH2;
agrupacion_nucleos(old_total_size+1:new_total_size,:)=[nuclei1;nuclei2;nuclei3];
agrupacion_hipotalamos(old_total_sizeH+1:new_total_sizeH,:)=[hypothalamus1;hypothalamus2;hyp
othalamus3];


cd('C:\Users\aborges\Documents\MATLAB\Glucose_admin_BOLD\6_results_signal_change_variab15\re
covery')
nuclei1=load('nuclei_mean_T2_star_part1','ascii');size2=size(nuclei1(:,1),1);
nuclei2=load('nuclei_mean_T2_star_part2','ascii');size2b=size(nuclei2(:,1),1);
nuclei3=load('nuclei_mean_T2_star_part3','ascii');size2c=size(nuclei3(:,1),1);sizeN2=size2+s
ize2b+size2c;
hypothalamus1=load('hypothalamus_mean_T2_star_part1','ascii');sizeh2=size(hypothalamus1(:,1)
,1);
hypothalamus2=load('hypothalamus_mean_T2_star_part2','ascii');sizeh2b=size(hypothalamus2(:,1
),1);
hypothalamus3=load('hypothalamus_mean_T2_star_part3','ascii');sizeh2c=size(hypothalamus3(:,1
),1);sizeH2=sizeh2+sizeh2b+sizeh2c;
old_total_size=new_total_size;new_total_size=old_total_size+sizeN2;
old_total_sizeH=new_total_sizeH;new_total_sizeH=old_total_sizeH+sizeH2;
agrupacion_nucleos(old_total_size+1:new_total_size,:)=[nuclei1;nuclei2;nuclei3];
agrupacion_hipotalamos(old_total_sizeH+1:new_total_sizeH,:)=[hypothalamus1;hypothalamus2;hyp
othalamus3];
%%%
```

```
nuclei1=load('nuclei_mean_T2_star_part1','ascii');size2=size(nuclei1(:,1),1);
nuclei2=load('nuclei_mean_T2_star_part2','ascii');size2b=size(nuclei2(:,1),1);
nuclei3=load('nuclei_mean_T2_star_part3','ascii');size2c=size(nuclei3(:,1),1);sizeN2=size2+s
ize2b+size2c;
hypothalamus1=load('hypothalamus_mean_T2_star_part1','ascii');sizeh2=size(hypothalamus1(:,1)
,1);
hypothalamus2=load('hypothalamus_mean_T2_star_part2','ascii');sizeh2b=size(hypothalamus2(:,1
),1);
hypothalamus3=load('hypothalamus_mean_T2_star_part3','ascii');sizeh2c=size(hypothalamus3(:,1
),1);sizeH2=sizeh2+sizeh2b+sizeh2c;
old_total_size=new_total_size;new_total_size=old_total_size+sizeN2;
old_total_sizeH=new_total_sizeH;new_total_sizeH=old_total_sizeH+sizeH2;
agrupacion_nucleos(old_total_size+1:new_total_size,:)=[nuclei1;nuclei2;nuclei3];
agrupacion_hipotalamos(old_total_sizeH+1:new_total_sizeH,:)=[hypothalamus1;hypothalamus2;hyp
othalamus3];


cd('C:\Users\aborges\Documents\MATLAB\Glucose_admin_BOLD\7_results_signal_change_variab15\re
covery')
nuclei1=load('nuclei_mean_T2_star_part1','ascii');size2=size(nuclei1(:,1),1);
nuclei2=load('nuclei_mean_T2_star_part2','ascii');size2b=size(nuclei2(:,1),1);
nuclei3=load('nuclei_mean_T2_star_part3','ascii');size2c=size(nuclei3(:,1),1);sizeN2=size2+s
ize2b+size2c;
hypothalamus1=load('hypothalamus_mean_T2_star_part1','ascii');sizeh2=size(hypothalamus1(:,1)
,1);
hypothalamus2=load('hypothalamus_mean_T2_star_part2','ascii');sizeh2b=size(hypothalamus2(:,1
),1);
hypothalamus3=load('hypothalamus_mean_T2_star_part3','ascii');sizeh2c=size(hypothalamus3(:,1
),1);sizeH2=sizeh2+sizeh2b+sizeh2c;
old_total_size=new_total_size;new_total_size=old_total_size+sizeN2;
old_total_sizeH=new_total_sizeH;new_total_sizeH=old_total_sizeH+sizeH2;
agrupacion_nucleos(old_total_size+1:new_total_size,:)=[nuclei1;nuclei2;nuclei3];
agrupacion_hipotalamos(old_total_sizeH+1:new_total_sizeH,:)=[hypothalamus1;hypothalamus2;hyp
othalamus3];
%%%
```

```
agrupacion_hipotalamos(old_total_sizeH+1:new_total_sizeH,:)=[hypothalamus1;hypothalamus2;hyp
othalamus3];

cd('C:\Users\aborges\Documents\MATLAB\Glucose_admin_BOLD\8_results_signal_change_variab15\re
covery')
nuclei1=load('nuclei_mean_T2_star_part1','ascii');size2=size(nuclei1(:,1),1);
nuclei2=load('nuclei_mean_T2_star_part2','ascii');size2b=size(nuclei2(:,1),1);
nuclei3=load('nuclei_mean_T2_star_part3','ascii');size2c=size(nuclei3(:,1),1);sizeN2=size2+s
ize2b+size2c;
hypothalamus1=load('hypothalamus_mean_T2_star_part1','ascii');sizeh2=size(hypothalamus1(:,1)
,1);
hypothalamus2=load('hypothalamus_mean_T2_star_part2','ascii');sizeh2b=size(hypothalamus2(:,1
),1);
hypothalamus3=load('hypothalamus_mean_T2_star_part3','ascii');sizeh2c=size(hypothalamus3(:,1
),1);sizeH2=sizeh2+sizeh2b+sizeh2c;

old_total_size=new_total_size;new_total_size=old_total_size+sizeN2;
old_total_sizeH=new_total_sizeH;new_total_sizeH=old_total_sizeH+sizeH2;
agrupacion_nucleos(old_total_size+1:new_total_size,:)=[nuclei1;nuclei2;nuclei3];
agrupacion_hipotalamos(old_total_sizeH+1:new_total_sizeH,:)=[hypothalamus1;hypothalamus2;hyp
othalamus3];
%%%
```

```
hypothalamus2=load('hypothalamus_mean_T2_star_part2','ascii');sizeh2b=size(hypothalamus2(:,1
),1);
hypothalamus3=load('hypothalamus_mean_T2_star_part3','ascii');sizeh2c=size(hypothalamus3(:,1
),1);sizeH2=sizeh2+sizeh2b+sizeh2c;
old_total_size=new_total_size;new_total_size=old_total_size+sizeN2;
old_total_sizeH=new_total_sizeH;new_total_sizeH=old_total_sizeH+sizeH2;
agrupacion_nucleos(old_total_size+1:new_total_size,:)=[nuclei1;nuclei2;nuclei3];
agrupacion_hipotalamos(old_total_sizeH+1:new_total_sizeH,:)=[hypothalamus1;hypothalamus2;hyp
othalamus3];
%%%
```

```
nuclei1=load('nuclei_mean_T2_star_part1','ascii');size2=size(nuclei1(:,1),1);
nuclei2=load('nuclei_mean_T2_star_part2','ascii');size2b=size(nuclei2(:,1),1);
nuclei3=load('nuclei_mean_T2_star_part3','ascii');size2c=size(nuclei3(:,1),1);sizeN2=size2+s
ize2b+size2c;
hypothalamus1=load('hypothalamus_mean_T2_star_part1','ascii');sizeh2=size(hypothalamus1(:,1)
,1);
hypothalamus2=load('hypothalamus_mean_T2_star_part2','ascii');sizeh2b=size(hypothalamus2(:,1
),1);
hypothalamus3=load('hypothalamus_mean_T2_star_part3','ascii');sizeh2c=size(hypothalamus3(:,1
),1);sizeH2=sizeh2+sizeh2b+sizeh2c;
old_total_size=new_total_size;new_total_size=old_total_size+sizeN2;
old_total_sizeH=new_total_sizeH;new_total_sizeH=old_total_sizeH+sizeH2;
agrupacion_nucleos(old_total_size+1:new_total_size,:)=[nuclei1;nuclei2;nuclei3];
agrupacion_hipotalamos(old_total_sizeH+1:new_total_sizeH,:)=[hypothalamus1;hypothalamus2;hyp
othalamus3];
%
cd('C:\Users\aborges\Documents\MATLAB\Glucose_admin_BOLD\11_results_signal_change_variab15\g
lucose')
nuclei1=load('nuclei_mean_T2_star_part1','ascii');size2=size(nuclei1(:,1),1);
nuclei2=load('nuclei_mean_T2_star_part2','ascii');size2b=size(nuclei2(:,1),1);
nuclei3=load('nuclei_mean_T2_star_part3','ascii');size2c=size(nuclei3(:,1),1);sizeN2=size2+s
ize2b+size2c;
hypothalamus1=load('hypothalamus_mean_T2_star_part1','ascii');sizeh2=size(hypothalamus1(:,1)
,1);
hypothalamus2=load('hypothalamus_mean_T2_star_part2','ascii');sizeh2b=size(hypothalamus2(:,1
),1);
hypothalamus3=load('hypothalamus_mean_T2_star_part3','ascii');sizeh2c=size(hypothalamus3(:,1
),1);sizeH2=sizeh2+sizeh2b+sizeh2c;
old_total_size=new_total_size;new_total_size=old_total_size+sizeN2;
old_total_sizeH=new_total_sizeH;new_total_sizeH=old_total_sizeH+sizeH2;
agrupacion_nucleos(old_total_size+1:new_total_size,:)=[nuclei1;nuclei2;nuclei3];
agrupacion_hipotalamos(old_total_sizeH+1:new_total_sizeH,:)=[hypothalamus1;hypothalamus2;hyp
othalamus3];


cd('C:\Users\aborges\Documents\MATLAB\Glucose_admin_BOLD\11_results_signal_change_variab15\r
ecovery')
nuclei1=load('nuclei_mean_T2_star_part1','ascii');size2=size(nuclei1(:,1),1);
nuclei2=load('nuclei_mean_T2_star_part2','ascii');size2b=size(nuclei2(:,1),1);
nuclei3=load('nuclei_mean_T2_star_part3','ascii');size2c=size(nuclei3(:,1),1);sizeN2=size2+s
ize2b+size2c;
hypothalamus1=load('hypothalamus_mean_T2_star_part1','ascii');sizeh2=size(hypothalamus1(:,1)
,1);
hypothalamus2=load('hypothalamus_mean_T2_star_part2','ascii');sizeh2b=size(hypothalamus2(:,1
),1);
hypothalamus3=load('hypothalamus_mean_T2_star_part3','ascii');sizeh2c=size(hypothalamus3(:,1
),1);sizeH2=sizeh2+sizeh2b+sizeh2c;
old_total_size=new_total_size;new_total_size=old_total_size+sizeN2;
old_total_sizeH=new_total_sizeH;new_total_sizeH=old_total_sizeH+sizeH2;
agrupacion_nucleos(old_total_size+1:new_total_size,:)=[nuclei1;nuclei2;nuclei3];
agrupacion_hipotalamos(old_total_sizeH+1:new_total_sizeH,:)=[hypothalamus1;hypothalamus2;hyp
othalamus3];
%
cd('C:\Users\aborges\Documents\MATLAB\Glucose_admin_BOLD')
save agrupacion_nucleos_mean_normalized_to_maximum_variab15 agrupacion_nucleos -ascii
save agrupacion_hipotalamos_mean_normalized_to_maximum_variab15  agrupacion_hipotalamos -
ascii
clear all
```

7. Grouping Files

```
cd('C:\Users\Blanca\Documents\MATLAB\Glucose_admin_BOLD\normalized_to_maximum')

nucleos=load('agrupacion_nucleos_median_normalized_to_maximum','ascii');s_nucleos=size(nucle
os(:,1));unos=ones(s_nucleos,1);

nucleos_salino=load('agrupacion_nucleos_saline_median_normalized_to_maximum','ascii');s_nucl
eos_s=size(nucleos_salino(:,1));ceros=zeros(s_nucleos_s,1);

ventriculos=load('agrupacion_ventriculos_median_normalized_to_maximum','ascii');s_ventr=size
(ventriculos(:,1));unos_v=ones(s_ventr,1);sietes_v=ones(s_ventr,1)+6;

ventriculos_salino=load('agrupacion_ventriculos_saline_median_normalized_to_maximum','ascii'
);s_ventr_s=size(ventriculos_salino(:,1));ceros_v=zeros(s_ventr_s,1);sietes_vs=ones(s_ventr_
s,1)+6;

hipocampo=load('agrupacion_hipocampos_median_normalized_to_maximum','ascii');s_hipocampo=siz
e(hipocampo(:,1));unos_hipocampo=ones(s_hipocampo,1);ochos_hipocampo=ones(s_hipocampo,1)+7;

hipocampo_salino=load('agrupacion_hipocampos_saline_median_normalized_to_maximum','ascii');s
_hipocampo_s=size(hipocampo_salino(:,1));ceros_hipocampo=zeros(s_hipocampo_s,1);ochos_hipoca
mpo_s=ones(s_hipocampo_s,1)+7;

matriz_global=[unos nucleos;ceros nucleos_salino;unos_v sietes_v ventriculos;ceros_v
sietes_vs ventriculos_salino;unos_hipocampo ochos_hipocampo hipocampo;ceros_hipocampo
ochos_hipocampo_s hipocampo_salino];
save nucelos_ventr_glucose_hipocamp_saline matriz_global -ascii
```

Appendix II: Publications

NeuroImage 64 (2013) 448–457

Contents lists available at SciVerse ScienceDirect

NeuroImage

journal homepage: www.elsevier.com/locate/ynimg

Imaging hypothalamic activity using diffusion weighted magnetic resonance imaging in the mouse and human brain ☆

Blanca Lizarbe [a], Ania Benítez [a,b], Manuel Sánchez-Montañés [b], Luis F. Lago-Fernández [b], María L. Garcia-Martin [c,d], Pilar López-Larrubia [a], Sebastián Cerdán [a,*]

[a] Instituto Investigaciones Biomédicas "Alberto Sols" CSIC-UAM, c/Arturo Duperier 4, Madrid 28029, Spain
[b] Departamento de Ingeniería Informática, Escuela Politécnica Superior, Universidad Autónoma de Madrid, Cantoblanco, Madrid 28049, Spain
[c] Resonancia Magnética Nuestra Señora del Rosario, Príncipe de Vergara 56, 28006 Madrid, Spain
[d] Andalusian Centre for Nanomedicine and Biotechnology (BIONAND), Málaga, Spain

ARTICLE INFO

Article history:
Accepted 11 September 2012
Available online 19 September 2012

Keywords:
Appetite regulation
Functional imaging
Cerebral activation
Diffusion weighted MRI
Image analysis
Biexponential diffusion

ABSTRACT

Hypothalamic appetite regulation is a vital homeostatic process underlying global energy balance in animals and humans, its disturbances resulting in feeding disorders with high morbidity and mortality. The objective evaluation of appetite remains difficult, very often restricted to indirect measurements of food intake and body weight. We report here, the direct, non-invasive visualization of hypothalamic activation by fasting using diffusion weighted magnetic resonance imaging, in the mouse brain as well as in a preliminary study in the human brain. The brain of fed or fasted mice or humans were imaged at 7 or 1.5 Tesla, respectively, by diffusion weighted magnetic resonance imaging using a complete range of b values ($10<b<2000$ s.mm^{-2}). The diffusion weighted image data sets were registered and analyzed pixel by pixel using a biexponential model of diffusion, or a model-free Linear Discriminant Analysis approach. Biexponential fittings revealed statistically significant increases in the slow diffusion parameters of the model, consistent with a neurocellular swelling response in the fasted hypothalamus. Increased resolution approaches allowed the detection of increases in the diffusion parameters within the Arcuate Nucleus, Ventromedial Nucleus and Dorsomedial Nucleus. Independently, Linear Discriminant Analysis was able to classify successfully the diffusion data sets from mice and humans between fed and fasted states. Present results are consistent with increased glutamatergic neurotransmission during orexigenic firing, a process resulting in increased ionic accumulation and concomitant osmotic neurocellular swelling. This swelling response is spatially extendable through surrounding astrocytic networks until it becomes MRI detectable. Present findings open new avenues for the direct, non-invasive, evaluation of appetite disorders and other hypothalamic pathologies helping potentially in the development of the corresponding therapies.

Introduction

The appetite impulse originates in the brain from an imbalance in the systemic and intrahypothalamic mechanisms controlling food intake and energy expenditure (Morton et al., 2006). Following a meal, increased insulin and leptin levels induce an anorexigenic response consisting in a reduction in food intake and an increase in energy expenditure, whereas in fasting periods decreased plasma levels of leptin and insulin promote increased food intake and energy expenditure. These systemic and intrahypothalamic neuroendocrine signals interact mainly in the Arcuate Nucleus (ARC), the Ventromedial Nucleus (VMN), Dorsomedial Nucleus (DMN) and the Paraventricular Nucleus (PVN), modifying the balance between the activity of orexigenic neurons, releasing Agouti Related Peptide (AgRP) or Neuropeptide Y (NPY), and anorexigenic neurons releasing Proomileanocortin (POMPCT) or Cocaine and Amphetamine Regulated Transcript (CART) (Coll et al., 2007). In addition to neuroendocrine signaling, appetite stimulation is known to involve hypothalamic increases in glutamatergic and gabaergic neurotransmissions (Delgado et al., 2011; van den Pol et al., 1990). Moreover, it has been recently reported (Spanswick et al., 2012) that the excitatory synaptic control of AgRP neurons is regulated by fasting and hormones, and that increased glutamatergic activity is a necessary requirement for a physiological response to fasting (Liu et al., 2012; Yang et al., 2011).

Despite the progress obtained in the interpretation of the molecular events underlying the fasting response, the direct evaluation of appetite regulation in the brain still remains difficult, very often limited to

Abbreviations: D_{slow}, Slow diffusion coefficient; D_{fast}, Fast diffusion coefficient; FDP, Fast diffusion phase; LDA, Linear Discriminant Analysis; SDP, Slow diffusion phase.

☆ This work was supported in part by grants SAF-2008-01327 and SAF2011-23622 to SC, grant CTQ-2010-20960-C02-02 to PLL, grants S-BIO-2006-0170 and S2010/BMD-2349 to SC, PLL and MSM and grant CAM/UAM (CCG10-UAM/TIC-5864) to LFLF. BL and ABSDC held predoctoral fellowships from the Spanish Ministry of Science and Technology (BES 2009-027615) and the Spanish Agency for International Cooperation and Development.

* Corresponding author. Fax: +34 91 585 4401.
E-mail address: scerdan@iib.uam.es (S. Cerdán).

1053-8119/$ – see front matter © 2012 Elsevier Inc. All rights reserved.
http://dx.doi.org/10.1016/j.neuroimage.2012.09.033

indirect measurements of food intake and body weight. On these grounds, the implementation of non-invasive methodologies for the evaluation of appetite entails considerable relevance. A variety of neuroimaging tools have been proposed including mainly positron emission tomography (PET) and functional magnetic resonance imaging (fMRI) methods (Carnell et al., 2011). PET studies provide information on cerebral activation by detecting the emitted positrons derived from the increased uptake of ^{18}F-deoxiglucose, an event revealing the metabolic coupling between glucose uptake, blood flow and neuronal activity in the hypothalamus during feeding-related stimuli (Gautier et al., 2000; Tataranni et al., 1999). Blood Oxygenation Level Dependent (BOLD) fMRI, infers regional neuronal activity from the changes in magnetic susceptibility that take place during the transition between oxygenated hemoglobin and deoxygenated hemoglobin, occurring after increased oxygen delivery to activated neurons in the hypothalamus of rats and humans (Mahankali et al., 2000; Matsuda et al., 1999). Finally, manganese enhanced magnetic resonance imaging (MEMRI), uses manganese ion accumulation as a surrogate marker of the increased calcium movements occurring during neuronal activation. MEMRI has revealed the time course of hypothalamic activation as a response to the systemic administration of different orexigenic or anorexigenic peptides (Parkinson et al., 2009). Notably, these previous approaches are not devoid of limitations to investigate hypothalamic physiology in animals and man, mainly derived from their reduced spatial and temporal resolution in the PET and BOLD fMRI approaches, and the potential neurotoxicity of Mn^{2+}, in the MEMRI technique. To overcome these limitations, we propose here the use of functional diffusion weighted imaging fDWI (Le Bihan, 2003) a novel functional approach improving the spatial and temporal resolution provided earlier by PET or BOLD and avoiding the use of the potentially toxic doses of manganese precluding the use of MEMRI in humans.

Materials and methods

Experimental models

The experimental protocols used in this study were approved by the appropriate institutional committees and met the guidelines of the appropriate government agency. Experiments with animals were carried out using healthy adult male C57BL/6 mice (n = 12) aged nine weeks. Each animal was investigated in two successive experimental conditions both receiving drinking water ad libitum; "fed"; receiving normal mice chow diet (A04 http://www.safe-diets.com/eng/home/home.html, SAFE Augy, France, 2900 kcal/kg), and "fasted"; following either 48 h (group 1, n = 6, 25 ± 4 g) or 16 h (group 2, n = 6, 26 ± 2 g) after complete food removal. In all small animal imaging experiments, anesthesia was initiated in a plexiglass induction box (Isofluorane 2%/99.9% O2, 1 mL/min) and maintained during the imaging time with a nose mask (Isofluorane 1%/O2 99.9% mixture, 1 mL/min). Anesthetized animals were placed in a water heated probe, which maintained the core body temperature at approximately 37 °C during scanning. The physiological state of the animal during the imaging process was monitored by the respiratory rate and body temperature using a Biotrig physiological monitor (Bruker Biospin, Ettlingen, Germany).

We performed a pilot study with human subjects to illustrate the potentialities of the proposed methodology in a routine clinical environment. Human participants in the study were six healthy male volunteers, aged 24–33. Conditions for the participation were: (1) healthy clinical trajectory without familiar history of obesity, diabetes or other endocrine disorders; (2) Body Mass Index (BMI) of 18.5–25, corresponding to normal body weight; and (3) volunteers were required to follow a balanced diet (2000–2500 cal/kg) during seven days prior to the basal image acquisitions, with no drinks other than water ad libitum, no medication or abnormal exercise. Specific instructions to follow a balanced diet were provided for each individual at the beginning of the study and the degree of compliance with these obtained individually before the imaging sessions. All individuals adhered correctly to the outlined protocol. Each volunteer was imaged in two successive conditions; first, "fed", after one week of a balanced diet and second "fasted", 24 h after food deprivation. Blood samples from the median cubital vein were drained before the "fed" and "fasted" image acquisitions and analyzed for routine biochemical parameters T3, T4, TSH and insulin levels.

MRI sequences

The magnetic resonance imaging (MRI) experiments with mice were performed on a 7.0-T horizontal-bore (16 cm) superconducting magnet equipped with a ^{1}H selective birdcage resonator of 23 mm and a 90 mm diameter gradient insert (36 gauss/cm). Imaging data were acquired using Hewlett-Packard console running Paravision 4.0 software (Bruker Medical Gmbh, Ettlingen, Germany) operating on a Linux environment.

Fig. 1 provides an overview of the acquisition and image analysis approaches implemented in this study and the regions of interest investigated, as illustrated for the mouse brain. A collection of diffusion weighted images of the fed and fasted mouse brain was obtained (left panel) and analyzed using either a biexponential diffusion model (upper right panels) or a model-independent Linear Discriminant Analysis approach (lower right panels). The set of DWI was acquired with the conditions indicated below, across an axial plane containing the hypothalamus (Paxinos and Franklin, 2001) with the diffusion gradient oriented along three orthogonal directions; Left–Right (L–R), Antero-Posterior (A–P) and Head–Feet (H–F). This structure was localized using a sagittal section showing the pituitary gland and selecting after the first axial section rostral to it, as indicated in Fig. 2A. This section is located anatomically Bregma −1.46 mm. In the six mice of group 1, the acquisition parameters were (Bruker Pharmascan, Bruker Medical Gmbh, Ettlingen, Germany): repetition time (TR) = 3000 ms, echo time (TE) = 51 ms, four shot EPI readout, averages (Av) = 3, Δ = 20 ms, δ = 4 ms, field of view (FOV) = 35 mm, acquisition matrix = 128 × 128, corresponding to an in-plane resolution of 296 × 296 μm^2, slice thickness of 1.5 mm, number of slices = 3, using a collection of five low b values (10<b<100 s.mm^{-2}) and six high b values (200<b<1800 s.mm^{-2}).

The six mice of group 2, were investigated using nine diffusion weighted images (DWI) acquired along the axial plane containing the hypothalamus, with b values (300<b<2000 s.mm^{-2}). Acquisition parameters were (Bruker AVANCE III, Bruker Medical Gmbh, Ettlingen, Germany): repetition time (TR) = 3000 ms, echo time (TE) = 31 ms, four shot EPI readout, averages (Av) = 3, Δ = 20 ms, δ = 4 ms, field of view (FOV) = 21 mm, acquisition matrix = 128 × 128, corresponding to an in-plane resolution of 164 × 164 μm^2, slice thickness of 1.25 mm and number of slices = 3.

T_2-weighted (T_{2w}) spin echo anatomical images were acquired previous to the DWI with improved resolution to localize and resolve precisely the hypothalamic region in every mouse. Axial T_{2w} images across the section containing the hypothalamus were acquired using the rapid acquisition with relaxation enhancement (RARE) sequence with the following parameters: TR = 3200 ms, TE = 60 ms, RARE factor = 8, Av = 3, FOV = 38 mm (Pharmascan console), 21 mm (AVANCE III console), acquisition matrix = 256 × 256 corresponding to an in-plane resolution of 148 × 148 μm^2 (Pharmascan console) or 80 × 80 μm^2 (AVANCE III console), number of slices = 3 and slice thickness = 1.5 mm (Pharmascan console), or 1.25 mm (AVANCE III console).

The magnetic resonance imaging (MRI) experiments with human volunteers were performed in the Magnetic Resonance Unit of the Hospital Nuestra Señora del Rosario (Madrid, Spain), using a GE Medical Systems 1.5-T horizontal-bore superconducting magnet, equipped with a ^{1}H quadrature head resonator. Prior to the imaging experiments, volunteers signed up an informed consent and confidentiality document. Image acquisitions were medically supervised by the neuroradiology

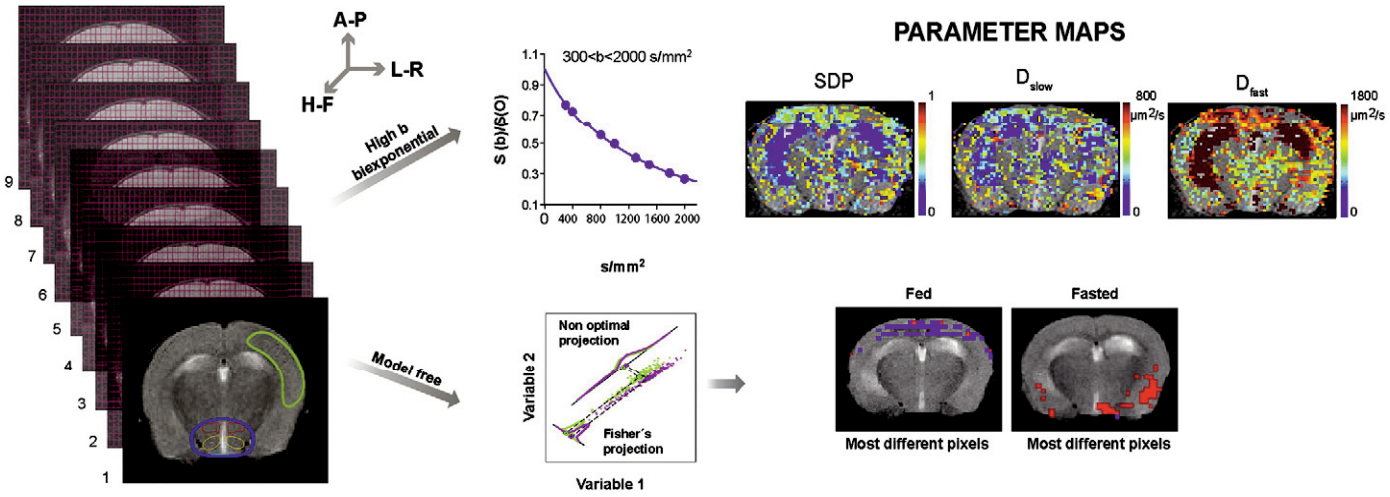

Fig. 1. Overview of the methodology. Diffusion weighted images ($10<b<2000$ s.mm^{-2}) are acquired consecutively in the same slice, in three diffusion directions A–P, L–R and H–F. The diffusion data set is analyzed with two independent approaches: a biexponential model fit (upper panels) and a Fisher LDA (lower panels). From the biphasic model, colored maps of the independent parameters fitted are obtained, (SDP, FDP, D_{slow}, D_{fast}). Investigated areas were the complete hypothalamus (circled dark blue, excluding the third ventricle) and its substructures and the somatosensory cortex (circled in green). Individual hypothalamic nuclei investigated are depicted in light blue (Arcuate Nucleus), yellow (Ventromedial Nucleus) and red (Dorsomedial Nucleus). Using Fisher LDA, the entire diffusion imaging data set from the fed and fasted brains, can be classified between the two feeding sates: with the most different pixels representing the fed (blue) or fasted (red) pixels. The overview is illustrated with the mouse brain data.

and clinical laboratory staff of the clinic. Multi b-value diffusion weighted images were acquired using 6 b values ($200<b<1200$ s.mm^{-2}). T_2-weighted (T_{2W}) spin echo anatomical images were acquired in every subject in the same plane as the DWI, using a rapid acquisition with Fast Relaxation Fast Spin Echo (FRFSE) sequence in coronal orientations. Acquisition parameters were: TR = 3200 ms, TE = 90 ms, Echo number = 1, Echo Train Length = 8, Av = 4, FOV = 240 mm, acquisition matrix = 512 × 512, corresponding to an in-plane resolution of 468.7 × 468.7 µm^2, and slice thickness = 3 mm.

Image analysis

Images acquired with the small animal or human scanners were transformed in DICOM format and exported to external HP Z-400 Workstations. Image analysis was performed as described below, using Statistical Parametric Mapping Software (SPM, http://www.fil.ion.ucl.ac.uk/spm/software) and a collection of in-house developed programs (Matlab v7, The Mathworks, Nattick, MA, USA) for non-linear model fitting and classification of diffusion weighted images using Linear Discriminant Analysis.

Selection of ROIs

In the mouse brain, the cortical area, the hypothalamus and the hypothalamic nuclei ARC, DMN and VMN, were selected manually based on the anatomical descriptions given by the mouse brain atlas (Paxinos and Franklin, 2001). Fig. 1 (leftmost panels) illustrates the localization of the different ROIs in a representative mouse brain. In the human images, hypothalamic and cortical ROIs were selected with the assistance of experienced clinical neuroradiologists (Fig. 4A).

Diffusion model

We used the biexponential model of attenuation of the DWI signal (Niendorf et al., 1996), as described by the expression;

$$S(b)/S(0) = SDP \cdot \exp(-b \cdot D_{slow}) + FDP \cdot \exp(-b \cdot D_{fast}) \quad (1)$$

where, $S(b)$ and $S(0)$ represent the individual pixel intensities in the presence and absence of diffusion gradient, b indicates the diffusion weighting factor (s.mm^{-2}), SDP represents the slow diffusion phase containing water molecules moving with a slow diffusion coefficient D_{slow}, and FDP refers to the fast diffusion phase containing the water molecules moving with a fast diffusion coefficient D_{fast}. The addition of diffusion phases represents the total water molecules contributing to the signal decay ($SDP + FDP = 1$).

Parameter fitting and statistical analysis

Parameters of the biexponential model were determined independently for each voxel and direction in the two feeding states, using the non-linear least-squares fitting Trust-Region algorithm, customized to limit parameter ranges and optimize the goodness of fit. In particular, the goodness of fit (r^2) was restricted to be higher than 0.9 to guarantee an optimal fitting. Parameters are presented as mean ± standard deviation within the considered ROIs in each animal or human. Statistical comparisons between the fed and fasted conditions were made constructing a cumulative, representative ROI that grouped the contributions of the individual ROIs selected from each mouse or human. The statistical analysis was made first using unpaired Student's *t* test, comparing each pair of fed and fasted cumulative ROIs. Further differences were assessed using a multiple linear regression model with the generalized estimating equation (GEE), a process that uses robust standard error estimates taking into account within-subjects correlations (Burton et al., 1998). All statistical analyses were performed using SPSS (*IBM Statistical Package for the Social Sciences*, 2000, http://www.spss.com).

Model-free DWI analyses

We also implemented a model-free classification algorithm, based on Fisher Linear Discriminant Analysis (Fisher LDA, Hastie et al., 2001). This model-free approach, allowed to investigate whether the DWI images could be automatically classified into the "fed" and "fasted" groups, without constrains imposed by the biexponential model. LDA constructs a projection of the original data onto a low dimensional subspace trying to maximize the separation amongst the different classes. When there are only two classes, as in the present case (fed/fasted), this subspace is one-dimensional. Hence, the projection may be interpreted as an Appetite Index that can be used to discriminate between the two conditions (see Fig. 1).

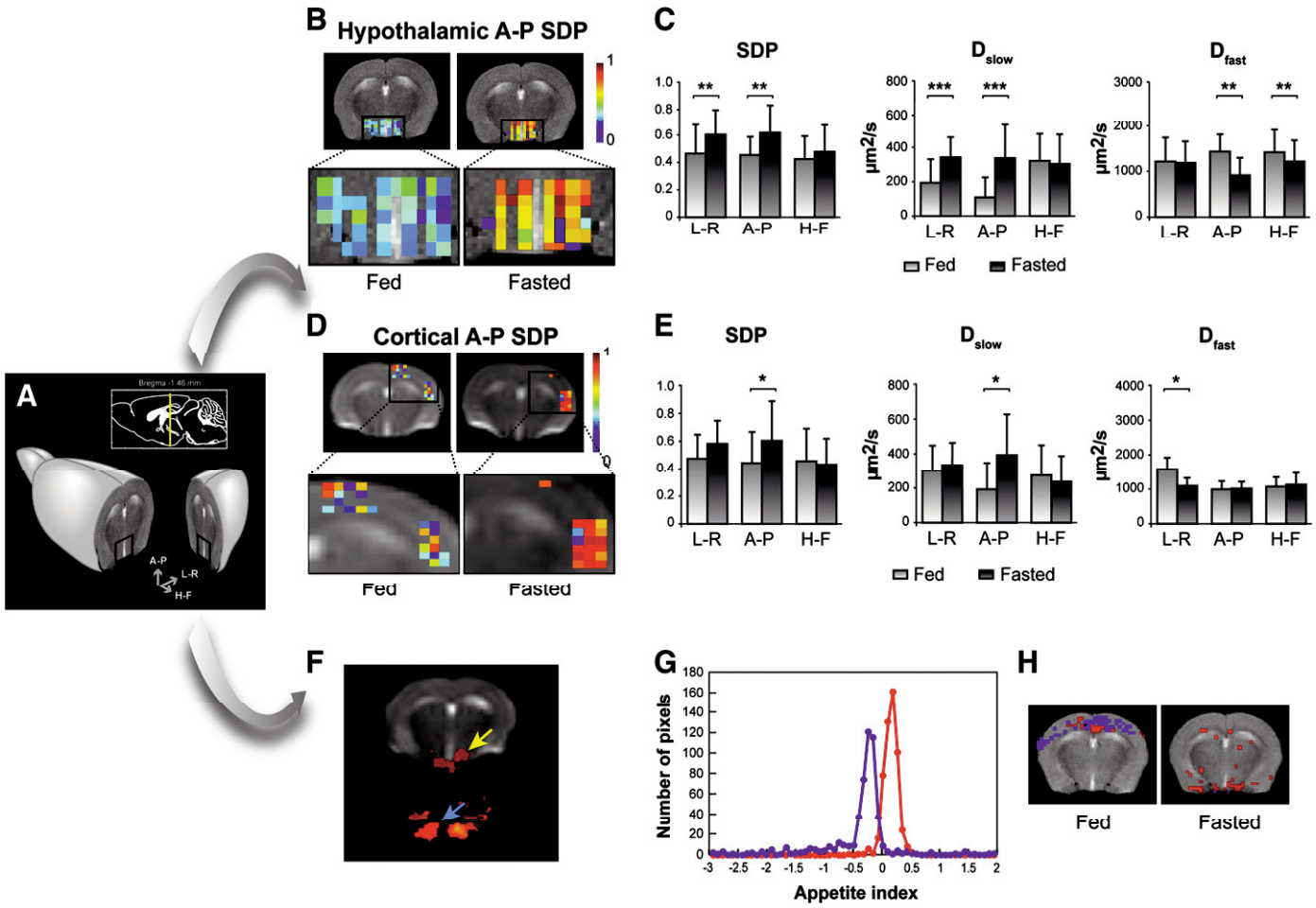

Fig. 2. Imaging appetite by fDWI in the mouse brain. A: Axial and coronal MRI sections containing the hypothalamus in a representative mouse brain model and in a brain atlas (inset). B: Hypothalamic A–P SDP color maps obtained from the DWI of fed or fasted animals (upper panels), superimposed to the corresponding T_2-weighted (T_{2w}) anatomical brain images. The hypothalamic region is shown enlarged in the lower panels. C: Values of hypothalamic SDP, D_{slow} and D_{fast} parameters (mean ± SD) in the L–R, A–P and H–F directions. The number of pixels (N) used in the comparisons was: $N_{fed} = 120$, $N_{fasted} = 141$ in L–R; $N_{fed} = 95$, $N_{fasted} = 82$ in L–R and $N_{fed} = 201$, $N_{fasted} = 176$ in H–F, respectively. D: Cortical areas investigated from a representative mouse brain, in the fed and fasted states (upper images). The A–P SDP values are shown superimposed to anatomical T_{2w} images. The corresponding enlargements of the cortical areas are shown below. E: SDP, D_{slow} and D_{fast} values (mean ± sd) of six mice in the fed and fasted conditions, and statistical differences (*$p<0.05$, **$p<0.005$, ***$p<0.001$, Student's *t* test). $N_{fed} = 7$, $N_{fasted} = 21$ in L–R; $N_{fed} = 31$, $N_{fasted} = 32$ in A–P; and $N_{fed} = 57$, $N_{fasted} = 71$ in H–F. F: SPM analysis of the areas that best differentiate the fed and fasted hypothalamus in a representative mouse brain. Note the hypothalamic (yellow arrow) and vascular (blue arrow) activations. G: "Appetite Index" histogram of the fed (blue) and fasted (red) pixels as projected over the calculated LDA vector. Note the almost complete resolution of fed and fasted histograms. H: Panels that illustrate the localization in the mouse brain image of the 5% lowest (fed) and highest (fasted) points located at each end of the Appetite Index histogram.

Results

The effects of fasting in the mouse brain using DWI

Fig. 2A shows the anatomical localization of MRI sections used to localize the hypothalamus in the mouse brain and the directions of diffusion measurements. Hypothalamic activation after 48 h of fasting is conveniently detected by fDWI as a shift to red in the fasted condition, in the diffusion maps shown in Fig. 2B. The upper panels show the hypothalamic SDP maps (A–P direction) in the fed and fasted conditions, superimposed on the corresponding anatomical T_{2w} images from the whole brain. These hypothalamic SDP maps are shown enlarged in the corresponding lower panels. The shift from blue to orange and red, revealing increased SDP, is clearly detected in the fasted condition. Artworks in Fig. 2C summarize the mean values, standard deviations and comparative statistical significances of the diffusion parameters (SDP, D_{slow} and D_{fast}), from six mice under the fed and fasted conditions, investigated in three orthogonal directions (L–R, A–P and H–F). SDP and D_{slow} increased significantly with fasting ($p<0.005$ and $p<0.001$) in the L–R and A–P directions, whereas D_{fast} decreased in the A–P and H–F orientations ($p<0.005$).

The impact of this fasting paradigm was investigated additionally in the cerebral somatosensory cortex of the same animals, obtaining a different, albeit significant, diffusion response (Fig. 2D). In particular, subsidiary effects of fasting become significant as reflected by the red-shift in the A–P SDP parameter of fasted animals (2D, upper right panels), reflecting most probably, motor activations related to the feeding impulse. Enlarged SDP maps with improved resolution in this region are shown below (2D, lower panels). Mean values, standard deviations and statistical significance of the different diffusion parameters are shown in the corresponding bar graphs of the panels in Fig. 2E. SDP and D_{slow} increase significantly ($p<0.05$) in the A–P direction and D_{fast} decreases ($p<0.05$) in the L–R measurements.

Notably, the model independent analysis of the diffusion weighted data sets using Linear Discriminant Analysis (LDA) (Figs. 2F–H) was also able to classify successfully all mice investigated between the fed and fasted states. This indicates that the intrinsic differences between fed and fasted brains may be detected even automatically, independently

of the diffusion model used. Fig. 2F shows how SPM processing detected, as activated areas by the fasting paradigm, an area including the hypothalamus (yellow arrow) and an area of subsidiary vascular activation with the carotid arteries and the jugular veins (blue arrow). Taken together this evidence reveals a highly complex cerebrovascular response to the fasting paradigm involving not only a hypothalamic activation but also an additional vascular adaptation. LDA was applied to detect the most different pixels between the fed and fasted image data sets of every mouse. Results from a representative mouse are illustrated in Figs. 2G and H. The Fisher LDA projection (Appetite Index, Fig. 2G) separates optimally the pixels of the fed (blue) and fasted (red) states. The pixels that are most representative of each state, located at the edges of the histogram (<5% or >95%), are shown in Fig. 2H, superimposed on the corresponding T_{2w} images. Using a leave one out cross validation strategy, it was possible to classify correctly, as fed or fasted, the image data sets from all mice investigated, when using the diffusion data sets acquired with the whole range of b values (six high b and five low b). However, using only the six highest b value data sets, only five mice out of the six mice investigated were classified correctly between fed and fasted states. This suggests that the microvascular contributions emphasized by the low b values are needed to obtain the optimal discriminant power required to classify correctly the images of every mouse between the fed and fasted states.

We investigated then the possibilities to resolve the effects of fasting in individual hypothalamic nuclei with shorter fasting times (16 h) and increased image resolution obtainable after a console upgrade. Fig. 3A shows the anatomical localization of MRI sections used to identify the hypothalamus in the mouse brain and the directions of diffusion measurements. The inset on the top shows the anatomical localization of the hypothalamic Dorsomedial Nucleus (DMN, red), Ventromedial Nucleus (VMN, yellow) and Arcuate Nucleus (ARC, light blue). Hypothalamic activation after 16 h of fasting is revealed by fDWI as an increment of D_{slow} coefficients in the fasted condition depicted in the diffusion maps and bar graphs of Figs. 3B and C. The upper panels of Fig. 3B show the hypothalamic D_{slow} maps (H–F direction) in the fed and fasted conditions of a representative mouse, superimposed on the corresponding anatomical T2w images from the whole brain. The lower panels in Fig. 3B show the hypothalamic D_{slow} maps with augmented resolution, depicting clearly a shift to the red that reveals an increase in D_{slow}. Fig. 3C summarizes the mean values, standard deviations and comparative statistical significances of the slow diffusion parameters in the L–R, A–P and H–F directions from the six mice under the fed and fasted conditions. D_{slow} increased significantly with fasting in the A–P ($p<0.01$) and H–F ($p<0.001$) directions.

Figs. 3D–I show the effects of the 16 h fasting in the Arcuate Nucleus, the Ventromedial Nucleus and the Dorsomedial Nucleus, respectively. The upper panels of Figs. 3D, F and H depict the D_{slow} maps (H–F direction) in the fed and fasted conditions of a representative mouse, superimposed on co-localized T_{2w} images. The lower panels depict enlarged corresponding D_{slow} maps showing very significant increases in the H–F direction ($p<0.001$). The bar graphs of Figs. 3E–I show the mean ± sd of D_{slow} values from the six mice of group 2 for each investigated nucleus. Significant increases ($p<0.001$) in D_{slow} were detected in all nuclei in the H–F direction. The DMN and VMN nuclei showed also significantly increased SDP (L–R, $p<0.001$; H–F, $p<0.05$,) and (A–P; $p<0.05$), respectively.

The effects of fasting in the human brain using DWI

Table 1 shows the results for the blood samples taken from the cubital vein of the human volunteers before the “fed” and “fasted” image acquisitions. Blood samples were analyzed for routine biochemical and endocrine parameters including; glucose, cholesterol, triglycerides, HDL, LDL, T3, T4, TSH and insulin. Values of these parameters fell within the normal clinical range both in the “fed” and “fasted” conditions for every individual.

Fig. 4A shows the localization of MRI sections containing the hypothalamus in a human brain model and the directions of our DWI measurements. The diffusion maps shown in Fig. 4B show that fDWI visibly detects the hypothalamic activation induced by 24 h of fasting. The upper images show the hypothalamic SDP maps (H–F direction) in the fed and fasted conditions, superimposed on the corresponding anatomical T_{2w} images from the whole brain. These hypothalamic diffusion maps are shown enlarged in the corresponding lower images. The fasted condition is clearly detected by a shift to orange and red of the SDP color map, revealing a significant increase in SDP. Bar graphs in Fig. 4C summarize the mean values, standard deviations and comparative statistical significances of the diffusion parameters (SDP, D_{slow} and D_{fast}) fitted as described in the Materials and methods section. We investigated six healthy volunteers under the fed and fasted conditions, monitoring the diffusion of water molecules in three orthogonal directions (L–R, A–P and H–F). As in the mouse brain, we found a significant increase of SDP (A–P; $p<0.05$, H–F: $p<0.001$) and D_{slow} (H–F; $p<0.05$) with fasting. However, the human brain did not show a significant cortical activation associated with the fasting paradigm (Figs. 4D and E). The resolution of individual hypothalamic substructures was not possible when using the clinical 1.5 T scanner. Even under these unfavorable field conditions, our results show that the detection of hypothalamic activation is feasible by DWI, becoming most probably much improved at higher magnetic fields of 3 T and 7 T.

LDA of the human hypothalamic data set was also able to separate successfully the diffusion weighted images from the fasted and fed conditions (Figs. 4F and G), implying again that the intrinsic differences between fDWI data sets in the two feeding conditions, are independent of the diffusion model used. A distribution of the fed and fasted projections from the hypothalamus of a representative subject is illustrated in the histogram (Appetite Index, Fig. 4F). In Fig. 4G, the upper images show enlarged hypothalamic areas that best discriminate the fed (blue pixels) and fasted (red pixels) groups and the corresponding localizations in the anatomical T_{2w} images of the human brain (lower panels). An evaluation of the accuracy of classifications between fed and fasted states, as performed with the leave one out strategy, classified correctly the imaging data sets of five out of the six subjects, the same percentage obtained in the mouse brain images acquired with six b values under similar conditions.

Discussion

We report here that fasting results in significant changes in the diffusion parameters of cerebral water in mice and humans providing a novel approach for the objective, non-invasive, fully translational evaluation of the feeding impulse in vivo. Our data are consistent with previous applications of fDWI to cerebral activation studies, in particular the visual activation in humans (Le Bihan et al., 2006) and with in vitro DWI measurements of induced neuronal activity (Flint et al., 2009). In these cases, neuronal activation was associated with increments of the slow diffusion parameters in the activated areas, a finding proposed to reveal a relative redistribution of water molecules between the fast (FDP) and slow (SDP) diffusion phases, most probably reflecting, activation-induced increases in neurocellular volume (swelling) (Le Bihan et al., 2006).

The interpretation of the physiological or pathological changes in water diffusion parameters in the in vivo brain has been a matter of debate in the last decades. Early physiological interpretations described the existence of two dynamically different diffusion phases, fast and slow, attributed initially to the extracellular and intracellular environments, respectively. Further studies showed that the volume fractions of the intra- and extracellular phases predicted by DWI did not match those determined histologically (Niendorf et al., 1996; Sehy et al., 2002), implying that factors additional to morphological compartmentalization contributed appreciably to the diffusion environments detected by MRI in the brain (Garcia-Martin et al., 2001). More recently, the slow diffusion phase (SDP), containing the water

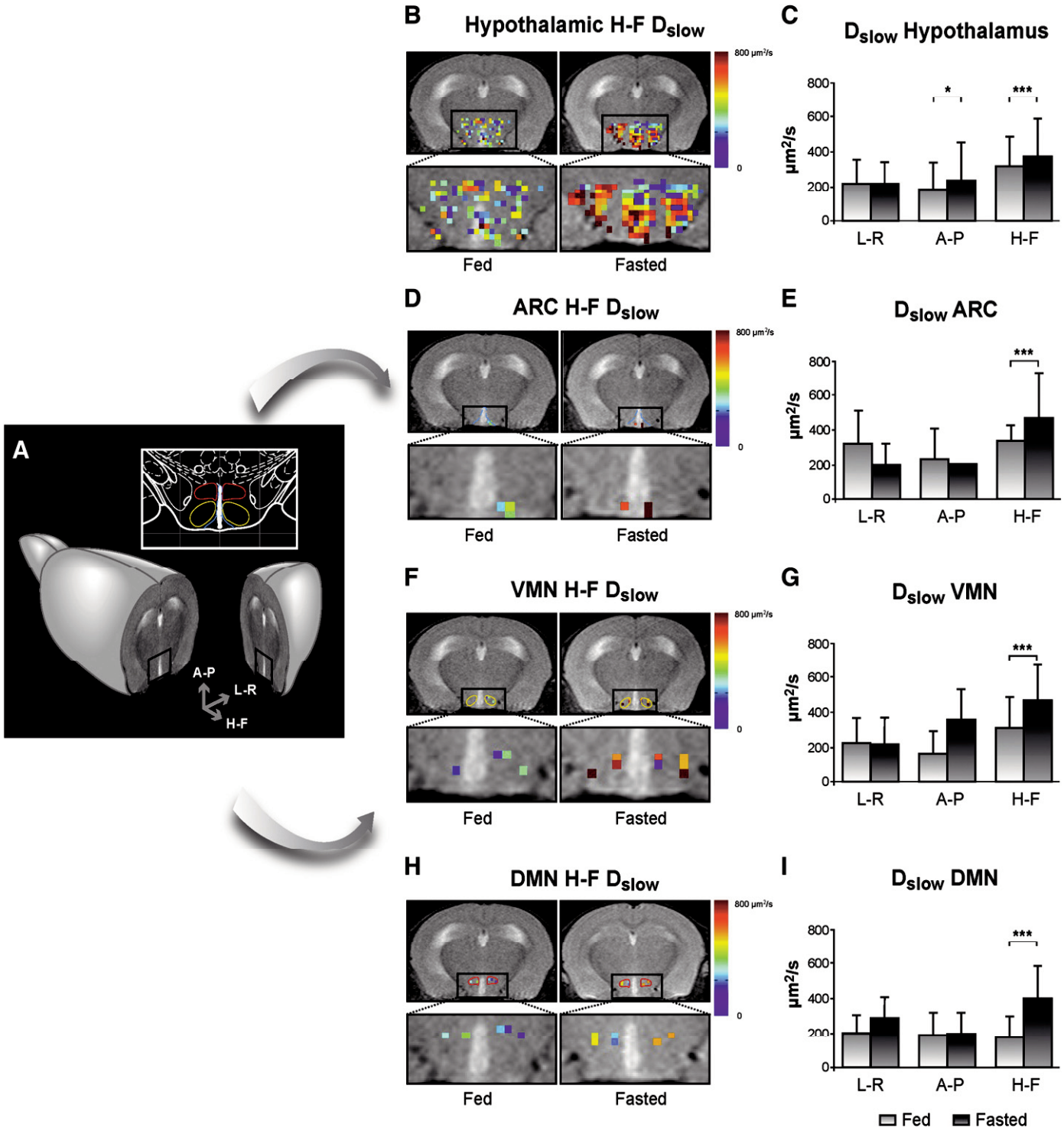

Fig. 3. Imaging appetite by fDWI in the hypothalamic nuclei of the mouse brain. A: Axial MRI section containing the hypothalamus in a representative mouse brain and in a brain atlas (inset) showing the localization of the main periventricular hypothalamic nuclei: Dorsomedial Nucleus (DMN, red), Ventromedial Nucleus (VMN, yellow) and Arcuate Nucleus (Arc, light blue). B: Hypothalamic H–F D_{slow} color maps from fed or fasted mice, superimposed to T_{2w} images. The hypothalamic region is depicted enlarged in the lower panels. C: Values of hypothalamic D_{slow} (mean ± SD) in the L–R, A–P and H–F directions for 6 mice in the fed state and after 16 h of fasting, and statistical differences (*$p<0.05$, **$p<0.005$, ***$p<0.001$, Student's *t* test). The number of pixels (N) used in the comparison was; $N_{fed}=255$, $N_{fasted}=215$ in L–R; $N_{fed}=150$, $N_{fasted}=130$ in A–P and $N_{fed}=306$, $N_{fasted}=463$ in H–F measurements. D: H–F D_{slow} parameter maps of the Arcuate Nucleus in the fed (left) or fasted (right) states in a representative mouse, superimposed to T_{2w} images. The region is shown enlarged in the bottom panels. E: D_{slow} values (mean ± SD) of the ARC of six mice in the fed state and after 16 h of fasting in the three directions of measurement and statistical differences between states ($p<0.001$, using GEE statistical methods) in the H–F direction. $N_{fed}=11$, $N_{fasted}=13$ in L–R, $N_{fed}=3$, $N_{fasted}=2$ in A–P and $N_{fed}=4$, $N_{fasted}=13$ in H–F. F: H–F D_{slow} parameter maps of VMN in the fed (left) or fasted (right) states for a representative mouse, superimposed to T_{2w} images. The hypothalamic region is shown enlarged in the bottom panels. G: D_{slow} values (mean ± SD) of the VMN of six mice in the fed state and after 16 h of fasting, in the three directions of measurement, and statistical differences between states (H–F direction $p<0.001$, Student's *t* test). $N_{fed}=25$, $N_{fasted}=17$ in L–R; $N_{fed}=12$, $N_{fasted}=5$ in A–P and $N_{fed}=22$, $N_{fasted}=29$ in H–F. H: H–F D_{slow} parameter maps of the DMN of a representative mouse, superimposed to T_{2w} images of the mouse brain (upper panels) and with the hypothalamic area enlarged (bottom panels). I: D_{slow} values (mean ± SD) of the DMN of six mice in the fed or fasted states, in the three directions (L–R, A–P, H–F) with statistical differences ($p<0.001$) in the H–F direction. $N_{fed}=9$, $N_{fasted}=8$ in L–R, $N_{fed}=15$, $N_{fasted}=11$ in the A–P direction and $N_{fed}=19$,$N_{fasted}=23$ in the H–F direction.

Table 1
Blood concentrations of relevant biochemical parameters in each of the six human volunteers, determined before each imaging session.

Volunteer/blood concentration[a] (units)	1		2		3		4		5		6		Mean volunteer values[b]		Reference values[b]
Condition	Fed	Fasted	Fed	Fasted	Fed	Fasted	Fed	Fasted	Fed	Fasted	Fed	Fasted	Fed	Fasted	
Glucose (mg/dL)	98	88	87	79	90	79	95	77	88	83	86	80	90.7	81	65–105
Colesterol (mg/dL)	190	175	161	162	112	126	131	125	155	162	219	227	161.3	162.8	130–240
Triglycerides (mg/dL)	97	47	63	45	32	41	51	47	67	35	129	87	73.2	50.3	35–155
HDL-cholesterol (mg/dL)	63	58	42	43	40	43	48	46	36	39	36	37	44.2	44.3	> 32
LDL-cholesterol (mg/dL)	108	108	106	110	66	75	73	70	106	116	157	173	102.7	108.7	< 180
T3 (ng/mL)	1.1	1	1	0.9	1.2	1.1	1.	0.9	1	1	1.3	1.2	1.1	1	0.75–1.78
T4 (mcg/dL)	6.3	7.6	7.9	8.9	7.8	9.3	7.6	7.7	7.6	7.7	7.6	7.8	7.5	8.2	6.09–12.23
TSH (mcIU/mL)	1.4	0.6	0.7	0.6	2	1.9	1.6	0.9	0.7	0.4	1.2	0.8	1.3	0.9	0.34–5.6
Insulin (mcIU/mL)	6.2	3.1	5.5	<3	3.7	<3	<3	<3	3	<3	3.6	<3	4.4	<3	<25

[a] Determinations were performed using clinically validated protocols by the Analytical Biochemistry Laboratory Services of the Clinica Nuestra Sra. Del Rosario (Madrid). Briefly, glucose was measured using the glucose oxidase method (One touch Ultra, LifeScan, Johnson and Johnson, Issy-les-Moulineaux, FR). Total serum cholesterol and triglycerides were measured enzymatically using a CHOD-PAP test (Boehringer-Mannheim, DE); T3, T4 and TSH determinations used the Accubind-ELISA kit and insulin with the insulin ELISA kit (Millipore, Billerica, MA, USA).

[b] Mean values of the parameters in both feeding conditions are also provided, as well as reference values for healthy adult conditions.

molecules with slow diffusion coefficient (D_{slow}), has been suggested to represent dynamically restricted water molecules associated with membranes and cytoskeleton structures. Conversely, the fast diffusion phase (FDP), containing the water molecules with a fast diffusion coefficient (D_{fast}), has been proposed to represent the remaining, freely moving, solvent water molecules (Niendorf et al., 1996) (Fig. 4, upper panels). On these grounds, increases in SDP detected by MRI upon neural activation (Le Bihan, 2007) reveal a relative increment of water molecules diffusing in the vicinity of the membrane and cytoskeleton structures. This is consistent with the large increments in monovalent and divalent cation transports occurring during the action potentials, thought to be localized initially in the vicinity of the neural

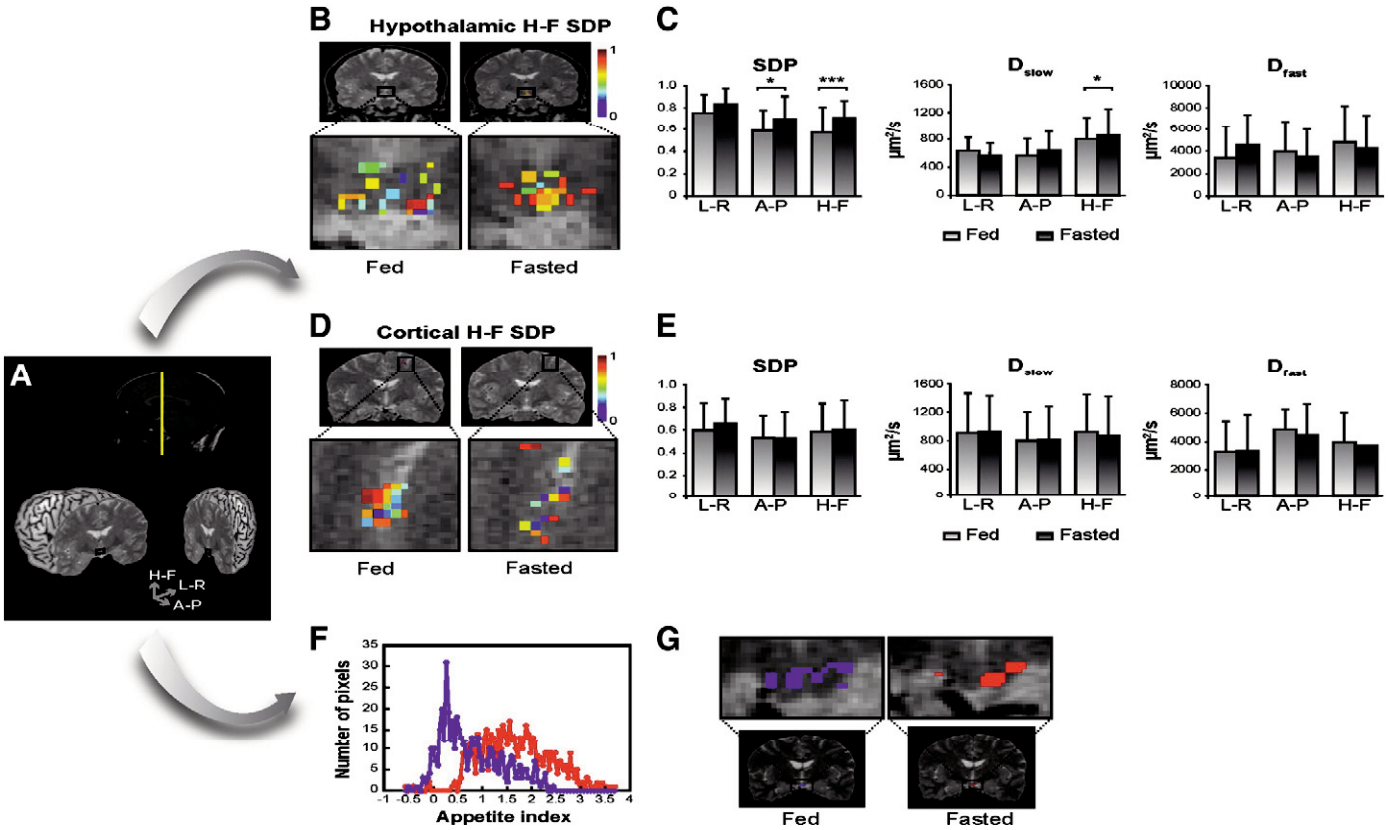

Fig. 4. Imaging appetite in the human brain. A: Coronal and sagittal sections containing the hypothalamus in a representative human brain. B: Parameter maps showing the H–F SDP pixel values from six volunteers in the fed and fasted conditions, superimposed to anatomical T_{2w} images (upper panels). The lower panels show enlarged hypothalamic maps. C: Bar graphs of SDP, D_{slow} and D_{fast} parameters (mean ± SD) of six human subjects in the fed and fasted conditions. The number of pixels (N) used in the comparisons is: $N_{fed} = 7$, $N_{fasted} = 4$ in L–R; $N_{fed} = 13$, $N_{fasted} = 12$ in A–P and $N_{fed} = 24$, $N_{fasted} = 16$ in H–F, with significant increases in A–P ($p<0.05$) and H–F ($p<0.001$) SDP and H–F ($p<0.05$) D_{slow}, (GEE protocol). D: Cortical areas analyzed in the human brain, in the fed and fasted conditions (upper panels), with H–F SDP values superimposed to anatomical T_{2w} images. The corresponding enlargements of the cortical areas are shown below. E: Bar graphs of SDP, D_{slow} and D_{fast} values (mean ± SD) in the fed and fasted states. $N_{fed} = 55$, $N_{fasted} = 114$ in L–R; $N_{fed} = 104$, $N_{fasted} = 106$ in A–P and $N_{fed} = 102$, $N_{fasted} = 83$ in H–F. F: "Appetite Index" histogram for the fed (blue) and fasted (red) human hypothalamus calculated using LDA. G: Identification of the areas representing the position of the 5% of the points located in the lower (fed) and upper (fasted) extremes of the Appetite Index histogram.

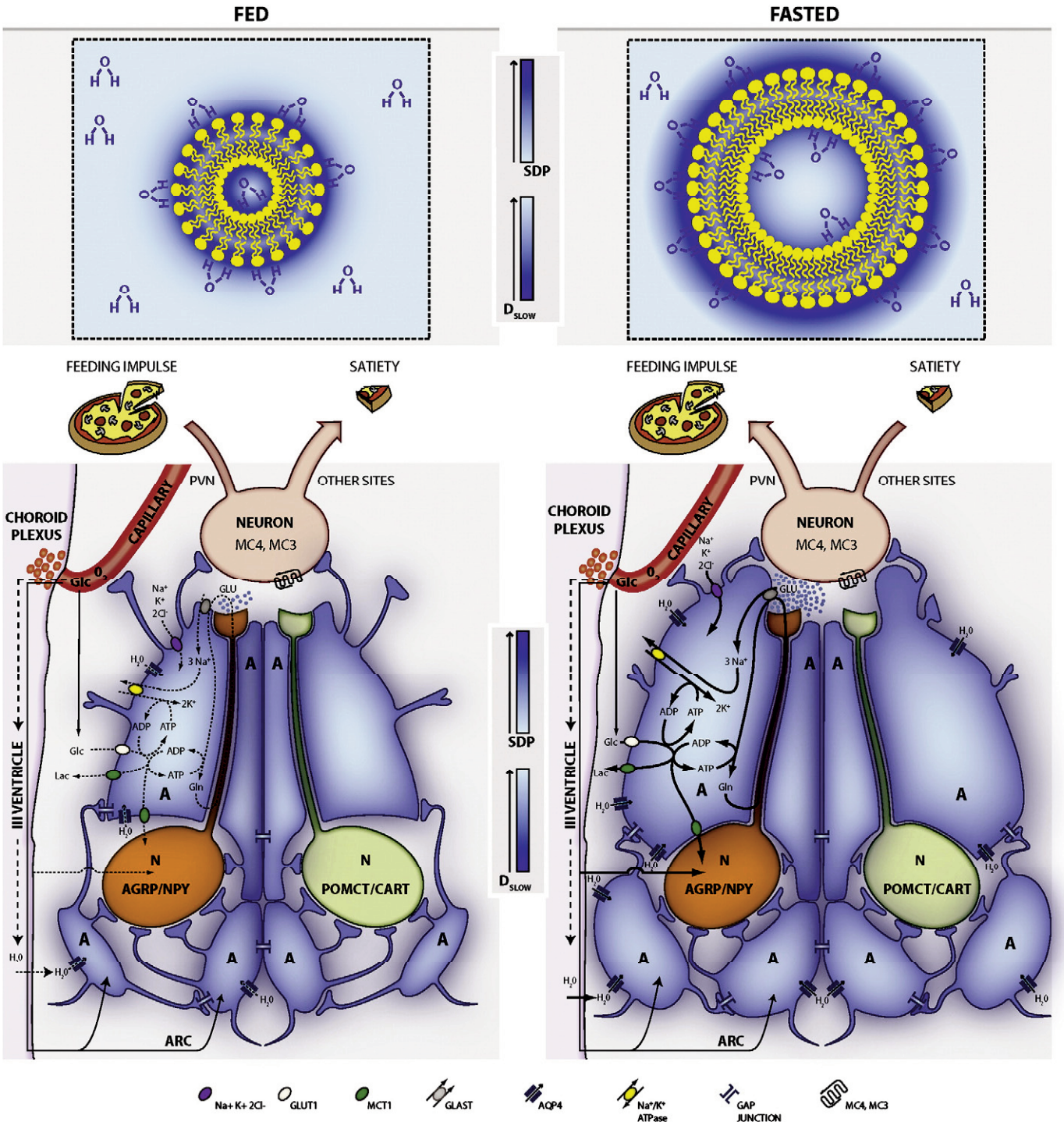

Fig. 5. Neuroglial metabolic coupling and astrocytic volume changes underlie the orexigenic hypothalamic activation as detected by fDWI. The upper panels illustrate the effects of volume changes in the phase distribution (SDP) and dynamics (D_{slow}) of water molecules around the plasma membrane, under the fed (left) and fasted (right) conditions. Water molecules close to the plasma membrane (dark blue) experience more restricted diffusional motions than those far apart (light blue). Increases in astrocytic volume (right) produce; (i) an increase in the available membrane surface, augmenting the contribution of diffusionally restricted water molecules (increased SDP, more water molecules in the dark blue area) and (ii) a decrease in the average obstructions allowing faster average water diffusion (increased D_{slow}, faster diffusion in the light blue area). The lower panels illustrate the neuroglial metabolic coupling mechanisms and associated volume responses in the fed (left) and fasted (right) hypothalamus. During orexigenic neurotransmission, excess glutamate released to the synaptic cleft by AGRP/NPYY neurons (orange) is recaptured by surrounding astrocytes (blue), together with $3Na^+$, through the astrocytic glutamate cotransporters GLAST (gray). Intracellular sodium ions thus incorporated are extruded to the extracellular space, through the electrogenic Na^+/K^+ ATPase (yellow), incorporating two intracellular K^+ ions. Astrocytic glutamate produces glutamine, through glutamine synthase, which is later recaptured by the neurons to operate the glutamine cycle. Astrocytic ATP molecules required for glutamine synthesis and the Na/K^+ ATPase, are generated from plasma glucose, after transport through GLUT1 (white), by anaerobic glycolysis and the tricarboxylic acid cycle. Lactate produced is extruded through the monocarboxylate transporter (MCT1, green) and potentially oxidized by surrounding neurons. Additional K^+ ions may be incorporated to the astrocyte through the $Na^+K^+2Cl^-$ cotransporter (purple), resulting in increased intracellular K^+ concentrations and thus triggering, an osmotically driven, aquaporin 4 (AQP4) mediated (blue channel), water transport and astrocytic swelling. Under fasting conditions (lower right), orexigenic firing is increased (darker lines) as well as glutamatergic neurotransmission (increased glutamate in the synaptic cleft), resulting in augmented ionic and water trafficking (darker arrows, more water influx through AQP4). The accumulated K^+ in one astrocyte may be transferred to the neighboring astroglia, through gap junctions (inverted brackets), providing a spreading mechanism for the swelling response through the astrocyte syncithium. The central color coded bar graphs, represent variations of SDP (increase as dark blue) and D_{slow} (increase as light blue), as detected by fDWI. A: Astrocyte, ARC: Arcuate Nucleus, PVN: Paraventricular Nucleus, MC4, MC3: Melanocortin receptors, N: Neuron, AGRP/NPY: Agouti Related Protein/NeuroPeptideY, POMPCT/CART: Proopiomielanocortin Transcript/Cocaine and Amphetamine Regulated Transcript. Mechanisms are shown only in one astrocyte for simplicity.

membranes. The redistribution may also reflect the concomitant increment of glial volume reported to occur during neuronal activation (Andrew and MacVicar, 1994; Hertz et al., 2007; Le Bihan, 2007). In our case, the increase in diffusion parameters detected during fasting, might reveal the osmotic swelling of glial cells in the vicinity of stimulated orexigenic synapses, as expected to occur during increased glutamatergic neurotransmission (Hansson et al., 2000; Simard and Nedergaard, 2004) (Fig. 5, lower panels). Importantly, these changes become detectable even after 16 h of fasting in mice and may be even localized within the subhypothalamic regions as the Arcuate Nucleus, the Ventromedial Nucleus and the Dorsomedial Nucleus.

More specifically, under fasting conditions, excess glutamate released to the orexigenic cleft is recaptured by surrounding astrocytes, by Na^+ dependent cotransport mainly through the GLAST/EAAT1 and GLT-1/EAAT2 transporters, with a $3Na^+$ per glutamate stoichiometry (Anderson and Swanson, 2000). The three sodium ions incorporated in this way, are extruded to the extracellular space, in exchange with two potassium ions through the Na^+/K^+ ATPase. Astrocytic ATP required for the operation of the Na^+/K^+ ATP-ase and glutamine synthesis during activation by fasting, is thought to be derived from increased glucose consumption and metabolism by oxidative and glycolytic pathways (Violante et al., 2009). This increased metabolic demand results in an increased hypothalamic microvascular blood flow, a circumstance consistent with the changes detected here by SPM and LDA under low b weightings (Fig. 2D). Additional K^+ ions accumulated in the extracellular space during orexigenic firing, may enter the astrocyte by stimulation of the $Na^+/K^+/2Cl^-$ cotransporter (Hertz et al., 2007). Indeed, increased K^+ concentrations are known to be tightly coupled to neuronal activation, and have been detected using metallographic microscopic imaging approaches (Goldschmidt et al., 2004). Taken together, these processes lead to intracellular potassium accumulation during activation, a circumstance triggering a concomitant water influx and volume increase of the astrocytes, mainly mediated through the highly abundant aquaporin AQP-4 (Badaut et al., 2002). The osmotic swelling response associated with orexigenic stimulation, is proposed to occur initially in few astrocytes, those surrounding the orexigenic clefts, but can be rapidly extended to a plethora of neighboring astrocytes, through the numerous interconnecting gap junctions of the network arrangement (Halassa and Haydon, 2010). This increases significantly the spatial distribution of the orexigenic activation and makes it MRI detectable. The osmotic swelling response associated with hypothalamic fasting appears not to be isotropic, suggesting smaller anatomical restrictions to volume increase in the directions where the increase in diffusion parameters is observed.

The fDWI approach to the fasting paradigm explored here is not devoid of limitations. In particular, a higher anatomical resolution is desirable, but limited at this field by the S/N obtainable, particularly at high b values. This may be improved by increasing the number of averages, at the compromise of augmenting linearly the image acquisition time. In this respect, the use of single shot EPI readout may help to decrease the acquisition time. However, this is a very demanding technique at high fields, leading frequently to distorted hypothalamic geometry, making difficult in our hands an adequate pixel by pixel analysis of the hypothalamus and its substructures. Additional limitations may derive from the constrains imposed by the biexponential model, in particular by the potential influence of microvascular flow on the diffusion coefficient measurements (Autio et al., 2011; Miller et al., 2007). On these grounds, the implementation of integral dynamic model considering diffusion and flow would represent a considerable improvement (Le Bihan, 2008). In any case, model imposed limitations may be overcome through the use of a model-free approach, as the LDA strategy proposed here. Finally, despite its inherent limitations, fDWI presents valuable advantages over other non-invasive methods of investigating hypothalamic physiology. fDWI provides improved anatomical resolution over the PET FDG method, highlights diffusion alterations, an event not detectable by fMRI BOLD and avoids the use of potentially toxic Mn^{2+} doses required by MEMRI, becoming then fully translational to the clinic.

Conclusion

In summary, our results show that hypothalamic activation by fasting in mice or humans can be detected non-invasively by diffusion weighted magnetic resonance imaging through changes in the water diffusion parameters. These findings may prove useful in the diagnostic imaging of appetite disorders and can be extended easily to visualize other hypothalamic activation dysfunctions.

Acknowledgments

Authors are indebted to Dr. Diana Quiñones Tapia for expert neuroradiological assistance during the human studies and to Mr. Javier Pérez CSIC, for careful, professional drafting of the illustrations.

References

Anderson, C.M., Swanson, R.A., 2000. Astrocyte glutamate transport: review of properties, regulation, and physiological functions. Glia 32, 1–14.
Andrew, R.D., MacVicar, B.A., 1994. Imaging cell volume changes and neuronal excitation in the hippocampal slice. Neuroscience 62, 371–383.
Autio, J.A., Kershaw, J., Shibata, S., Obata, T., Kanno, I., Aoki, I., 2011. High b-value diffusion-weighted fMRI in a rat forepaw electrostimulation model at 7 T. NeuroImage 57, 140–148.
Badaut, J., Lasbennes, F., Magistretti, P.J., Regli, L., 2002. Aquaporins in brain: distribution, physiology, and pathophysiology. J. Cereb. Blood Flow Metab. 22, 367–378.
Burton, P., Gurrin, L., Sly, P., 1998. Extending the simple linear regression model to account for correlated responses: an introduction to generalized estimating equations and multi-level mixed modelling. Stat. Med. 17, 1261–1291.
Carnell, S., Gibson, C., Benson, L., Ochner, C.N., Geliebter, A., 2011. Neuroimaging and obesity: current knowledge and future directions. Obes. Rev. 13, 43–56.
Coll, A.P., Farooqi, I.S., O'Rahilly, S., 2007. The hormonal control of food intake. Cell 129, 251–262.
Delgado, T.C., Violante, I.R., Nieto-Charques, L., Cerdan, S., 2011. Neuroglial metabolic compartmentation underlying leptin deficiency in the obese ob/ob mice as detected by magnetic resonance imaging and spectroscopy methods. J. Cereb. Blood Flow Metab. 31, 2257–2266.
Flint, J., Hansen, B., Vestergaard-Poulsen, P., Blackband, S.J., 2009. Diffusion weighted magnetic resonance imaging of neuronal activity in the hippocampal slice model. NeuroImage 46, 411–418.
Garcia-Martin, M.L., Ballesteros, P., Cerdan, S., 2001. The metabolism of water in cells and tissues as detected by NMR methods. Prog. Nucl. Magn. Reson. Spectrosc. 39, 41–77.
Gautier, J.F., Chen, K., Salbe, A.D., Bandy, D., Pratley, R.E., Heiman, M., Ravussin, E., Reiman, E.M., Tataranni, P.A., 2000. Differential brain responses to satiation in obese and lean men. Diabetes 49, 838–846.
Goldschmidt, J., Zuschratter, W., Scheich, H., 2004. High-resolution mapping of neuronal activity by thallium autometallography. NeuroImage 23, 638–647.
Halassa, M.M., Haydon, P.G., 2010. Integrated brain circuits: astrocytic networks modulate neuronal activity and behavior. Annu. Rev. Physiol. 72, 335–355.
Hansson, E., Muyderman, H., Leonova, J., Allansson, L., Sinclair, J., Blomstrand, F., Thorlin, T., Nilsson, M., Ronnback, L., 2000. Astroglia and glutamate in physiology and pathology: aspects on glutamate transport, glutamate-induced cell swelling and gap-junction communication. Neurochem. Int. 37, 317–329.
Hastie, T., Tibshirani, R., Friedman, J., 2001. The elements of statistical learning: data mining, inference and prediction. Springer Series in Statistics. New York.
Hertz, L., Peng, L., Dienel, G.A., 2007. Energy metabolism in astrocytes: high rate of oxidative metabolism and spatiotemporal dependence on glycolysis/glycogenolysis. J. Cereb. Blood Flow Metab. 27, 219–249.
Le Bihan, D., 2003. Looking into the functional architecture of the brain with diffusion MRI. Nat. Rev. Neurosci. 4, 469–480.
Le Bihan, D., 2007. The 'wet mind': water and functional neuroimaging. Phys. Med. Biol. 52, R57–R90.
Le Bihan, D., 2008. Intravoxel incoherent motion perfusion MR imaging: a wake-up call. Radiology 249, 748–752.
Le Bihan, D., Urayama, S., Aso, T., Hanakawa, T., Fukuyama, H., 2006. Direct and fast detection of neuronal activation in the human brain with diffusion MRI. Proc. Natl. Acad. Sci. U. S. A. 103, 8263–8268.
Liu, T., Kong, D., Shah, B.P., Ye, C., Koda, S., Saunders, A., Ding, J.B., Yang, Z., Sabatini, B.L., Lowell, B.B., 2012. Fasting activation of AgRP neurons requires NMDA Receptors and involves spinogenesis and increased excitatory tone. Neuron 73, 511–522.
Mahankali, S., Liu, Y., Pu, Y., Wang, J., Chen, C.W., Fox, P.T., Gao, J.H., 2000. In vivo fMRI demonstration of hypothalamic function following intraperitoneal glucose administration in a rat model. Magn. Reson. Med. 43, 155–159.
Matsuda, M., Liu, Y., Mahankali, S., Pu, Y., Mahankali, A., Wang, J., DeFronzo, R.A., Fox, P.T., Gao, J.H., 1999. Altered hypothalamic function in response to glucose ingestion in obese humans. Diabetes 48, 1801–1806.

Miller, K.L., Bulte, D.P., Devlin, H., Robson, M.D., Wise, R.G., Woolrich, M.W., Jezzard, P., Behrens, T.E., 2007. Evidence for a vascular contribution to diffusion FMRI at high b value. Proc. Natl. Acad. Sci. U. S. A. 104, 20967–20972.
Morton, G.J., Cummings, D.E., Baskin, D.G., Barsh, G.S., Schwartz, M.W., 2006. Central nervous system control of food intake and body weight. Nature 443, 289–295.
Niendorf, T., Dijkhuizen, R.M., Norris, D.G., van Lookeren Campagne, M., Nicolay, K., 1996. Biexponential diffusion attenuation in various states of brain tissue: implications for diffusion-weighted imaging. Magn. Reson. Med. 36, 847–857.
Parkinson, J.R., Chaudhri, O.B., Bell, J.D., 2009. Imaging appetite-regulating pathways in the central nervous system using manganese-enhanced magnetic resonance imaging. Neuroendocrinology 89, 121–130.
Paxinos, G., Franklin, K.B.J., 2001. The Mouse Brain in Stereotaxic Coordinates. Academic Press, New York.
Sehy, J.V., Ackerman, J.J., Neil, J.J., 2002. Evidence that both fast and slow water ADC components arise from intracellular space. Magn. Reson. Med. 48, 765–770.
Simard, M., Nedergaard, M., 2004. The neurobiology of glia in the context of water and ion homeostasis. Neuroscience 129, 877–896.
Spanswick, D.C., Simonds, S.E., Cowley, M.A., 2012. Transmitter time: synaptic plasticity and metabolic memory in the hypothalamus. Cell Metab. 15, 275–276.
Tataranni, P.A., Gautier, J.F., Chen, K., Uecker, A., Bandy, D., Salbe, A.D., Pratley, R.E., Lawson, M., Reiman, E.M., Ravussin, E., 1999. Neuroanatomical correlates of hunger and satiation in humans using positron emission tomography. Proc. Natl. Acad. Sci. U. S. A. 96, 4569–4574.
van den Pol, A.N., Wuarin, J.P., Dudek, F.E., 1990. Glutamate, the dominant excitatory transmitter in neuroendocrine regulation. Science 250, 1276–1278.
Violante, I.R., Anastasovska, J., Sanchez-Canon, G.J., Rodrigues, T.B., Righi, V., Nieto-Charques, L., Parkinson, J.R., Bloom, S.R., Bell, J.D., Cerdan, S., 2009. Cerebral activation by fasting induces lactate accumulation in the hypothalamus. Magn. Reson. Med. 62, 279–283.
Yang, Y., Atasoy, D., Su, H.H., Sternson, S.M., 2011. Hunger states switch a flip-flop memory circuit via a synaptic AMPK-dependent positive feedback loop. Cell 146, 992–1003.

frontiers in
NEUROENERGETICS

REVIEW ARTICLE
published: 13 June 2013
doi: 10.3389/fnene.2013.00006

Hypothalamic metabolic compartmentation during appetite regulation as revealed by magnetic resonance imaging and spectroscopy methods

Blanca Lizarbe[1], Ania Benitez[1,2], Gerardo A. Peláez Brioso[1,2], Manuel Sánchez-Montañés[2], Pilar López-Larrubia[1], Paloma Ballesteros[3] and Sebastián Cerdán[1]*

[1] Department of Experimental Models of Human diseases, Laboratory of Imaging and Spectroscopy by Magnetic Resonance, Instituto de Investigaciones Biomédicas "Alberto Sols" CSIC/UAM, Madrid, Spain
[2] Departmento de Informática, Escuela Politécnica Superior, Universidad Autónoma de Madrid, Cantoblanco, Madrid, Spain
[3] Laboratorio de Síntesis Orgánica e Imagen Molecular por Resonancia Magnética, Facultad de Ciencias, Universidad Nacional de Educación a Distancia, Unidad Asociada al CSIC, Madrid, Spain

Edited by:
Mary McKenna, University of Maryland, USA

Reviewed by:
Caroline Rae, University of New South Wales, Australia
Brenda Bartnik-Olson, Loma Linda University, USA

***Correspondence:**
Sebastián Cerdán, Department of Experimental Models of Human diseases, Instituto de Investigaciones Biomédicas "Alberto Sols" CSIC/UAM., c/ Arturo Duperier 4, Madrid 28029, Spain
e-mail: scerdan@iib.uam.es

We review the role of neuroglial compartmentation and transcellular neurotransmitter cycling during hypothalamic appetite regulation as detected by Magnetic Resonance Imaging (MRI) and Spectroscopy (MRS) methods. We address first the neurochemical basis of neuroendocrine regulation in the hypothalamus and the orexigenic and anorexigenic feed-back loops that control appetite. Then we examine the main MRI and MRS strategies that have been used to investigate appetite regulation. Manganese-enhanced magnetic resonance imaging (MEMRI), Blood oxygenation level-dependent contrast (BOLD), and Diffusion-weighted magnetic resonance imaging (DWI) have revealed Mn^{2+} accumulations, augmented oxygen consumptions, and astrocytic swelling in the hypothalamus under fasting conditions, respectively. High field ^{1}H magnetic resonance *in vivo*, showed increased hypothalamic myo-inositol concentrations as compared to other cerebral structures. ^{1}H and ^{13}C high resolution magic angle spinning (HRMAS) revealed increased neuroglial oxidative and glycolytic metabolism, as well as increased hypothalamic glutamatergic and GABAergic neurotransmissions under orexigenic stimulation. We propose here an integrative interpretation of all these findings suggesting that the neuroendocrine regulation of appetite is supported by important ionic and metabolic transcellular fluxes which begin at the tripartite orexigenic clefts and become extended spatially in the hypothalamus through astrocytic networks becoming eventually MRI and MRS detectable.

Keywords: appetite regulation, hypothalamus, neuroendocrine signaling, neuroglial compartmentation, magnetic resonance imaging, magnetic resonance spectroscopy

The hypothalamus is a small cerebral structure responsible for the integral homeostasis of vital systemic functions including global energy metabolism, appetite, thirst and osmoregulation, thermoregulation, circadian rhythms, and some fundamental survival responses such as aggressiveness (Swaab et al., 1992; Ganong, 1993; Lin et al., 2011). It operates as a highly sophisticated neuroendocrine transducer, sensing peripheral endocrine signals and transforming them in intracerebral excitatory or inhibitory neurotransmitter events that deliver the homeostatic response back to the periphery (McEwen, 1989; Levin et al., 2011). Hypothalamic function involves frequently the operation of highly elaborated feed-back control loops (**Figure 1**).

Activation of the hypothalamic interface is thought to proceed essentially in two steps, an initial endocrine activation, involving the receptor-mediated interaction of the hormone or neuropeptide with the presynaptic terminal, followed either by the activation or inhibition of excitatory or inhibitory neurotransmitter release at the postsynaptic cleft. The neurotransmitters glutamate and GABA play a central role in this process mediating glutamatergic (Tong et al., 2007) or GABAergic (Xu et al., 2012) neurotransmissions through specific neuronal pathways of the hypothalamus. These pathways trigger eventually the release of hypothalamic neuropeptides or hormones to the blood stream, to other hypothalamic structures and the hypophysis (McEwen, 1989; Thorburn and Proietto, 1998) or activate the brain stem autonomic neurocircuitry (Palkovits, 1999), all these events geared to maintain systemic homeostasis.

In the last decades, important progress has been reached characterizing the initial endocrine step, identifying the corresponding systemic and intrahypothalamic neuropeptides and receptors or the morphological pathways and tracts transmitting these signals within the different hypothalamic nuclei or even to extra-hypothalamic structures (McEwen, 1989; Lantos et al., 1995). Progress has been slower, however, in the characterization

Abbreviations: MRI, Magnetic Resonance Imaging; MRS, Magnetic Resonance Spectroscopy; MEMRI, Manganese-enhanced Magnetic Resonance Imaging; BOLD, Blood Oxygenation Level-dependent contrast; DWI, Diffusion-weighted Imaging; DIA, Dehydration-induced Anorexia.

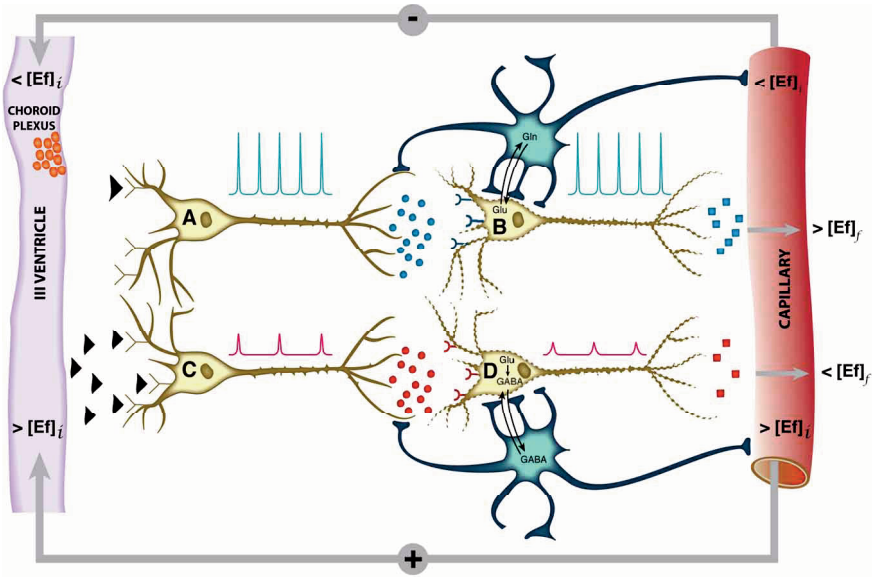

FIGURE 1 | Schematic representation of the neuroendocrine interface and feed-back control loops. Neuroendocrine integration may involve both, neurons receiving endocrine signals and releasing neurotransmitters (A, C) or neurons receiving neurotransmitter signals and releasing neuropeptides or hormones (B, D). A typical feed-back control loop is illustrated. The initial decrease in plasma concentration of an endocrine inhibitory effector ($<[Ef]_i$), passes the blood brain barrier, releasing the inhibition of neuron A and triggering action potentials (blue spikes) and the synaptic release of an excitatory neurotransmitter as glutamate (blue circles). This activates neuron B and triggers the release of an endocrine signal resulting eventually in an increase in the final plasma concentration of the effector ($>[Ef]_f$). Glutamatergic neurotransmission involves necessarily the operation of the neuroglial glutamine cycle. The initial increase in the plasma concentration of the effector ($>[Ef]_i$) inhibits neuron C, decreasing the frequency and amplitude of the action potentials and triggering the release of an inhibitory neurotransmitter as GABA (red circles). This causes neuron D to reduce or suspend the release of the effector Ef, resulting eventually in an homeostatic reduction in the plasma concentration of ($<[Ef]_f$),. GABAergic neurotransmission involves necessarily the neuroglial glutamate-GABA cycle. Both negative and positive feed-back loops tend to maintain the plasma concentration of the effector Ef stable within a narrow range. Glu, glutamate; Gln, glutamine; GABA, γ-aminobutyric acid.

of the neurotransmitter events underlying the neuroendocrine response. In this respect, early interpretations conceived the hypothalamic response as a neuronal only event. The evolution of the tripartite synapse concept (Araque et al., 1999; Halassa et al., 2007; Santello et al., 2012), however, revealed the essential role of astroglia in the modulation of synaptic neurotransmission, gaining for astrocytes a fundamental role in neuroendocrine signaling (Garcia-Ovejero et al., 2005; Garcia-Segura et al., 2008). In some important cases, as in thyroid hormones, astrocytes are even required not only to modulate synaptic transmission, but to generate the active endocrine response (Mohacsik et al., 2011). Furthermore, glutamatergic or GABAergic neurotransmissions involve necessarily the operation of transcellular cycles of glutamate and GABA between neurons and astrocytes (Hertz, 2004; Dienel and Hertz, 2005), stressing the fundamental role of neuroglial compartmentation in hypothalamic function. However, further improvements in our understanding of the role of metabolic compartmentation in neuroendocrine function have been often hampered by the limited accessibility of sufficiently robust non-invasive methods to monitor neuronal activation and transcellular neurotransmitter cycling in the hypothalamus *in vivo*.

Magnetic Resonance Imaging (MRI) and Spectroscopy (MRS) approaches are known to be well endowed to observe hypothalamic morphology and function. Briefly, Manganese-enhanced MRI (MEMRI) techniques allow to monitor neuronal activation through the accumulation of Mn^{2+} and its effects in T_1-weighted images (Koretsky and Silva, 2004), Blood Oxygen Level-dependent (BOLD) methods detect cerebral activation through associated hemoglobin deoxygenation and perfusion changes (Zhu et al., 1998; Logothetis and Wandell, 2004) and Diffusion-weighted Imaging (DWI) visualize microstructural changes in the diffusion coefficient of water (Le Bihan, 2003), reflecting most probably activation induced neurocellular swelling events. In addition, ^{1}H MRS *in vivo* is able to characterize the metabolic profile of the hypothalamus and its changes during activation (Duarte et al., 2012) and ^{13}C MRS provides comprehensive information on neuroglial oxidative metabolism and neurotransmitter cycling (Cruz and Cerdan, 1999; Gruetter et al., 2003; Rothman et al., 2003). Taken together, these techniques are beginning to yield precious information on hypothalamic physiology. However, a critical overview of the information gained with the different methods and an integrative interpretation of the results obtained becomes currently necessary, to be able to recapitulate and design more precisely the protocols of future strategies.

In this review, we examine the information gained thus far with these approaches and provide an integrative interpretation that highlights the vital role of hypothalamic neuroglial compartmentation in the cerebral control of global energy homeostasis *in vivo*.

HYPOTHALAMIC CONTROL OF APPETITE

Recent years have witnessed an important development in the understanding of the hypothalamic mechanisms involved in appetite control and global energy homeostasis (Coll et al., 2007). Appetite control is currently understood to operate on the balance of positive and negative peripheral signals from the adipose tissue, the pancreas, and the gastrointestinal tract, modulating intrahypothalamic and brain stem autonomic activities that determine the early hunger or satiety responses and the long-term body weight and energy balance (Schwartz and Morton, 2002; Morton et al., 2006). Peripheral signals from the gut include mainly peptide YY (PYY), oxyntomodulin (OXM), ghrelin, glucagon-like peptide 1 (GLP-1), and colecystokinin (CCK). Adipose tissue, pancreatic, and gut-derived peptides influence the hypothalamic circuitry providing short-term hunger or satiety signals and resulting in the long term in anabolic (−) or catabolic (+) effects in energy expenditure, increasing or decreasing body weight. In particular, these mediators modulate the activation of the arcuate (ARC), paraventricular (PVN), dorsomedial nuclei (DMN), and ventromedial nuclei (VMN) of the hypothalamus which control food intake through a delicate balance of orexigenic and anorexigenic pathways operated by specific neurons and neuropeptides (Stanley et al., 2005).

Figure 2 illustrates our current views on the mechanism of appetite control within the hypothalamus. Hypothalamic control of energy homeostasis involves the modulation of orexigenic (stimulation of food intake) and anorexigenic (satiety signals) pathways, that determine the positive or negative balance between food intake and energy expenditure (Schwartz et al., 2000; Schwartz and Morton, 2002; Morton et al., 2006). Briefly, leptin and insulin produced by fat tissues and pancreas, circulate in blood in amounts proportional to body fat and blood glucose. These long-term systemic effectors reach easily the hypothalamic ARC nucleus, an area of relatively permeable Blood Brain Barrier (BBB) and thus highly accessible to activation by systemic effectors. Insulin and leptin, inhibit the orexigenic Neuropeptide Y (NPY) and Agouti-related Peptide (AgRP) neurons (purple) and activate the anorexigenic neurons (green) of the melanocortin (α-MSH)/cocaine and amphetamine-regulated transcript (CART) pathways, resulting in decreased food intake and increased energy expenditure. Long-term increases in leptin or insulin lead to receptor desensitization

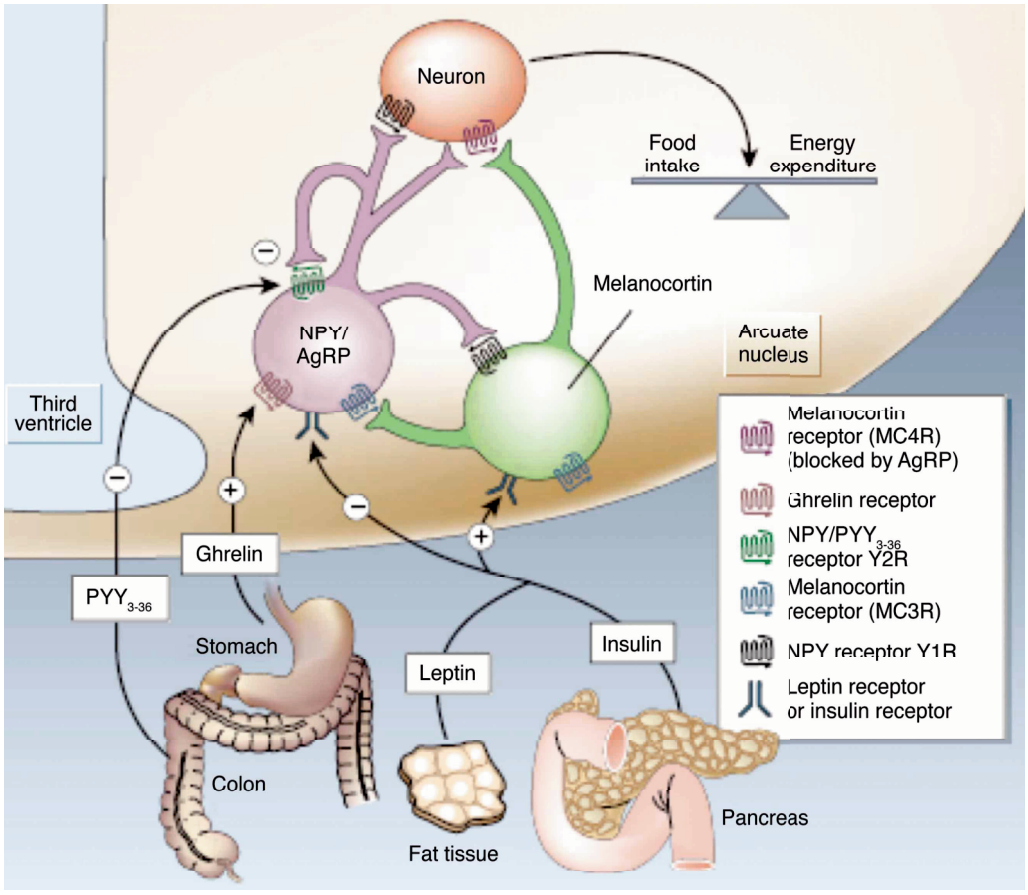

FIGURE 2 | Hypothalamic control of global energy balance. Appetite is regulated by a complex feed-back loop involving endocrine signals originated in peripheral tissues and intrahypothalamic peptides. Leptin and insulin inhibit the orexigenic NPY/AgRP neurons (purple) and stimulate the anorexigenic melanocortin neurons (green), resulting in a reduction of food intake. Ghrelin or PYY_{3-36} activate or inhibit the NPY/AgRP neurons resulting in orexigenic or anorexigenic responses, respectively. Taken from Schwartz and Morton (2002). Reproduced with permission of the publisher.

and insulin or leptin "resistance" increasing plasma glucose levels and fat accumulation, producing eventually obesity and diabetes. Ghrelin and peptide PYY_{3-36}, released by the stomach and the colon, respectively, provide the Arcuate with positive or negative short-term signals of appetite or satiety through the selective activation or inhibition of the NPY/AgRP neurons, resulting in hunger or satiety, respectively (Tang-Christensen et al., 2004).

Despite these important advances in the understanding of the endocrine processes controlling food intake and energy expenditure, less is known on how these modify the neuroglial metabolic coupling mechanisms supporting the activation or inhibition of the orexigenic or anorexigenic pathways. However, important evidence supports the crucial role of glutamatergic or GABAergic neurotransmissions on hypothalamic function (Collin et al., 2003; Hentges et al., 2004). In particular, intracerebral glutamate administration is known to elicit an intense orexigenic response (Stanley et al., 1993) while knock out mice in glutamate or GABA vesicular transporters are known to exhibit altered feeding behavior (Tong et al., 2007; Xu et al., 2012). Notably, how glutamatergic or GABAergic neurotransmissions are modulated by orexigenic or anorexigenic stimuli *in vivo* has not been directly addressed.

MAGNETIC RESONANCE IMAGING STUDIES OF HYPOTHALAMIC APPETITE REGULATION

MANGANESE-ENHANCED MAGNETIC RESONANCE IMAGING (MEMRI)

MEMRI is currently thought to directly reflect the neuronal accumulation of Mn^{2+} through Voltage-dependent Calcium Channels in stimulated brain areas, an event that extends transynaptically and enables MEMRI to map neuronal connectivities (Pautler, 2004). Mn^{2+} accumulation may actually exceed the neuronal tracts and extend to surrounding astrocytes and astrocytic networks, since abundant gap junctions exist in astrocytes (Andrew et al., 1981) and neuronal activation has shown to elicit astrocytic intracellular and intercellular Ca^{2+} waves (Jaffe, 2006, 2008, 2010). Paramagnetic Mn^{2+} ions mimic closely the size of diamagnetic Ca^{2+}, thus providing an ideal surrogate probe to monitor Ca^{2+} dynamics during neuronal activation. Hydrated Mn^{2+} ions are classically known to induce a strong reduction in the T_1 of water, resulting in bright contrast in T_1-weighted images in those activated areas accumulating Mn^{2+} (Lee et al., 2005). MEMRI is not devoid from limitations, since Mn^{2+} administration is known to become neurotoxic, competing with endogenous Ca^{2+} fluxes, pertubing hypothalamic levels of metabolites and interfering with the operation of vital metabolic pathways as the tricarboxylic acid cycle and neurotransmitter cycles (Zwingmann et al., 2003, 2004).

Despite these limitations, MEMRI has been successfully used to detect brain activity (Aoki et al., 2002) and neuronal architecture (Aoki et al., 2004) in rodents since the early 2000s, when the first application to the study of hypothalamic functionality appeared (Morita et al., 2002). Morita et al. detected increases in T_1-weighted images in the rat brain after intravenously infusing $MnCl_2$, but they had to disrupt the BBB for manganese to diffuse properly through the brain. As an activation agent, they injected NaCl to the rat brain and found signal increases in areas involved in central osmotic regulation, including the hypothalamic area. Their observations were validated by a positive correlation with c-Fos expression levels in the activated areas and demonstrated, for the first time to our knowledge, the possibility of studying hypothalamic functionality with Mn^{2+}-enhanced MRI, although this required BBB disruption. Later on, in 2006, MEMRI was successfully implemented without compromising the BBB (Yu et al., 2005) to map regions of accumulated sound-evoked activity in mice, after intraperitoneal administration of $MnCl_2$. Soon after, the first MEMRI study of hypothalamic activation associated with feeding, without compromising the BBB (Kuo et al., 2006) was published. Authors infused intravenously $MnCl_2$ during the MRI acquisition protocol and compared signal enhancement in the hypothalamus of fed or overnight-fasted mice, obtaining significant differences in different hypothalamic nuclei. This revealed that region-specific Mn^{2+} enhancement in the mouse brain could be modulated by fasting. Since then, several MEMRI studies have focused on the hypothalamic functionality associated to feeding, by studying the effect of peptide administration and its pathways of activation (Chaudhri et al., 2006; Parkinson et al., 2009; Hankir et al., 2011), cerebral activation in transgenic mice (Delgado et al., 2011) and hypothalamic response to alterations of food intake (Just and Gruetter, 2011; Anastasovska et al., 2012).

Finally, recent years have witnessed growing interest on MEMRI applications, geared to a better understanding of the molecular mechanisms by which Mn^{2+} produces alterations of the hypothalamic physiological processes. In particular, a significant number of publications focused on studies combing MEMRI with other imaging or spectroscopic techniques (Delgado et al., 2011; Just et al., 2011; Gutman et al., 2012), or even using MEMRI information to understand other functional techniques (Silva, 2012).

Figure 3 provides a useful frame for these concepts illustrating the use of MEMRI in the hypothalamus of control and obese mice. Mn^{2+} infused in the tail vein of normal and obese mice resulted in a larger increase in the intensity of the Arcuate and VMN of obese animals as compared to the controls, a circumstance revealing the orexigenic stimulation of obese animals and the high anatomical and neurophysiological resolution of the approach.

BLOOD OXYGENATION LEVEL DEPENDENT (BOLD) CONTRAST

BOLD imaging is one of the most widely used techniques to study brain function in animals and man, based on detecting increases in oxygen consumption and associated hemodynamic responses during neuronal activation. In the neuronal activation process, the ratio between deoxyhemoglobin (paramagnetic) and oxyhemoglobin (diamagnetic) changes, and by studying this ratio, BOLD (Ogawa et al., 1990) can successfully map brain activity.

The use of functional neuroimaging in the study of appetite control started in the late nineties, by monitoring the hypothalamic function after glucose uptake in obese or lean humans (Matsuda et al., 1999), demonstrating for the first time the existence of differential hypothalamic function between lean and obese subjects. Almost at the same time, BOLD imaging

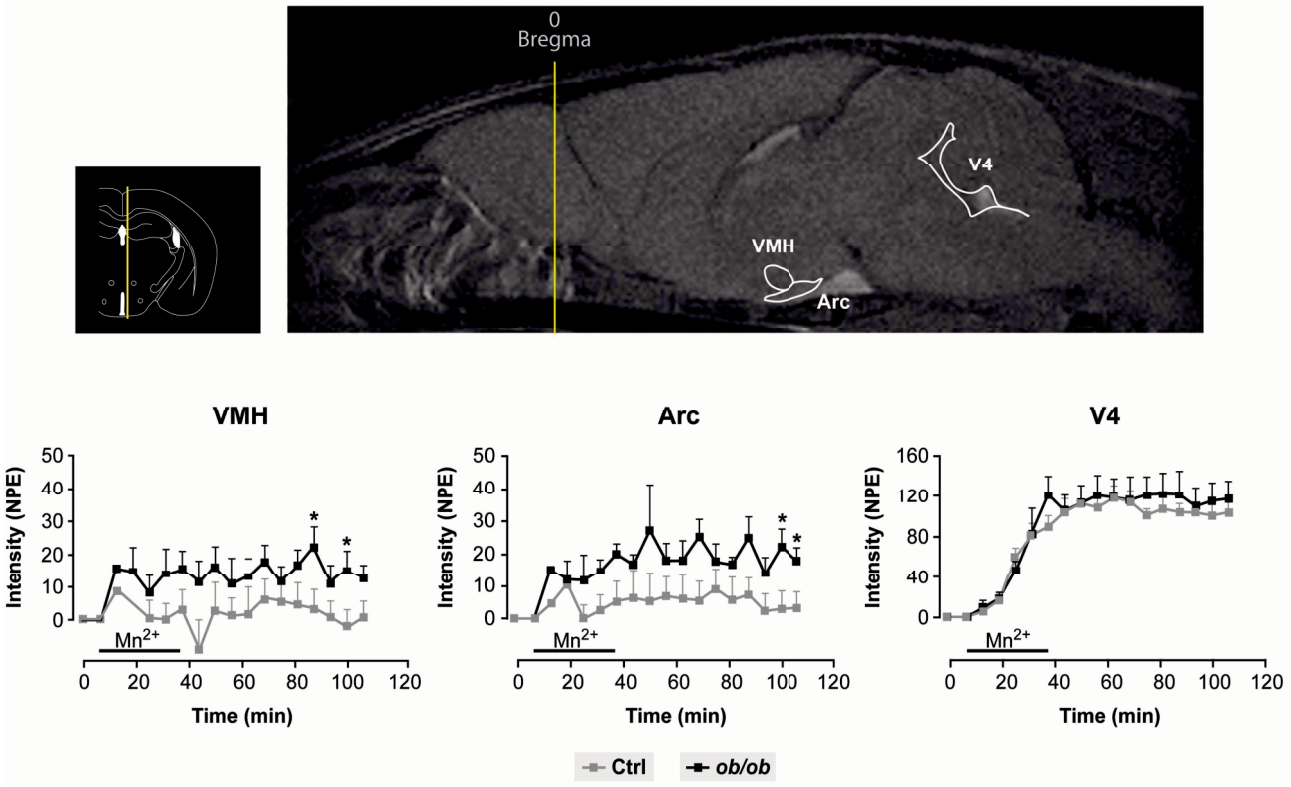

FIGURE 3 | Representative MEMRI response in obese and control mice. Inset upper left: Localization of the hypothalamus, third and fourth ventricles in an anatomical atlas (Paxinos and Franklin, 2001). Upper right: Mn^{2+} induced increase in MR signal intensity (MEMRI) in the arcuate nucleus (Arc), ventromedial nucleus (VMH) and the fourth ventricle (V4). Lower panels: Kinetics of MEMRI increase in VMH, Arc and V4 during and after Mn^{2+} infusion. Note that the obese animals (black squares) show a larger increase in MEMRI than the controls (gray squares) in VMH and Arc, but not in V4, revealing a specific obesity effect in these hypothalamic nuclei. Taken from Delgado et al. (2011). Reproduced with permission of the publisher.

detected hypothalamic functionality in a rat model following intraperitoneal glucose administration (Mahankali et al., 2000) by recording significant decreases of the MRI signal in the hypothalamic region after the injection. A few years later, a positive correlation between blood-oxygenation-level-dependent (BOLD) contrast fMRI and c-fos protein expression was established in activated areas of the rat brain after the administration of anorexigenic agents (Stark et al., 2006), thus validating the use of BOLD in anesthetized rats to identify the pathways of brain response to appetite-modulating signals. Also in rats, different hypothalamic response to glucose administration was detected in lean and obese animals (Chen et al., 2007), with an attenuated BOLD response in obese rats that was positively correlated with the percentage of positive NPY cells in the hypothalamus, and with significantly lower levels of 5-hydroxytryptamine (5-HT). Since then, the use of BOLD imaging for the study of appetite regulation in animals has generated an important number of contributions, mainly related to the effects on hypothalamic activation after the administration of different diets or peptides to rats (Min et al., 2011; Li et al., 2012) and its correlation with endogenous levels of neuropeptides.

In humans, early fMRI studies started investigating cerebral activation with food pictures (Killgore et al., 2003) and the hypothalamic response to different tastes and calories (Smeets et al., 2005). It soon became clear that appetite in humans was the result of very complex and interrelated neuronal circuits, including not only hypothalamus and brainstem, which are the principal homeostatic brain areas regulating body weight, but also corticolimbic and higher cortical regions. Consequently, different authors investigated the neuronal networks that responded to specific orexigenic or anorexigenic signals (Batterham et al., 2007; Miller et al., 2007; Malik et al., 2008). Currently, the applications of BOLD fMRI on studies of appetite regulation are mainly dedicated to the study of hypothalamic response to glucose (Vidarsdottir et al., 2007; Purnell et al., 2011), to the establishment of differences between fMRI responses in obese and non-obese humans (Tomasi et al., 2009), and to the effects of appetite modulating hormones derived from the gastrointestinal tract and adipose tissue, mainly ghrelin (Jones et al., 2012), insulin (Guthoff et al., 2010) and leptin (Baicy et al., 2007; Farooqi et al., 2007).

Figure 4 illustrates a representative application of BOLD imaging to appetite regulation in a study that monitored hypothalamic activation in humans, as induced by a paradigm that showed images of high- and low-calorie foods. Briefly, fMRI was applied to investigate cerebral responses of 13 healthy women by

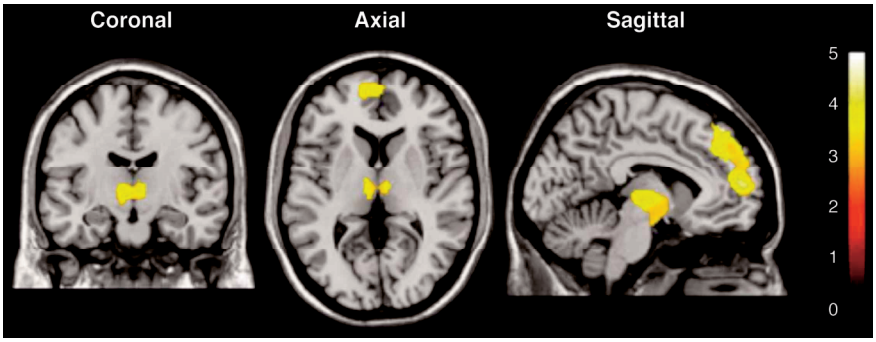

FIGURE 4 | Statistical parametric maps of brain activated regions in the human brain, as measured by BOLD, during the presentation of high-calorie food images. The color bar reflects the scale of the SPM statistic used for the analysis. The dorsolateral and medial prefrontal cortex, the thalamus and the hypothalamus showed significant activation ($P < 0.005$) relative to the control pictures of non-edible food related utensils Reproduced from Killgore et al. (2003) with permission of the publisher.

presenting three categories of images: high-calorie, low-calorie and non-edible food-related utensils. They found areas of activation common to food stimuli regardless of the calorie content, such as the bilateral amygdala/hippocampus region. Besides, high-calorie food stimuli were found to be associated with significant clusters of activation within the medial and dorsolateral prefrontal cortex, medial dorsal thalamus, hypothalamus, corpus callosum, and cerebellum.

DIFFUSION-WEIGHTED IMAGING (DWI)

Diffusion-weighted Imaging (DWI) provides information on the diffusion behavior of water molecules in biological tissues, and can be used to probe and define tissue structures at microscopic scales (Le Bihan, 2003). Since its introduction in 1985, it is the modality of choice for the assessment of stroke in patients (Schellinger et al., 2000) and for studies of white matter diseases (Hagmann et al., 2007).

The interpretation of the biophysical models underlying diffusion changes observed in physiological or pathological states has been a matter of debate in the last decades. Indeed, several models that overcome the conventional monoexponential approach of diffusion (Le Bihan, 2003) have been proposed (Assaf et al., 2002; Jensen and Helpern, 2010; Grinberg et al., 2011).

Conventional DWI has been used to the study of appetite regulation in the hypothalamus (Alkan et al., 2008). This study compared apparent diffusion coefficients (ADC) values in brain regions of obese and non-obese human subjects. Among other areas, the hypothalamus of obese subjects was found to have higher ADC values than the hypothalamic areas of lean patients. Results were explained as an alteration of fluid distribution in obese subjects due to a vasogenic edema. In fact, it has been demonstrated that consumption of fat-rich diets activates proinflammatory responses in the hypothalamus (De Souza et al., 2005), and that, in mice, the ability of high fat diets to induce obesity depends upon the neuronal expression of the mediator of inflammatory signaling MyD88 (Kleinridders et al., 2009). Furthermore, the relationship between hypothalamic inflammation and obesity has become a matter of study and debate (Wisse and Schwartz, 2009; Wang et al., 2012), and DWI is ideally endowed to evaluate its existence *in vivo* (Cazettes et al., 2011). Recent results from our laboratories (Lizarbe et al., 2013) suggest that hypothalamic inflammation may occur not only in obesity, but also transiently during fasting states.

Some years ago, the behavior of diffusion in biological tissues was suggested to represent slow and fast diffusion phases of water that were modified during neuronal activation process (Niendorf et al., 1996; Le Bihan et al., 2006). Since then, several contributions have used the biphasic model to detect and describe more precisely brain activation using DWI in man and studies *in vitro* (Flint et al., 2009; Kohno et al., 2009; Aso et al., 2013). Even model-free approaches have been proposed that confirm and extend the results obtained with the biexponential model (Lizarbe et al., 2013). The use of functional DWI (fDWI) in the study of hypothalamic activation associated to feeding came also from this study. Our results showed that the diffusion coefficients of water in the hypothalamus changed with fasting in both mice and humans. In mice, it became possible to detect changes in individual hypothalamic nuclei, including the ARC, the DMN and the VMN. On these grounds, the application of fDWI to the study of brain activation in general and hypothalamic activity in particular, appears to open a new avenue within the functional neuroimaging field, even in humans. Diffusion changes associated to activation are thought to occur closer -temporally and spatially- to the activated areas than the physiological changes detected with BOLD (Le Bihan et al., 2006), avoiding the use of potentially toxic Mn^{+2} doses. Besides, the possibility of using DWI to detect directional differences through the implementation of Diffusion Tensor Imaging approaches (Le Bihan et al., 2001; Ahn and Lee, 2011) may allow the investigation of neuronal tracts and their potential alterations under different kinds of appetite-related disturbances.

An example on the use of DWI imaging in the study of hypothalamic activation is illustrated in **Figure 5**, through the changes observed in the diffusion parameters of water in different hypothalamic nuclei including the ARC, VMN, and DMN, depicted in **Figure 5A** (Lizarbe et al., 2013). Panels **5B,D,F,**

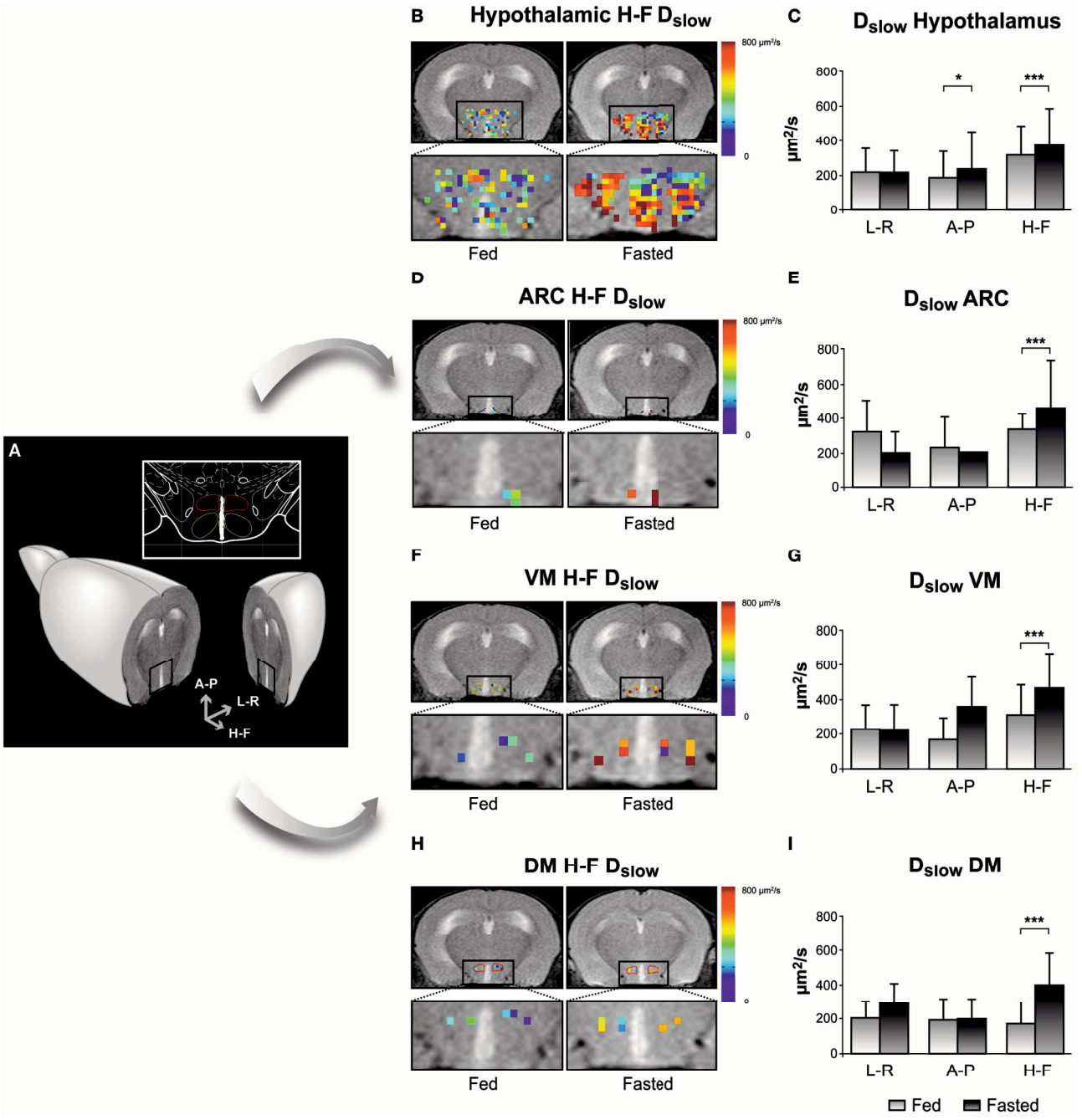

FIGURE 5 | Imaging appetite by fDWI in the hypothalamic nuclei of the mouse brain. (A) Axial MRI section containing the hypothalamus in a representative mouse brain and in a brain atlas (inset) showing the localization of the main periventricular hypothalamic nuclei: Dorsomedial Nucleus (DMN, red), Ventromedial Nucleus (VMN, yellow), and Arcuate Nucleus (Arc, blue). **(B,D,F,H)** Hypothalamic color maps of diffusion parameters from fed or fasted mice, superimposed to T_{2w} images in different hypothalamic nuclei. The hypothalamic region is depicted enlarged in the corresponding lower panels. **(C,E,G,I)** D_{slow} bar graphs of parameter values corresponding to the **(B,D,F,H)** panels, respectively. $^{*}p < 0.05$, $^{***}p < 0.001$. Reproduced from Lizarbe et al. (2013) with permission of the publisher.

and **H** show parameter maps of the slow diffusion coefficient (D_{slow}) of a representative mouse in the fed (left) or overnight-fasted (right) state, in the hypothalamus, ARC, VMN, and DMN nuclei, respectively. Bar graphs in panels **5C,E,G,** and **I** show mean values of the same parameter in six mice. The significant increase of D_{slow} with fasting in all nuclei may be interpreted as the consequence of activation-induced astrocytic swelling.

MULTINUCLEAR MAGNETIC RESONANCE SPECTROSCOPY STUDIES OF APPETITE REGULATION

The use of imaging methods may be complemented by several advanced spectroscopy strategies including mainly ^{1}H MRS *in vivo* and *ex vivo* ^{1}H and ^{13}C HRMAS. These methods have been shown to overcome the need to use large voxel volumes, a limitation precluding earlier the applications of MRS *in vivo* to hypothalamic physiology.

HIGH FIELD ^{1}H MRS *in vivo*

High field ^{1}H MRS (14.1 Tesla) has been shown to be able to obtain high quality metabolic profiles from the mouse hypothalamus *in vivo* either unilaterally (2.2 μL voxels) or bilaterally (4.4 μL voxels) (Lei et al., 2010; Duarte et al., 2012). Authors reported that the metabolic profile of the hypothalamus is different from other cerebral structures as the hippocampus, containing larger concentration of γ-aminobutyric acid and myo-inositol and lower concentrations of taurine (**Figure 6A**). High field ^{1}H MRS was used to characterize the effects of Mn^{2+} in the metabolic profile of the rat hypothalamus under the paradigm of Dehydration-induced Anorexia (DIA) (Just and Gruetter, 2011). Results showed that γ-aminobutyric acid had an essential role in the maintenance of energy homeostasis in the hypothalamus, independently of the condition investigated. Glutamate, glutamine, and taurine, however, appeared to respond more accurately to Mn^{2+} exposure. When comparing DIA and overnight fasting, GABA levels increased in both, but lactate increased significantly only in DIA. Taken together, these studies showed that high field ^{1}H MRS *in vivo* coupled with MEMRI, could provide very relevant information on the hypothalamic mechanisms involved in the control of food intake, global energy balance, and body weight control in rodents.

^{13}C AND ^{1}H HIGH RESOLUTION MAGIC ANGLE SPINNING SPECTROSCOPY

^{13}C Magnetic Resonance Spectroscopy is a method that has shown previously an enormous potential in the investigation of neuroglial coupling mechanisms, both *in vivo* and *in vitro* (Cruz and Cerdan, 1999; Gruetter et al., 2003; Rothman et al., 2003; Rodrigues et al., 2009). However, the low natural abundance of ^{13}C (1.1%) and the reduced sensitivity of the method, imposed the use of relatively large voxel sizes *in vivo*, exceeding significantly the dimensions of the hypothalamus. To overcome this, a novel collection of High Resolution Magic Angle Spinning (HRMAS) ^{13}C methods *ex vivo* were implemented recently. By acquiring NMR spectra of biopsy samples, inclined 54.7° with respect to the static magnetic field, the dipolar couplings that broaden the resonances *in vivo* are removed and high resolution spectra similar to those obtained in solution, can be obtained from samples as small as 5–10 mg, a size comparable with that of the rodent brain hypothalamus. Using this technology, authors investigated (**Figure 6B**) the effects of overnight fasting and ghrelin administration on the metabolic profile and the incorporation of ^{13}C from (1-^{13}C) glucose into hypothalamic metabolites (Violante et al., 2009). Overnight fasting induced significant increases in ^{13}C incoporation into (2-^{13}C) GABA and (3-^{13}C) lactate, while the infusion of the orexigenic peptide ghrelin did not affect ^{13}C labeling in these metabolites. These results revealed that overnight fasting appears to increase GABAergic neurotrasmission and glycolysis, but additional factors other

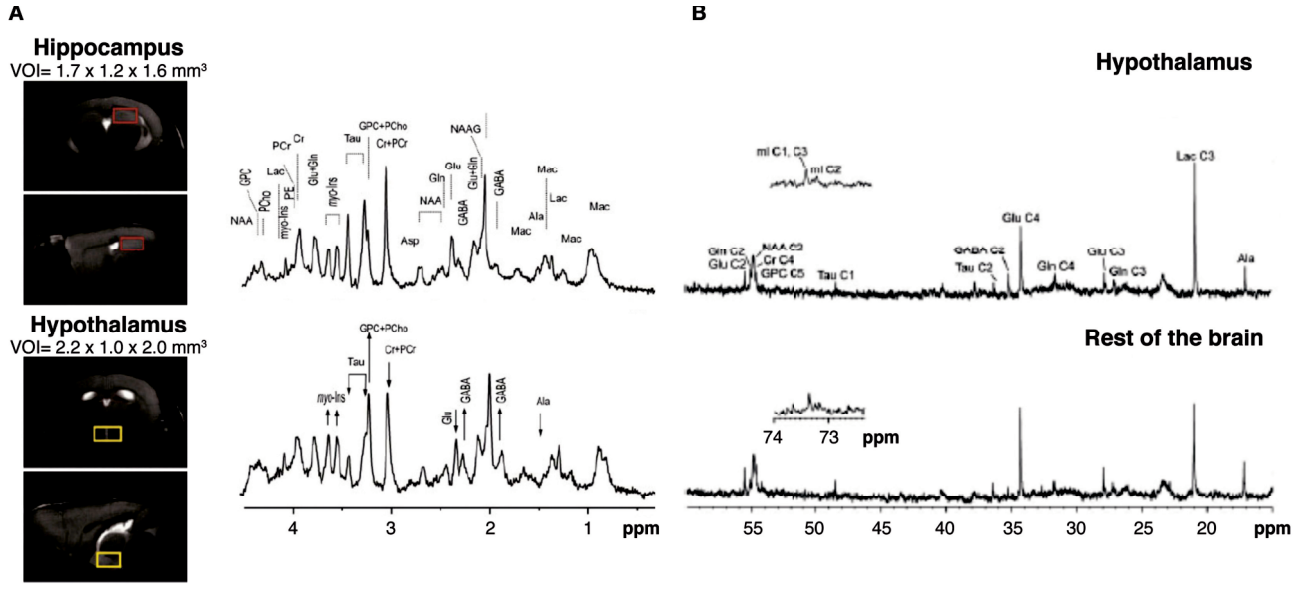

FIGURE 6 | Multinuclear NMR spectroscopy of the hypothalamus. (A) ^{1}H MRI *in vivo* from selected voxels of mouse hypothalamus (lower panels, yellow region) as compared to the hippocampus (upper panels, red region) and corresponding 1H NMR spectra. Note the relative increases in hypothalamic GABA and myo-inositol (arrow up) and the decreases in glutamate and taurine content (arrow down). Taken from Lei et al. (2010) and reproduced with permission of the publisher. **(B)** Representative ^{13}C HRMAS of hypothalamic biopsies (top) prepared after (1-^{13}C) glucose infusion as compared to the rest of the brain (bottom) in a fasted mouse. Reproduced from Violante et al. (2009) with permission of the publisher.

than ghrelin were required to elicit this complex hypothalamic response.

The neuroglial mechanisms underlying leptin signaling in the hypothalamus were recently investigated in control and ob/ob mice, combining MEMRI with ^{1}H and ^{13}C HRMAS and infusions of (1-^{13}C) glucose, a primarily neuronal substrate or (2-^{13}C) acetate, a predominantly glial substrate (Delgado et al., 2011). Leptin defficient obese mice showed increased MEMRI contrast in the ARC and VMN (**Figure 3**) and augmented ^{13}C accumulation in the hypothalamic glutamate and glutamine carbons from (1-^{13}C) glucose, but not from ^{13}C acetate. Together, this evidence showed for the first time that the increased MEMRI effect associated to neuronal activation of the orexigenic pathways in the obese mice was accompanied by increased oxidative metabolism and glutamate-glutamine cycling. Together with earlier ^{13}C HRMAS evidences on increased GABAergic performance after overnight fasting, the picture emerges that orexigenic stimulation results in increased glutamatergic and GABAergic neurotransmission, implying augmented transcellular cycling of glutamate-glutamine and GABA between neurons and astrocytes. Present results support the view that the synaptic transmission events supporting neuroendocrine signaling in the hypothalamus follow similar neuroglial compartmentation mechanisms to other types of cerebral sensorial or motor activations.

RECAPITULATION

In summary, the evidence accumulated recently by MRI and MRS methodologies has contributed importantly to investigate the role of metabolic compartmentation during neuroendocrine regulation in the hypothalamus. **Figure 7** provides an integrative interpretation on the role of neuroglial compartmentation during appetite regulation, as revealed by MEMRI, BOLD, DWI as well as by ^{1}H and ^{13}C NMR spectroscopy.

Briefly, the firing of orexigenic neurons involves voltage dependent Na^{+} and Ca^{2+} channels. Mn^{2+} substitutes Ca^{2+}, accumulating in excited neurons during depolarization (Koretsky and Silva, 2004; Silva et al., 2004). In addition, glutamatergic neurotransmission is known to be associated to intracellular and intercellular astrocyte to astrocyte calcium waves transmitted through gap junctions (Jaffe, 2006, 2008). Mn^{2+} could thus accumulate in astrocytic networks as well. These astrocytic arrangements may reach millimeter sizes, becoming then detectable under conventional MRI resolution conditions. At present it is not clear which neuronal or astroglial mechanism is predominant, but it can be safely thought that both contribute to the observed MEMRI effect. Excess glutamate released to the orexigenic cleft under fasting or obese conditions, is recaptured by surrounding astrocytes, by Na^{+} dependent cotransport mainly through the GLAST/EAAT1 and GLT-1/EAAT2 transporters, in a $3Na^{+}$ per glutamate stoichiometry (Anderson and Swanson, 2000). The three sodium ions incorporated in this way, are extruded to the extracellular space, in exchange with two potassium ions entering the astrocytic interior through the electrogenic Na^{+}/K^{+} ATPase (Glynn, 1993; Pellerin and Magistretti, 1994). The astrocytic ATP required for the operation of the Na^{+}/K^{+} ATPase and glutamine synthesis during activation by fasting, is thought to be derived from increased glucose consumption and metabolism by oxidative and glycolytic pathways in neurons and astrocytes (Cerdan et al., 2006; Violante et al., 2009; Delgado et al., 2011). Indeed, orexigenic stimulation results in lactate accumulation in the hypothalamus and increased labeling of glutamate, glutamine and GABA from (1-^{13}C) glucose as reflected by ^{13}C HRMAS. This reveals that hypothalamic activation by fasting involves the excitation of both glutamatergic (activatory) and GABAergic (inhibitory) terminals, as expected for an hypothalamic feed-back loop mechanism (**Figure 1**). In addition, the increased metabolic demand in the hypothalamus induced by fasting, results in an increased microvascular blood flow and hemoglobin deoxygenation, a circumstance underlying the changes observed by BOLD and DWI imaging (Lizarbe et al., 2013).

The volume changes inferred in the hypothalamus during orexigenic activation merit further attention. The K^{+} ions accumulated in the extracellular space during the orexigenic action potentials, may enter surrounding astrocytes through stimulation of the $Na^{+}/K^{+}/2Cl^{-}$ cotransporter (Hertz et al., 2007), a circumstance that might trigger concomitant water influx and astrocytic volume increase (Jayakumar and Norenberg, 2010), primarily-mediated through the highly abundant aquaporin AQP-4 of astrocytic membranes (Badaut et al., 2002). It should be noted here that increased K^{+} concentrations are known to be tightly coupled to neuronal activation, and have been detected using metallographic microscopic imaging approaches (Goldschmidt et al., 2004). In addition, EAAT1 glutamate sodium cotransporter has been shown to cause water influx together with glutamate transport (MacAulay et al., 2001) and the activation of the GABA receptors $GABA_{A}$Rs has been recently proposed to be involved with cell volume regulation processes and water exchange in the brain (Cesetti et al., 2011). On these grounds, increased astrocytic volume may become an important determinant of the alterations in diffusion parameters observed by DWI. The osmotic swelling response associated to orexigenic stimulation, is proposed here to occur initially in the few astrocytes surrounding the activated orexigenic clefts (**Figure 1**), but can be rapidly extended, to a plethora of neighboring astrocytes, through the numerous interconnecting gap junctions of the network arrangement (Halassa and Haydon, 2010) as mentioned above for Mn^{2+} accumulations.

The volume changes inferred by DWI find an adequate support when considering the increases in hypothalamic *myo*-inositol levels detected by high field ^{1}H MRS (Lei et al., 2010). The relative increases in osmolite content between the hypothalamus and other areas of the brain as detected by ^{1}H MRS *in vivo*, indicate that volume regulation processes in the hypothalamus may play an important role in hypothalamic function.

In summary, the above sections indicate that MRI and MRS methodologies have provided important insight into the hypothalamic mechanisms underlying appetite regulation. Briefly, MEMRI approaches reveal neuroglial manganese accumulation, BOLD shows concomitant oxygen consumption and associated hemodynamic responses and DWI discloses water diffusion changes compatible with glial swelling. ^{1}H and ^{13}C MRS have revealed osmolite accumulation and increased glutamatergic

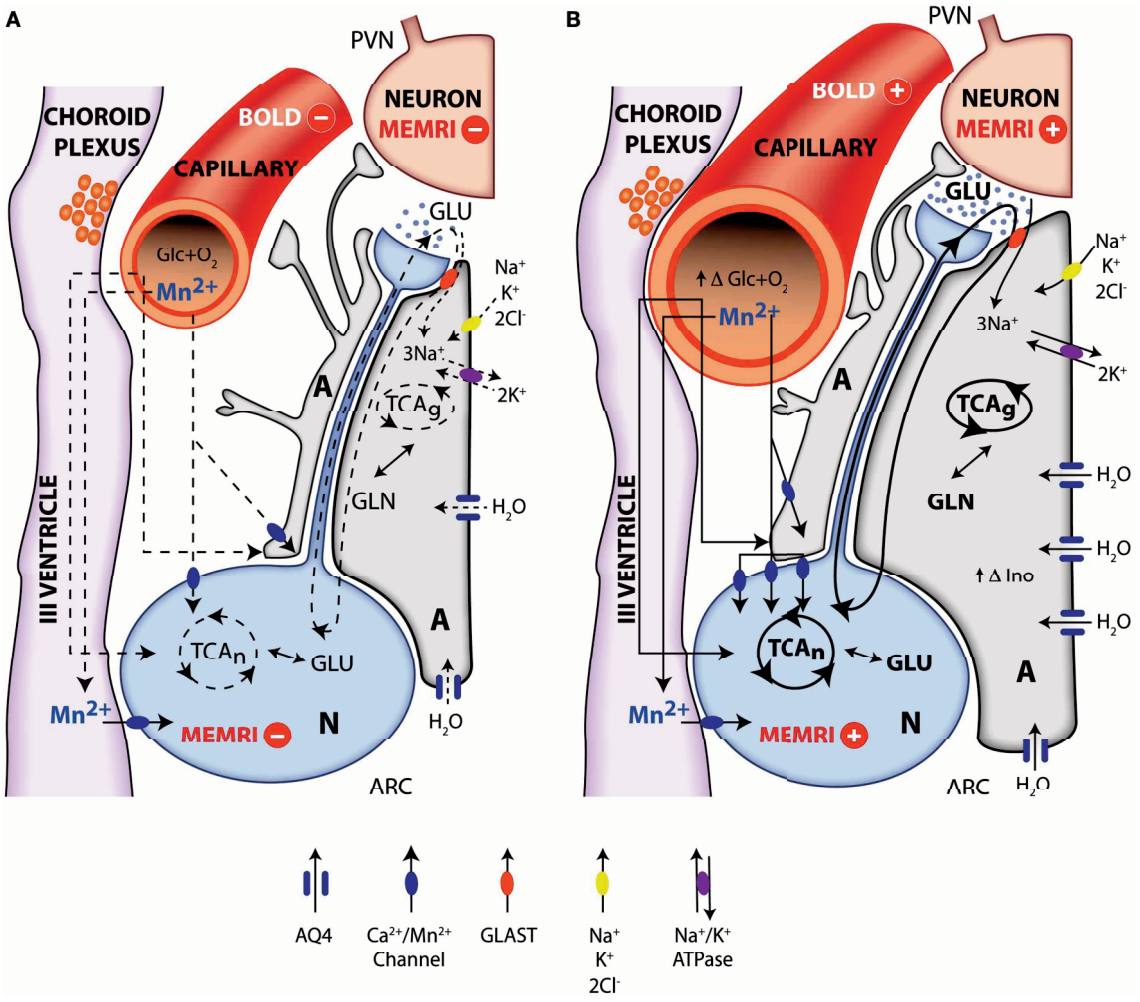

FIGURE 7 | Integrative interpretation of orexigenic activation in the hypothalamus as detected by MEMRI, BOLD, fDWI, and multinuclear magnetic resonance spectroscopy. Neuroglial metabolic coupling mechanisms and volume changes in astrocytes and capillaries of the hypothalamus underlie the orexigenic response from resting **(A)** to activated **(B)** states. Briefly, during orexigenic neurotransmission, excess glutamate released to the synaptic cleft by AGRP/NPYY neurons (N, blue) is recaptured by surrounding astrocytes (A, gray), together with $3Na^+$. Intracellular sodium ions incorporated are extruded to the extracellular space, through the electrogenic Na^+/K^+ATPase, incorporating two intracellular K^+ ions. Astrocytic glutamate produces glutamine, through glutamine synthase, which is later recaptured by the neurons to operate the glutamate-glutamine cycle. Additional K^+ ions may be incorporated to the astrocyte through the $Na^+K^+2Cl^-$ cotransporter, resulting in increased intracellular K^+ concentrations and thus triggering an osmotically driven, aquaporin 4 (AQP4) mediated (blue channel), water transport, producing astrocytic swelling. Glucose and oxygen are delivered through capillary to astrocytes and neurons, and Mn^{2+} ions enter neurons and astrocytes through calcium channels. Under resting conditions **(A)**, oxidative metabolism and glutamatergic neurotransmission depict basal levels (dotted lines). Under activated orexigenic conditions **(B)**, oxidative metabolism and glutamatergic neurotransmission are increased (darker lines, increased glutamate in the synaptic cleft) as revealed by ^{13}C HRMAS, resulting in augmented ionic and water trafficking to astrocytes (darker arrows, increased water influx through AQP4). The accumulated K^+ in one synaptic astrocyte may be transferred to the neighboring astroglia, through gap junctions, providing a spreading mechanism for the swelling response through the astrocyte syncytium, becoming measurable by fDWI. Astrocytic volume changes are thought to underlie the increased hypothalamic myo-inostol content observed by ^1H HRMAS. Glucose and oxygen demand increase (increasing capillary volume) during neuronal activation, and the ratio between deoxyhemoglobin and oxyhemoglobin changes causing the BOLD effect and the increased ^{13}C labeling of glutamate and GABA. Neuronal accumulation of Mn^{2+} through voltage dependent calcium channels increase with neuronal activation (higher number of channels and darker lines), causing the MEMRI effect.

and GABAergic neurotransmissions. Taken together, these results suggest an important role for hypothalamic metabolic compartmentation during appetite regulation, as in other cerebral activations. Naturally, these interpretations do not exclude additional contributions to MRI or MRS from other potential mechanisms.

Finally, the approaches reviewed here may provide a valuable tool to further investigate glutamatergic or GABAergic neurotransmissions in the hypothalamic control of global energy balance and in the development of improved treatments against feeding disorders, obesity, and diabetes. In addition, this arsenal of new methodologies may be easily extended to explore other

hypothalamic functions, opening a new avenue in the research of hypothalamic performance *in vivo*.

ACKNOWLEDGMENTS

This work was supported in part by grants SAF-2008-01327 and SAF2011-23622 to Sebastián Cerdán, grant CTQ-2010-20960-C02-02 to Pilar López, grants S-BIO-2006-0170 and S2010/BMD-2349 to Sebastián Cerdán, Pilar López-Larrubia, and Manuel Sánchez-Montañés. Blanca Lizarbe and Ania Benitez held predoctoral fellowships from the Spanish Ministry of Science and Technology (BES 2009-027615) and the Spanish Agency for International Cooperation and Development. The expert assistance of Mr. Javier Pérez, CSIC with the final drafting of the illustrations is gratefully acknowledged.

REFERENCES

Ahn, S., and Lee, S. K. (2011). Diffusion tensor imaging: exploring the motor networks and clinical applications. *Korean J. Radiol.* 12, 651–661. doi: 10.3348/kjr.2011.12.6.651

Alkan, A., Sahin, I., Keskin, L., Cikim, A. S., Karakas, H. M., Sigirci, A., et al. (2008). Diffusion-weighted imaging features of brain in obesity. *Magn. Reson. Imaging* 26, 446–450. doi: 10.1016/j.mri.2007.10.004

Anastasovska, J., Arora, T., Sanchez Canon, G. J., Parkinson, J. R., Touhy, K., Gibson, G. R., et al. (2012). Fermentable carbohydrate alters hypothalamic neuronal activity and protects against the obesogenic environment. *Obesity (Silver Spring)* 20, 1016–1023. doi: 10.1038/oby.2012.6

Anderson, C. M., and Swanson, R. A. (2000). Astrocyte glutamate transport: review of properties, regulation, and physiological functions. *Glia* 32, 1–14. doi: 10.1002/1098-1136(200010)32:1<1::AID-GLIA10>3.0.CO;2-W

Andrew, R. D., MacVicar, B. A., Dudek, F. E., and Hatton, G. I. (1981). Dye transfer through gap junctions between neuroendocrine cells of rat hypothalamus. *Science* 211, 1187–1189. doi: 10.1126/science.7466393

Aoki, I., Tanaka, C., Takegami, T., Ebisu, T., Umeda, M., Fukunaga, M., et al. (2002). Dynamic activity-induced manganese-dependent contrast magnetic resonance imaging (DAIM MRI). *Magn. Reson. Med.* 48, 927–933. doi: 10.1002/mrm.10320

Aoki, I., Wu, Y. J., Silva, A. C., Lynch, R. M., and Koretsky, A. P. (2004). *In vivo* detection of neuroarchitecture in the rodent brain using manganese-enhanced MRI. *Neuroimage* 22, 1046–1059. doi: 10.1016/j.neuroimage.2004.03.031

Araque, A., Parpura, V., Sanzgiri, R. P., and Haydon, P. G. (1999). Tripartite synapses: glia, the unacknowledged partner. *Trends Neurosci.* 22, 208–215. doi: 10.1016/S0166-2236(98)01349-6

Aso, T., Urayama, S., Fukuyama, H., and Le Bihan, D. (2013). Comparison of diffusion-weighted fMRI and BOLD fMRI responses in a verbal working memory task. *Neuroimage* 67, 25–32. doi: 10.1016/j.neuroimage.2012.11.005

Assaf, Y., Ben-Bashat, D., Chapman, J., Peled, S., Biton, I. E., Kafri, M., et al. (2002). High b-value q-space analyzed diffusion-weighted MRI: application to multiple sclerosis. *Magn. Reson. Med.* 47, 115–126. doi: 10.1002/mrm.10040

Badaut, J., Lasbennes, F., Magistretti, P. J., and Regli, L. (2002). Aquaporins in brain: distribution, physiology, and pathophysiology. *J. Cereb. Blood Flow Metab.* 22, 367–378. doi: 10.1097/00004647-200204000-00001

Baicy, K., London, E. D., Monterosso, J., Wong, M. L., Delibasi, T., Sharma, A., et al. (2007). Leptin replacement alters brain response to food cues in genetically leptin-deficient adults. *Proc. Natl. Acad. Sci. U.S.A.* 104, 18276–18279. doi: 10.1073/pnas.0706481104

Batterham, R. L., Ffytche, D. H., Rosenthal, J. M., Zelaya, F. O., Barker, G. J., Withers, D. J., et al. (2007). PYY modulation of cortical and hypothalamic brain areas predicts feeding behaviour in humans. *Nature* 450, 106–109. doi: 10.1038/nature06212

Cazettes, F., Cohen, J. I., Yau, P. L., Talbot, H., and Convit, A. (2011). Obesity-mediated inflammation may damage the brain circuit that regulates food intake. *Brain Res.* 1373, 101–109. doi: 10.1016/j.brainres.2010.12.008

Cerdan, S., Rodrigues, T. B., Sierra, A., Benito, M., Fonseca, L. L., Fonseca, C. P., et al. (2006). The redox switch/redox coupling hypothesis. *Neurochem. Int.* 48, 523–530. doi: 10.1016/j.neuint.2005.12.036

Cesetti, T., Ciccolini, F., and Li, Y. (2011). GABA not only a neurotransmitter: osmotic regulation by GABA(A)R signaling. *Front. Cell Neurosci.* 6:3. doi: 10.3389/fncel.2012.00003

Chaudhri, O. B., Parkinson, J. R., Kuo, Y. T., Druce, M. R., Herlihy, A. H., Bell, J. D., et al. (2006). Differential hypothalamic neuronal activation following peripheral injection of GLP-1 and oxyntomodulin in mice detected by manganese-enhanced magnetic resonance imaging. *Biochem. Biophys. Res. Commun.* 350, 298–306. doi: 10.1016/j.bbrc.2006.09.033

Chen, M., Zhang, T. M., Luo, S. L., Zhou, C., Wu, X. M., Zhou, N. N., et al. (2007). Functional magnetic resonance imaging and immunohistochemical study of hypothalamic function following oral glucose ingestion in rats. *Chin. Med. J.* 120, 1232–1235.

Coll, A. P., Farooqi, I. S., and O'Rahilly, S. (2007). The hormonal control of food intake. *Cell* 129, 251–262. doi: 10.1016/j.cell.2007.04.001

Collin, M., Backberg, M., Ovesjo, M. L., Fisone, G., Edwards, R. H., Fujiyama, F., et al. (2003). Plasma membrane and vesicular glutamate transporter mRNAs/proteins in hypothalamic neurons that regulate body weight. *Eur. J. Neurosci.* 18, 1265–1278. doi: 10.1046/j.1460-9568.2003.02840.x

Cruz, F., and Cerdan, S. (1999). Quantitative 13C NMR studies of metabolic compartmentation in the adult mammalian brain. *NMR Biomed.* 12, 451–462. doi: 10.1002/(SICI)1099-1492(199911)12:7<451::AID-NBM571>3.0.CO;2-E

De Souza, C. T., Araujo, E. P., Bordin, S., Ashimine, R., Zollner, R. L., Boschero, A. C., et al. (2005). Consumption of a fat-rich diet activates a proinflammatory response and induces insulin resistance in the hypothalamus. *Endocrinology* 146, 4192–4199. doi: 10.1210/en.2004-1520

Delgado, T. C., Violante, I. R., Nieto-Charques, L., and Cerdan, S. (2011). Neuroglial metabolic compartmentation underlying leptin deficiency in the obese ob/ob mice as detected by magnetic resonance imaging and spectroscopy methods. *J. Cereb. Blood Flow Metab.* 31, 2257–2266. doi: 10.1038/jcbfm.2011.134

Dienel, G. A., and Hertz, L. (2005). Astrocytic contributions to bioenergetics of cerebral ischemia. *Glia* 50, 362–388. doi: 10.1002/glia.20157

Duarte, J. M., Lei, H., Mlynarik, V., and Gruetter, R. (2012). The neurochemical profile quantified by *in vivo* 1H NMR spectroscopy. *Neuroimage* 61, 342–362. doi: 10.1016/j.neuroimage.2011.12.038

Farooqi, I. S., Bullmore, E., Keogh, J., Gillard, J., O'Rahilly, S., and Fletcher, P. C. (2007). Leptin regulates striatal regions and human eating behavior. *Science* 317, 1355. doi: 10.1126/science.1144599

Flint, J., Hansen, B., Vestergaard-Poulsen, P., and Blackband, S. J. (2009). Diffusion weighted magnetic resonance imaging of neuronal activity in the hippocampal slice model. *Neuroimage* 46, 411–418. doi: 10.1016/j.neuroimage.2009.02.003

Ganong, W. F. (1993). "Central regulation of visceral function," in *Review of Medical Physiology*, ed W. F. Ganong (Connecticut, CT: Appleton and Lange Pub.), 208–230.

Garcia-Ovejero, D., Azcoitia, I., Doncarlos, L. L., Melcangi, R. C., and Garcia-Segura, L. M. (2005). Glia-neuron crosstalk in the neuroprotective mechanisms of sex steroid hormones. *Brain Res. Brain Res. Rev.* 48, 273–286. doi: 10.1016/j.brainresrev.2004.12.018

Garcia-Segura, L. M., Lorenz, B., and Doncarlos, L. L. (2008). The role of glia in the hypothalamus: implications for gonadal steroid feedback and reproductive neuroendocrine output. *Reproduction* 135, 419–429. doi: 10.1530/REP-07-0540

Glynn, I. M. (1993). Annual review prize lecture. 'All hands to the sodium pump'. *J. Physiol.* 462, 1–30.

Goldschmidt, J., Zuschratter, W., and Scheich, H. (2004). High-resolution mapping of neuronal activity by thallium autometallography. *Neuroimage* 23, 638–647. doi: 10.1016/j.neuroimage.2004.05.023

Grinberg, F., Farrher, E., Kaffanke, J., Oros-Peusquens, A. M., and

Shah, N. J. (2011). Non-Gaussian diffusion in human brain tissue at high b-factors as examined by a combined diffusion kurtosis and biexponential diffusion tensor analysis. *Neuroimage* 57, 1087–1102. doi: 10.1016/j.neuroimage.2011.04.050

Gruetter, R., Adriany, G., Choi, I. Y., Henry, P. G., Lei, H., and Oz, G. (2003). Localized *in vivo* 13C NMR spectroscopy of the brain. *NMR Biomed.* 16, 313–338. doi: 10.1002/nbm.841

Guthoff, M., Grichisch, Y., Canova, C., Tschritter, O., Veit, R., Hallschmid, M., et al. (2010). Insulin modulates food-related activity in the central nervous system. *J. Clin. Endocrinol. Metab.* 95, 748–755. doi: 10.1210/jc.2009-1677

Gutman, D. A., Magnuson, M., Majeed, W., Keifer, O. P. Jr., Davis, M., Ressler, K. J., et al. (2012). Mapping of the mouse olfactory system with manganese-enhanced magnetic resonance imaging and diffusion tensor imaging. *Brain Struct. Funct.* 218, 527–537. doi: 10.1007/s00429-012-0413-6

Hagmann, P., Kurant, M., Gigandet, X., Thiran, P., Wedeen, V. J., Meuli, R., et al. (2007). Mapping human whole-brain structural networks with diffusion MRI. *PLoS ONE* 2:e597. doi: 10.1371/journal.pone.0000597

Halassa, M. M., and Haydon, P. G. (2010). Integrated brain circuits: astrocytic networks modulate neuronal activity and behavior. *Annu. Rev. Physiol.* 72, 335–355. doi: 10.1146/annurev-physiol-021909-135843

Halassa, M. M., Fellin, T., and Haydon, P. G. (2007). The tripartite synapse: roles for gliotransmission in health and disease. *Trends Mol. Med.* 13, 54–63. doi: 10.1016/j.molmed.2006.12.005

Hankir, M. K., Parkinson, J. R., Minnion, J. S., Addison, M. L., Bloom, S. R., and Bell, J. D. (2011). Peptide YY 3-36 and pancreatic polypeptide differentially regulate hypothalamic neuronal activity in mice *in vivo* as measured by manganese-enhanced magnetic resonance imaging. *J. Neuroendocrinol.* 23, 371–380. doi: 10.1111/j.1365-2826.2011.02111.x

Hentges, S. T., Nishiyama, M., Overstreet, L. S., Stenzel-Poore, M., Williams, J. T., and Low, M. J. (2004). GABA release from proopiomelanocortin neurons. *J. Neurosci.* 24, 1578–1583. doi: 10.1523/JNEUROSCI.3952-03.2004

Hertz, L. (2004). Intercellular metabolic compartmentation in the brain: past, present and future. *Neurochem. Int.* 45, 285–296. doi: 10.1016/j.neuint.2003.08.016

Hertz, L., Peng, L., and Dienel, G. A. (2007). Energy metabolism in astrocytes: high rate of oxidative metabolism and spatiotemporal dependence on glycolysis/glycogenolysis. *J. Cereb. Blood Flow Metab.* 27, 219–249. doi: 10.1038/sj.jcbfm.9600343

Jaffe, L. (2006). The discovery of calcium waves. *Semin. Cell Dev. Biol.* 17, 229. doi: 10.1016/j.semcdb.2006.02.003

Jaffe, L. F. (2008). Calcium waves. *Philos. Trans. R. Soc. Lond. B Biol. Sci.* 363, 1311–1316. doi: 10.1098/rstb.2007.2249

Jaffe, L. F. (2010). Fast calcium waves. *Cell Calcium* 48, 102–113. doi: 10.1016/j.ceca.2010.08.007

Jayakumar, A. R., and Norenberg, M. D. (2010). The Na-K-Cl Co-transporter in astrocyte swelling. *Metab. Brain Dis.* 25, 31–38. doi: 10.1007/s11011-010-9180-3

Jensen, J. H., and Helpern, J. A. (2010). MRI quantification of non-Gaussian water diffusion by kurtosis analysis. *NMR Biomed.* 23, 698–710. doi: 10.1002/nbm.1518

Jones, R. B., McKie, S., Astbury, N., Little, T. J., Tivey, S., Lassman, D. J., et al. (2012). Functional neuroimaging demonstrates that ghrelin inhibits the central nervous system response to ingested lipid. *Gut* 61, 1543–1551. doi: 10.1136/gutjnl-2011-301323

Just, N., Cudalbu, C., Lei, H., and Gruetter, R. (2011). Effect of manganese chloride on the neurochemical profile of the rat hypothalamus. *J. Cereb. Blood Flow Metab.* 31, 2324–2333. doi: 10.1038/jcbfm.2011.92

Just, N., and Gruetter, R. (2011). Detection of neuronal activity and metabolism in a model of dehydration-induced anorexia in rats at 14.1 T using manganese-enhanced MRI and 1H MRS. *NMR Biomed.* 24, 1326–1336. doi: 10.1002/nbm.1694

Killgore, W. D., Young, A. D., Femia, L. A., Bogorodzki, P., Rogowska, J., and Yurgelun-Todd, D. A. (2003). Cortical and limbic activation during viewing of high- versus low-calorie foods. *Neuroimage* 19, 1381–1394. doi: 10.1016/S1053-8119(03)00191-5

Kleinridders, A., Schenten, D., Konner, A. C., Belgardt, B. F., Mauer, J., Okamura, T., et al. (2009). MyD88 signaling in the CNS is required for development of fatty acid-induced leptin resistance and diet-induced obesity. *Cell Metab.* 10, 249–259. doi: 10.1016/j.cmet.2009.08.013

Kohno, S., Sawamoto, N., Urayama, S., Aso, T., Aso, K., Seiyama, A., et al. (2009). Water-diffusion slowdown in the human visual cortex on visual stimulation precedes vascular responses. *J. Cereb. Blood Flow Metab.* 29, 1197–1207. doi: 10.1038/jcbfm.2009.45

Koretsky, A. P., and Silva, A. C. (2004). Manganese-enhanced magnetic resonance imaging (MEMRI). *NMR Biomed.* 17, 527–531. doi: 10.1002/nbm.940

Kuo, Y. T., Herlihy, A. H., So, P. W., and Bell, J. D. (2006). Manganese-enhanced magnetic resonance imaging (MEMRI) without compromise of the blood-brain barrier detects hypothalamic neuronal activity *in vivo*. *NMR Biomed.* 19, 1028–1034. doi: 10.1002/nbm.1070

Lantos, T. A., Gorcs, T. J., and Palkovits, M. (1995). Immunohistochemical mapping of neuropeptides in the premamillary region of the hypothalamus in rats. *Brain Res. Brain Res. Rev.* 20, 209–249. doi: 10.1016/0165-0173(94)00013-F

Le Bihan, D. (2003). Looking into the functional architecture of the brain with diffusion MRI. *Nat. Rev. Neurosci.* 4, 469–480. doi: 10.1038/nrn1119

Le Bihan, D., Mangin, J. F., Poupon, C., Clark, C. A., Pappata, S., Molko, N., et al. (2001). Diffusion tensor imaging: concepts and applications. *J. Magn. Reson. Imaging* 13, 534–546. doi: 10.1002/jmri.1076

Le Bihan, D., Urayama, S., Aso, T., Hanakawa, T., and Fukuyama, H. (2006). Direct and fast detection of neuronal activation in the human brain with diffusion MRI. *Proc. Natl. Acad. Sci. U.S.A.* 103, 8263–8268. doi: 10.1073/pnas.0600644103

Lee, J. H., Silva, A. C., Merkle, H., and Koretsky, A. P. (2005). Manganese-enhanced magnetic resonance imaging of mouse brain after systemic administration of MnCl2: dose-dependent and temporal evolution of T1 contrast. *Magn. Reson. Med.* 53, 640–648. doi: 10.1002/mrm.20368

Lei, H., Poitry-Yamate, C., Preitner, F., Thorens, B., and Gruetter, R. (2010). Neurochemical profile of the mouse hypothalamus using *in vivo* 1H MRS at 14.1T. *NMR Biomed.* 23, 578–583. doi: 10.1002/nbm.1498

Levin, B. E., Magnan, C., Dunn-Meynell, A., and Le Foll, C. (2011). Metabolic sensing and the brain: who, what, where, and how? *Endocrinology* 152, 2552–2557.

Li, J., An, R., Zhang, Y., Li, X., and Wang, S. (2012). Correlations of macronutrient-induced functional magnetic resonance imaging signal changes in human brain and gut hormone responses. *Am. J. Clin. Nutr.* 96, 275–282. doi: 10.3945/ajcn.112.037440

Lin, D., Boyle, M. P., Dollar, P., Lee, H., Lein, E. S., Perona, P., et al. (2011). Functional identification of an aggression locus in the mouse hypothalamus. *Nature* 470, 221–226. doi: 10.1038/nature09736

Lizarbe, B., Benitez, A., Sanchez-Montanes, M., Lago-Fernandez, L. F., Garcia-Martin, M. L., Lopez-Larrubia, P., et al. (2013). Imaging hypothalamic activity using diffusion weighted magnetic resonance imaging in the mouse and human brain. *Neuroimage* 64, 448–457. doi: 10.1016/j.neuroimage.2012.09.033

Logothetis, N. K., and Wandell, B. A. (2004). Interpreting the BOLD signal. *Annu. Rev. Physiol.* 66, 735–769. doi: 10.1146/annurev.physiol.66.082602.092845

MacAulay, N., Gether, U., Klaerke, D. A., and Zeuthen, T. (2001). Water transport by the human Na^+-coupled glutamate cotransporter expressed in Xenopus oocytes. *J. Physiol.* 530, 367–378. doi: 10.1111/j.1469-7793.2001.0367k.x

Mahankali, S., Liu, Y., Pu, Y., Wang, J., Chen, C. W., Fox, P. T., et al. (2000). *In vivo* fMRI demonstration of hypothalamic function following intraperitoneal glucose administration in a rat model. *Magn. Reson. Med.* 43, 155–159. doi: 10.1002/(SICI)1522-2594(200001)43:1<155::AID-MRM20>3.0.CO;2-5

Malik, S., McGlone, F., Bedrossian, D., and Dagher, A. (2008). Ghrelin modulates brain activity in areas that control appetitive behavior. *Cell Metab.* 7, 400–409. doi: 10.1016/j.cmet.2008.03.007

Matsuda, M., Liu, Y., Mahankali, S., Pu, Y., Mahankali, A., Wang, J., et al. (1999). Altered hypothalamic function in response to glucose ingestion in obese humans. *Diabetes* 48, 1801–1806. doi: 10.2337/diabetes.48.9.1801

McEwen, B. S. (1989). "Endocrine effects on the brain and their relationship to behavior," in

Basic Neurochemistry, eds G. Siegel, B. Agranoff, R. W. Albers, and P. Molinoff (New York, NY: Raven Press), 893–913.

Miller, J. L., James, G. A., Goldstone, A. P., Couch, J. A., He, G., Driscoll, D. J., et al. (2007). Enhanced activation of reward mediating prefrontal regions in response to food stimuli in Prader-Willi syndrome. *J. Neurol. Neurosurg. Psychiatry* 78, 615–619. doi: 10.1136/jnnp.2006.099044

Min, D. K., Tuor, U. I., Koopmans, H. S., and Chelikani, P. K. (2011). Changes in differential functional magnetic resonance signals in the rodent brain elicited by mixed-nutrient or protein-enriched meals. *Gastroenterology* 141, 1832–1841. doi: 10.1053/j.gastro.2011.07.034

Mohacsik, P., Zeold, A., Bianco, A. C., and Gereben, B. (2011). Thyroid hormone and the neuroglia: both source and target. *J. Thyroid. Res.* 2011:215718. doi: 10.4061/2011/215718

Morita, H., Ogino, T., Seo, Y., Fujiki, N., Tanaka, K., Takamata, A., et al. (2002). Detection of hypothalamic activation by manganese ion contrasted T(1)-weighted magnetic resonance imaging in rats. *Neurosci. Lett.* 326, 101–104. doi: 10.1016/S0304-3940(02)00330-0

Morton, G. J., Cummings, D. E., Baskin, D. G., Barsh, G. S., and Schwartz, M. W. (2006). Central nervous system control of food intake and body weight. *Nature* 443, 289–295. doi: 10.1038/nature05026

Niendorf, T., Dijkhuizen, R. M., Norris, D. G., Van Lookeren Campagne, M., and Nicolay, K. (1996). Biexponential diffusion attenuation in various states of brain tissue: implications for diffusion-weighted imaging. *Magn. Reson. Med.* 36, 847–857. doi: 10.1002/mrm.1910360607

Ogawa, S., Lee, T. M., Kay, A. R., and Tank, D. W. (1990). Brain magnetic resonance imaging with contrast dependent on blood oxygenation. *Proc. Natl. Acad. Sci. U.S.A.* 87, 9868–9872. doi: 10.1073/pnas.87.24.9868

Palkovits, M. (1999). Interconnections between the neuroendocrine hypothalamus and the central autonomic system. Geoffrey Harris Memorial Lecture, Kitakyushu, Japan, October 1998. *Front. Neuroendocrinol.* 20:4. doi: 10.1006/frne.1999.0186

Parkinson, J. R., Chaudhri, O. B., and Bell, J. D. (2009). Imaging appetite-regulating pathways in the central nervous system using manganese-enhanced magnetic resonance imaging. *Neuroendocrinology* 89, 121–130. doi: 10.1159/000163751

Pautler, R. G. (2004). *In vivo*, trans-synaptic tract-tracing utilizing manganese-enhanced magnetic resonance imaging (MEMRI). *NMR Biomed.* 17, 595–601. doi: 10.1002/nbm.942

Paxinos, G., and Franklin, K. (2001). *The Mouse Brain in Stereotaxic Coordinates.* New York, NY: Academic Press.

Pellerin, L., and Magistretti, P. J. (1994). Glutamate uptake into astrocytes stimulates aerobic glycolysis: a mechanism coupling neuronal activity to glucose utilization. *Proc. Natl. Acad. Sci. U.S.A.* 91, 10625–10629. doi: 10.1073/pnas.91.22.10625

Purnell, J. Q., Klopfenstein, B. A., Stevens, A. A., Havel, P. J., Adams, S. H., Dunn, T. N., et al. (2011). Brain functional magnetic resonance imaging response to glucose and fructose infusions in humans. *Diabetes. Obes. Metab.* 13, 229–234. doi: 10.1111/j.1463-1326.2010.01340.x

Rodrigues, T. B., Fonseca, C. P., Castro, M. M., Cerdan, S., and Geraldes, C. F. (2009). 13C NMR tracers in neurochemistry: implications for molecular imaging. *Q. J. Nucl. Med. Mol. Imaging* 53, 631–645.

Rothman, D. L., Behar, K. L., Hyder, F., and Shulman, R. G. (2003). *In vivo* NMR studies of the glutamate neurotransmitter flux and neuroenergetics: implications for brain function. *Annu. Rev. Physiol.* 65, 401–427. doi: 10.1146/annurev.physiol.65.092101.142131

Santello, M., Cali, C., and Bezzi, P. (2012). Gliotransmission and the tripartite synapse. *Adv. Exp. Med. Biol.* 970, 307–331. doi: 10.1007/978-3-7091-0932-8_14

Schellinger, P. D., Jansen, O., Fiebach, J. B., Pohlers, O., Ryssel, H., Heiland, S., et al. (2000). Feasibility and practicality of MR imaging of stroke in the management of hyperacute cerebral ischemia. *AJNR* 21, 1184–1189.

Schwartz, M. W., and Morton, G. J. (2002). Obesity: keeping hunger at bay. *Nature* 418, 595–597. doi: 10.1038/418595a

Schwartz, M. W., Woods, S. C., Porte, D. Jr., Seeley, R. J., and Baskin, D. G. (2000). Central nervous system control of food intake. *Nature* 404, 661–671.

Silva, A. C. (2012). Using manganese-enhanced MRI to understand BOLD. *Neuroimage* 62, 1009–1013. doi: 10.1016/j.neuroimage.2012.01.008

Silva, A. C., Lee, J. H., Aoki, I., and Koretsky, A. P. (2004). Manganese-enhanced magnetic resonance imaging (MEMRI): methodological and practical considerations. *NMR Biomed.* 17, 532–543. doi: 10.1002/nbm.945

Smeets, P. A., De Graaf, C., Stafleu, A., Van Osch, M. J., and Van Der Grond, J. (2005). Functional magnetic resonance imaging of human hypothalamic responses to sweet taste and calories. *Am. J. Clin. Nutr.* 82, 1011–1016.

Stanley, B., Ha, L., Spears, L., Dee, M. (1993). Lateral hypothalamic injections of glutamate, kainic acid, D, L-alpha-amino-3-hydroxy–5-methyl-isoxazole propionic acid or N-methyl-D-aspartic acid rapidly elicit transient eating in rats. *Brain Res.* 613, 88–95. doi: 10.1016/0006-8993(93)90458-Y

Stanley, S., Wynne, K., McGowan, B., and Bloom, S. (2005). Hormonal regulation of food intake. *Physiol. Rev.* 85, 1131–1158. doi: 10.1152/physrev.00015.2004

Stark, J. A., Davies, K. E., Williams, S. R., and Luckman, S. M. (2006). Functional magnetic resonance imaging and c-Fos mapping in rats following an anorectic dose of m-chlorophenylpiperazine. *Neuroimage* 31, 1228–1237. doi: 10.1016/j.neuroimage.2006.01.046

Swaab, D. F., Hofman, M. A., Mirmiran, M., Ravid, R., and Van Leewen, F. W. (Eds.). (1992). *The Human Hypothalamus in Health and Disease*, Vol. 93 (Progress in Brain Research). Amsterdam, Elsevier, 3–455.

Tang-Christensen, M., Vrang, N., Ortmann, S., Bidlingmaier, M., Horvath, T. L., and Tschop, M. (2004). Central administration of ghrelin and agouti-related protein (83-132) increases food intake and decreases spontaneous locomotor activity in rats. *Endocrinology* 145, 4645–4652. doi: 10.1210/en.2004-0529

Thorburn, A. W., and Proietto, J. (1998). Neuropeptides, the hypothalamus and obesity: insights into the central control of body weight. *Pathology* 30, 229–236. doi: 10.1080/00313029800169366

Tomasi, D., Wang, G. J., Wang, R., Backus, W., Geliebter, A., Telang, F., et al. (2009). Association of body mass and brain activation during gastric distention: implications for obesity. *PLoS ONE* 4:e6847. doi: 10.1371/journal.pone.0006847

Tong, Q., Ye, C., McCrimmon, R. J., Dhillon, H., Choi, B., Kramer, M. D., et al. (2007). Synaptic glutamate release by ventromedial hypothalamic neurons is part of the neurocircuitry that prevents hypoglycemia. *Cell Metab.* 5, 383–393. doi: 10.1016/j.cmet.2007.04.001

Vidarsdottir, S., Smeets, P. A., Eichelsheim, D. L., van Osch, M. J., Viergever, M. A., Romijn, J. A., et al. (2007). Glucose ingestion fails to inhibit hypothalamic neuronal activity in patients with type 2 diabetes. *Diabetes* 56, 2547–2550. doi: 10.2337/db07-0193

Violante, I. R., Anastasovska, J., Sanchez-Canon, G. J., Rodrigues, T. B., Righi, V., Nieto-Charques, L., et al. (2009). Cerebral activation by fasting induces lactate accumulation in the hypothalamus. *Magn. Reson. Med.* 62, 279–283. doi: 10.1002/mrm.22010

Wang, X., Ge, A., Cheng, M., Guo, F., Zhao, M., Zhou, X., et al. (2012). Increased hypothalamic inflammation associated with the susceptibility to obesity in rats exposed to high-fat diet. *Exp. Diabetes Res.* 2012:847246. doi: 10.1155/2012/847246

Wisse, B. E., and Schwartz, M. W. (2009). Does hypothalamic inflammation cause obesity? *Cell Metab.* 10, 241–242.

Xu, Y., O'Brien, W. G. 3rd, Lee, C. C., Myers, M. G. Jr., and Tong, Q. (2012). Role of GABA release from leptin receptor-expressing neurons in body weight regulation. *Endocrinology* 153, 2223–2233. doi: 10.1210/en.2011-2071

Yu, X., Wadghiri, Y. Z., Sanes, D. H., and Turnbull, D. H. (2005). *In vivo* auditory brain mapping in mice with Mn-enhanced MRI. *Nat. Neurosci.* 8, 961–968. doi: 10.1038/nn1477

Zhu, X. H., Kim, S. G., Andersen, P., Ogawa, S., Ugurbil, K., and Chen, W. (1998). Simultaneous oxygenation and perfusion imaging study of functional activity in primary visual cortex at different visual stimulation frequency: quantitative correlation between BOLD and CBF changes. *Magn. Reson. Med.* 40, 703–711. doi: 10.1002/mrm.1910400510

Zwingmann, C., Leibfritz, D., and Hazell, A. S. (2003). Energy metabolism in astrocytes and

neurons treated with manganese: relation among cell-specific energy failure, glucose metabolism, and intercellular trafficking using multinuclear NMR-spectroscopic analysis. *J. Cereb. Blood Flow Metab.* 23, 756–771. doi: 10.1097/01.WCB.0000056062.25434.4D

Zwingmann, C., Leibfritz, D., and Hazell, A. S. (2004). Brain energy metabolism in a sub-acute rat model of manganese neurotoxicity: an *ex vivo* nuclear magnetic resonance study using [1-13C]glucose. *Neurotoxicology* 25, 573–587. doi: 10.1016/j.neuro.2003.08.002

Conflict of Interest Statement: The authors declare that the research was conducted in the absence of any commercial or financial relationships that could be construed as a potential conflict of interest.

Received: 12 March 2013; accepted: 28 May 2013; published online: 13 June 2013.

Citation: Lizarbe B, Benitez A, Peláez Brioso GA, Sánchez-Montañés M, López-Larrubia P, Ballesteros P and Cerdán S (2013) Hypothalamic metabolic compartmentation during appetite regulation as revealed by magnetic resonance imaging and spectroscopy methods. Front. Neuroenergetics ***5****:6. doi: 10.3389/fnene.2013.00006*

REVISIÓN

Control´hipotalámico´de´las´interacciones´neuroendocrinas´

Blanca´Lizarbe´y´Sebastián´Cerdán*

Instituto de Investigaciones Biomédicas "Alberto Sols" CSIC/UAM, c/ Arturo Duperier 4. 28029 Madrid (España).
e-mail: scerdan@iib.uam.es

Recibido el 27 de marzo de 2013 *An. Real Acad. Farm. Vol 79, Nº 1 (2013), pag. 90i110*
FISIOLOGIA Y CONTROL CEREBRAL DEL COMPORTAMIENTO.´ Mesa Redonda celebrada en la Real Academia Nacional de Farmacia el día 29 de noviembre del 2012. Coordinadora: A. M. PascualiLeone Académica de Número de la RANF.

RESUMEN´

El hipotálamo juega en los mamíferos superiores un papel central en la integración de funciones vitales como la regulación del metabolismo energético global, la saciedad y el hambre, el control de la presión sanguínea y la temperatura corporal, la sed, hidratación y metabolismo salino del organismo, y las funciones testiculares y ováricas, entre otras. Muchas de estas funciones neuroendocrinas se realizan mediante el control del funcionamiento de la hipófisis, utilizando un complejo sistema de retroalimentación que modula la secreción de una gran variedad de hormonas hipofisarias con efectos sistémicos de vital importancia, incluyendo las hormonas tiroideas o la hormona del crecimiento, entre otras. El hipotálamo consta de aproximadamente una docena de subestructuras, conocidas como núcleos hipotalámicos, que se encargan de controlar los diversos procesos. Hasta muy recientemente no ha sido posible evaluar la función hipotalámica directamente in vivo, un aspecto que se resolvía mediante procedimientos indirectos como la determinación de cambios en el peso corporal, eliminación de líquidos, alteraciones en la termorregulación o desequilibrios en el perfil de hormonas en sangre. En esta revisión describiremos toda una nueva serie de métodos de imagen no invasiva para la evaluación directa de la función hipotalámica y su impacto potencial en nuestro conocimiento actual de la regulación de las interacciones neuroendocrinas, con especial referencia a la regulación hipotalámica del apetito *in vivo*.

Palabras clave: Hipotálamo; Núcleos hipotalámicos; Control del apetito; Imagen por Resonancia Magnética; Espectroscopía por Resonancia Magnética.

ABSTRACT

Control of hypothalamic neuroendocrine interactions

The hypothalamus plays in higher mammals a central role in the integration of vital functions as the regulation of global energy metabolism, satiety and hunger, the control of blood pressure and body temperature, thirst, hydration and electrolyte metabolism, testicular and or ovarian functions, among others. Many of these neuroendocrine functions are performed through the control of the performance of the hypophysis, using a complex system of feedı˜back loops that modulate the secretion of large variety of hypophysary hormones with systemic effects of vital importance, including the thyroid and growth hormones, among others. The hypothalamus has approximately a dozen of substructures, known as hypothalamic nuclei, which control the different processes. Until very recently, it has not been possible to evaluate directly the hypothalamic function in vivo, an aspect solved through indirect measurements as the determination of bodyweight changes, liquid elimination and alterations in thermoregulation or disequilibria in the hormonal profiles in blood. In this review we shall describe a novel series of noni˙invasive imaging and spectroscopy methods for the direct evaluation of hypothalamic function and their potential impact on our current knowledge of neuroendocrine regulation, with special reference to the hypothalamic regulation of appetite *in vivo*.

Keywords: Hypothalamus; Hypothalamic nuclei; Appetite control; Magnetic Resonance Imaging; Magnetic Resonance Spectroscopy.

1. INTRODUCCIÓN´

El hipotálamo es una pequeña˜ estructura cerebral responsable del equilibrio homeostático de funciones sistémicas vitales como el metabolismo energético global, el apetito, la sed y la regulación˜osmótica, la termorregulación, los ritmos circadianos y algunas respuestas fundamentales para la supervivencia como la agresividad (1,2). La evaluación˜de su actividad fisiológica *in vivo* se ha realizado, hasta muy recientemente, empleando métodos indirectos como las medidas de peso corporal e ingesta de alimentos, o abordajes invasivos, midiendo concentraciones de hormonas en sangre o mediante la implantación˜ de microelectrodos (3,4).

Los procedimientos no invasivos de evaluación˜de la función˜hipotalámica, han permanecido limitados hasta muy recientemente, por las dificultades impuestas en la adquisición˜ de imágenes por las reducidas dimensiones del hipotálamo y por la complejidad de los procesos retroalimentación˜que subyacen a la función˜hipotalámica.

Las nuevas tecnologías de Resonancia Magnética proporcionan herramientas robustas que permiten superar estas limitaciones, habiendo proporcionado en la˜última década, resultados funcionales importantes sobre la fisiología˜hipotalámica in vivo (5,6).

En este contexto, resulta apropiado revisar el progreso adquirido hasta ahora y evaluar críticamente las ventajas e inconvenientes de cada abordaje.

El presente trabajo revisará˜la información˜generada mediante la aplicación˜ al hipotálamo de técnicas de imagen y espectroscopía˜por Resonancia Magnética, proporcionando algunas recomendaciones para futuras aplicaciones.

Dada la diversidad de las funciones hipotalámicas, este trabajo se centrará˜ principalmente en la regulación˜del apetito y metabolismo energético global, una de las funciones hipotalámicas con mayor repercusión˜ fisiopatológica y socioeconómica.

Comenzaremos con una breve descripción˜de los mecanismos fisiológicos de control del apetito, para describir después˜las tecnologías MRI utilizadas en su evaluación, incluyendo BOLD (Blood Oxygenation Level Dependent contrast; Contraste basado en la oxigenación˜de la sangre), MEMRI (Manganese Enhanced Magnetic Resonance Imaging; Resonancia Magnética potenciada en captación˜de Mn^{2+}) y DWI (Diffusion Weighted Magnetic Resonance Imaging; Resonancia magnética potenciada en difusión).

Terminaremos con una revisión˜ crítica de las contribuciones de la espectroscopía˜por Resonancia Magnética, tanto *in vivo* como en el˜"ángulo mágico"˜ (HRMAS; High Resolution Magic Angle Spinning) y una propuesta de actividades futuras.

2. CONTROL HIPOTALÁMICO DEL APETITO

Nuestro conocimiento sobre los mecanismos hipotalámicos que regulan el apetito y la homeostasis energética ha progresado considerablemente en los últimos años (7). El control del apetito se entiende, en el contexto actual, como el resultado de un complejo balance entre señales periféricas e intrahipotalámicas que controlan, a corto plazo, la sensación˜de hambre o saciedad, y a largo plazo, la regulación˜del peso corporal y balance energético (8).

Estos procesos parecen incluir además, la participación˜de otras estructuras cerebrales, corticales, límbicas y del tronco cerebral. Las principales señales periféricas son la leptina, una hormona producida en el tejido adiposo, y la insulina, una hormona proveniente del páncreas. Además, participan como señales del estado energético periférico, péptidos que provienen del estómago, como el

péptido YY (PYY), la oxintomodulina (OXM), la grelina, el péptido análogo de glucagón˜1˜(GLP11) y la colecistokininina (CKK). Estas señales pasan con facilidad la frágil barrera hematoencefálica del hipotálamo y, una vez allí,˜ modulan la actividad catabólica (+) o anabólica (1)˜ de los núcleos Arcuado (ARC), Ventromedial (VMN), Dorsomedial (DMN) y Paraventricular (PVN) (Figura 1). Estos controlan la ingesta de comida mediante procesos altamente evolucionados de˜"feedıback"˜o retroalimentación˜entre señales orexigénicas (de estimulación˜de apetito) y anorexigénicas (de saciedad) (9).

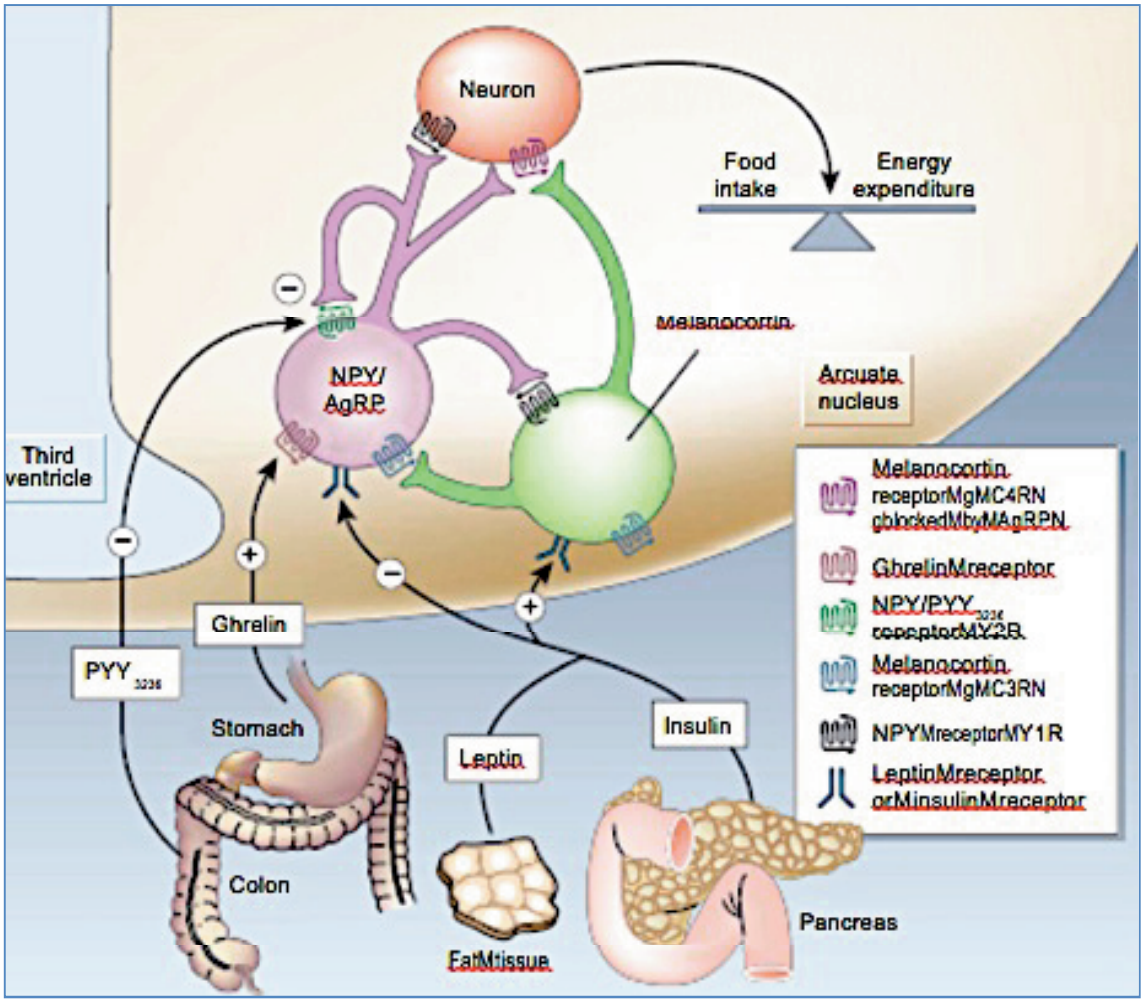

Figura 1.- Control hipotalámico del balance energético global. El apetito está˜regulado por un balance complejo que involucra señales endocrinas originadas en los tejidos periféricos y péptidos intrahipotalámicos. La leptina y la insulina inhiben las neuronas orexigénicas NPY/AgRP (morado) y estimulan las neuronas anorexigénicas de melacnocortina (verde), produciendo una disminución˜ del apetito. La grelina o el pétido PYY3ı36 inhiben las NPY/AgPR resultando en respuestas orexigénicas o anorexigénicas, respectivamente. Imagen obtenida de (10) y reproducida con permiso de la revista.

La Figura 1 resume estos procesos incluyendo, las hormonas leptina e insulina , que pueden tener distinto efecto dependiendo de su concentración˜en

sangre, las señales periféricas con efectos orexigénicos (grelina) o anorexigénicos (PYY) (10) y los componentes de señalización˜intrahipotalámicos. Las cantidades de leptina e insulina circulan en sangre en función˜de la cantidad de grasa corporal y de los niveles de glucosa, respectivamente, llegando al hipotálamo a través˜del núcleo ARC, donde la barrera hematoencefálica (BBB) resulta altamente permeable. La llegada en exceso de estas señales inhibe la activación˜ de las neuronas orexigénicas del Neuropeptido Y (NPY) y Agouti Related Peptide (AgRP) (color morado) y activa las neuronas anorexigénicas de melacortina (α1MSH) y del transcrito regulado por anfetamina (Cocaine1Anphetamine1Regulated Transcript; CART) (en verde). Este balance tiene como consecuencia una disminución˜de la ingesta de comida (saciedad) y un incremento del gasto energético. Los niveles bajos de leptina e insulina en sangre promueven, en cambio, la activación˜de las neuronas orexigénicas y la inhibición˜ de las anorexigénicas, produciendo un aumento de la sensación˜de hambre y un ahorro en el gasto energético.

La acción˜de la grelina y el péptido PYY3136, segregados en el estómago y en el colon, respectivamente, proporcionan al núcleo ARC señales positivas (grelina) y negativas (PYY) que a corto plazo promueven sensaciones de hambre y saciedad, respectivamente, mediante la activación˜ o˜ inhibición˜ selectiva de los grupos neuronales específicos del hipotálamo (11). A más˜largo plazo, los niveles altos de leptina e insulina en sangre pueden producir una desensibilización˜ de sus receptores, originando fenómenos de resistencia a la insulina y/o leptina, aumentando los niveles de glucosa en plasma y la acumulación˜de lípidos, que pueden causar eventualmente diabetes y obesidad.

3. ESTUDIOS DE MRI DE LA REGULACIÓN´HIPOTALÁMICA DEL APETITO

Las técnicas de imagen más˜utilizadas en estudios de regulación˜del apetito in vivo son: BOLD, MEMRI y DWI. BOLD infiere la actividad neuronal en las regiones cerebrales activadas por los niveles de deoxihemoglobina paramagnética y los cambios en perfusión˜sanguínea (12,13). MEMRI utiliza la acumulación˜de Mn^{2+} paramagnético durante la activación˜ neuronal, un fenómeno que refleja competitivamente la acumulación˜de Ca^{2+} durante los potenciales de acción˜(14). DWI detecta la activación˜neuronal por los cambios en los parámetros de difusión˜ del agua, consecuencia de los flujos transcelulares de iones que ocurren durante la neurotransmisión˜ (15), aunque también˜ se han atribuido los cambios a la aparición˜de procesos inflamatorios relacionados con la obesidad (16,17).

A continuación, se proporciona una descripción˜detallada de la información˜ conseguida con cada una de estas metodologías.

BOLD

BOLD es una de las técnicas más˜ utilizadas para estudiar la actividad funcional del cerebro, tanto animales como en seres humanos. Se empleó˜para de detectar, a finales de los años noventa, la respuesta del hipotálamo a administraciones de glucosa (18,19). En ambos estudios, uno con seres humanos y el otro con ratas, se administró˜ glucosa a sujetos ayunados y se detectó˜ una disminución˜ significativa de la señal de resonancia en hipotálamo tras su administración. En el estudio con humanos, se comparó˜la atenuación˜de la señal entre personas obesas y personas no obesas, resultando la inhibición˜ de las primeras mucho menor y demostrando *in vivo* por primera vez la existencia de una funcionalidad alterada en el hipotálamo de sujetos obesos.

Unos años más˜tarde, se estableció˜la primera correlación˜de BOLD, como contraste de los centros de regulación˜del apetito en animales, con un marcador de activación˜neuronal muy establecido, cıFos (20). Esta correlación˜se verificó˜un tiempo después˜ (21), en un estudio en el que se comparó˜ el efecto de la administración˜de 2ıdeoxyıDı˜glucosa en los núcleos hipotalámicos con mapas de actividad de cıFos en los mismos. Desde entonces, el uso de la técnica BOLD para el estudio de la regulación˜ del apetito en animales ha generado un número importante de contribuciones, sobre todo relacionadas con los efectos de activación˜ hipotalámica tras la administración˜ de diferentes dietas o péptidos (22,23).

En los estudios con seres humanos, se ha dedicado un esfuerzo considerable a estudiar la contribución˜ de otras zonas cerebrales extrahipotalámicas a la regulación˜ integral del apetito, utilizando estimulaciones del apetito mediante activaciones visuales (fotografías de comida) (24), o respuestas específicas a distintos sabores (25).

La Figura 2, ilustra una aplicación˜ representativa de la imagen BOLD aplicada a un estudio de regulación˜ del apetito. Este estudio monitorizó˜ la actividad cerebral de voluntarios humanos tras visualizar fotografías de alimentos calóricos y no calóricos y de utensilios relacionados con la comida, pero no comestibles. Se encontraron˜ áreas de activación˜ comunes a los estímulos de comida, independientemente de su contenido calórico, como la amígdala o el hipocampo. Solamente las fotografías de alimentos de alto valor calórico activaron las zonas del hipotálamo, entre otras regiones.

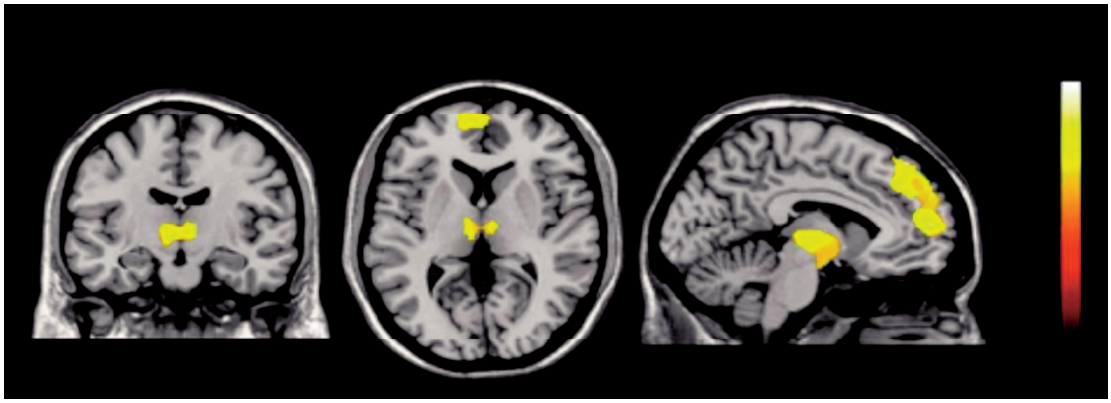

Figura 2.- Mapas paramétricos estadísticos (SPM) de las regiones activadas en el cerebro humano, medidos con BOLD, durante la visualización˜de imágenes de alto contenido calórico. La barra de color refleja la escala de la estadística SPM utilizada para el análisis. La corteza prefrontal y dorsolateral, el tálamo y el hipotálamo muestran activación˜significativa ($p<0.005$) relativamente a la activación˜detectada tras mostrar fotografías de utensilios no comestibles. Reproducido de (29) con permiso del editor.

Estos estudios, demostraron que el apetito en seres humanos es el resultado de un complejo entramado de redes neuronales que incluye, además˜ del hipotálamo y del tronco encefálico, regiones corticolímbicas y corticales. Esta múltiple regulación˜está˜relacionada aparentemente con los efectos cerebrales de recompensa a la ingesta de comida, con los estímulos del apetito presentes en el ambiente, y con otros factores cognitivos o incluso emocionales (26).

En este contexto, se han investigado con˜éxito las respuestas funcionales a señales orexigénicas y anorexigénicas en el cerebro humano. Estudios BOLD de administración˜del péptido PYY a voluntarios humanos sanos (27) con niveles altos de PYY en plasma indicaron que, como sucede en los estados alimentados, la activación˜cerebral de la corteza orbitofrontal caudolateral (OFC) predice la ingesta de comida. Por lo contrario, niveles bajos de PYY en plasma, como sucede en condiciones de ayuno, es la actividad hipotalámica la está˜correlacionada con la ingesta de comida. Así˜se pudo demostrar por primera vez que la presencia de una señal de saciedad post-ingesta cambia las zonas de activación˜cerebral.

Casi al mismo tiempo, en estudios de administración˜de grelina, una señal orexigénica (28) se pudo demostrar que la respuesta neuronal a estímulos visuales relacionados con el apetito era superior también˜en la zona OFC, y en otras regiones implicadas en la codificación˜de incentivos del apetito. En definitiva este trabajo demostró,˜que la presencia de señales metabólicas como la grelina podía˜ favorecer el consumo de alimentos mediante la activación˜de zonas del sistema hedónico.

Más˜recientemente, las aplicaciones de BOLD en estudios de regulación˜del apetito cubren principalmente tres˜ámbitos: la respuesta hipotalámica a la glucosa en condiciones normales o patológicas (29,30), las diferencias en control cerebral

de apetito en personas obesas (31), y los efectos de las hormonas y péptidos en la regulación˜del apetito(32-34).

MEMRI

La imagen MEMRI refleja de una forma directa y no invasiva la acumulación˜ de Mn^{2+} en las neuronas activadas, a través˜de los canales de calcio dependientes del voltaje. Esta se extiende trans-sinápticamente, y permite la creación˜de mapas de conectividad neural por contraste de Mn^{2+} (35). Muy posiblemente, la acumulación˜ de Mn^{2+} excede los tractos neuronales y se extiende hasta los astrocitos y redes de astrocitos circundantes, a través˜de las numerosas gap-˜ junctions que existen entre los mismos (36). En particular, ha sido posible demostrar que la activación˜neuronal va acompañada de ondas intracelulares y extracelulares de Ca^{2+} (37,38). Los iones de Mn^{2+} presentan un radio iónico es muy similar al del Ca^{2+}, por lo que pueden mimetizar muy adecuadamente y de manera competitiva las acumulaciones de Ca^{2+} durante la activación˜neuronal.

Sin embargo, en contraste con los iones Ca^{2+} que son diamagnéticos, los iones Mn^{2+} son paramagnéticos, por lo que inducen una reducción˜muy importante del tiempo de relajación˜ T1 del agua, que resulta fácilmente detectable en imágenes de resonancia pesadas en T1. Así,˜las˜áreas de activación˜y˜acumulación˜ de Mn^{2+} aparecen claramente más˜brillantes que las que no lo acumulan, en lo que se conoce como efecto MEMRI (Manganese Enhanced Magnetic Resonance Imaging) (39).

La técnica MEMRI presenta, sin embargo, una limitación˜importante, debido a que el Mn^{2+} presenta notables efectos neurotóxicos. Esto se debe a su competición˜con los flujos intracelulares de Ca^{2+}, una circunstancia que termina por alterar procesos metabólicos vitales como el ciclo tricarboxílico, los intercambios neurogliales de los neurotransmisores glutamato o GABA y los niveles fisiológicos de metabolitos hipotalámicos (40-42). Por ello, MEMRI sólo puede ser utilizada hasta ahora en animales de experimentación.

A pesar de sus limitaciones, MEMRI se ha utilizado con˜éxito para detectar actividad cerebral en ratones, y su arquitectura y conectividad neuronal, desde el comienzo de los años dos mil (43,44). Las primeras aplicaciones de MEMRI al estudio de la activación˜ hipotalámica relacionada con el control apetito, aparecieron en 2006 (45,46).

En su trabajo, Kuo et al. compararon la activación˜detectada en hipotálamo de ratones alimentados o ayunados, encontrando regiones específicas de activación, y siendo los primeros en conseguir la entrada directa de Mn^{2+} sanguíneo al hipotálamo, sin necesitar de la rotura previa de la barrera hematoencefálica.

Por su parte, Chaudri et al. encontraron diferentes patrones de activación˜ en el hipotálamo de ratones tras administrar oxintomodulina (OXM) y GLP-1, ambas hormonas anorexigénicas y generadas en el estómago. La administración˜de OXM produjo en una disminución˜ del contraste en la imagen, indicando una disminución˜de la actividad neuronal, en los núcleos ARC, PVN y supraóptico del hipotálamo. GLP-1˜causó,˜sin embargo, una disminución˜del contraste solamente en el PVN, y un incremento del mismo en el núcleo VMN. Este estudio mostró˜por primera vez cómo dos péptidos aparentemente similares podían tener distintos patrones de activación˜hipotalámica. Desde entonces, varios grupos han focalizado su trabajo a la aplicación˜ de MEMRI para el estudio de la funcionalidad hipotalámica en la regulación˜ del apetito; con estudios de administración˜ de péptidos (47-49), activación˜ cerebral en ratones transgénicos (50) y respuesta hipotalámica a alteraciones de ingesta de comida (51,52). Además, durante los últimos años, el creciente interés˜ en las aplicaciones de MEMRI y su posible interacción˜con diversos procesos hipotalámicos, ha generado la aparición˜de un número elevado de trabajos que combinan MEMRI con otras técnicas, sobre todo espectroscópicas con objeto de validar con MEMRI los diversos abordajes (50,53,40,54).

La Figura 3 muestra un ejemplo representativo de la utilización˜de MEMRI en el hipotálamo. Se trata de la comparación˜ de la actividad neuronal de los núcleos hipotalámicos en ratones normales y ratones genéticamente obesos (ob/ob), en condiciones de alimentación˜ad libitum. En este estudio, se infundió˜ Mn^{2+} en la vena de la cola de ratones control y de ratones obesos, deficientes en leptina, y se analizó˜la intensidad de señal resultante en los núcleos VMN (o VMH) y ARC, y la zona del cuarto ventrículo (V4). El contraste de manganeso comporta un mayor incremento de señal específico en los ratones obesos (en negro) que en los controles (en gris), en los núcleos ARC y VMN; algo que no sucede en el V4. Esta circunstancia revela una mayor estimulación˜orexigénica de los animales obesos, selectiva en ARC y VMN, en las mismas condiciones de alimentación˜ que los controles.

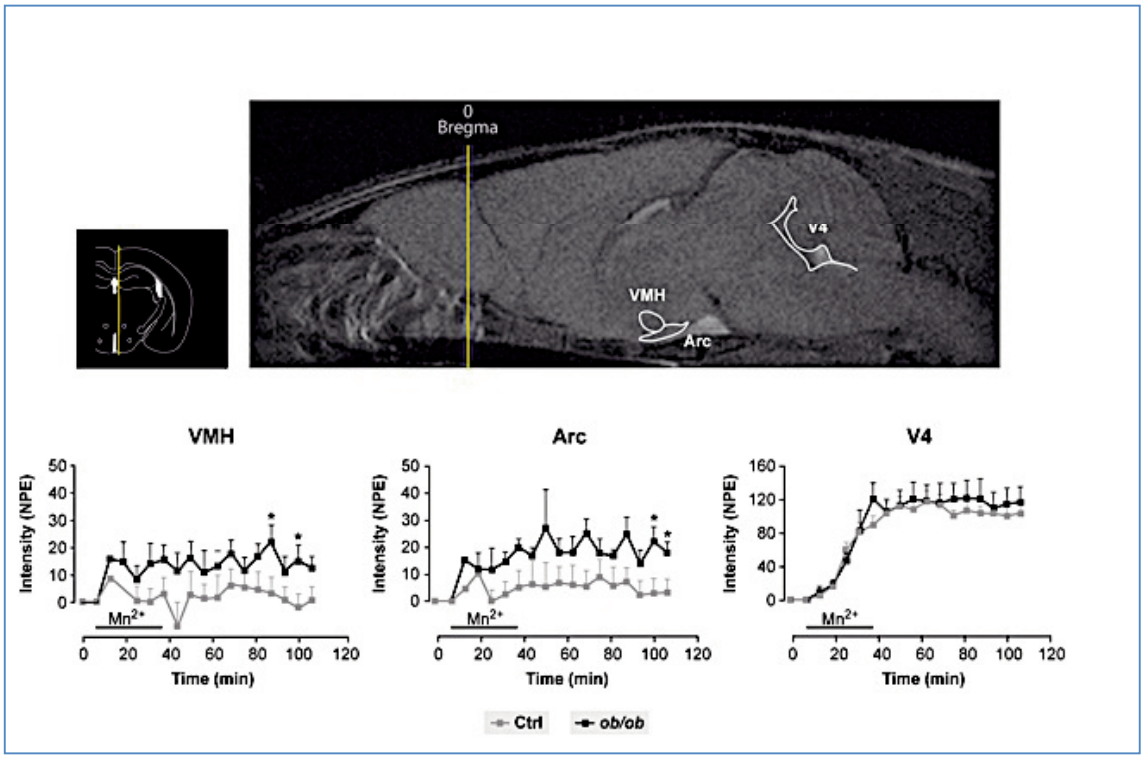

Figura 3.- Respuesta MEMRI en ratones obesos y ratones control. Inserto superior izquierdo: Localización del hipotálamo, tercer y cuarto ventrículo en un atlas anatómico [81]. Superior derecha: Incremento de señal inducido por el contraste de Mn2+ (MEMRI) en el núcleo ARC, VMN y en el cuarto ventrículo (v4). Paneles inferiores: cinética del incremento MEMRI en ARC, VMN y V4. Los ratones obesos (círculos negros) presentan mayor señal con los controles (círculos grises) en los núcleos hipotalámicos, pero no el ventrículo, revelando un efecto específico en estos. Reproducida de (50) con el permiso de la revista.

DWI

La interpretación de los modelos biofísicos que subyacen a los cambios en la difusión browniana del agua en estados fisiológicos y patológicos, ha representado un motivo de discusión frecuente en las últimas décadas.

La difusión de las moléculas de agua es un proceso aleatorio, y en medios homogéneos, el decaimiento de la señal de resonancia magnética se puede describir por una función monoexponencial caracterizada por un coeficiente de difusión D.

En la señal observada con DWI, sin embargo, lo que se obtiene es resultado de la integración de los desplazamientos microscópicos de todas las moléculas de agua presentes en un vóxel, por lo que D, se define mejor mediante un parámetro de difusión aparente (ADC) (55).

En relación con el control del apetito, algunos grupos han estudiado el papel del ADC en distintas regiones cerebrales de pacientes obesos y no obesos (16). Este estudio mostró que, el hipotálamo de los pacientes obesos presenta un mayor

valor de ADC, muy posiblemente debido a una distribución˜neurovascular alterada de fluidos, como ocurre en el edema vasogénico. De hecho, se ha demostrado que la obesidad está˜asociada a una respuesta inflamatoria crónica, caracterizada por una producción˜ anormal de adipokinas y la activación˜ de algunas rutas de señalización˜pro-inflamatorias. Esta una situación˜produce la inducción˜de varios marcadores de inflamación˜(56) y que apoya las evidencias de que las dietas de alto contenido calórico activan respuestas proinflamatorias en el hipotálamo (57,58). Esto sugiere que las respuestas inflamatorias podrían ser las verdaderas responsables de la resistencia a insulina y leptina inducida por las dietas de alto contenido calórico (59,60). Adicionalmente, la inflamación˜ puede directamente dañar el tejido cerebral, aumentando la permeabilidad de los vasos sanguíneos y causando eventualmente un incremento del número de células inflamatorias en el líquido cefalorraquídeo y en los espacios perivasculares en el cerebro (61).

En este sentido, un trabajo reciente (62), ha permitido determinar que los sujetos con mayor peso corporal presentan reducciones significativas en la integridad vascular de las estructuras cerebrales relacionadas con el control del apetito y los nuevos resultados de nuestro laboratorio, sugieren que la respuesta inflamatoria podría˜ ocurrir no solo en la obesidad, sino también˜ de forma transitoria en estados de ayuno (63).

En otros estudios, se han utilizado los cambios en ADC para describir la activación˜neuronal en seres humanos, en animales y biopsias ex vivo (15, 64-66), asociando la disminución˜ del ADC observada a un aumento de volumen neurocelular, ligado a la activación˜neuronal. De hecho, el aumento de volumen neurocelular causado por la activación˜neuronal ha sido demostrado también˜por otras técnicas (67-69). El amplio rango de valores de difusión˜ con los que se trabajaba en estos estudios, originó˜ la aparición˜ de modelos de difusión˜ más˜ elaborados, como el biexponencial (70).

Interesantemente, otros estudios demostraron que el cambio de señal de difusión˜ tras activación˜ neuronal se produce antes que el cambio detectado mediante las técnicas BOLD (65,71).

En este contexto, la primera aplicación˜ fDWI al estudio del control del apetito, fue publicada recientemente por nuestro laboratorio (63). Nuestros resultados mostraron que los coeficientes de difusión˜del agua en el hipotálamo cambian en situaciones de ayuno, tanto en ratones como en seres humanos. En ratones, fue posible detectar cambios en los núcleos ARC, DMN y VMN. Sobre esta base, es posible afirmar que la aplicación˜ de fDWI al estudio de la activación˜ cerebral en general, y de la hipotalámica en particular, abre un nuevo camino en neuroimagen funcional; donde los cambios detectados mediante las técnicas de difusión˜ocurren anteriormente a los detectados en BOLD (70), evitando además˜el

uso potencialmente tóxico de las técnicas MEMRI. Además, la capacidad de DWI de detectar diferencias en la dirección˜ preferencial de la difusión˜ mediante la implementación˜de medidas del tensor de difusión˜(DTI) (72,73) permitirá˜en el futuro, la investigación˜no invasiva de tractos neuronales específicos y sus posibles alteraciones en desordenes del apetito.

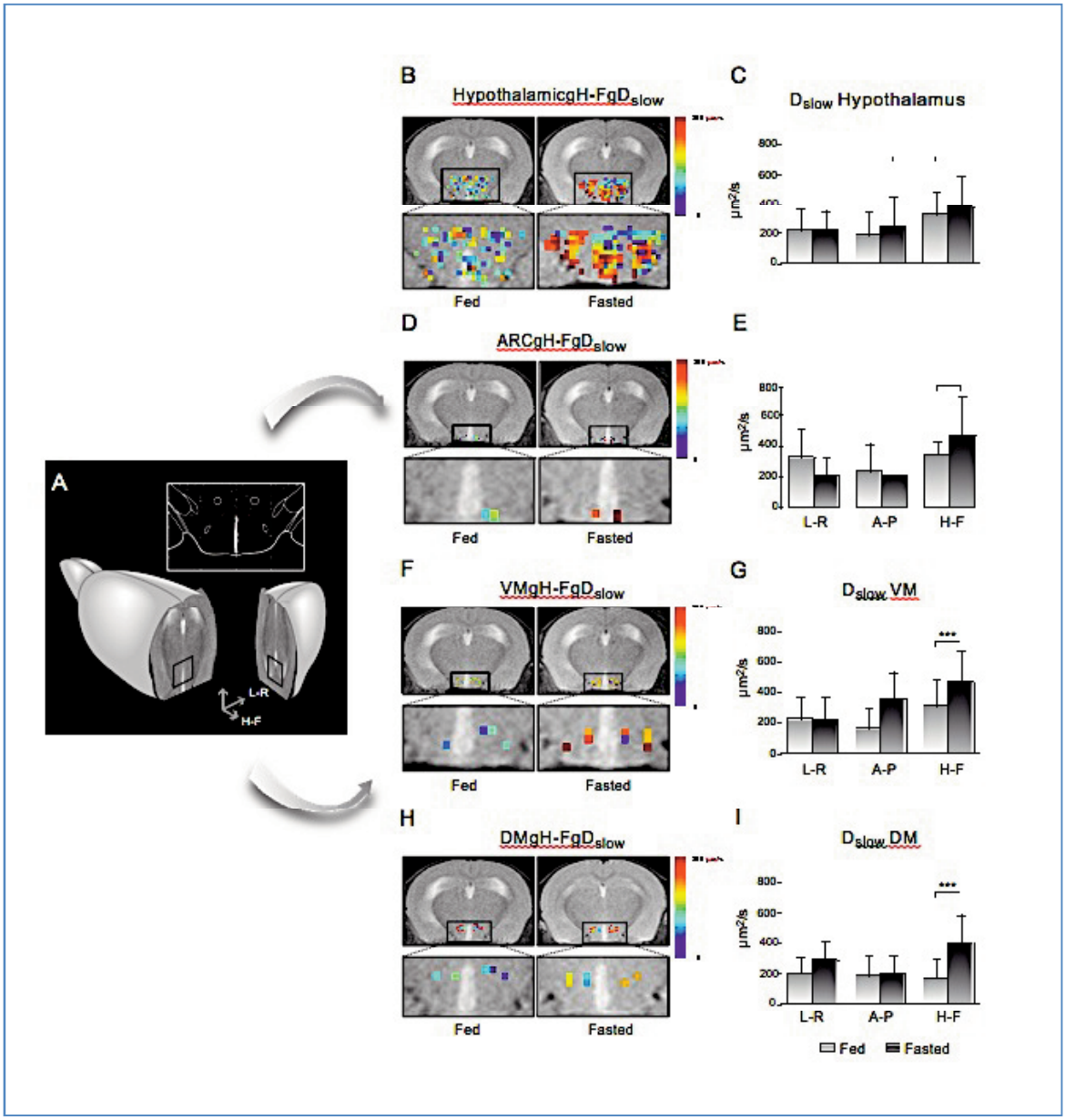

Figura 4.- Representación˜del apetito mediante fDWI en los núcleos hipotalámicos del cerebro de ratón. A: Sección˜axial que contiene el hipotálamo de un ratón˜representativo y un inserto de un atlas anatómico que muestra la localización˜de los núcleos; DMN (rojo), VMN (amarillo) y ARC (azul). B, D, F, H: Mapas de color de la difusión˜en ratones alimentados (izquierda) y ayunados (derecha), superpuestos a imágenes pesadas en T2 (T2w). La región˜hipotalámica se muestra expandida en los correspondientes paneles inferiores. C, E, G, I: Gráficos de barras del promedio del coeficiente de difusión˜lenta (Dslow) correspondiente a cada uno de los paneles B, D, F, H, respectivamente. Reproducido de (63) con permiso de la revista.

La Figura 4 muestra un ejemplo representativo del uso de fDWI en el estudio de activación˜hipotalámica en ratones, mediante los cambios observados en los parámetros de difusión˜ del agua en distintos núcleos hipotalámicos, incluyendo el ARC, VMN y DMN, cuya localización˜anatómica puede observarse en detalle en el panel 5A. Los paneles 5B, 5D, 5F y 5H muestran los mapas paramétricos del coeficiente lento de la difusión˜ (Dslow) de un animal representativo en estado alimentado (izquierda) y tras un ayuno nocturno (derecha) en el hipotálamo, ARC, VMN y ARC, respectivamente. Los gráficos de barras en los paneles 5C, 5E, 5G y 5I representan los valores promedio del parámetro correspondiente en siete animales. El incremento significativo de Dslow con el ayuno se puede interpretar como consecuencia del incremento de volumen celular consecuencia de la activación˜neuronal (60).

4. ESTUDIOS DE MRS DE LA REGULACIÓN´HIPOTALÁMICA DEL APETITO

Los métodos de imagen pueden ser completados por varias técnicas espectroscópicas, principalmente in vivo ^{1}H MRS y ex vivo ^{1}H y ^{13}C HRMAS. Estos métodos han demostrado, recientemente, haber superado las restricciones que impedían previamente evaluar adecuadamente la fisiología˜ hipotalámica, principalmente por la necesidad de utilizar grandes volúmenes de tejido para alcanzar suficiente resolución.

In vivo ^{1}H MRS de alto campo

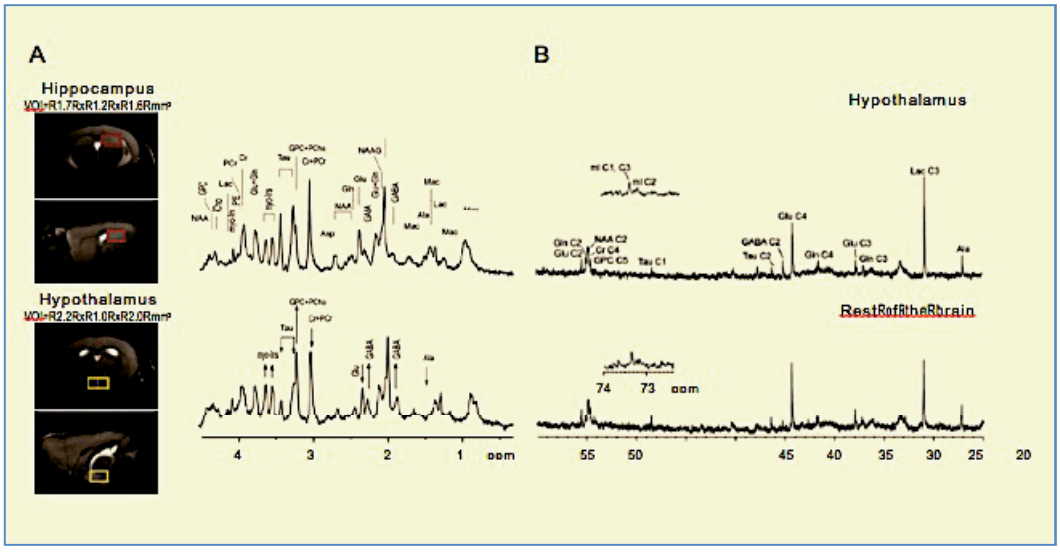

Figura 5.- Espectroscopía˜multinuclear del hipotálamo. Izquierda: Espectroscopía˜in vivo de ^{1}H en el hipocampo (paneles superiores) y en el hipotálamo (paneles inferiores) y sus correspondientes espectros. Nótese los incrementos relativos de GABA y myo-inositol (flecha hacia arriba) y decrecimientos de glutamato y taurina (flecha hacia abajo). Reproducido de (75) con permiso de la revista. Derecha: Espectro de ^{13}C HRMAS de biopsias hipotalámicas (arriba) preparado después˜de la administración˜ de [1-^{13}C] glucosa, comparado con el resto del cerebro (abajo) en un ratón˜ ayunado. Reproducido de (80) con permiso de la revista.

La espectroscopía de ^{1}H MRS de alto campo (14.1T) se ha utilizado para obtener perfiles metabólicos de elevada calidad en el hipotálamo de ratón *in vivo* (74,75). Los autores describieron que el perfil metabólico del hipotálamo es diferente del de otras estructuras cerebrales como el hipocampo.

En particular, el hipotálamo contiene concentraciones más altas de ácido γ-aminobutírico (GABA) y myo-inositol, y menores concentraciones de taurina (Figura 5A). Por otro lado, la espectroscopía de ^{1}H alto campo también se ha utilizado de forma combinada con técnicas de imagen (52). En este caso, los autores estudiaron la activación hipotalámica en ratas mediante el paradigma de Anorexia Inducida por Deshidratación (DIA), en ratas ayunadas una noche y en ratas control. El contraste de Mn^{2+} detectó activación neuronal en dos núcleos hipotalámicos: en el hipotálamo lateral (LH) y en el Periventricular (PVN), revelando una activación superior en las ratas con DIA. Por otro lado, en el perfil metabólico analizado con espectroscopia a 14.1T, se encontraron incrementos significativos de GABA en las dos condiciones respecto a las ratas control, mientras que el lactato aumentó solamente en las ratas DIA. En su conjunto, estos estudios muestran como la espectroscopia de alto campo *in vivo* acoplada con MEMRI, puede proporcionar una información muy relevante sobre los mecanismos hipotalámicos de control del apetito, balance energético global y control de peso en roedores.

Espectroscopía ^{13}C y ^{1}H de alto campo en ángulo mágico

La espectroscopía de ^{13}C es un método que ha mostrado un gran potencial en la investigación de los mecanismos de acoplamiento neuroglial tanto *in vivo* como *in vitro* (76-79). La baja abundancia natural del ^{13}C (1,1%), sin embargo, y la baja sensibilidad del método, imponían la necesidad de utilizar vóxeles de tamaño relativamente grande *in vivo*, que excedían significativamente las dimensiones del hipotálamo.

Para superar este inconveniente, nuestro laboratorio ha implementado recientemente una nueva colección de métodos espectroscópicos *ex vivo*, concretamente la espectroscopía de ^{13}C alta resolución de ángulo mágico (HRMAS). Adquiriendo espectros de resonancia magnética de biopsias hipotalámicas, con la muestra inclinada 54.7 grados con respecto al campo magnético estático, se eliminan los acoplamientos dipolares que ensanchan las resonancias *in vivo*, y se obtienen espectros de alta resolución de la biopsia similares a los que se obtienen en solución. Notablemente, estos espectros pueden obtenerse con muestras de tan solo 5-10 mg, un tamaño similar al del hipotálamo en roedores. Utilizando esta tecnología, se han investigado los efectos del ayuno nocturno y de la administración de grelina en el perfil metabólico, así como la incorporación de ^{13}C desde (1-^{13}C) glucosa en los metabolitos hipotalámicos (80).

Los resultados mostraron que el ayuno nocturno induce incrementos significativos en la incorporación de ^{13}C en (2-^{13}C) GABA y (3-^{13}C) Lactato, mientras que la infusión del péptido orexigénico no afectó al marcaje en ^{13}C de los metabolitos. Estos resultados revelaron que el ayuno parece incrementar las neurotransmisiones GABAérgicas y la glucolisis. Sin embargo, la infusión de grelina no induce los mismos efectos, indicando que factores adicionales a la la grelina resultan necesarios para mimetizar la compleja respuesta hipotalámica.

Finalmente, se han investigado recientemente los mecanismos neurogliales relacionados con la señalización de la leptina en el hipotálamo, empleando ratones ob/ob, deficientes en leptina, y ratones control (50). Este estudio combinó técnicas MEMRI con ^{1}H y ^{13}C HRMAS, empleando infusiones de (1-^{13}C) glucosa, un sustrato principalmente neuronal, o de (2-^{13}C) acetato, un sustrato primordialmente glial. Los ratones deficientes en leptina mostraron un contraste de Mn^{2+} aumentado en los núcleos hipotalámicos (Figura 3) y una acumulación incrementada de ^{13}C, solamente en los carbonos de glutamato y glutamina derivados de (1-^{13}C) glucosa, pero no en los derivados de (2-^{13}C) acetato.

El abordaje combinado MEMRI-^{13}C HRMAS mostró por primera vez que el incremento en la señal MEMRI asociada a la activación neuronal de las rutas orexigénicas, ocurre simultáneamente con un incremento en el metabolismo oxidativo y en el ciclo gultamato-glutamina que soporta la neurotransmisión glutamatérgica. Considerando estas observaciones junto con las evidencias de aumento de neurotransmisiones GABAérgicas (80), los resultados parecen indicar que la estimulación orexigénica del hipotálamo resulta en un incremento de neurotransmisiones GABAérgicas y glutamatérgicas, implicando un aumento de los ciclos transcelulares de glutamato-glutamina y GABA entre neuronas y astrocitos. En general, los resultados adquiridos hasta ahora indican que los eventos de transmisión sináptica que soportan la señalización neuroendocrina en el hipotálamo siguen unos mecanismos de compartimentación neuroglial similares a otros tipos de activaciones sensoriales o motoras, pero bajo control hormonal.

5. CONCLUSIONES Y PERSPECTIVAS FUTURAS.

Las secciones anteriores han resumido la información obtenida sobre la función hipotalámica de regulación del apetito *in vivo*, utilizando técnicas de imagen y espectroscopía por Resonancia Magnética. Los resultados revelan que la estimulación orexigénica está asociada a: un incremento de perfusión sanguínea del hipotálamo como revelan las técnicas BOLD, un incremento de actividad neuronal glutamatérgica y GABAérgica como revelan los estudios MEMRI y ^{13}C HRMAS y un incremento de volumen neuroglial compatible con la acumulación de

iones asociada al disparo de las neuronas orexigénicas y a fenómenos inflamatorios, como revelan las técnicas fDWI.

Estas características hacen que la transmisión˜neuroendocrina durante el apetito adopte mecanismos sinápticos similares a otras formas de estimulación˜ sensorial o motora. Sin embargo, en las sinapsis neuroendocrinas, la transmisión˜ del mensaje glutamatérgico o GABAérgico, parece estar controlada principalmente por la concentración˜sanguínea del efector hormonal que podría˜interaccionar adicionalmente con elementos del sistema inmunitario y de la cascada inflamatoria, resultando en el sistema más˜complejo de neuroregulación˜que conocemos.

Por otro lado, las técnicas de Resonancia Magnética han permitido diseñar un nuevo escenario para los mecanismos neuroendocrinos que subyacen a la regulación˜ del apetito. A pesar del progreso alcanzado, varios aspectos importantes permanecen aún˜por esclarecer. En particular, la discriminación˜entre neurotransmisiones activadoras e inhibidoras resulta difícil mediante estas metodologías, pues ambas conducen al mismo resultado espectroscópico o de imagen. Tampoco resulta posible incrementar aún˜más˜la resolución˜espacial y temporal de la imaginería˜ mejorando la resolución˜ obtenida de los núcleos hipotalámicos y alcanzando resoluciones celulares o subcelulares. La combinación˜ de técnicas MRI o MRS con abordajes electrofisiológicos hipotalámicos y la utilización˜de imanes de campo magnético superior al actual podría˜contribuir a superar estas limitaciones.

Finalmente, los abordajes MRI y MRS descritos en esta revisión˜para la elucidación˜de los mecanismos de regulación˜hipotalámica del apetito *in vivo*, pueden ser fácilmente extendidos a otras funciones hipotalámicas incluyendo, la sed y osmoregulación, la regulación˜de la presión˜sanguínea, la termorregulación, los ritmos circadianos y algunas manifestaciones de agresividad.

6. AGRADECIMIENTOS

Los autores manifiestan su agradecimiento a D. Javier Pérez CSIC, por su competencia en la preparación de las ilustraciones.

Este trabajo ha sido financiado en parte por las ayudas: SAF-2008-01327, SAF2011-23622 del Ministerio de Economía y Competitividad y S2010/BMD-2349 de la Comunidad de Madrid concedidas a Sebastián Cerdán y la beca predoctoral BES 2009-027615 del Ministerio de Economía y Competitividad concedida a Blanca Lizarbe.

7. ABREVIATURAS

ARC: núcleo Arcuado, **AgRP:** Agouti related protein, **BOLD:** Contraste en Imagen por Resonancia Magnética ponderada en el nivel de oxigenación de la sangre, **CART:** transcrito regulado por cocaína y anfetamina, **DIA:** Anorexia inducida por deshidratación, DMD: núcleo dorsomedial, **DWI:** Imagen por Resonancia Magnética ponderada en difusión, **MEMRI:** Imagen por Resonancia Magnética ponderada en captación de manganeso, **MRI:** Imagen por Resonancia Magnética, **MRS:** Espectroscopía por Resonancia Magnética, **MSH:** ruta de la melanocortina, **NPY:** neuropéptido Y, **VMN:** núcleo Ventromedial, **V4:** cuarto ventrículo.

8. REFERENCIAS

1. Lin, D., et al.(2011) Functional identification of an aggression locus in the mouse hypothalamus. Nature. 470(7333): p. 221-6.
2. Swaab, D.F., Hofman, M.A., Mirmiran, M., Ravid, R., van Leewen, F.W. Eds.(1992) The human hypothalamus in health and disease. Proceedings of the 17th International Summer School of Brain Research. Amsterdam, The Netherlands, 26-30 August 1991. Prog Brain Res. 93: p. 1-481.
3. Mori, Y., et al.(1991) Chronic recording of electrophysiological manifestation of the hypothalamic gonadotropin-releasing hormone pulse generator activity in the goat. Neuroendocrinology. 53(4): p. 392-5.
4. Sani, S., et al.(2009) Microelectrode recording in the posterior hypothalamic region in humans. Neurosurgery. 64(3 Suppl): p. ons161-7; discussion ons167-9.
5. Carnell, S., et al.(2012) Neuroimaging and obesity: current knowledge and future directions. Obes Rev. 13(1): p. 43-56.
6. Gibson, C.D., et al.(2010) Neuroimaging, gut peptides and obesity: novel studies of the neurobiology of appetite. J Neuroendocrinol. 22(8): p. 833-45.
7. Coll, A.P., I.S. Farooqi, and S. O'Rahilly(2007) The hormonal control of food intake. Cell. 129(2): p. 251-62.
8. Morton, G.J., et al.(2006) Central nervous system control of food intake and body weight. Nature. 443(7109): p. 289-95.
9. Stanley, S., et al.(2005) Hormonal regulation of food intake. Physiol Rev. 85(4): p. 1131-58.
10. Schwartz, M.W. and G.J. Morton(2002) Obesity: keeping hunger at bay. Nature. 418(6898): p. 595-7.
11. Tang-Christensen, M., et al.(2004) Central administration of ghrelin and agouti-related protein (83-132) increases food intake and decreases spontaneous locomotor activity in rats. Endocrinology. 145(10): p. 4645-52.
12. Logothetis, N.K. and B.A. Wandell(2004) Interpreting the BOLD signal. Annu Rev Physiol. 66: p. 735-69.
13. Zhu, X.H., et al.(1998) Simultaneous oxygenation and perfusion imaging study of functional activity in primary visual cortex at different visual stimulation frequency: quantitative correlation between BOLD and CBF changes. Magn Reson Med. 40(5): p. 703-11.
14. Koretsky, A.P. and A.C. Silva(2004) Manganese-enhanced magnetic resonance imaging (MEMRI). NMR Biomed. 17(8): p. 527-31.

15. Darquie, A., et al.(2001) Transient decrease in water diffusion observed in human occipital cortex during visual stimulation. Proc Natl Acad Sci U S A. 98(16): p. 9391-5.

16. Alkan, A., et al.(2008) Diffusion-weighted imaging features of brain in obesity. Magn Reson Imaging. 26(4): p. 446-50.

17. Mueller, K., et al.(2011) Sex-dependent influences of obesity on cerebral white matter investigated by diffusion-tensor imaging. PLoS One. 6(4): p. e18544.

18. Mahankali, S., et al.(2000) In vivo fMRI demonstration of hypothalamic function following intraperitoneal glucose administration in a rat model. Magn Reson Med. 43(1): p. 155-9.

19. Matsuda, M., et al.(1999) Altered hypothalamic function in response to glucose ingestion in obese humans. Diabetes. 48(9): p. 1801-6.

20. Stark, J.A., et al.(2006) Functional magnetic resonance imaging and c-Fos mapping in rats following an anorectic dose of m-chlorophenylpiperazine. Neuroimage. 31(3): p. 1228-37.

21. Dodd, G.T., S.R. Williams, and S.M. Luckman(2010) Functional magnetic resonance imaging and c-Fos mapping in rats following a glucoprivic dose of 2-deoxy-D-glucose. J Neurochem. 113(5): p. 1123-32.

22. Li, J., et al.(2012) Correlations of macronutrient-induced functional magnetic resonance imaging signal changes in human brain and gut hormone responses. Am J Clin Nutr. 96(2): p. 275-82.

23. Min, D.K., et al.(2011) Changes in differential functional magnetic resonance signals in the rodent brain elicited by mixed-nutrient or protein-enriched meals. Gastroenterology. 141(5): p. 1832-41.

24. Killgore, W.D., et al.(2003) Cortical and limbic activation during viewing of high- versus low-calorie foods. Neuroimage. 19(4): p. 1381-94.

25. Smeets, P.A., et al.(2005) Functional magnetic resonance imaging of human hypothalamic responses to sweet taste and calories. Am J Clin Nutr. 82(5): p. 1011-6.

26. Berthoud, H.R.(2004) Neural control of appetite: cross-talk between homeostatic and non-homeostatic systems. Appetite. 43(3): p. 315-7.

27. Batterham, R.L., et al.(2007) PYY modulation of cortical and hypothalamic brain areas predicts feeding behaviour in humans. Nature. 450(7166): p. 106-9.

28. Malik, S., et al.(2008) Ghrelin modulates brain activity in areas that control appetitive behavior. Cell Metab. 7(5): p. 400-9.

29. Purnell, J.Q., et al.(2011) Brain functional magnetic resonance imaging response to glucose and fructose infusions in humans. Diabetes Obes Metab. 13(3): p. 229-34.

30. Vidarsdottir, S., et al.(2007) Glucose ingestion fails to inhibit hypothalamic neuronal activity in patients with type 2 diabetes. Diabetes. 56(10): p. 2547-50.

31. Tomasi, D., et al.(2009) Association of body mass and brain activation during gastric distention: implications for obesity. PLoS One. 4(8): p. e6847.

32. Baicy, K., et al.(2007) Leptin replacement alters brain response to food cues in genetically leptin-deficient adults. Proc Natl Acad Sci U S A. 104(46): p. 18276-9.

33. Guthoff, M., et al.(2010) Insulin modulates food-related activity in the central nervous system. J Clin Endocrinol Metab. 95(2): p. 748-55.

34. Jones, R.B., et al.(2012) Functional neuroimaging demonstrates that ghrelin inhibits the central nervous system response to ingested lipid. Gut. 61(11): p. 1543-51.

35. Pautler, R.G.(2004) In vivo, trans-synaptic tract-tracing utilizing manganese-enhanced magnetic resonance imaging (MEMRI). NMR Biomed. 17(8): p. 595-601.

36. Andrew, R.D., et al.(1981) Dye transfer through gap junctions between neuroendocrine cells of rat hypothalamus. Science. 211(4487): p. 1187-9.

37. Jaffe, L.F.(2008) Calcium waves. Philos Trans R Soc Lond B Biol Sci. 363(1495): p. 1311-6.

38. Jaffe, L.F.(2010) Fast calcium waves. Cell Calcium. 48(2-3): p. 102-13.

39. Lee, J.H., et al.(2005) Manganese-enhanced magnetic resonance imaging of mouse brain after systemic administration of MnCl2: dose-dependent and temporal evolution of T1 contrast. Magn Reson Med. 53(3): p. 640-8.

40. Just, N., et al.(2011) Effect of manganese chloride on the neurochemical profile of the rat hypothalamus. J Cereb Blood Flow Metab. 31(12): p. 2324-33.

41. Zwingmann, C., D. Leibfritz, and A.S. Hazell(2003) Energy metabolism in astrocytes and neurons treated with manganese: relation among cell-specific energy failure, glucose metabolism, and intercellular trafficking using multinuclear NMR-spectroscopic analysis. J Cereb Blood Flow Metab. 23(6): p. 756-71.

42. Zwingmann, C., D. Leibfritz, and A.S. Hazell(2004) Brain energy metabolism in a sub-acute rat model of manganese neurotoxicity: an ex vivo nuclear magnetic resonance study using [1-^{13}C]glucose. Neurotoxicology. 25(4): p. 573-87.

43. Aoki, I., et al.(2002) Dynamic activity-induced manganese-dependent contrast magnetic resonance imaging (DAIM MRI). Magn Reson Med. 48(6): p. 927-33.

44. Aoki, I., et al.(2004) In vivo detection of neuroarchitecture in the rodent brain using manganese-enhanced MRI. Neuroimage. 22(3): p. 1046-59.

45. Chaudhri, O.B., et al.(2006) Differential hypothalamic neuronal activation following peripheral injection of GLP-1 and oxyntomodulin in mice detected by manganese-enhanced magnetic resonance imaging. Biochem Biophys Res Commun. 350(2): p. 298-306.

46. Kuo, Y.T., et al.(2006) Manganese-enhanced magnetic resonance imaging (MEMRI) without compromise of the blood-brain barrier detects hypothalamic neuronal activity in vivo. NMR Biomed. 19(8): p. 1028-34.

47. Hankir, M.K., et al.(2011) Peptide YY 3-36 and pancreatic polypeptide differentially regulate hypothalamic neuronal activity in mice in vivo as measured by manganese-enhanced magnetic resonance imaging. J Neuroendocrinol. 23(4): p. 371-80.

48. Parkinson, J.R., O.B. Chaudhri, and J.D. Bell(2009) Imaging appetite-regulating pathways in the central nervous system using manganese-enhanced magnetic resonance imaging. Neuroendocrinology. 89(2): p. 121-30.

49. Parkinson, J.R., et al.(2009) Differential patterns of neuronal activation in the brainstem and hypothalamus following peripheral injection of GLP-1, oxyntomodulin and lithium chloride in mice detected by manganese-enhanced magnetic resonance imaging (MEMRI). Neuroimage. 44(3): p. 1022-31.

50. Delgado, T.C., et al.(2011) Neuroglial metabolic compartmentation underlying leptin deficiency in the obese ob/ob mice as detected by magnetic resonance imaging and spectroscopy methods. J Cereb Blood Flow Metab. 31(12): p. 2257-66.

51. Anastasovska, J., et al.(2012) Fermentable carbohydrate alters hypothalamic neuronal activity and protects against the obesogenic environment. Obesity (Silver Spring). 20(5): p. 1016-23.

52. Just, N. and R. Gruetter(2011) Detection of neuronal activity and metabolism in a model of dehydration-induced anorexia in rats at 14.1 T using manganese-enhanced MRI and ^{1}H MRS. NMR Biomed. 24(10): p. 1326-36.

53. Gutman, D.A., et al.(2013) Mapping of the mouse olfactory system with manganese-enhanced magnetic resonance imaging and diffusion tensor imaging. Brain Struct Funct. 218(2): p. 527-37.

54. Silva, A.C.(2012) Using manganese-enhanced MRI to understand BOLD. Neuroimage. 62(2): p. 1009-13.
55. Le Bihan, D.(2003) Looking into the functional architecture of the brain with diffusion MRI. Nat Rev Neurosci. 4(6): p. 469-80.
56. Bastard, J.P., et al.(2006) Recent advances in the relationship between obesity, inflammation, and insulin resistance. Eur Cytokine Netw. 17(1): p. 4-12.
57. De Souza, C.T., et al.(2005) Consumption of a fat-rich diet activates a proinflammatoryresponse and induces insulin resistance in the hypothalamus. Endocrinology. 146(10): p. 4192-9.
58. Wang, X., et al.(2012) Increased hypothalamic inflammation associated with the susceptibility to obesity in rats exposed to high-fat diet. Exp Diabetes Res. 2012: p. 847246.
59. Kleinridders, A., et al.(2009) MyD88 signaling in the CNS is required for development of fatty acid-induced leptin resistance and diet-induced obesity. Cell Metab. 10(4): p. 249-59.
60. Wisse, B.E. and M.W. Schwartz(2009) Does hypothalamic inflammation cause obesity? Cell Metab. 10(4): p. 241-2.
61. Man, S., E.E. Ubogu, and R.M. Ransohoff(2007) Inflammatory cell migration into the central nervous system: a few new twists on an old tale. Brain Pathol. 17(2): p. 243-50.
62. Cazettes, F., et al.(2011) Obesity-mediated inflammation may damage the brain circuit that regulates food intake. Brain Res. 1373: p. 101-9.
63. Lizarbe, B., et al.(2013) Imaging hypothalamic activity using diffusion weighted magnetic resonance imaging in the mouse and human brain. Neuroimage. 64: p. 448-57.
64. Flint, J., et al.(2009) Diffusion weighted magnetic resonance imaging of neuronal activity in the hippocampal slice model. Neuroimage. 46(2): p. 411-8.
65. Kohno, S., et al.(2009) Water-diffusion slowdown in the human visual cortex on visual stimulation precedes vascular responses. J Cereb Blood Flow Metab. 29(6): p. 1197-207.
66. Yacoub, E., et al.(2008) Decreases in ADC observed in tissue areas during activation in the cat visual cortex at 9.4 T using high diffusion sensitization. Magn Reson Imaging. 26(7): p. 889-96.
67. Andrew, R.D. and B.A. MacVicar(1994) Imaging cell volume changes and neuronal excitation in the hippocampal slice. Neuroscience. 62(2): p. 371-83.
68. Hansson, E., et al.(2000) Astroglia and glutamate in physiology and pathology: aspects on glutamate transport, glutamate-induced cell swelling and gap-junction communication. Neurochem Int. 37(2-3): p. 317-29.
69. Stroman, P.W., et al.(2008) Magnetic resonance imaging of neuronal and glial swelling as an indicator of function in cerebral tissue slices. Magn Reson Med. 59(4): p. 700-6.
70. Le Bihan, D., et al.(2006) Direct and fast detection of neuronal activation in the human brain with diffusion MRI. Proc Natl Acad Sci U S A. 103(21): p. 8263-8.
71. Aso, T., et al.(2013) Comparison of diffusion-weighted fMRI and BOLD fMRI responses in a verbal working memory task. Neuroimage. 67: p. 25-32.
72. Ahn, S. and S.K. Lee(2011) Diffusion tensor imaging: exploring the motor networks and clinical applications. Korean J Radiol. 12(6): p. 651-61.
73. Le Bihan, D., et al.(2001) Diffusion tensor imaging: concepts and applications. J Magn. Reson Imaging. 13(4): p. 534-46.

74. Duarte, J.M., et al.(2012) The neurochemical profile quantified by in vivo ^{1}H NMR spectroscopy. Neuroimage. 61(2): p. 342-62.

75. Lei, H., et al.(2010) Neurochemical profile of the mouse hypothalamus using in vivo ^{1}H MRS at 14.1T. NMR Biomed. 23(6): p. 578-83.

76. Cruz, F. and S. Cerdan(1999) Quantitative ^{13}C NMR studies of metabolic compartmentation in the adult mammalian brain. NMR Biomed. 12(7): p. 451-62.

77. Gruetter, R., et al.(2003) Localized in vivo ^{13}C NMR spectroscopy of the brain. NMR Biomed. 16(6-7): p. 313-38.

78. Rodrigues, T.B., et al.(2009) ^{13}C NMR tracers in neurochemistry: implications for molecular imaging. Q J Nucl Med Mol Imaging. 53(6): p. 631-45.

79. Rothman, D.L., et al.(2003) In vivo NMR studies of the glutamate neurotransmitter flux and neuroenergetics: implications for brain function. Annu Rev Physiol. 65: p. 401-27.

80. Violante, I.R., et al.(2009) Cerebral activation by fasting induces lactate accumulation in the hypothalamus. Magn Reson Med. 62(2): p. 279-83.

81. Paxinos, G., Franklin, K., The Mouse Brain in Stereotaxic Coordinates2001, New York: Academic Press.